Investigation into energy dissipation in equal channel angular extrusion

Lupoi, Rocco

Award date:
2008

Awarding institution:
University of Bath

Investigation into Energy Dissipation in Equal Channel Angular Extrusion

UNIVERSITY OF
BATH

Rocco Lupoi

A thesis submitted for the degree of Doctor of Philosophy
University of Bath
Department of Mechanical Engineering
May 2008

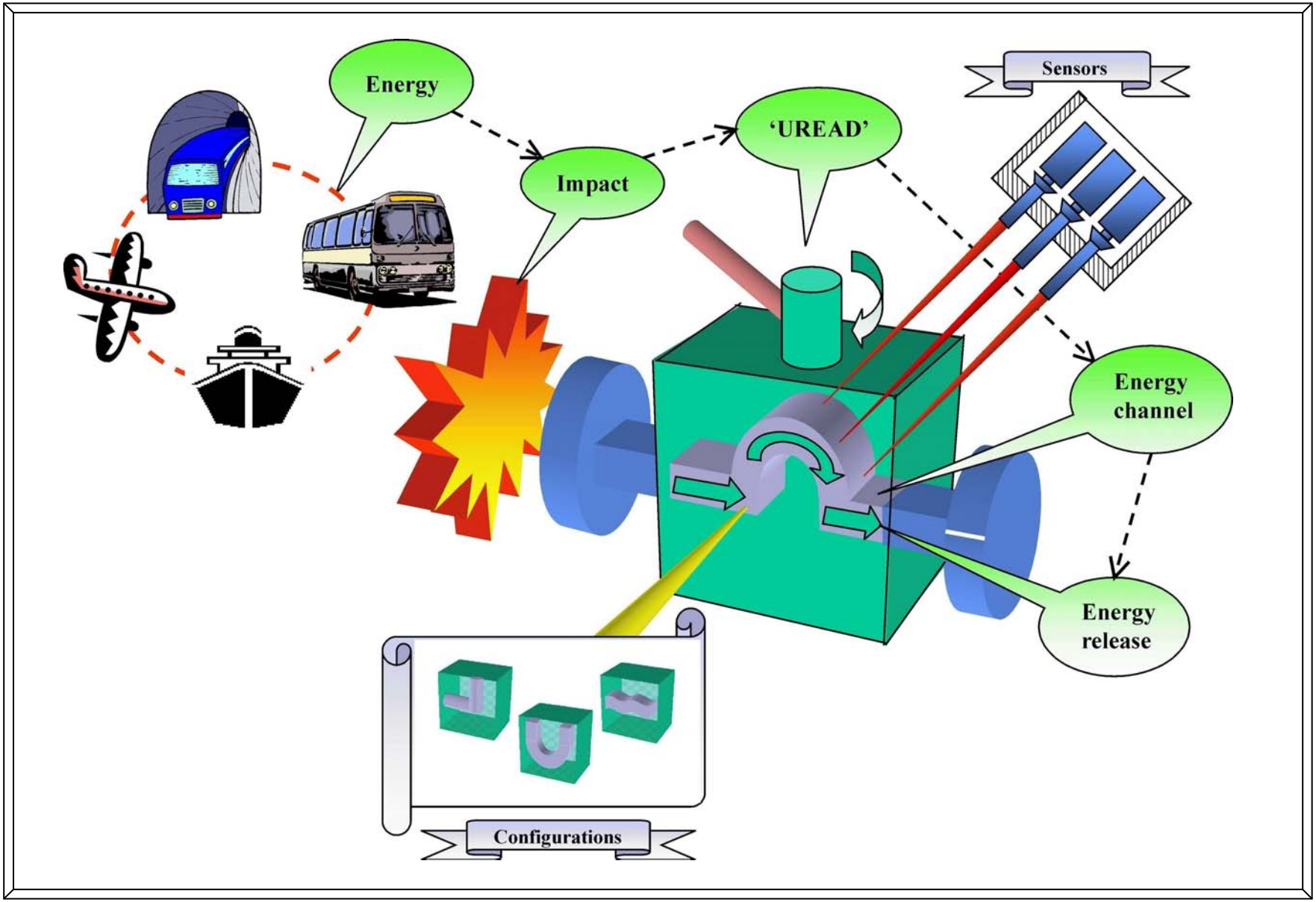
Energy
Impact
'UREAD'
Sensors
Energy channel
Energy release
Configurations


“ Vorrei dedicare il lavoro di questa Tesi alla mia Famiglia, ed in particolare a mio Nonno Giuseppe e mia Nonna Teresa
I would like to dedicate this thesis to my Family, and in particular to my Grandfather Giuseppe and my Grandmother Teresa ”

ABSTRACT

The field of energy absorption is definitely one the most important in engineering design, as many types of static and dynamic structures, designed and built for different purposes and tasks, require energy absorption capabilities under loading conditions. This thesis is aimed at the introducing experimental and theoretical analyses of a novel and revolutionary technique to dissipate unwanted energy in engineering systems.

An extensive literature review on existing energy absorbers was undertaken in relevant application fields such as structural and personal protection. Hence, devices attached to buildings and designed to dissipate energy due to severe earthquakes have been discussed and compared. Types considered, in this review, are mainly based on friction, viscoelasticity and material yielding mechanisms. Furthermore, methodologies to strengthen structures against impacts such as those used in armoured walls are described, and their capabilities assessed. In addition techniques to protect the human body against dangerous loads were reviewed, and important issues for chest and head protection, leg defences in football and safety in motorcycles have been investigated. Experimental results about energy absorption in crash tests have been studied. Also, as an example the use of current technologies to dissipate energy during landing operations in aircrafts have been considered. A classified chart of energy absorption devices in different applications has been produced and referenced. In general most energy absorption devices were shown to be capable to eventually dissipate dangerous and unwanted energy, but poor reusability and predictability after impact were not part of the design process. The research base in this thesis is a novel energy dissipation technique capable of designing Universal Reusable Energy Absorption Devices (UREAD). This technique exploits the principles and working mechanisms that are used in extrusion of deformable materials through intersecting channels. Such mechanism of deformation is known in literature as Equal Channel Angular Extrusion (ECAE). ECAE is one of the severe plastic deformation processes.

A theoretical analysis of internal pressure and stresses developed at the interface with the tools has been presented for channels of different geometrical parameters. In addition, energy absorption capabilities have been analysed by the Upper Bound

method. Also, a numerical solution based on the implementation of the Finite Element Analysis, in ANSYS commercial package was obtained to show the intensity of stress distribution in the deforming material and the tools surrounding it.

UREAD devices of different dimensions and geometries were designed, manufactured and tested using an experimental set up constructed for this work. Circular and square cross-sectional channels were tested using various deformable materials. Experimental results were compared with theoretical distributions, and several analogies were highlighted and discussed.

Special tools were designed and manufactured to study experimentally the normal stresses at contact surfaces using the so called “Pressure Pin Technique”.

Also, an experimental apparatus has been built to simulate the potential implementation of UREAD devices against the occurrence of heavy impacts and the effect of the energy absorber was experimentally measured at the instant of ground impact.

ACKNOWLEDGEMENTS

I would like to state my deepest thankfulness to my Supervisor Dr. Osman, for giving me the opportunity to study for a PhD degree. I sincerely do not have enough words to express my appreciation for his help and time provided along all these years, from experimental and theoretical investigations, to the writing of articles and the presentation of papers in conferences. His comments, suggestions, advices, criticism and observations have extremely improved my skills as an engineer, and have provided an exceptional guidance in every single field of study.

I would also like to say thank you to all technicians and apprentices in the Department of Mechanical Engineering Laboratories, who made possible the progress of my project by making tools and granting precious advice. Special thanks go to Robert Pepler, David Wood, Vijay Rajput and Steve Coomes, who directly supported my work by machining dies and providing instrumentation equipment; and thanks to Andy Galloway, Richard Weston, Colin Brain, Andy Green, Brian Purnell for their help and recommendations.

Many thanks to the University of Bath, Mechanical Engineering Department, for sponsoring my project, and for providing an excellent work environment. I would also like to express my gratitude to my flat-mates and close friends; in particular to Domenico, Lorena, Stephanie, Diego, Jacque, Killian, Ramon, Carla, Maria, Marta, Margarida, Luisa, Eduardo, Paolo, Reme and the SOAR music band. A special thank you goes to my girlfriend Despina.

Above all, I must say thanks to my Dad, my Mum and my Grandparents for the infinite support and trust they provided me with all along these years.

NOMENCLATURE

Symbols		Units
α	Shear angle	degrees
γ	Channels inclination angle	degrees
δ	Descend angle	degrees
ε	Strain	-
η	Landing platform elastic displacement	mm
μ	Friction coefficient	-
σ	Normal stress on horizontal direction	N/mm^2
τ_k	Deformable material yield shear stress	N/mm^2

Alphabet

A	Channel cross sectional area	mm^2
b	Width of the vertical channel	mm
D	Diameter	mm
E	Energy absorbed	J
E_{re} (%)	Impact energy reduction	-
E_t	Impact energy	J
E_{UREAD}	Energy absorbed by the UREAD device during impact	J
F	Total force on the cavity corner boundary	N
Fa	Impact force maximum amplitude	N
F_d	Forming pressure	N
Fi	Impact force on the landing platform	N
F_r, F_l	Forces acting on the right and left hand side tool	N
$F_{t,r}$, $F_{t,l}$	Friction forces on the right and left hand side tool	N
g	Gravitational acceleration	m/s^2
G	Area of the velocity discontinuity surface	mm^2
h	Width of the horizontal channel	mm
H	Landing frame height	m

l	Length of the velocity discontinuity surface	mm
L	Stroke length	mm
L_h	Material length in the horizontal channel	mm
m	Friction factor	-
m_1, m_2	Mass of the main block and sliding structure of the landing carriage	Kg
N, J	Intersecting channels in UREAD devices	-
p	Pressure on the cavity corner boundary	N/mm^2
p_{ave} , $p_{ave,m}$	Average pressures on the cavity corner boundary	N/mm^2
p_c	Pressure acting on the pin head	N/mm^2
p_d	Forming pressure	N
p_{ext}	Average extrusion pressure	N/mm^2
p_n	Pressure on the material in the horizontal channel	N/mm^2
p_r , p_l	Pressure acting on the right and left hand side tool	N/mm^2
q	Pressure on the material in the vertical channel	N/mm^2
R_1, R_2	Vertical forces components on cavity corner boundary	N
s	Pin distance	mm
S	Resistance force	N
t_c	Free fall time	sec
v_1	Material vertical velocity component	mm/s
v_2	Material horizontal velocity component	mm/s
v_f	Exit velocity of the landing carriage	mm/s
v_i	Initial velocity of the landing carriage	mm/s
v_n , v_m	Vertical components of the exit velocity and impact velocity	mm/s
v_r	Relative velocity	mm/s
v_t	Horizontal component of the exit velocity	mm/s
W	Deformation work	J
X	Weight positioning distance	mm
Z	Impact distance of the landing carriage	mm

TABLE OF CONTENTS

LIST OF FIGURES

Page

LIST OF TABLES

Page

Chapter 1

INTRODUCTION

In the prehistoric time, humans used to live gathered in very small communities, when only little and cold shelters were available in nature. However, the first ever source of energy was discovered by chance: the fire. Since that day, the standard of living of humans significantly improved. It was then possible to light dark places, to defeat the cold and to fight wild animals. On the other hand, problems that were rather unknown before had emerged and needed to be overcome. As an example, it became easy to be injured or killed due to an accident. It is realized that the benefits of new discoveries of energy usage, are rather useful but dangerous in some respect, if not controlled or used without consideration to safety.

History has mainly been written by important inventions that led humanity to significantly improve the quality of living and life expectancy. In particular, a crucial drive is certainly given to the progress in discovering the sources of energy, and the way to use them. However, the concept of energy remained unknown, until Galileo and Newton published their studies in 1600 and 1700 A.C [1,2]. Further to that, a big goal was achieved when it was discovered that energy could be transformed and used in different ways. Therefore, research efforts were put not only in energy sources, but also in possible applications. Thomas Newcomen invented the “steam machine” [3], which was further developed by James Watt [4]. This invention was capable of transforming heat energy into mechanical energy. On the base of such invention, a very fast and fascinating progress was made over the years to follow. However, as with the increase in energy sources, the boost in available and usable energy also led to negative consequences and major accidents. In 1771, a french engineer Nicolas-Joseph Cugnot had the first ever car crash when his vehicle hit a wall at the Paris Arsenal [5].

Around 1934 a scientist named Enrico Fermi and his collaborators found an alternative way to generate or release energy [6]. He discovered that a huge quantity of energy can be released by atom splitting. A new era began and the way to produce energy

drastically changed with the invention and development of nuclear power stations. Unfortunately, the working principles of the Fermi's theory were also used in order to design and produce massive destructive weapons such as the atomic bomb. On August 6 and 9, 1945, the cities of Hiroshima and Nagasaki were destroyed by the first atomic bombs used in warfare. The world was astonished and scared due to the release of such destructive large amount of energy. Once again, energy revealed itself to be fatal, when produced in such large quantities.

Other energy devices, such as the petrol and jet engines were ultimately developed in the last three decades. With modern jet powered aircraft, the distance between Europe and the USA is now crossed in no more than seven hours. However, the amount of potential development of energy did not show its limits yet in this sector. In fact, on the 16th of July 1969 another scientific milestone was also achieved, when Neil Armstrong, Michael Collins and Edwin Aldrin, piloted the shuttle "Apollo11" through space and landed on the moon [7]. Dealing with the big amount of energy required to take off a shuttle from a platform and drive it, is a very critical issue. Fatal accidents may occur, as platforms easily explode when little and occasional events occurs.

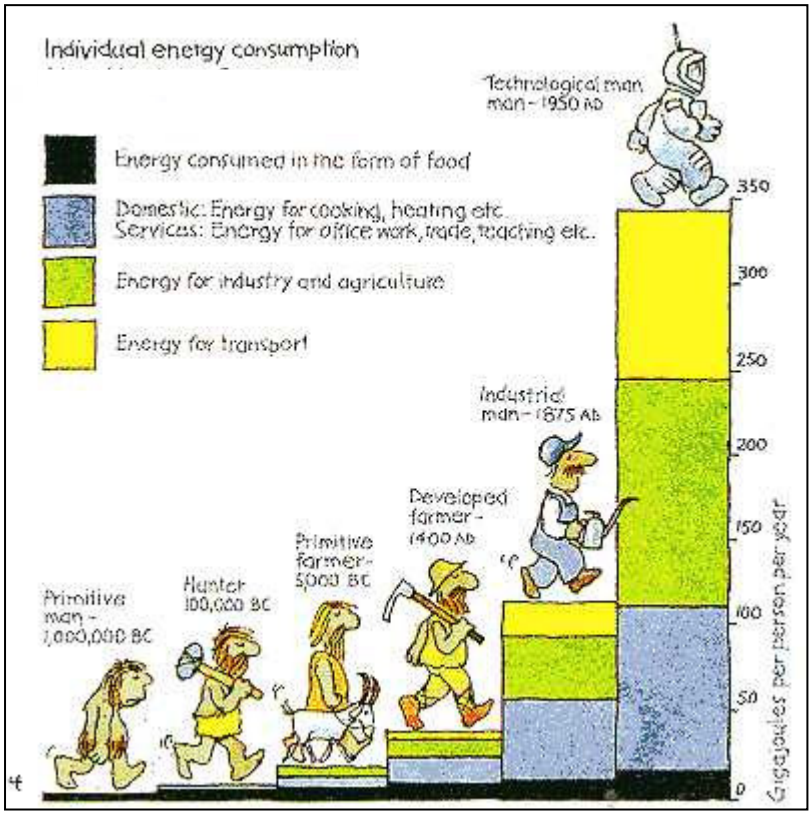

Figure 1.1 Progression of energy consumption [8]

The use and production of energy has therefore drastically enhanced. An example of it is given in Figure 1.1 [8], which shows the individual energy consumption from the primitive man to the technological man. It can be realized that the global requirement and use of energy has dramatically increased, especially during the last century.

Nowadays, even static structures such as buildings can be an image of the high level of energy which surrounds us. With the invention and development of talented techniques combined with the acknowledge of materials behaviour, buildings can now reach considerable heights, therefore have high levels of potential energy, also with fashionable geometries. Despite that, many people have died under the action of energy release, triggered by earthquakes and tsunamis, as it dramatically happened on the 26th of December 2004 in Asia, and many other times before.

It can therefore be concluded that since the discovery of “fire”, scientists always put considerable efforts on the most efficient way to produce and transform energy for all sorts of application. However, in many cases, greater difficulties were experienced in dissipating it in such a way to prevent injuries and disasters. Scientists realized that research was needed in the field of energy absorption; therefore some general solutions were considered and one of the first energy absorbers, the “spring”, was invented.

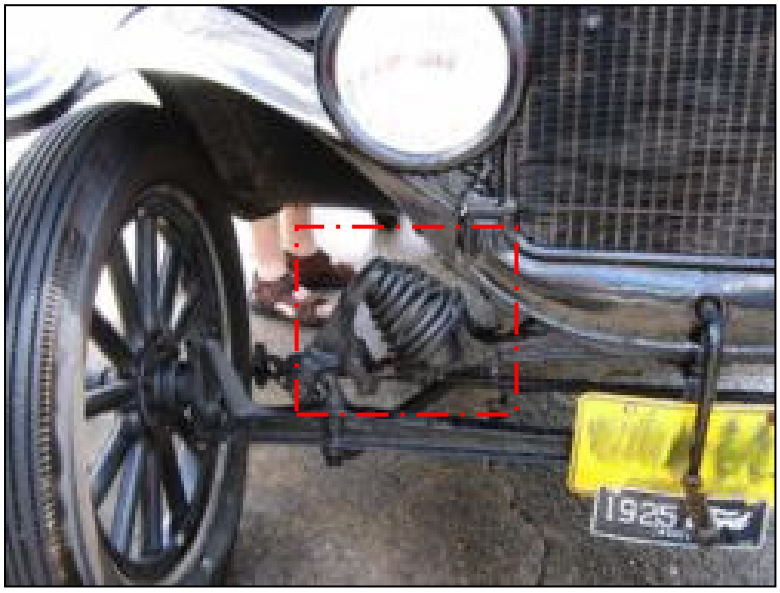

Figure 1.2 Coiled spring in the Ford Model T [11]

Springs (bar types) were widely used as energy absorbers in stagecoaches [9], and coiled springs were implemented with great success by Samuel Pratt in furniture in 1828 [10], during the Victorian period. Decades later, coiled springs were developed as energy absorbers in new transports vehicles, such as cars. Figure 1.2 [11] shows a coiled spring used for the Ford Model T (1908) suspension structure. However, the spring invention dates back to the third century B.C., when the Greek engineer Ctesibius of Alexandria developed a method for the manufacturing of simple bronze spring devices, mainly used as eyebrow tweezers and later on for catapults applications. On the other hand, the "coiled spring" was firstly developed in the 15th century by clockmakers. They had the inspiration of replacing the system of weights used to power clocks, with much lighter spring loaded devices [12].

Nevertheless, other techniques to dissipate energy were developed and devices invented, alongside springs. As an example is the concept of "dry-friction", which was firstly employed in order to design a shock absorber for automotive applications in the early 1900's [13]. Such devices were simply two arms connected by a bolt with a friction disk between them. Tightening or loosening the bolt adjusts the frictional resistance. They were designed to damp the vertical vibrations of a spring (leaf type) in the suspension system. Although this methodology was abandoned for car applications not later then 1940s [13], dry-friction energy absorption devices did find a large scale applications against earthquakes in structural design [14].

Later on in the 20th century, researchers and engineers finalised the development and design of another category of energy absorbers, which used fluids or viscous material in order to dissipate unwanted energy. Fluid energy absorbers were successfully implemented in many application fields, concerning the dissipation of relatively low energy levels such as in cars, to the absorption of severe intensities of energy such as in structures. Figure 1.3 [15] shows a large fluid shock absorber installed in the San Francisco-Oackland bay bridge, and used for the retrofit of the structural frame against the occurrence of earthquakes.

Figure 1.3 Fluid damper installed in a building [15]

Nowadays, in the field of energy absorption, considerable progress has been made. Devices and techniques have been developed to dissipate large unwanted energy based upon metallic foams, honeycomb structures and arrangements exploiting material plastic deformation in general.

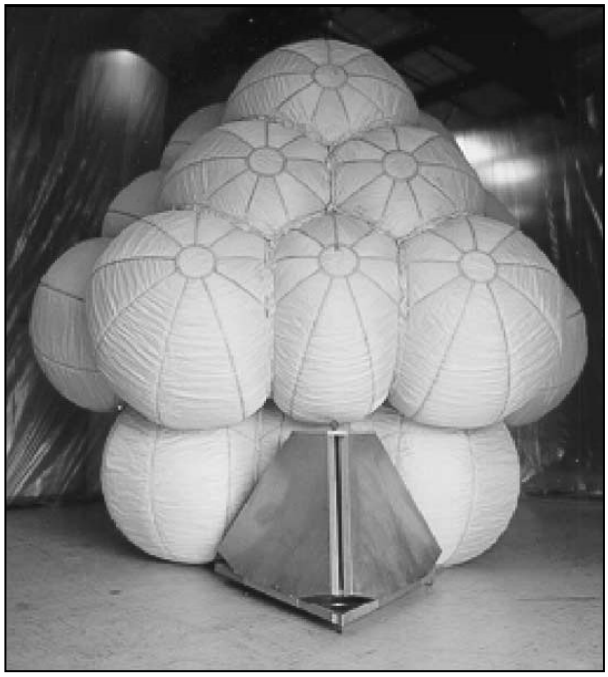

Figure 1.4 Mars Pathfinder airbag landing system [17]

A remarkable invention was ultimately developed in 1968 by Allen Breed [16], to prevent injuries in the field of transport. He invented a “Sensor and safety system”, the world's first electromechanical automotive airbag. Concepts relying on such invention were expanded to the safety in space transports too[17]. Figure 1.4 shows the Mars Pathfinder airbag landing system, which was designed to provide protection upon the impact with the surface of the planet Mars.

However, despite the number of devices available in the market, research has not yet discovered a solution to the several disadvantages of current arrangements to dissipate energy. Some usually get destroyed in the process, hence they have to be replaced; and some provide high levels of rebound force that may pose a danger. Also, some devices lack flexibility and cannot be incorporated in new structures and designs. The way to dissipate unwanted energy will become a very critical field, that certainly requires more knowledge and research, in order to provide a higher level of protection to current and future general structures.

This thesis presents a concept and an analysis of an innovative methodology to design Universal Reusable Energy Absorption Devices (UREAD), capable of dissipating undesired energy, and based on the working principles of the Equal Channel Angular Extrusion (ECAE) process. In this process, a solid deformable material is forced to flow inside intersecting channels of equal cross sectional area, machined within a hard tool. As *“Eureka-Magazine”* (edition of May 2005) emphasized, “it looks like to be able to totally change just about everything in the field of energy absorption in engineering design”.

The research programme of this work explores various research fields linked to the potential development of innovative energy dissipation devices. The aims of this work are:

1) To analyze theoretically and experimentally the energy dissipation mechanism in several types of UREAD devices, and study the effect of geometrical parameters.

2) To investigate the contact pressure at the interface between the tool and the deformable material. Contact pressure is the principle cause of tool cracks, hence it affects tool life.

3) To demonstrate the effectiveness and potential use of UREAD devices in real situations.

The above aims are implemented through various objectives which are demonstrated in this thesis, which comprises eight chapters:

Chapter 1 introduce the reader to the topic of energy and its consequences.

Chapter 2 gives a literature review of most relevant energy absorption devices for selected application fields. They are described in their working mechanisms and loading behaviour.

Chapter 3 gives an introduction to the working principles of the UREAD technology to dissipate undesired energy. It is however become appropriate to introduce the Equal Channel Angular Extrusion process in this chapter. In addition, a review of theoretical techniques to predict stresses in material forming processes is presented.

Chapter 4 presents the development of a theoretical study on the Channel Angular Extrusion (CAE) and Equal Channels Angular Extrusion (ECAE) processes. Analytical formulas to predict forming stresses and energy dissipation, by using the Slab method and the Upper Bound technique has been attempted. The application of Finite Element Analysis using ANSYS is introduced.

Chapter 5 gives details of the experimental set up programme for the loading behaviour of various types of UREAD devices. A comparison between theoretical and experimental results is included in this chapter.

Chapter 6 covers the experimental programme for tool stresses using the Pressure Pin technique in the UREAD devices.

Chapter 7 introduces a potential application of the UREAD technique. It covers the design of a special experimental arrangement, which has been used to demonstrate the use of UREAD energy absorption units in heavy impacts, in a manner similar to landing of aircrafts.

Chapter 8 presents the conclusions of the present work, and gives some recommendations for future research into the UREAD technology.

At last, in order to complete the information provided in this thesis, several details are included in a number of appendices, along with a selected number of the author's publications.

Chapter 2

LITERATURE REVIEW

2.1 ENERGY ABSORPTION DEVICES INTRODUCTION

Recent advances and developments in science and engineering have brought modern life to be rather active and competitive compared to the steady self sufficient environment of the past centuries. Innovative and fast industrial processes as well as high speed transportations facilities are nowadays part of the high demand of new products throughout the world. As a consequence of this, risk at work or during passive life considerably increased. Also, there is, now more then ever, demand for a higher degree of personal and public protection against structural and mechanical failure. Therefore a wide market has emerged for innovative design of passive and active safety measures and devices aimed at personal, mechanical and structural protection. Energy absorbing units and devices, which dissipate kinetic energy during an impact or intense dynamic loading, can be classified and assigned to a specific category or a field of application.

2.2 ENERGY ABSORPTION DEVICES FOR STRUCTURES

Recent damaging earthquakes and hurricanes provide powerful reminders on how vulnerable many of our systems are to the forces of nature. Even in advanced industrial nations, the built environment is still quite susceptible to total failure due to natural disasters. Consequently, a principal challenge in structural engineering design is the development of innovative design concepts that provide improved protection to structures, along with their occupants and contents. Destructive environmental forces also include those due to wind, waves and earthquakes. Figure 2.1 shows the disastrous effects on an oil platform, located in the Atlantic ocean, after it was hit by high speed

wind of a typhoon. The columns of the platform were bent under the forces of the wind, causing the structure to collapse. Fortunately in this case, the oil station staff and

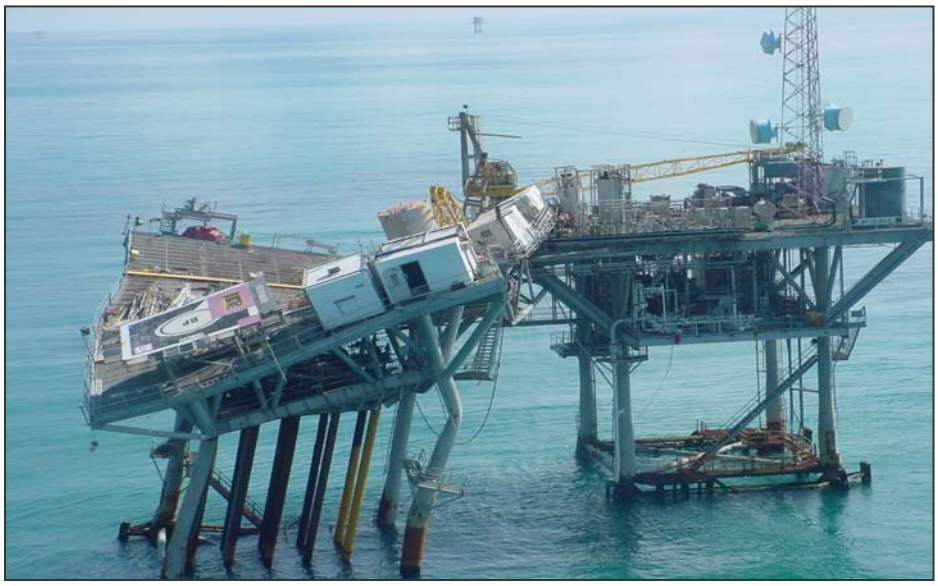

Figure 2.1 Oil station damaged by high speed wind [Mc.Carthy Building Company records, USA]

working crew were evacuated before the arrival of the storm. Scaring, and spectacular at the same time, is the circumstance shown on Figure 2.2, where three twisters were developing in the middle of the Atlantic ocean, right in front of a merchant ship. The velocity of the wind across the twister can reach 400 km/h, that is sufficient to cause disastrous consequences on structures and passengers.

Figure 2.2 Three twisters threaten a merchant ship [Mc.Carthy Building Company records, USA]

Many places located around the world that may seem safe from these natural big events, sometimes are threatened or eventually hit by similar natural events. For example, the tornado in Birmingham City (July 2005, UK) and the recent terrible Asian seaquake (December 2004) that caused the death of thousands of people. Modern technologies provide the knowledge to build prominent infrastructures such as oil stations, big ships, stadiums and skyscrapers. However, energy must be absorbed when they are subjected to unfavourable circumstances, and hence research areas covering the protection and defence of buildings have been considered by many researchers. Many energy absorption devices had been developed and implemented in structures to protect them from sudden impacts or vibrations.

2.2.1 Metallic Dampers

One effective technique available for the dissipation of large amounts of energy, for example when a structure is hit by an earthquake, is the use of inelastic (plastic) deformation of metallic materials, such as lead, mild steel and metal alloys. In traditional steel structures, seismic design relies upon the post yield ductility of structural members to provide the required dissipation of energy. In order to effectively include these devices in the design of an actual structure, one must be able to characterize their non-linear force-displacement behaviour under different cyclic loads. Several of the devices that employ such a technique differ by the working mechanism. One example is the torsional beam device [18]. It is made of a beam and sleeve elements, and join the main structure using anchors. When a torsional load is applied in the structure, the developed energy is dissipated by the plastic deformation of the sleeve.

Another possible solution is to employ plastic deformation capabilities of thin metallic sheets. A typical design is shown in Figure 2.3 [19, 20]. It consists of several X-shaped elements attached to horizontal beams. The supporting beams are meant to be rigid and linked to the structural frame, but the X-shaped elements can elastically or plastically deform under applied loads and hence absorb high energy when needed.

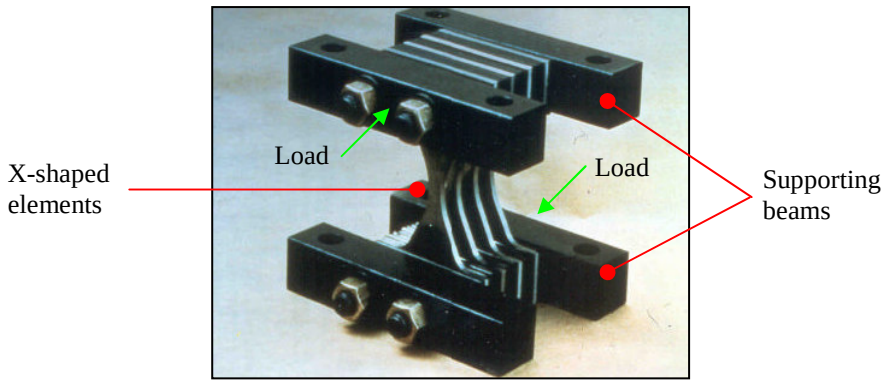

Figure 2.3 Typical design of a metallic damper [19]

The deforming element has to be designed in such a way that the damper will be the first to fail on its smallest cross sectional area, and therefore the whole yielding process is developed always across specific zones of a thin X-shaped element, and the mode of failure is therefore controllable. The energy absorption level is controlled by the number of X-elements within the unit and can be estimated through the cross section of the element, the distance it is allowed to move before collapse and the material strength of the elements [18].

Another possible way to dissipate energy in structures by metal deformation is given by the employment of U-shaped metal strips, as shown in Figure 2.4 [21]. In this case, when relative motion occurs, energy is dissipated away through plastic deformation of a thin strip, typically made out of mild steel. Such a strip is fixed between two adjacent

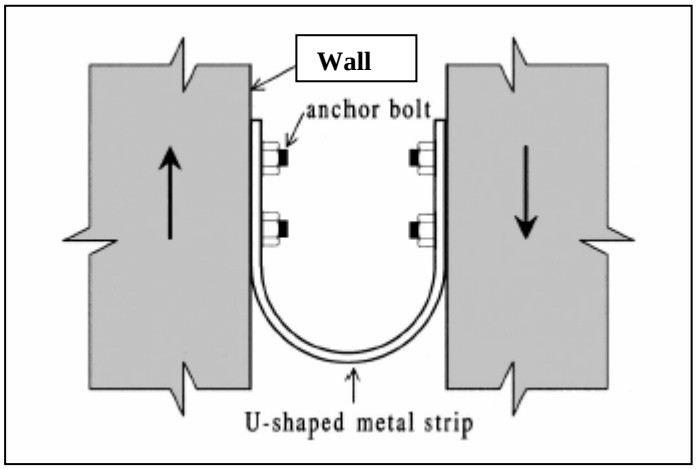

Figure 2.4 U-shaped steel strip as energy absorption device [21]

walls by several anchor bolts. The particular design of this device can operate with very large displacements and have a lifetime in excess of 100 cycles with properly designed mild steel strips [21].

Another device designed to dissipate energy in structural applications was invented by Robinson [22], and it is shown in Figure 2.5. It employs plastic deformation, but differs from the previously introduced metallic dampers in design and working mechanism. The device is made of two annular external plates, and a movable central plate positioned between them. The space between the central plate and the external plates is filled with lead. The lead core is also surrounded by thin annular plates of steel, separated by layers of rubber. In order to achieve a mechanical bond between the inner

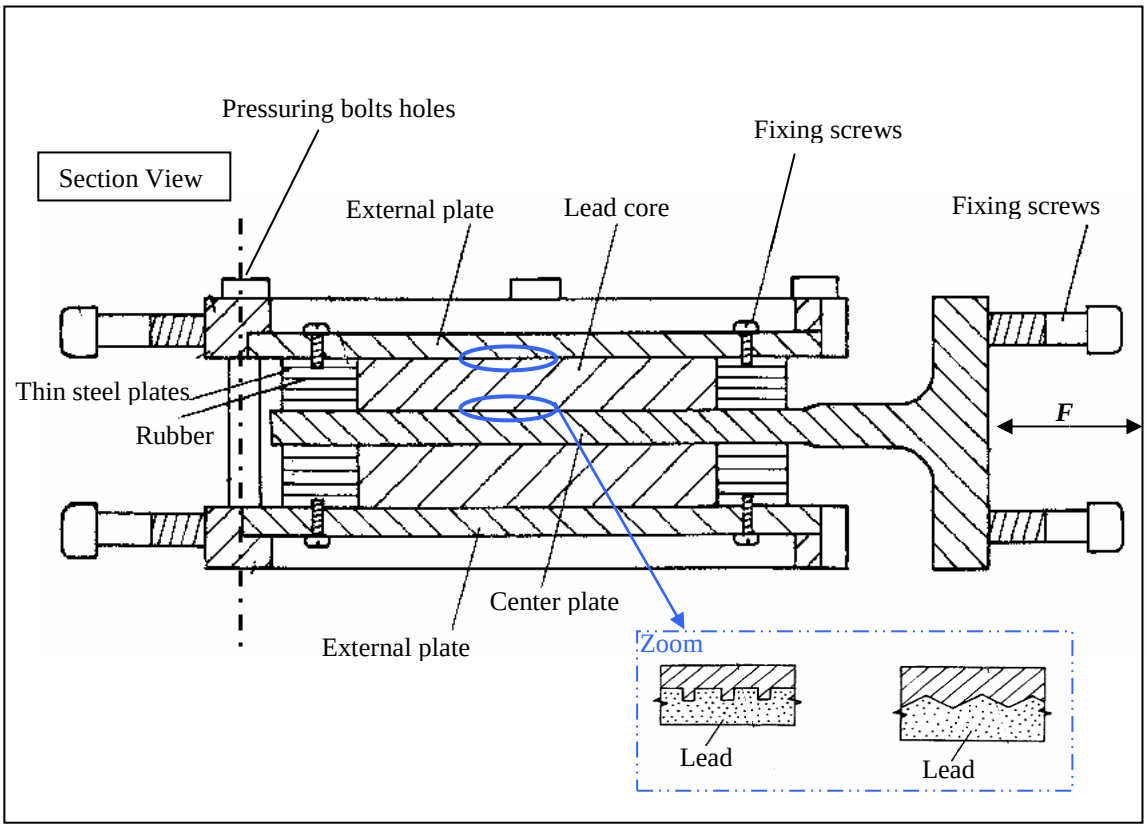

Figure 2.5 Cyclic energy absorber by Robinson [22]

and outer surface of the external plates and the lead core, grooves are machined at the contact interface, as the zoom inset shows in Figure 2.5. The energy is dissipated by the shearing of the lead, when the central plate moves. Because lead recrystallizes at room temperature, this device is technically capable of performing multi-cycle loops, with the

same force response. However, the working mechanism requires a constant hydrostatic pressure on the lead, at least 50 MPa, in order to make it flow through the grooves. Such a pressure is applied by the tightening of the pressurising bolts, shown in Figure 2.5. This device is designed to be sensitive for very small displacements. Figure 2.6 [23] shows a typical hysteretic behaviour of this type of device, for a displacement of ± 6.5mm.

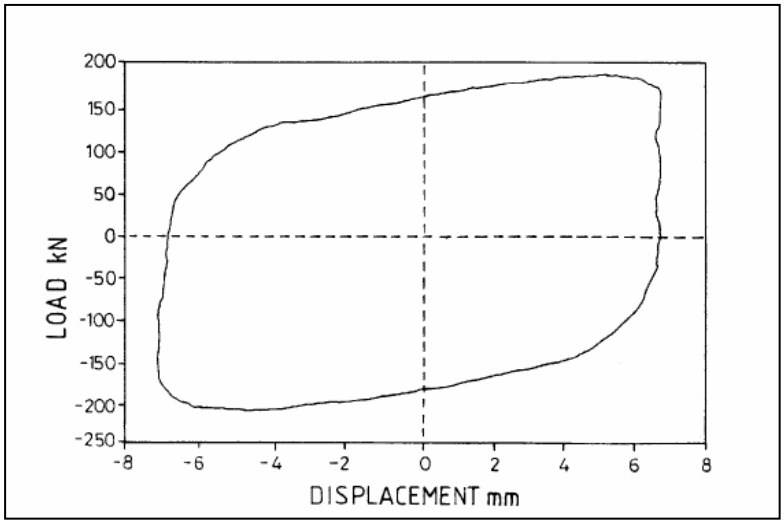

Figure 2.6 Hysteretic loop for the Robinson energy absorber [23]

Energy dissipation devices in structural applications that uses the plastic deformation of lead were studied since the 1970s [23], developed and largely implemented in countries such as New Zealand [24]. However, the flexibility in design and implementation of metallic dampers encouraged the commercial market to support the development of several products where they were implemented in both new and retrofit constructions. Nowadays, a large number of structures exist in Japan, Italy and United States that include several metallic dampers [18].

2.2.2 Friction Dampers

Friction is a form of energy dissipation that results through relative motion between two elements. Dampers that utilize the mechanism of dry solid friction for example are used to provide energy dissipation through a rubbing action (in dry conditions the energy

dissipation due to friction is a maximum and hence involves high wear at the interface). The so-called Limited Slip Bolted joint (LSB), intended for seismic control of large panel structures, is shown in Figure 2.7 [18]. A connecting plate links two rigid

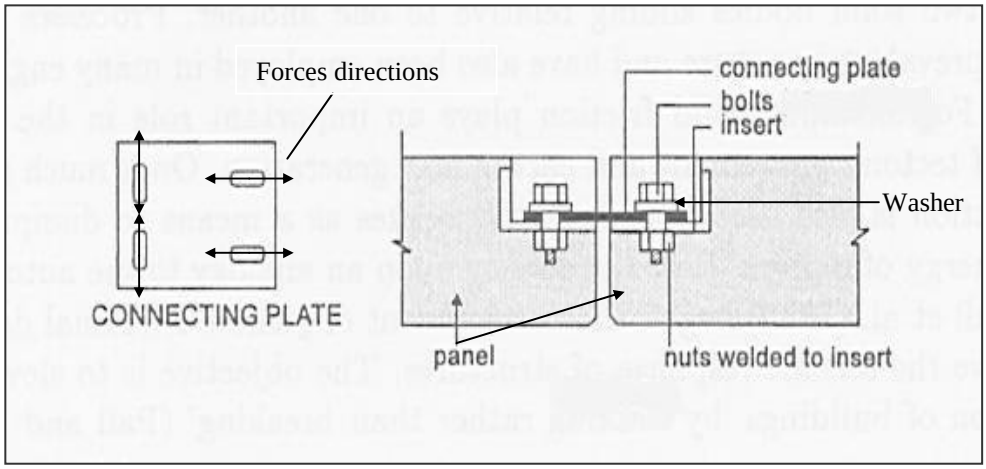

Figure 2.7 LSB friction damper device [18]

panels together. In case of significant structural loading, a relative motion of the panels occurs and the developed energy is dissipated by friction forces between the sliding plate and the bolt washers. The experimental loading behaviour against displacement was shown to be nearly linear, but varied under different frictional conditions [18]. The unit will cease to operate when the bolts fail.

A similar arrangement to the LSB device was designed by Filiatrault [21], in order to provide structural protection to wooden structures. Energy is dissipated by local friction forces that develop nearby a “slotted slip joint” when a load is applied, as shown in Figure 2.8 [21]. Such a device, particularly simple in design, does not interfere with the architectural or construction requirements and can also be applied for the seismic upgrading of existing wooden structures.

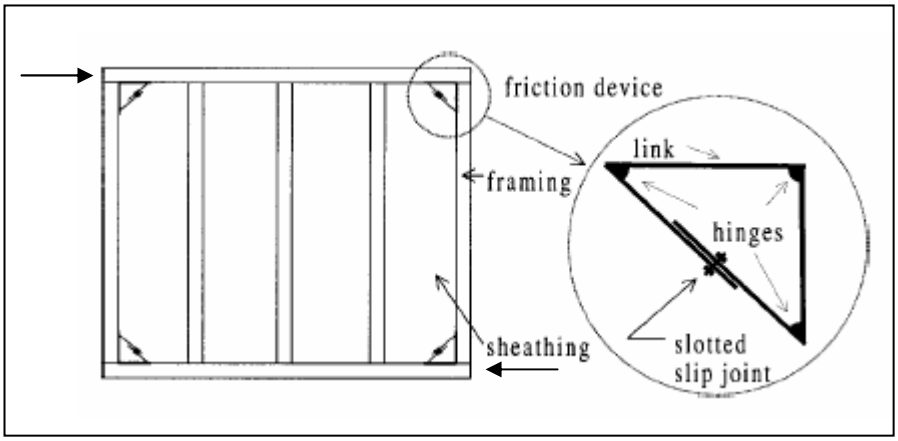

Figure 2.8 Friction device for wooden structures by Filiatrault [21]

The Energy Dissipating Restraint (EDR) is another device based on friction. It is manufactured by Fluor Daniel and sketched in Figure 2.9 [25]. This design incorporates two supports, thought to eventually attach the unit to walls and structures. The internal design includes a spring of a length L_{0}, positioned between two cylindrical friction pads made out of bronze. With regards to the working mechanism, a bolt is used to pre-tension the spring and to transform the actual spring force into a normal pressure acting on the contact pads. In this way, the static and dynamic friction between the pads and the external case will control the movement of the rod along the damper axis. This causes energy to dissipate during the process.

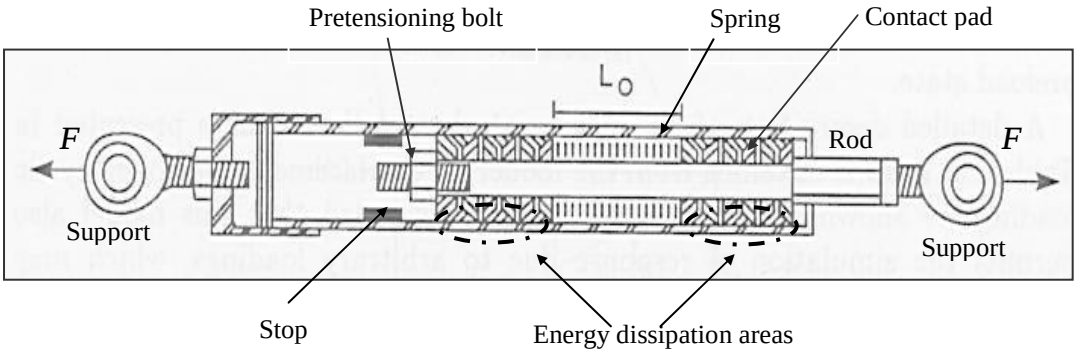

Figure 2.9 EDR device geometrical configuration [25]

.

The Friction Damper Device (FDD), shown in Figure 2.10 [26], is an alternative device. This is a passive control device that is designed to dissipate seismic input energy and protect buildings from structural damage during moderate and severe earthquakes. The design introduces frictional pad disks as a solution to dissipate energy. The unit is supposed to be connected to a structural frame through two side plates and one central plate. Figure 2.11 [26] shows some loading conditions. When a load is applied, the

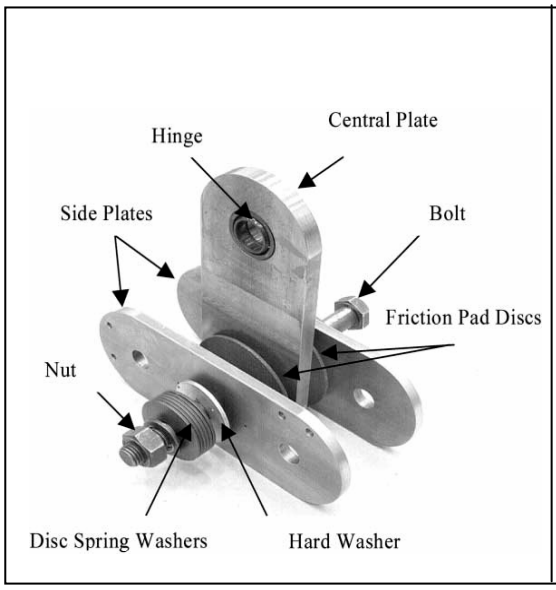

Figure 2.10 FDD design [26]

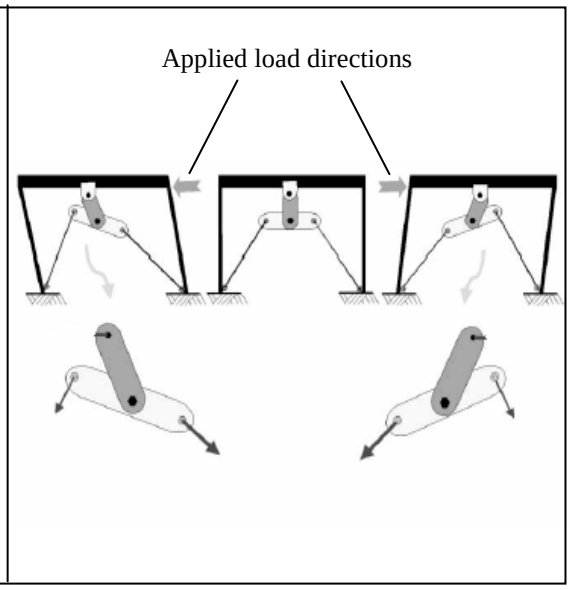

Figure 2.11 FDD working mechanism [26]

side and central plates rotate in opposite directions, and slide against one another. Hence, rotational friction between the pads and the central plate occurs. The hinge, shown in Figure 2.10, is meant to increase the relative rotation between the plate and the disks, hence increasing the total energy dissipation in the system. A radial spring is slotted through the bolt in order to return the unit to its initial position after loading. Experimental results have shown a linear energy dissipation characteristic of the FDD against the displacement amplitude of the frame, for a specific unit [26].

The rotational friction principle was again used for another design [27]. In this case, the energy is absorbed by rotational friction between a number of washers and some link connections to the main structure. The rotational resistance depends upon the dimensions and material of the washers and the pressure exerted by the bolts. In order to maximise the energy dissipation level, the washers are made of a special material, such

as ferodo, cast iron or stainless steel, and are preloaded by high strength bolts. However, the experimental force behaviour of such devices was shown to be strongly dependent on the surface temperature and loading frequency [27].

2.2.3 Viscoelastic (VE) Dampers

Many materials can obviously be classified as solids or fluids. However, viscoelastic material are neither liquid nor solid, they share certain properties and the characteristics of both. Rubber, silicon, and some kind of polymer fall within this type of materials. The shear stress of viscoelastic materials is a function of the shear strain, shear rate and time [28]. The application of viscoelestic materials to vibration control can be dated back to the 1950s [18], when it was first used on aircraft as a mean of controlling vibration, then in anti-seismic devices as shown in Figure 2.12 [29]. The device shown consists of viscoelastic material layers bonded within steel plates. When inserted in a structure, shear deformation and hence energy dissipation takes place when the structural vibration induces cyclic relative motion between the outer plates and the center plate.

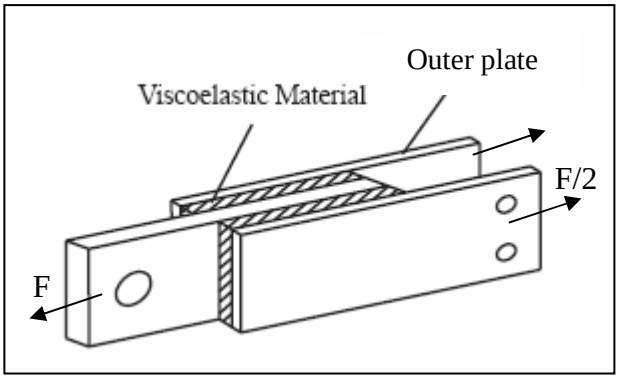

Figure 2.12 Typical viscoelastic damper configuration [29]

The mechanical behaviour of Viscoelastic (VE) materials is strongly dependent on the external ambient conditions, therefore external/internal temperature and excitation

frequency have to be taken into account for an effective design of these dampers when incorporated into structural applications.

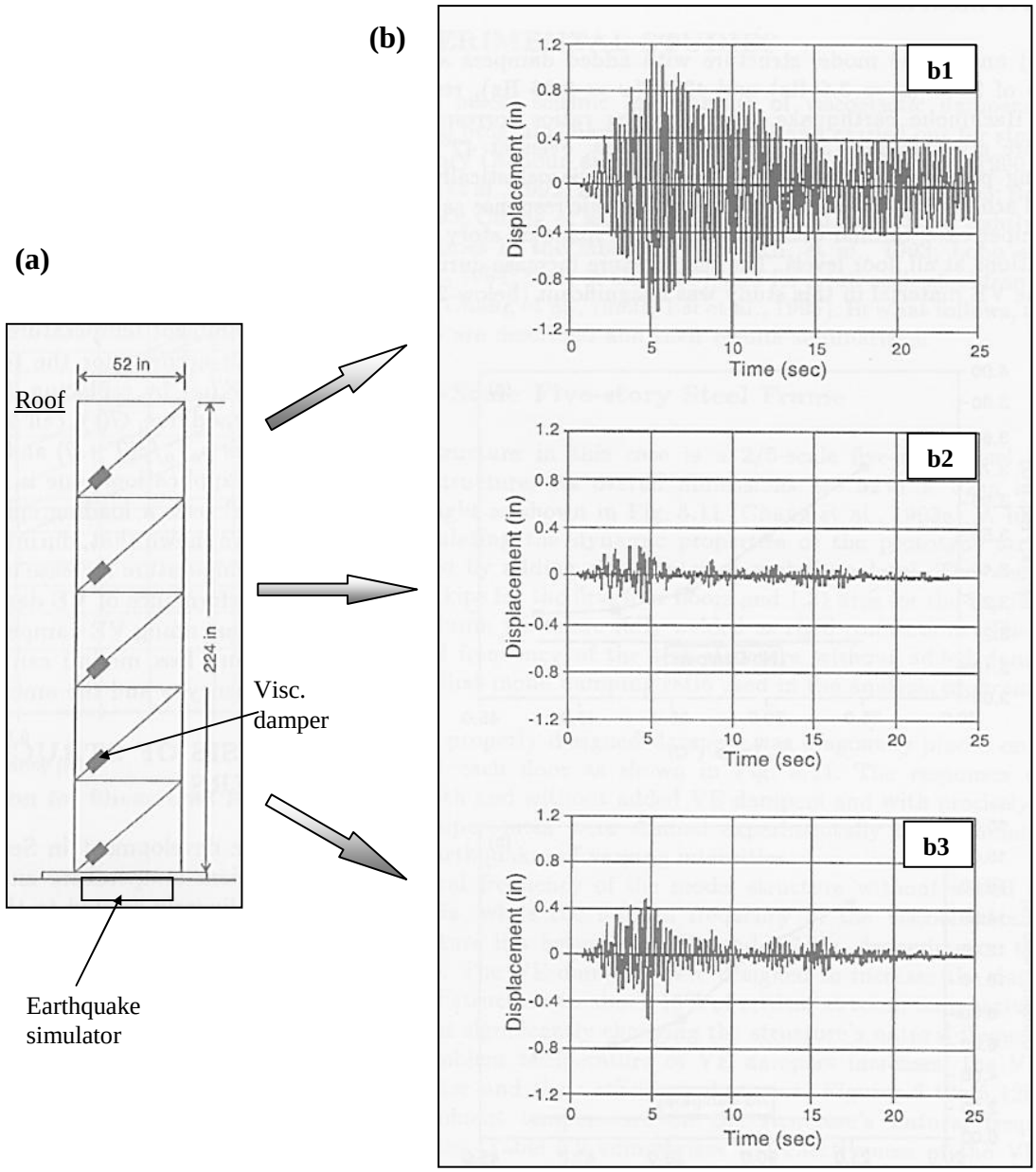

Figure 2.13 a) Viscoelestic dampers testing set up. b) Roof displacement time histories; b1) no damper added. b2) with dampers at 25^0. b3) with dampers at 42^0 [18]

A typical experimental set up is shown in Figure 2.13(a), where viscoelastic dampers devices were fitted in a five-story structure. Due to the simple design and significant practicability, viscoelestic dampers did find success for many years in structural applications. More then 20000 Visco Elastic dampers were installed in the twin towers

of the World Trade Center (USA, NY) [18], to limit wind building vibrations to levels below human perception.

2.2.4 Viscofluids Dampers

Fluids are an effective medium that can be employed in order to achieve the desired level of passive control. Significant effort has been directed in recent years towards the development of viscous fluid dampers for structural applications, primarily through the conversion of technology from the military and heavy industry.

Park [30] modelled an industrial viscous damper that was designed to provide vibration control in piping networks or seismic control in base isolation systems. In case of severe structural loading, a piston is forced to move within a case (damper housing) filled of a viscous fluid. In such a damper, the energy is dissipated through theviscosity of the fluid.

An alternative device that introduced the concept of Visco Damping Walls (VDW) was introduced by Yeung and Pan [31], and it is shown in Figure 2.14 [31]. In this design, the piston is simply a steel plate which is constrained to move along its actual plane except within a narrow parallelepiped container filled with a viscous fluid. For this design, the number of plates within the structural frame controls the energy absorption level, and again it is as efficient for forces applied along the vertical and horizontal directions.

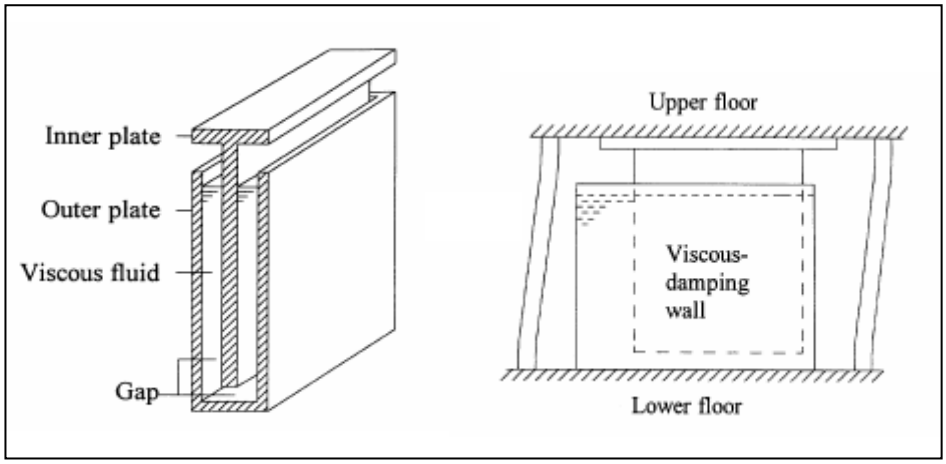

Figure 2.14 Typical design and working mechanism of a VDW damper [31]

There is, however, another class of fluid dampers that relies upon the flow of fluids within a closed container. In this design the piston acts not to shear the fluid locally, but to force the fluid to pass through small orifices. As a result, extremely high levels of energy dissipation are possible, but a corresponding sophisticated internal design is required, as for the so-called Taylor device [32].

2.2.5 Tuned Mass Dampers

The modern concept of Tuned Mass Damper (TMD) for structural application has its roots in dynamic vibration absorbers. The damping, in this case, is achieved by transferring some of the structural vibration energy to a tuned mass damper which, in its simplest form, consists of a mass-spring system, as shown in Figure 2.15 [33]. The tuned mass damper is a small oscillator which is attached to the main structure and eventually subjected to excitations. The natural frequency of the device is adjusted close to the building natural frequency so that the vibration energy can be immediately transferred to the TMD unit and dissipated away.

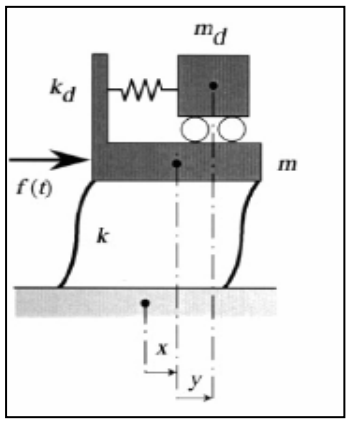

Figure 2.15 The idea of the Tuned Mass Damper [33]

Theoretical investigations about the TMD behaviour and best ways to retrofit a structural response with such a device can be found in the literature [18,34,33]. TMD devices recently found successful applications in wind turbines, in order to reduce the vibrational displacement response of a turbine tower due to strong wind excitations [35].

2.2.6 Tuned Liquid Dampers

In this category, attention shifts to another class of dynamic vibration absorber, named Tuned Liquid Dampers (TLD), in which liquids are used to provide all the necessary energy dissipation characteristics. With regards to this concept, one of the first prototypes was built by Frahm [36] in the early 1900s and it is shown in Figure 2.16. This device was used as an anti-rolling tank for ship applications. The two tanks were designed in such a way to tune the frequency motion of water to the fundamental rolling frequency of the ship in order to successfully reduce ship rolling.

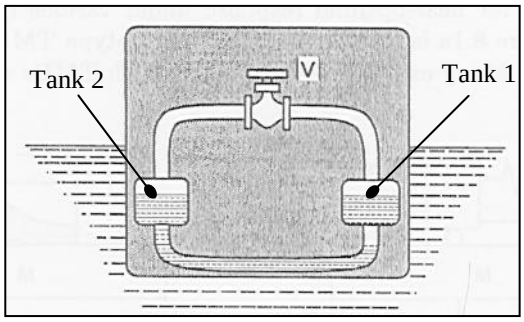

Figure 2.16 Tuned Liquid Damper by Frahm [36]

Bauer [37] first suggested the use of TLD in buildings to reduce the overall response due to strong wind or earthquakes. With respect to the working mechanism, a container is completely filled with two immiscible fluids to dampen the structural response through the motion of the interface.

From the examples discussed in this section, it is clear that tuned liquid dampers operate on the same basic principle as tuned mass dampers. Due to this simple physical concept, no activation mechanism is required. Therefore, maintenance cost is minimized. However, the mathematical theory describing the motion of a fluid can be quite complex. Also, for large energies, big and heavy quantities of fluid need to be accumulated. Therefore, for this type of dampers, flexibility and adaptability can be hardly achieved within average sized structures.

2.2.7 Shape Memory Alloys (SMA)

Considerable research and development have also been directed at other methods, such as the possible use of innovative shape memory materials for sensing and control purposes. This class of smart materials can be incorporated into structural members or systems components in the form of embedded sensors or actuation elements, capable of modifying the structural behaviour in response to significant external loads.

The shape memory effect of an alloy is generally referred by its ability to switch from a crystalline phase known as martensite to austenite, after crossing a critical temperature [38]. The material property which is of interest in structural applications is mainly the austenitic state, better known as super-elastic state, illustrated in Figure 2.17 [39]. For small strain levels (elastic loading) the material responds with high stiffness, but at intermediate levels of strain the stiffness reduces. High stiffness returns again when large deformation or strain is applied. Also, since the super-elastic state ideally displays

.

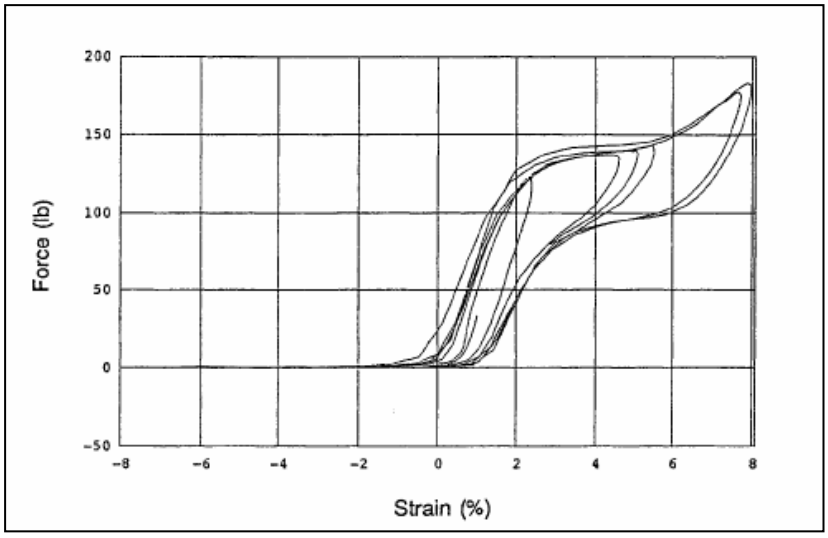

Figure 2.17 Experimental super-elastic behaviour of Nitilon [39]

hysteretic behaviour with zero residual strain, an energy absorbing device made of this material would theoretically provide a self-centering mechanism. In Figure 2.17, three distinct phases are recognized. Initially the material is stiff and elastic, then it becomes softer and after crossing approximately 6% of strain it becomes stiff again. Other attractive properties associated with smart materials include insensitivity to

environmental temperature changes when heat-treated, and their excellent fatigue and corrosion resistance [18]. By implementing this material in structures, the advantage is that for low levels of seismic excitation the structure behaves elastically; while for higher earthquake intensities Smart Materials can dissipate large amounts of energy. Studies on the possible implementation and potential of smart materials have been carried out by Cozzarelli [40]. However, it seems that no large-scale structural test involving the use of shape memory alloys as energy dissipation devices have been reported. This could be because of the high cost of such materials. Nevertheless, successful implementations can be found in countries such as Italy, where several safety bars made of SMA and steel were used to retrofit the church of San Giorgio in Trignano [41].

2.2.8 Active Bracing Systems

Active Bracing Systems (ABS) possess a kind of intelligence in order to dissipate energy in the most efficient way. The idea behind these smart techniques is that the device can sense what the building is experiencing, and through electronic and hydraulic feedback the system adjusts itself to absorb the required level of energy [42].

A preliminary evaluation of this active bracing system demonstrates several key advantages. The system can be used in buildings of any height, and the efficiency of the dampers is better compared to passive systems. In addition, it allows for more architectural flexibility. Applications of these active systems include structures such as bridges, buildings, towers and off-shore platforms, and also they can be used to retrofit existing structures. This is applied in Japan, where the excessive lateral oscillations of modern and old steel structures is easily controlled by such active systems [42,43].

Although active dissipation systems have a wide range of potential advantages, the final design is usually complex and laborious from the point that mechanical and electrical devices are connected together. In addition, the use of fluids certainly requires a frequent and expensive maintenance.

2.2.9 Impact Protection Systems

The concept of impact protection becomes important when considering the necessity to protect specific buildings or areas against possible threats. It is the case for example in banks, where special walls or mirrors have to be used in order to face unexpected blast attacks, similarly in military infrastructures, where special technologies are employed to provide high defensive levels of walls and bracings in general. Also, the demand on higher impact protection to public buildings increased considerably over the last few years, mainly as a consequence of the dramatic attacks in the USA (New York, 2001) that drastically raised people's fear from terror attacks [44].

In order to provide impact protection to structures, defensive armours are generally used. They can basically be described as specially designed walls, made of a specific material or a mixture of material in layers such as steel, aluminium, concrete and ceramics [45,46,47,48] that can be used in order to reinforce the existing structure. Steel fiber reinforced concrete is usually used to provide massive armour in defending buildings, especially against the impact of projectiles. In order to evaluate the energy absorption capabilities of this type of barrier, a small-scale plate is built from this material and hit by a bullet, then the damage is assessed [49]. The results of such experimental investigation are represented in Table 2.1 [49], counting only experimental data of bullets that perforated the armour. The energy dissipated was calculated

Caliber (mm)	Fiber ratio (kg/m^3)	Average (J/cm)	Number of data points
5.56	0	320	8
5.56	80	345	8
7.62 AP	0	394	4
7.62 AP	80	403	22
12.7 AP	0	1022	11
12.7 AP	40	1035	6
12.7 AP	80	1048	37
12.7 AP	120	1130	20

Table 2.1 Experimental energy dissipated per unit thickness (steel-fiber concrete armours) [49]

considering the impact and exit velocity of the bullet, and the thickness of the barrier. It is clear that the specific energy absorbed varies at different projectile calibres, and also it is strictly dependent on the quantity of fiber conglobated into the structure. In order to reach high values of energy absorption for such protective armour, significant barrier thicknesses are required. Also, materials with considerable resistance to impact forces are usually expensive, and manufacturing of such systems may involve sophisticated technological processes. Besides, impact protection becomes important also when considering severe loads that may originate from nature, such as tornados and storms. In fact, structures are necessary to provide protection to the civilian population against such events. Research is this field led to the designs of protective walls [50].

2.3 ENERGY ABSORPTION DEVICES FOR PERSONAL PROTECTION

The issue of protecting a human body against injuries dates as far back as recorded history, when ancient warriors used bronze, copper and iron armour in order to defend the body during battles. Therefore the body was protected, but such armour was heavy and uncomfortable, especially for people fighting on the ground such as the infantry. Nowadays, for the army, police and those that compete in the world of sports the use of protection equipment is essential. Sport shin and mount guards, ballistic vests, gardening gloves and protective helmets are standard devices that are used for protection. Researchers working in this field brought much development and innovation in terms of general personal safety.

2.3.1 Body Protection

Body armour is a highly competitive field with a large number of manufactures selling such protection devices. It is basically used to stop a bullet or any sharp object from penetrating to the human body. Stopping a weapon by dissipating the whole kinetic energy through the armour structure is only part of the problem. In this case, the bullet is usually decelerated and stopped in a distance of few millimetres. As a consequence of this, a sign is left on the armour and an impact shock penetrates to the human body, known as blunt trauma [51]. Because the human body can withstand only a certain

amount of blunt traumas, the body armour design should reduce such shocks to have minimum effects.

Traditionally, armours have been using a single material only, usually high hardness steel. However, the demands for lightweight armours for personal protection led to investigations into alternative technologies. In the last few decades, non-metallic materials, such as ceramics and composites, due to their low density, high hardness, high rigidity and strength in compression, have been increasingly incorporated into more efficient lightweight armour [52,53]. However, the low fracture toughness of ceramics has led to the final development of multi-material armour, in which a softer part is conglobated in order to provide resistance to tensile failure [52]. For this design, a common set of materials that may be used in armour structures is shown in Table 2.2, with some relevant mechanical properties.

Material	ρ (kg/m^3)	E (GPa)	v
Steel	7890	202	0.3
Ceramic (AD-96)	3720	303	0.21
Composite	1600	80	0.3

Table 2.2 Ceramic-Metal body armour typical set of materials [52]

The projectile deceleration mechanism through an armoured structure is in itself complex. However, the bullet penetration through the armour can be divided into steps [52]. Considering a ceramic-metal armour, the first step is the destruction of the head of the projectile, as a consequence of the first impact on the ceramic layer. During this stage, the impact energy of the projectile transmitted to the armour breaks the ceramics layer, which dissipate part of the energy through fragile failure. In the second stage, the bullet is now in contact with the metallic layer, hence the remaining energy will be absorbed by plastic deformation of the ductile thickness. Furthermore, the amount of kinetic energy that such a material can generally absorb during the deceleration process becomes important, and it can be seen by the graph in Figure 2.18 [54]. This shows the kinetic energy of a bullet against the penetration time using numerical simulations.

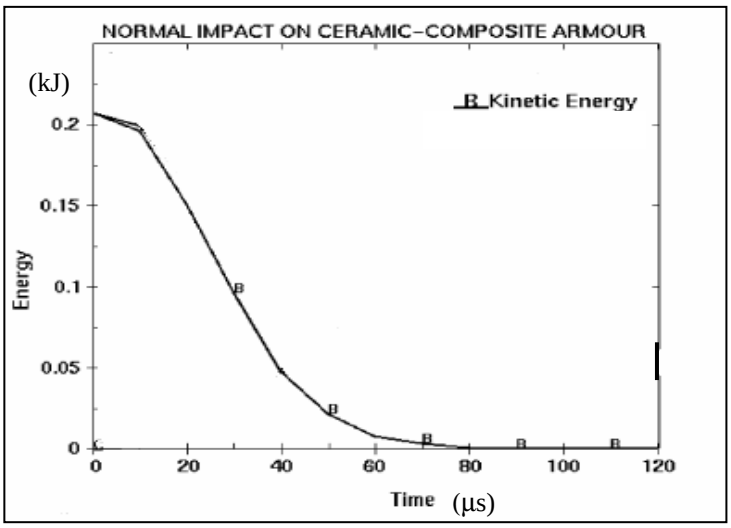

Figure 2.18 Simulated projectile kinetic energy as a function of the penetration time [54]

These results are obtained by computer simulations, under certain geometric and parametric settings [54]. As the figure reveals, the bullet kinetic energy is reduced from just above 0.2 kJ to zero in 90 μs [52].

Body armour made by extremely light materials such as fabrics and composites were investigated by Cleevely and Ramkumar [51,55]. The energy absorption capacity of a fabric is of primary importance in ballistic applications. Dynamic tensile tests are usually carried out, in order to understand the dynamic behaviour of the fabric. Experimental dynamic tests on a special type of light fabric named "Twaron" [56] has shown that the specific energy dissipation to failure point is significantly smaller at high strain rates than those at low strain rates. In fact, 35 MJ/m^3 and 18 MJ/m^3 of energy were dissipated for strain rates of 238 s^{-1} and 495 s^{-1} respectively. The material behaviour shown in the dynamic test is supported by numerical and experimental results obtained in an impact test, shown in Figure 2.19 [56]. The energy absorbed is plotted against the projectile impact energy. At low impact energy (corresponding to low strain rates), both experimental and numerical results show that the energy absorbed by the fabric increases with projectile impact energy. However, beyond a critical impact energy (corresponding to high strain rates), there is an abrupt decrease in the energy dissipated.

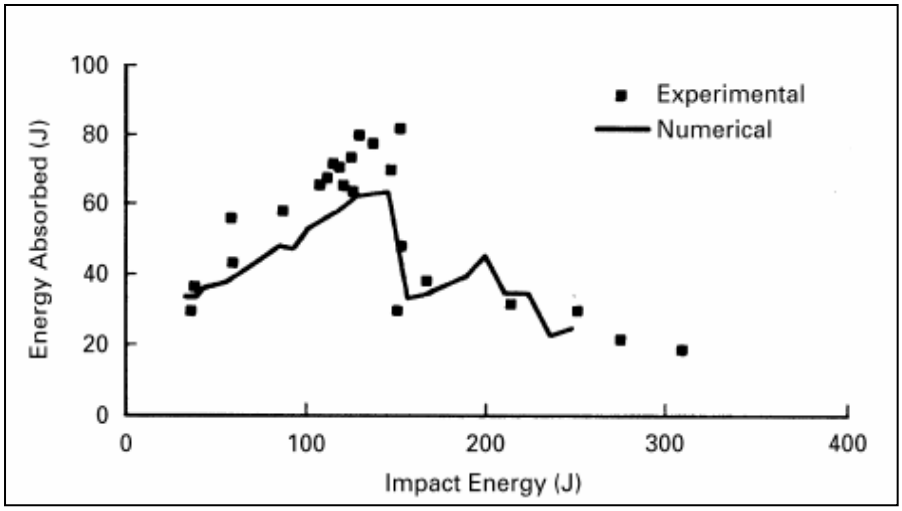

Figure 2.19 Impact testing on Twaron fabric, experimental and numerical results [56]

2.3.2 Head Protection

Particular attention has been always given to head protection, as it certainly is a region characterized by particular vulnerability. Heavy head protection devices were used in Roman wars. They were made of bronze and iron, sometimes covered by special typologies of leather in order to improve comfort.

Nowadays, modern technologies using light materials have provided significant improvements to helmets, for different fields of application, i.e. in buildings and sport. A typical helmet design morphology is shown in Figure 2.20 [57]. It is composed of three layers, basically an external shell, an impact protection layer and a soft comfort cover. It is designed to distribute the impact energy over a large area, thus avoiding concentrated loads, and to reduce to zero the residual loads transmitted to the head. On the other hand, the comfort foam usually consists of polyurethane or PVC [58], and is often covered by a layer of fabric. It is intended to improve the fit and comfort of the helmet on the head.

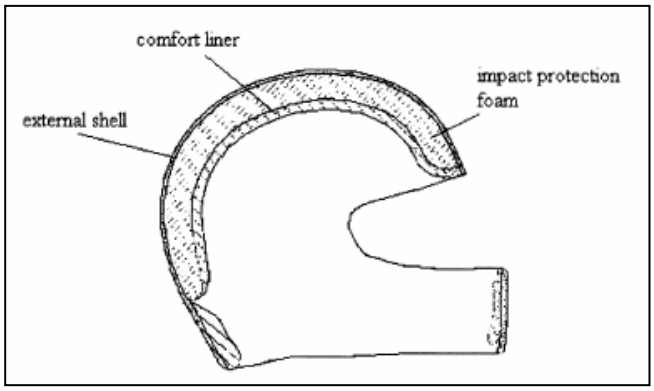

Figure 2.20 Typical helmet design [57]

Figure 2.21 (a) and (b) [59] shows experimental results from an impact test on a bicycle helmet at different impact energies (100 J, 50 J and 25 J), where several anvil shapes of anvil were used in order to simulate various impact circumstances. The time to absorb the maximum energy is another critical issue for describing the device protection performance. Shorter times imply a better performance.

Various international standards governing the performance of cricket, baseball, and ice hockey helmets for instance are now available. Some are given in Table 2.3 [60] where helmets are tested and certificated accordingly. For baseball helmets, a ball is fired at 27 m/s into the helmet, while for ice hockey helmets are dropped to on an anvil in a more conventional way.

However, during the service life of a helmet, environmental factors such as heat and water may lead to the degradation of energy absorption ability of many foams. According to some investigations [61], the yield stress of such foams is shown to decrease with increasing the percentage of relative humidity.

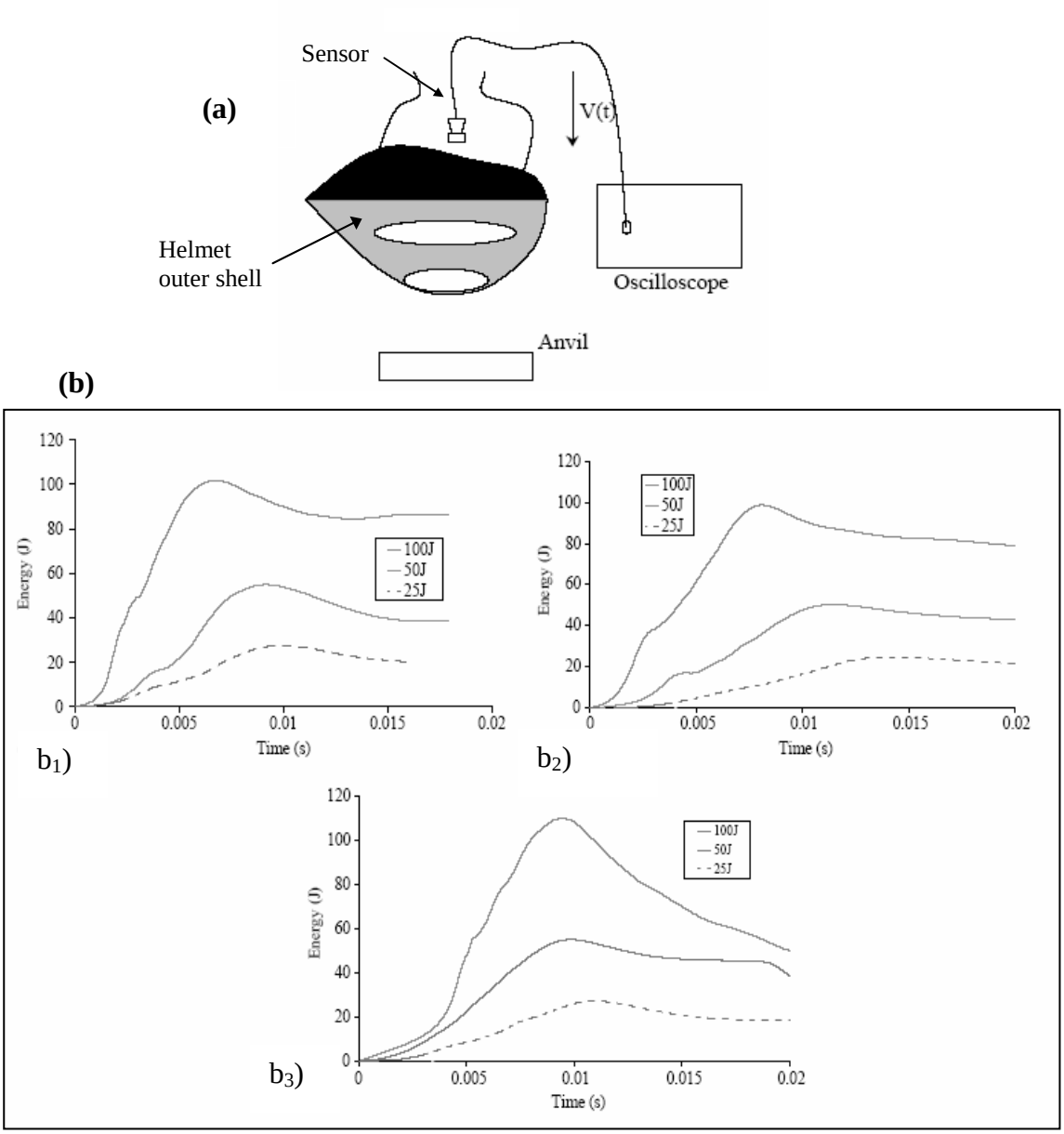

Figure 2.21 a) Impact testing set up for bicycle helmets. b) Impact test experimental results for bicycle helmets tested on: b1) flat anvil b2) hemispherical anvil b3) curbstone anvil [59]

	Cricket		Baseball	Ice hockey	
Standard	BS 7928[16]	AS 4499[17]	NOCSAE[18]	ASTM – F1045[19]	ISO[20] CSA 10256[21]
Impact test	Drop test of headform	Striker with ball (1.5 kg)	Ball fired at helmet	Drop test of headform	Drop test of headform
Impact energy	8.5 J	30 J	52 J	50 J	40 J
Anvil	Hemispherical	Striker dropped on to helmet	NOCSAE headform	MEP: flat, non-rigid	Flat, rigid
Assessment criterion	250 *g*	25% reduction in acceleration compared with bare headform test	Severity index (SI) <1500	275 *g*	275 *g* - CSA 300 *g* & Gadd <1500 –ISO

BS, British standard; AS, Australian/New Zealand standard; NOCSAE, National Operating Committee on Standards for Athletic Equipment; ASTM, American Society for Testing and Materials; ISO, International Standards Organization; CSA, Canadian standards; GSI, Gadd severity index (GSI and SI are functions of headform acceleration); MEP, modular elastomeric profiler, a semirigid anvil.

Table 2.3 International standards for testing cricket, baseball and ice hockey helmets [60]

In addition a very high level of head protection is certainly required for the head of car drivers against severe accidents. In this case, the airbag provide immediate head/facial protection against impact collision. Studies has shown that the risk of severe injuries due to a rear accident dramatically increases for small sized cars [62], which are of a very common use in European countries. This is because the car size does not allow for the incorporation of crushable energy absorbers, and usually there is not enough space for structural elements of the car to plastically deform by the formation of plastic hinges. As a consequence, passenger protection is mainly given by the seat, and

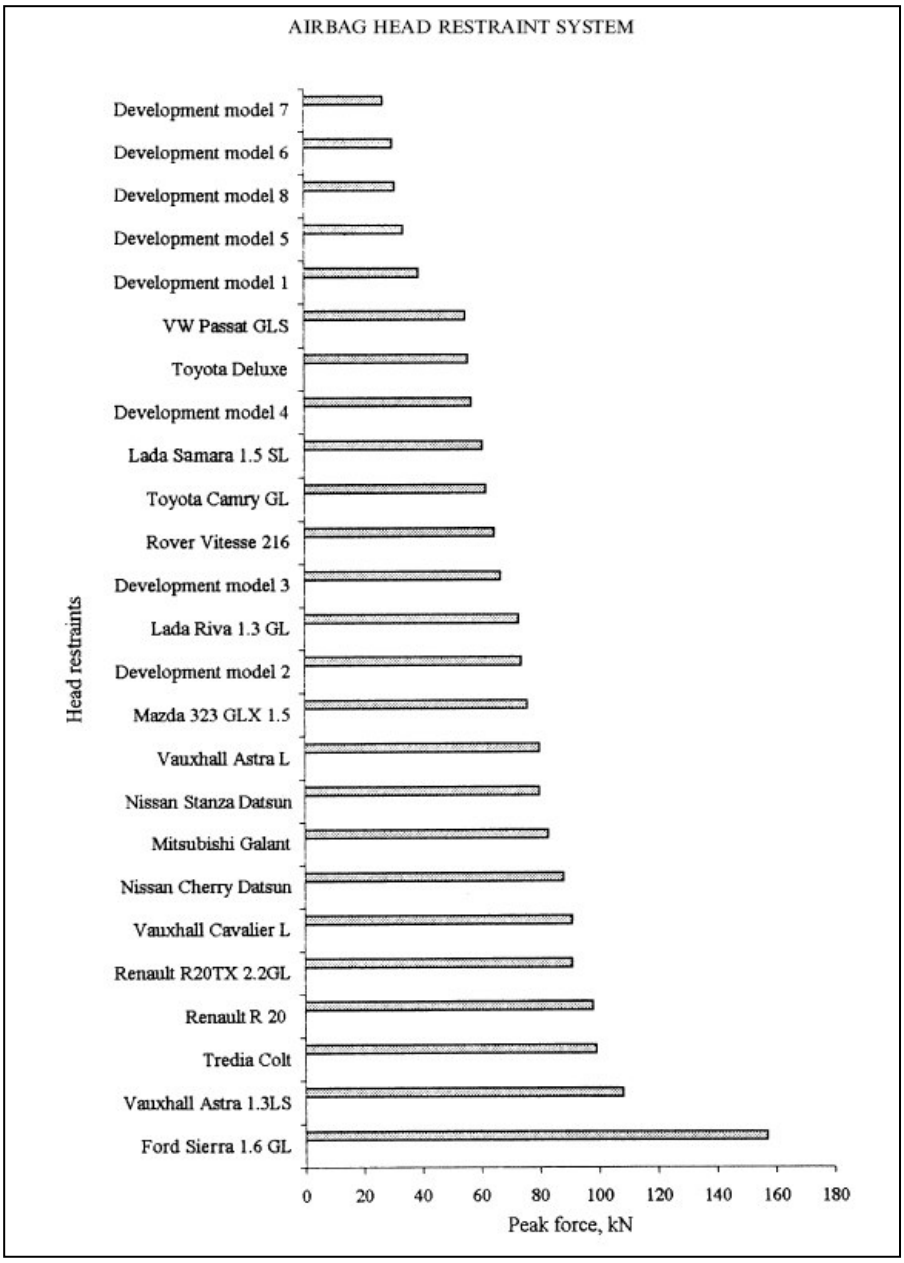

Figure 2.22 Peak force in various types of head restrains [63]

especially by the head restraints fixed on the top of the seat. Several tests were carried out on 25 different head restraints employed in car models[63]. Figure 2.22 [63] shows the experimental measurement of the peak force in such tests. It was found that models equipped with airbags experienced higher impact load reductions.

Aside from frontal and rear accidents, rollovers are very common casualties. Car roofs and their provision for protection were studied experimentally [64] where the deformation pattern and structural strength were assessed. Results are used to produce force diagrams against roof displacement, and have been shown to provide reliable data for roof crash predictions.

2.3.3 Leg Protection

The types of leg protectors vary significantly in geometry and material, according to the specific sport or industrial application. In football the overall level of injury to professional players is about 1000 times higher than that found in industrial occupations, which are traditionally regarded as a high risk [65]. For this reason, accurate protection is required, especially for the part located lower down the knee (tibia). Shin guards or protective pads are usually employed for this purpose. Shin guards can be categorized into four main groups based on their structure and material type, as shown in Table 2.4 [66]. The table also includes results from an impact test, where the peak force attenuation, as a percentage of the results of an unguarded model, was measured.

	[Drop height (cm)]			
	20	***30***	***40***	***50***
Maximum load attenuation	(%)	(%)	(%)	(%)
Plastic	18	15	14	12
Fiberglass	12	10	10	8
Air	23	17	16	16
Kevlar	15	10	9	9
Average guard	17	13	13	11

Table 2.4 Experimental impact results due to impact test on different football shin guard materials [66]

However, the findings of this study indicate that all proposed shin guards might be capable of providing some level of protection against tibia fractures. Significant differences in force attenuation of shin guard materials were recorded at large drop heights tests. It follows that some materials may be classified as more efficient than others in order to absorb a consistent level of impact energy and prevent injuries. Although heavier, thicker and longer pads may offer the best protection, athletes generally prefer lighter guards with a low profile that fit more comfortably. In this way, designs of future shin guards should aim to find a compromise where protection is maximized and player preferences are satisfied.

Similar protections are provided for motorcycles sport. Sakamoto [67] studied motorcyclist leg protection devices with respect to minimizing leg injuries occurring during eventual collision. It was emphasised that one of the main problems is the lack of space to fit energy absorbers on a motorbike. Nowadays the situation has improved due to the development of high technological materials and newer designs [68].

Leg protection is also required in cars, especially due to frontal accidents. Hotta [69] studied a possible solution against such types of injuries. An airbag can be fixed under the steering column, in order to protect knee and shin of the driver. When an accidents occur, the airbag will expand in order to provide protection and prevent injuries.

2.4 GENERAL APPLICATIONS ENERGY ABSORBERS

In addition to dissipation devices designed and manufactured for a defined application field such as structural or personal protection, there are some general methods that are characterized by not being complex, but adaptive to many applications. Such absorbers can be inside automobile bumpers, under lifts, along road barriers and used as crash protections in harbours [70]. Alghamdi [71] presented an energy dissipation mechanism made of a thin conical elements (frusta). On impacting the top surface, the conical element progressively yields into itself. Figure 2.23 [72] shows the load-deformation behaviour, when the element is totally inverted.

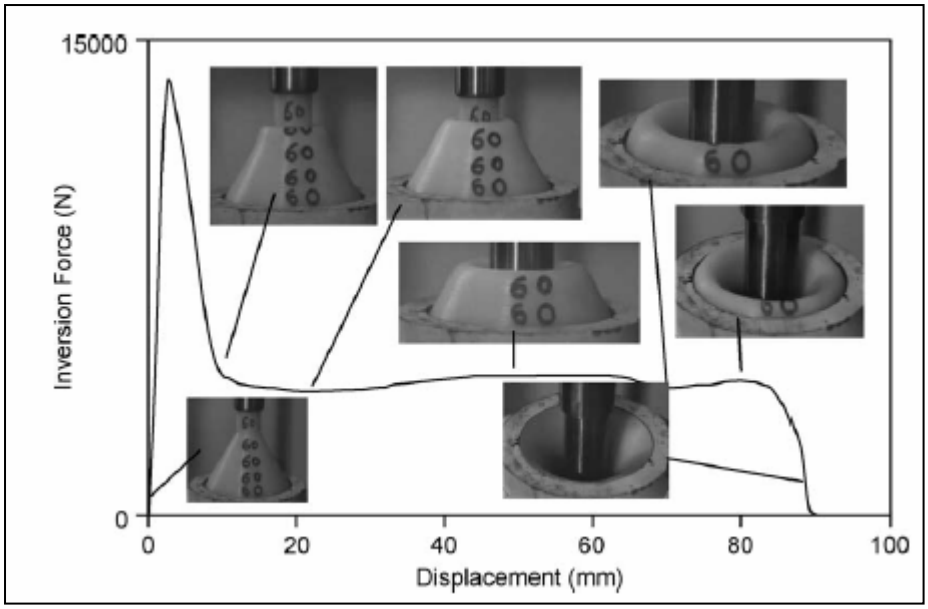

Figure 2.23 Experimental deformation stages of a frustum element [72]

The possibility to re-use the inverted frusta was also investigated by Alghamdi[72]. In this case, a specimen made out of commercial aluminium was inverted several times, but the specimen failed during its fourth inversion.

The use of polymeric composites and fabrics was investigated by Hamada [73]. He developed rods made out of polymers, and used them as energy absorption devices. Such rods are cylindrical, and characterized by a main body made out of unidirectional fiber, with braided fiber attached to the external surface. The purpose of the employment of braided elements is to reinforce the whole structure. Experimental results in Figure 2.24[73] shows that braided rods have better energy dissipation capabilities, because the load averaged to a nearly constant distribution for a longer displacement range then that for the unidirectional rods.

On the other hand, Altenhof [74] proposed the process of cutting a thin tube as a general method for energy absorption. Its operations are shown in Figure 2.25[74]. The cutter includes four blades each of which slide along the side of the tube. The forming load was reported to remain constant throughout the process.

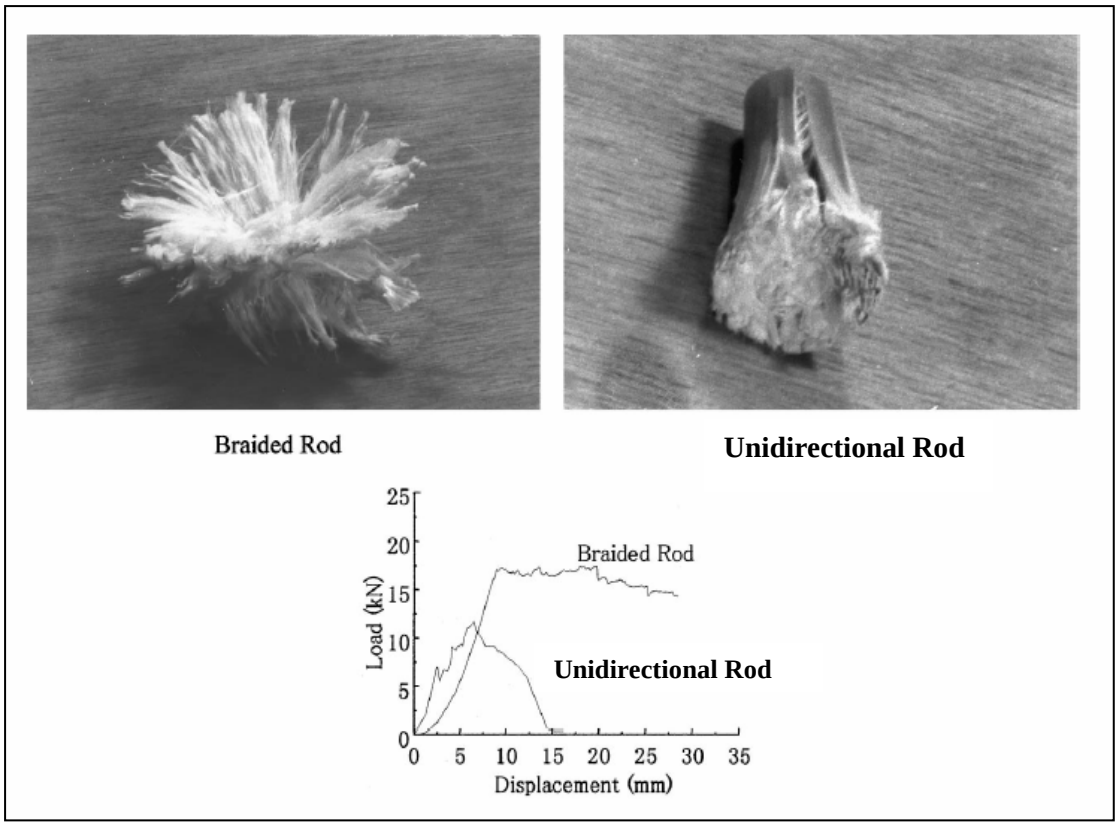

Figure 2.24 Experimental results on testing of Braided Rods [73]

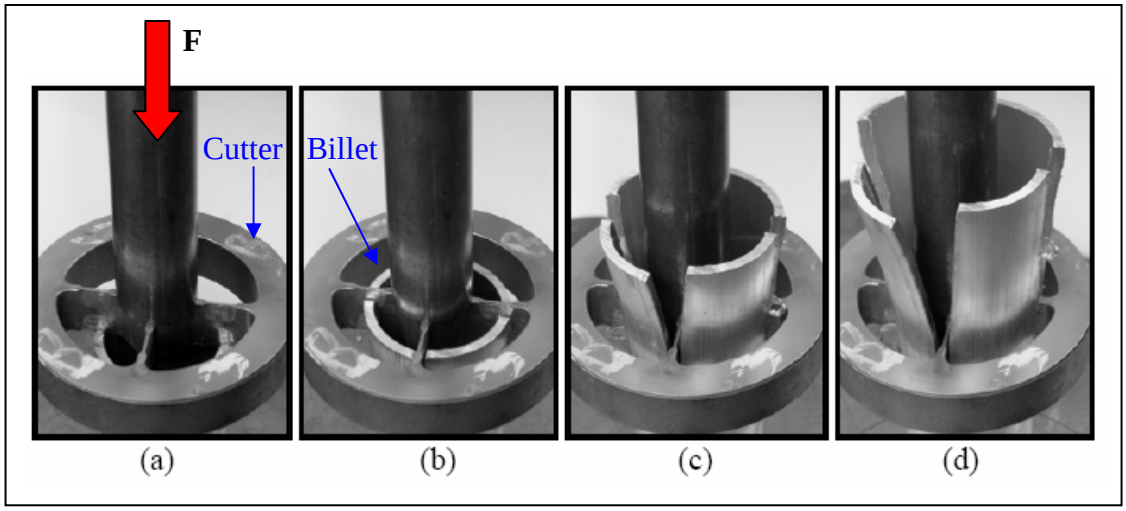

Figure 2.25 Dissipate energy by axial cutting of thin cylinders [74]

.

Due to the high demand on light and flexible products, researchers have investigated the possibility to design energy absorption devices, by using cellular materials such as honeycombs [75] or metallic foams, e.g. (Al–Si–Cu–Mg) [76]. Foams are well known to be extremely lightweight, and characterized by high strength and damping capabilities. They have been widely considered for aircrafts and satellites, structures and crash absorbers. However, due to the low specific weight of metallic foams, potential applications for frontal collisions in performance circuit vehicles, such as Formula 1 cars, have been investigated [77]. Structures for such cars may experience high energy impacts of 45kJ and above, with an average deceleration of 25g. For this application, aluminium foam was used, covered by a carbon skin in order to enhance energy absorption capabilities.

2.5 SPECIFIC ENERGY DISSIPATION DEVICES: AIRCRAFTS SHOCK ABSORBERS

2.4.1 Aircraft History

Nowadays, airplanes really occupy a predominant position in transport worldwide, especially for intercontinental and long journeys. As an example, Figure 2.26 [78]

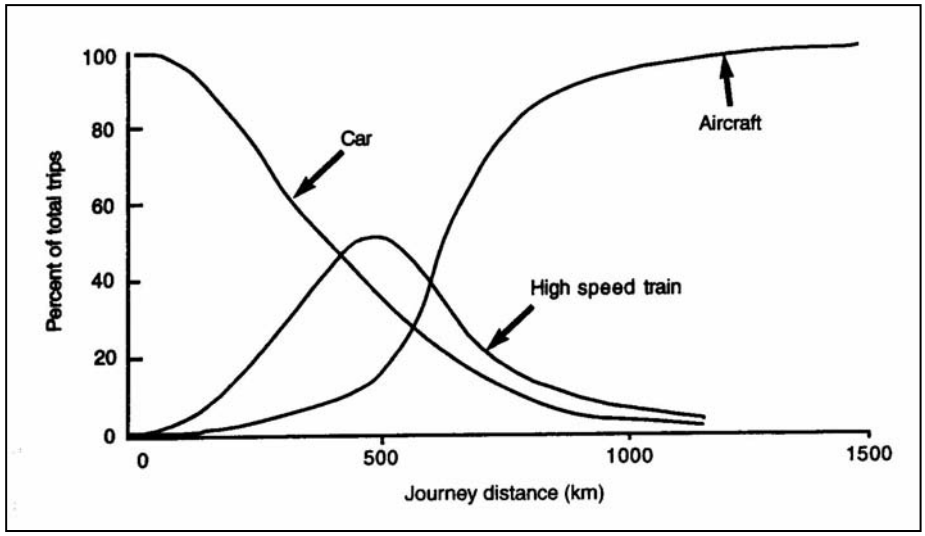

Figure 2.26 Transports methods against journey distance [78]

shows the actual preferred transports system, with respect to journey distance. For short travels, car and high-speed trains are still the dominant mode of transport. However, for destinations around and above 1000 km aircrafts seem to be the only fast and feasible way to travel.

It is a matter of fact that the airplane did not "just happened". Modern aircrafts used for transport and any other purpose are the result of the progressive understanding of natural lows that govern flying. The first ever-important milestone in aircraft travel happened not long time ago, on the 17th of December 1903. A powered human-carrying machine, designed and built by Orville and Wilbur Wright, marked the first flying machine [79]. It was capable of executing a successful sustained flight through the air.

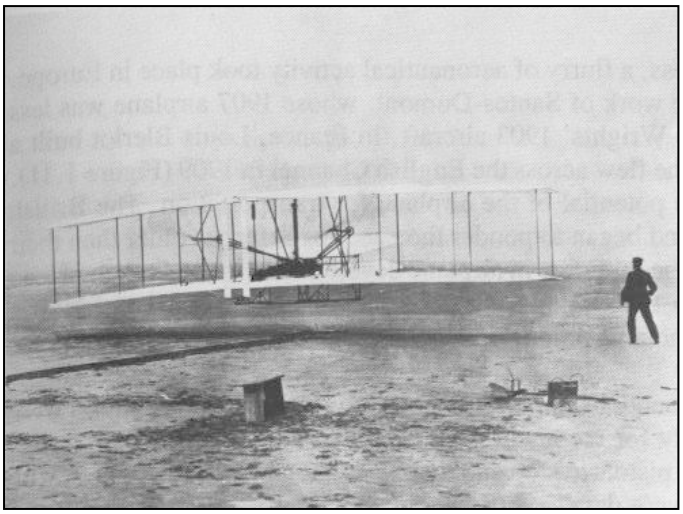

Figure 2.27 The Wright Flyer during its first take off [79]

Such machine, the *Wright Flyer*, is shown in Figure 2.27 during its first take off from the sand of Kill Devil Hill, North Carolina (US). The Wright brothers knew they achieved something important, never accomplished before, but they had no way of knowing the tremendous extent that such invention would have, in so little time. In 1909, Louis Bleriot built a remarkable monoplane, in which he successfully flew across the English Channel. [80]. This flight really showed the potential of an airplane in the field of transportation. However, maybe for the first time, the whole British population

felt less safe in their own island and began to enhance military defensive systems across the channel.

Since the first successful attempt by the Wright brothers, it did take not more then 80 years of intense research, before aircrafts could finally be developed to aerodynamic geometries and functionality [81].

2.4.2 Landing Gear Design and Energy Absorption

Landing gear design and structure must include a safety mechanism that is capable of absorbing severe static and inertia forces developed when the airplane touches the ground. Therefore, shock absorbers are known to be the most complex part of the landing gear. There are basically two types of shock absorber: those using a solid spring (steel or rubber), and those using a fluid spring with gas or oil, or a mixture of those two which is generally referred to as oleo-pneumatic. Figure 2.28 [82] compares the efficiency of various types of shock absorbers. The efficiency of a shock absorber is defined as the ratio between the area under the actual force - stroke curve, and the area under its ideal curve. Such ideal curve is defined by a rectangle covering the maximum stroke of the shock absorber, and the maximum force. Steel springs and air absorbers seem to provide the lesser absorption efficiency, while simple energy dissipation designs based on rubber are of average efficiencies, and much more complex mechanisms such as liquid or oleo-pneumatic springs are closer to high efficiencies.

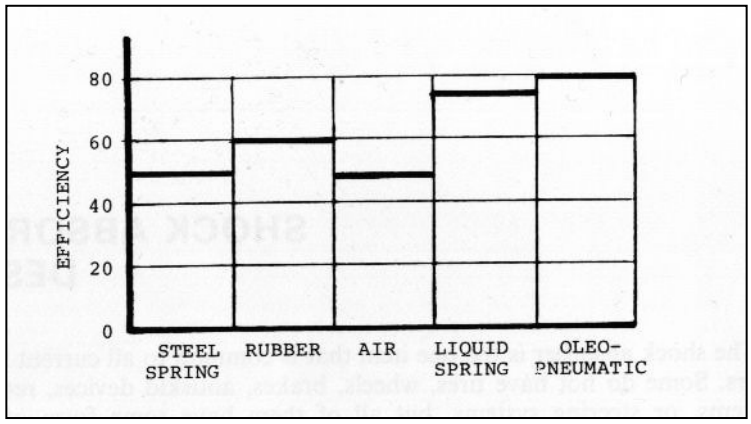

Figure 2.28 Shock absorber efficiency [82]

Figure 2.29 [82] shows a section of the typical design of a shock absorber in a landing gear based on rubber. Rubber disks are fixed in layers into the main structure, and the energy dissipation capacity is dependent on the specific material of the rubber disks, thickness and number of layers.

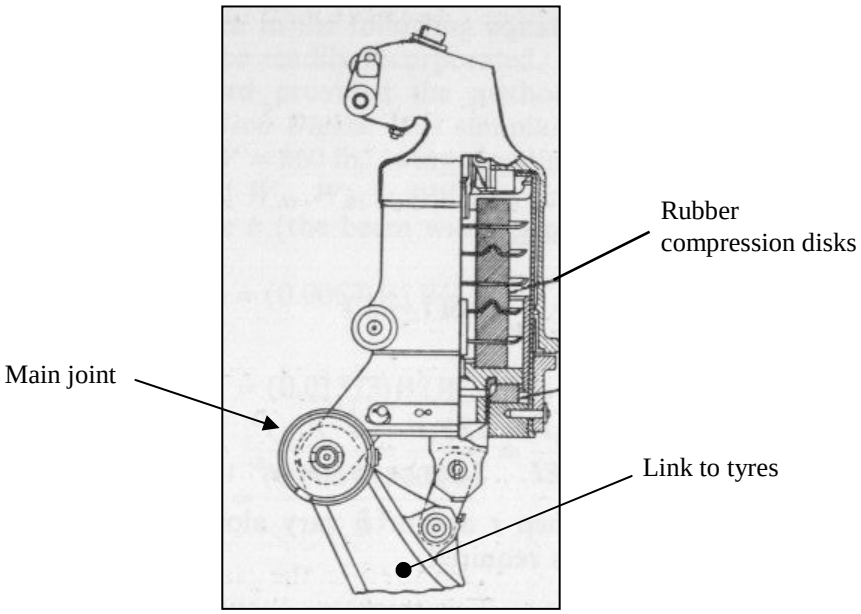

Figure 2.29 Typical rubber shock absorber [82]

An alternative to the previous described designs is the oleo-pneumatic shock absorbers. Its basic design consists of a chamber full of oil pushing against another chamber full of dry air (or nitrogen). In this case, energy is dissipated by the oil being forced through some compression orifices, and after the impact, the rebound is controlled by the air pressure (air spring) forcing the oil to flow back into its chamber through one or more recoil orifices [83]. Such devices are nowadays widely employed, as they provide the best efficiency and energy dissipation. On the other hand, the design and calibration of the design elements and internal parts can be complex and laborious. In addition, such shock absorbers are also required to be characterized by a soft behaviour during taxing operations for the comfort of passengers, but at the same time they must be capable of damping severe landing loads [83].

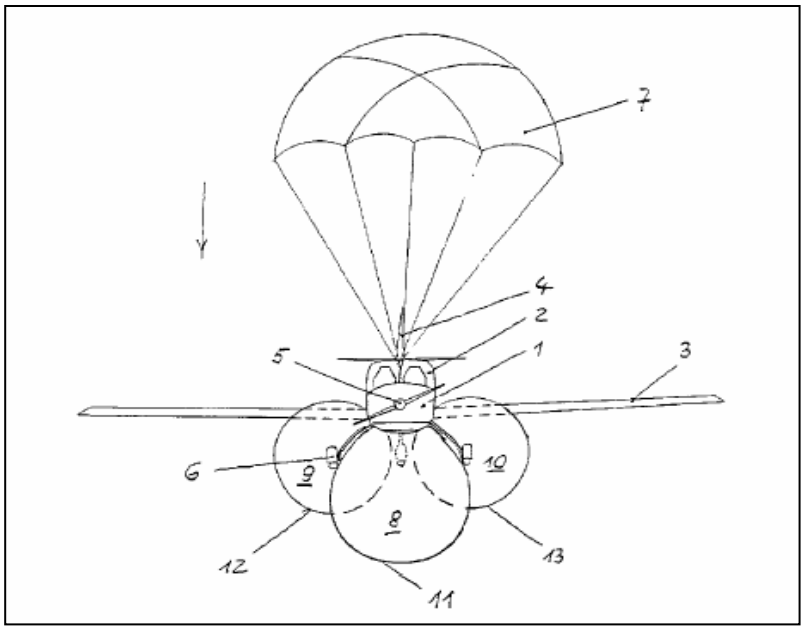

Figure 2.30 Protection airbags into the structure of an airplane, by Mellmann [84]

Another different arrangement was studied by Mellmann [84], who attempted to solve the problem of aircraft heavy-landings by the employment of several airbags within the body structure, as shown in Figure 2.30. The technique reduces the ground collision speed and absorbs dangerous impact energy during landing.

2.6 OVERVIEW OF ENERGY ABSORPTION DEVICES

The review of energy absorption techniques has shown that the field of energy absorption and energy dissipation is quite large and extends to most industrial applications. In an attempt to give an overview of the alternative techniques that dealt with energy absorption devices, a classified chart with the technical references are presented in Figure 2.31. A brief description of the devices is reported in the Appendix (A).

It is worth noting that not all devices and techniques used in energy dissipation are considered in this review.

Figure 2.31 Energy absorption devices overview

Reference list for Figure 2.31

[1] T.T Soong, G.F Dargush, "Passive energy dissipation systems in structural engineering", *Wiley*, 1996.
[2] Imad H. Mualla, Borislav Belev, "Performance of steel frames with a new friction damper deviceunder earthquake excitation", *Engineering Structures*, 24 (2002) 365–371.
[3] A.-P. WANG, "Dynamic analysis of a tall building with a tuned-mass damper device subjected to earthquake excitations", *Journal of Sound and* v*ibration* (2001) 244(1), 123-136.
[4] Y.L. Xu, Q. He, J.M. Ko, "Dynamic response of damper-connected adjacent buildings under earthquake excitation", *Engineering Structures*, 21 (1999) 135–148.
[5] Filiatrault, Tremblay "Design of tension-only concentrically based steel frames for seismic induced impact loading", *Engineering Structures*, 20(1998), 1087-1096.
[6] M. Shinoda, T. Uchimura, F. Tatsuoka, M. Tateyama, T. Natsuki, "A new simple method to substantially increase the seismic stability of reinforced soil structures", *Soil Dynamics and Earthquake Engineering*, 22 (2002), 1115–1123.
[7] H. J. Pradlwarter and G. I. SchuiRler, "Reliability of MDOF-systems with hysteretic devices", *Engineering Structures*, 20 (1998), 685-691.
[8] Kosuke Nagaya,Toshiyuki Fukushima, and Yasuhiro Kosugi, "Counteracting moment device for reduction of earthquakeinduced excursions of multi-level buildings", *J. Acoust. Soc.* Am. 105 (5), May 1999.
[9] Lyan-Ywan Lu, "Semi-active modal control for seismic structures with variable friction dampers", *Engineering Structures*, 26 (2004) 437–454.
[10] A. Moropoulou, A.S. Cakmak, N. Lohvyn, "Earthquake resistant construction techniques and materials on Byzantine monuments in Kiev", *Soil Dynamics and Earthquake Engineering*, 19 (2000) 603-615.
[11] Juan Enrique Martý´nez-Rueda, "On the Evolution of Energy Dissipation Devices for Seismic Design", *Earthquake Spectra*, Volume 18, No. 2, pages 309–346.
[12] Shyh Tzan, P.Pantelides, "Active structures considering energy dissipation through damping and plastic yielding", *Computers & Structures*, 66(1998), 411-433.
[13] Keiji Shiba, Shinji Mase, Yoshitaka Yabe and Kazuo Tamura, "Active/passive vibration control systems for tall buildings", *Smart Mater. Struct.* 7 (1998) 588–598.
[14] William Henry Robinson, "Torsional extrusion energy absorber", *USA Patent*, 1976, 3-953-012.
[15] Kazuto Seto, Yukito Matsumoto, "Active vibration control of multiple buildings connected with active control bridges in response to large earthquakes", Proceedings of the American Control Conference San Diego, California June 1999.
[16] Toshiyuki Kitada, Masahide Matsumura, Yukitoshi Otoguro, "Seismic retrofitting techniques using an energy absorption segment for steel bridge piers", *Engineering Structures*, 25 (2003), 621–635.
[17] William Henry Robinson "Cyclic energy absorber", *USA Patent*, 1974, 3-833-093.
[18] R.Park , "New Zealand innovations in the design of earthquake resistant structures", *The Structural Engineer*, (15 Jan 2002), 26-30.
[19] G. Anagnostides, A.C. Hargreaves, T.A. Wyatt "Development and applications of energy absorption devices based on friction", *J. Construct.Steel Research*, 13(1989), 317-336.
[20] R.Collins, B.Basu, B.Broderick, "Optimal Design of Multiple Tuned Mass Dampers (MTMDS) for Wind Turbine Towers Using SSA", *SECED Young Engineers Conference, University of Bath, 21-22 March 2005*.
[21] K. Li, A.P. Darby, "Innovative impact dampers for vibration control", *SECED Young Engineers Conference, University of Bath, 21-22 March 2005.*
[22] Catherine O'Sullivan, Biswajit Basu, "Distinct element analysis of base isolation with rolling rods", *SECED Young Engineers Conference, University of Bath, 21-22 March 2005*.
[23] R.S. Jangid, "Stochastic seismic response of structures isolated by rolling rods", *Engineering Structures*, 22 (2000), 937–946.
[24] M.Reinhorn, T.T.Soong, "Active bracing systems", *Modern Steel Constr.*, 33 (1993), 28-33.
[25] Mario Paolo Pietrangeli, "Progettazione e Costruzione di Ponti", *Masson*, 1996.
[26] Yi Li, Jian Bao Li, RouQi Zhang, "Energy-absorption performance of porous materials in sandwich composites under hyper velocity impact loading", *Composite Structures*, 64 (2004), 71–78.
[27] A.D.Foreman, "Optimizing the damage tolerance of carbon-fibre composites using hollow fibre layers", *Foreign object impact and energy absorbing structures (IMeche Seminar Publication),* 1998.
[28] EDWARDS , A. MATHEWSON, "The ballistic property of tool steel as a potential improvised armoured plate", *Int. J. Impact Engng*, 19 1997, 297- 309.
[29] Eduardo Moreno Almansa, Manuel Fernández Cánovas, "Behaviour of normal and steel fiber-reinforced concrete under impact of small projectiles", *Cement and Concrete Research*, 29 (1999), 1807–1814.
[30] Morril, Malvar, Crawford, Ferritto, "Blast resistant design and retrofit of reinforced concrete columns and walls", *Proceedings of the 2004 structures congress*, 2004.
[31] D.P. Gonc¸alves, F.C.L. de Melo , A.N. Klein, H.A. Al-Qureshi, "Analysis and investigation of ballistic impact on ceramic/metal composite armour", *International Journal of Machine Tools & Manufacture*, 44 (2004), 307–316.
[32] M.Lee, Y.H. Yo, "Analysis of ceramic/metal armour systems", *International Journal of Impact Engineering*, 25 (2001), 819–829.
[33] Z. Fawaz, W. Zheng, K. Behdinan, "Numerical simulation of normal and oblique ballistic impact on ceramic composite armours", *Composite Structures*, 63 (2004), 387–395.
[34] Holer, Weber, Tham, "Comparative analysis of oblique impact on ceramic composite systems", *International Journal of Impact Engineering*, 26 (2001), 333-344.
[35] S. Leigh Phoenix, Pankaj K. Porwal, "A new membrane model for the ballistic impact response and V50 performance of multi-ply fibrous systems", *International Journal of Solids and Structures*, 40 (2003) 6723–6765.
[36] B. L. LEE, T. F. WALSH, S. T. WON, H. M. PATTS, "Penetration Failure Mechanisms of Armor-Grade Fiber Composites under Impact", *Journal of Composite Materials*, 35(2001),1605-1631.
[37] V.B.C. Tan, T.E. Tay, W.K. Teo, "Strengthening fabric armour with silica colloidal suspensions", *International Journal of Solids and Structures*, 42 (2005), 1561–1576.
[38] Bazle A.Gama, Travis A. Bogetti, K.Fink, "Aluminum foam integral armor: a new dimension in armor design", *Composite Struc*, 52 (2001), 381-395.
[39] H.H. Billon, D.J. Robinson, "Models for the ballistic impact of fabric armour", *International Journal of Impact Engineering*, 5 (2001), 411-422.

[40] B.Parga Landa, Hernandez Olivares, "An analytical model to predict impact behavior of soft armours, *Int. J. Impact Eng.,* 3 (1995), 455-466.
[41] C.T. Lim, V.P.W. Shim, Y.H. Ng, "Finite-element modeling of the ballistic impact of fabric armor", *International Journal of Impact Engineering*, 28 (2003) 13–31.
[42] V.P.W. Shim, C.T. Lim, K.J. Foo, "Dynamic mechanical properties of fabric armour", *International Journal of Impact Engineering*, 25 (2001), 1-15.
[43] Seshadri Ramkumar, "Body armour composite fabrics: an overview", *International Textile Bulletin*, 48 (2002), 16-22.
[44] "Safe and sound – new developments in body armour", *Material World*, Sept 2002.
[45] Shinichi Sakamoto, "Research history of motorcycle leg protection", *SAE Transactions*, 99(1990), 1032.
[46] David F.Gerrard, "External knee support in rugby union", *Sport Medicine*, 25(5) 1998, 313-317.
[47] C.Francisco, W. Nightingale, Farshid Guliak, Richard Glisson, William Garret, "Comparison of soccer shin guards in preventing tibia fracture", *The Amer. J. of Sport Medicine*, 28(2000), 227-233.
[48] De-Shin Liu, Chia-Yuan Chang, Chin-Ming Fan, Shu-Lin Hsu, "Influence of environmental factors on energy absorption degradation of polystyrene foam in protective helmets", *Engineering Failure Analysis*, 10 (2003), 581–591.
[49] Luca Di Landro, Giuseppe Sala, Daniela Olivieri, "Deformation mechanisms and energy absorption of polystyrene foams for protective helmets", *Polymer Testing*,21 (2002), 217–228.
[50] N.J. Mills, C. Fitzgerald, A. Gilchrist, R. Verdejo, "Polymer foams for personal protection: cushions, shoes and helmets", *Composites Science and Technology*, 63 (2003), 2389–2400.
[51] A. Foreman, H. du Ross, and A. Huggins, "Design, manufacture, and test of lightweight composite sandwich helmets", *Plastics, Rubber and Composites*, 28 (1999), 252-258.
[52] Yeh-Liang Hsu, Chi-Yu Tai, Ting-Chin Chen, "Improving thermal properties of industrial safety helmets", *International Journal of Industrial Ergonomics*, 26 (2000), 109-117.
[53] A McIntosh, P McCrory, C F Finch, "Performance enhanced headgear: a scientific approach to the development of protective headgear", *Br J Sports Med* 2004, 38, 46–49.
[54] A S McIntosh, D Janda, "Evaluation of cricket helmet performance and comparison with baseball and ice hockey helmets", *Br J Sports Med* 2003, 37, 325–330.
[55] Barry D. Wilson, "Protective Headgear in Rugby Union", *Sports Med* 1998 May; 25 (5): 333-337.
[56] E. Spyrou, D. J. Pearsall and T. B. Hoshizaki, "Effect of local shell geometry and material properties on impact attenuation of ice hockey helmets", *Sports Engineering*, (2000) 3, 25-35.
[57] R. WILLINGER, D. BAUMGARTNER AND T. GUIMBERTEAU,"Dynamic Characterization of Motorcycle helmets: Modelling and Coupling with the Human Head", *Journal of Sound and vibration*, (2000) 235(4), 611-625.
[58] S.K. Hui, T.X. Yu, "Modelling of the effectiveness of bicycle helmets under impact", *International Journal of Mechanical Sciences*, 44 (2002) 1081–1100.
[59] Andrew S McIntosh, Paul McCrory, "Impact energy attenuation performance of football headgear", *Br J Sports Med* 2000, 34, 337–341.
[60] Chih-Han Chang, Li-Tung Chang, Guan-Liang Chang, "Head Injury in Facial Impact: A Finite Element Analysis of Helmet Chin Bar Performance", *Transactions of the ASME*, 122(2000), 640-646.
[61] RICHARD A. STRETCH, "The impact absorption characteristics of cricket batting helmets", *Journal of Sports Sciences*, 2000, 18, 959-964.
[62] David J.Chalmers, "Mouthguards", *Sport Medicine*, 25,5(1998), 339-349.
[63] P.Bemelmanns, P.Pfeiffer, "Shock absorption capacities of mouthguards in different type and thickness", *Int J. Sport Medicine*, 22(2001), 149-153.
[64] "A broad line of devices offers protection for the workers eyes and face", *National Safety News*, 117(1978), 70-74.
[65] Roderick I.Woods, "Specification of motorcyclists protective clothing designed to reduce road surface impact injuries", *ASTM Special technical publications*, 1237(1996), 3-22.
[66] David F.Gerrard, "The use of padding in rugby union", *Sport Medicine*, 25,5 (1998), 329-332.
[67] SHOP OF SNOWBOARDING web site.
[68] FIT SENIOR web catalogue.
[69] MOCAP web catalogue.
[70] TOSHIBA shock protector devices.
[71] ENIDINE web catalogue.
[72] PACKnMOVE web catalogue.
[73] Segesser, B., "The Shoe in Sport", *Year Book Medical*, 1989.
[74] Eleonora P. van der Putten, Chris J. Snijders, "Shoe design for prevention of injuries in sport climbing", *Applied Ergonomics*, 32 (2001), 379-387.
[75] "Foot protection: Shoes", *National Safety News*, 127 (1983), 66-67.
[76] Seung Min Lee, Tae Seong Lim, Dai Gil Lee, "Damage tolerance of composite toecap", Composite Structures, 67 (2005), 167–174.
[77] Michael L. Keating, "Football receiver training gloves", *US Patent*, 1999, 6-006-358.
[78] BIKERSITES web catalogue.
[79] Hermann, Raymond J.,"Slip resistant protective glove and method for manufacturing slip resistant glove", *European Patent*, EP 0-482-618-A1.
[80] Jaine Lara, Denise Turcot, "Comparison of two methods to evaluate the resistance of protective gloves to cutting by sharp blades", *ASTM Special Technical Publication*, 1237 (1996), 32-42.
[81] O. Calme, D. Bigaud, P. Hamelin, "3D braided composite rings under lateral compression", *Composites Science and Technology*, 65 (2005), 95–106.
[82] MARC R. SCHULTZ, MICHAEL W. HYER," Static Energy Absorption Capacity of Graphite-Epoxy Tubes", *Journal of COMPOSITE MATERIALS*, 35(2001),1747-1761.
[83] H. Hamada, K. Kameo, M. Sakaguchi, H. Saito, M. Iwamoto, "Energy-absorption properties of braided composite rods", *Composites Science and Technology*, 60 (2000), 723-729.
[84] A.S. Abosbaia, E. Mahdi, A.M.S. Hamouda, B.B. Sahari, A.S. Mokhtar, "Energy absorption capability of laterally loaded segmented composite tubes", *Composite Structures*, 70 (2005), 356–373.
[85] Guoxing Lu, Tongxi Yu, "Energy absorption of structures and materials", *Woodhead Publishing Limited*, 2003.

[86] A.A.A. Alghamdi, “Collapsible impact energy absorbers: an overview”, *Thin-Walled Structures*, 39 (2001), 189–213.
[87]] A.A.A. Alghamdi, “Reinversion of aluminium frustra”, *Thin-Walled Structures*, 40 (2002), 1037–1049.
[88] A.A.A. Alghamdi, A.A.N. Aljawi, T.M.-N. Abu-Mansour, “Modes of axial collapse of unconstrained capped frusta”, *International Journal of Mechanical Sciences*, 44 (2002), 1145–1161.
[89] Marc Zupan, C. Chen, N.A. Fleck, “The plastic collapse and energy absorption capacity of egg-box panels”, *International Journal of Mechanical Sciences*, 45 (2003), 851–871.
[90] V.S. Deshpande, N.A. Fleck, “Energy absorption of an egg-box material”, *Journal of the Mechanics and Physics of Solids* , 51 (2003), 187 – 208.
[91] Isao Nishimura, Toshikazu Yamada, Mitsuo Sakamoto, Takuji Kobori, “Control performance of active–passive composite tuned mass damper”, *Smart Mater. Struct.*,7 (1998), 637–653.
[92] H.F. Bauer, “Oscillations of immiscible liquids in a rectangular container: a new damper for excited structures”, *Journal of Sound and Vibration*, 93(1)(1984), 117-133.
[93] Douglas K Nims, Philip J. Richter, Robert E. Bachman, “The use of energy dissipation restraint for seismic hazard mitigation”, *Earthquake Spectra*, 9 (1993), 467-489.
[94] Ian D. Aiken, Douglas K. Nims, Andrew S. Whittaker, James M. Kelly, “Testing of passive energy dissipation systems”, *Earthquake Spectra*, 9 (1993), 335-370.
[95] S.W. Park, “Analytical modelling of viscoelastic dampers for structural and vibration control”, *International Journal of Solids and Structures*, 38 (2001), 8065-8092.
[96] G.F. Dargush, T.T. Soong, “Behaviour of metallic plate dampers in seismic passive energy dissipation systems”, *Earthquake Spectra*, 4 (1995), 545-568.
[97] William Henry Robinson, “Energy Absorber”, *US Patent*, (6,141,919), 2000.
[98] William Henry Robinson, “Cyclic energy absorber”, *US Patent*, (3,833,093), 1974.
[99] Davide Fugazza, “Shape memory alloy devices in earthquake engineering: mechanical properties, constitutive modelling and numerical simulations”, *Master degree dissertation, University of Pavia*, September 2003.
[100] Ngai Yeung, Austin D.E. Pan, “The effectiveness of viscous-damping walls for controlling wind vibrations in multi-story buildings”, *Journal of Wind Engineering and Industrial Aerodynamics*, 77&78 (1998), 337-348.
[101] Zhao-Dong Xu, Hong-Tie Zha, Ai-Qun Li, “Optimal analysis and experimental study on structures with viscoelastic dampers”, *Journal of Sound and Vibration*, 273 (2004), 607–618.
[102] “New technologies in earthquake engineering”, *Technical brochure, University of Buffalo, CSEE center*.
[103] Jeffrey Hanks, “Protective wall panel assembly”, *Patent*, W0 2004/065729 A1, 2004.
[104] John Joseph Holloway, “A garment having pockets to contain parotective body armour”, *Patent*, GB 2418832 A, 2006.
[105] Noaki Hotta, “Knee protection airbag apparatus”, *Patent*, US 2005/0062265 A1, 2005.
[106] Donald E. Godshaw, “Knee pad construction”, *Patent*, US 2006/0041986 A1, 2006.
[107] Shun Yi Jin, William Altenhof, “Comparison of the load/displacement and energy absorption performance of round and square AA6061-T6 extrusions under a cutting deformation mode”, *proceedings of the ICRASH 2006 Conference*, 2006.
[108] A. Kim, M.A. Hasan, S.H. Nahm, S.S. Cho, “Evaluation of compressive mechanical properties of Al-foams using electrical conductivity”, *Composite Structures*, 71 (2005), 191–198.
[109] Norman S.Currey, “Aircraft landing gear design: principles and practice”, *American Institute of Aeronautics and Astronautics*, 1988.
[110] Denis Howe, “Aircraft loading and structural layout”, *Professional Engineering*, 2004.
[111] Gerhard Mellmann, “Aircraft comprising a rescue device”, *International Patent*, W0 03/099656A1, 2003.
[112] Naoki Niwa, Takuji Kobori, Motoichi Takahashi, Tomohiko Hatada, Haruhiko Kurino, “Passive seismic response controlled high-rise building with high damping device”, *Earthquake Engineering and Structural Dynamics*, 24 (1995), 655-671.
[113] J. Latchford, E.C. Chirwa, “Airbag head restraint system”, IMechE, 2000, 214, 229-241.
[114] E.C. Chirwa, J.Latchford, P. Clavell, “Carbon skinned aluminum foam nose cones for high performance circuit vehicles”, *International Journal of Crashworthiness*, 2003(8), 1, 107-114.

Chapter 3

AN INNOVATIVE METHODOLOGY TO DISSIPATE ENERGY

3.1 COMMENTS ON EXISTING DISSIPATION DEVICES

The variety of designs and implementations of energy dissipation devices found in literature, certainly ascertain that energy absorption is a cross-discipline subject that incorporates many engineering concepts. As illustrated in the previous chapter, researchers have concentrated their efforts on the design and development of energy absorption devices that could be implemented for instance in buildings, in such a way to improve resistance against high forces for safety and human comfort.

The principles of metallic plastic deformation encouraged the development of torsional beam units and general metallic dampers. Although these devices are simple in design, flexibility is not completely achievable. In fact, in order to absorb large amounts of energy, usually bigger units are necessary or new parts must be added to the main structure. However, reusability is not a characteristic associated with these devices. After the first loading cycle, high plastic deformation occurs on the parts of the unit making it unsuitable for further use. Devices based on friction such as Limited Slip Bolted (LSB) dampers and Energy Dissipating Restraint (EDR) units can absorb energy of different severity (energy absorption levels). Such characteristics improve the flexibility and usability over metallic dampers. The mechanism and many parts of these devices may suffer wear, but are in theory reusable. However, when considering fatigue and surface wear, as the number of cycles increases, the effectiveness of frictional resistance decreases. In general, the behaviour of energy absorption units that are based on friction is unpredictable against the working conditions, time and frequency of usage. Energy absorption devices based on material properties such as viscoelastic units are simple in design, and have certain energy absorption capabilities. However, they have considerable design limitations in being sensitive to external environmental conditions, such as temperatures. Devices that dissipate energy throughout fluid viscosity, such as the Viscous Damping Walls (VDW) damper were introduced to

improve the general efficiency of dampers. However, in such designs fluids add some extra weight to the device and hence it becomes heavy and is not easy to handle.

On the other hand, investigations on building vibrations, due to severe loads, lead to the developments of Tuned Mass/Liquid Dampers. The natural frequency of these energy dissipating devices is tuned with the natural frequency of the building, hence the units must be replaced after any modification to the structure.

Active control of building vibrations through hydraulic systems presents strong potential advantages in terms of response efficiency and energy dissipation accuracy. Such designs are complex because of the combination of mechanical and electrical parts, and maintenance cost could be rather high.

Technologies and devices to absorb energy during landing operations of aircraft rely on standard energy absorption techniques that are based on the principles of steel/rubber/air springs and liquid/oleo-pneumatic dampers. However, the complexity and variety of parameters involved during landing operations, such as aircraft speed and landing angles, have to be taken into account during the design stage. Also, they must be capable of dissipating high levels of energy, when landing occurs, but also provide comfort to passengers during taxiing and slow motion operations. However, heavy-landings may still represent a problem, and the eventual integration of extra energy absorption units that may become active only in such occurrences becomes a necessity. However, this adds extra weight to the structure.

Human body defence devices such as body armour, helmets and leg protectors provide acceptable energy absorption capabilities and protection. However, problems were identified. In body armour, dangerous deformations could cause blunt traumas. In helmets and leg protectors, the high demand of fashionable devices is always in conflict with designs and geometries imposed by current technologies that aim at optimising protection and energy absorption levels.

Research on energy absorption is a crucial matter, when considering the need for ultimate safety and dissipation of unwanted energy. A novel methodology that showed to have good attributes for designing innovative energy absorption devices will be

presented in this work. Devices relying on this methodology can potentially replace or integrate with existing energy absorption units, to provide an optimum solution to the dissipation of unwanted energy.

3.2 BASE CONCEPTS AND IDEAS OF "UREAD" DEVICES

It is common in the metal forming field to relate to the idea that metals, in general, can undergo large amounts of deformation, either elastic or plastic. Energy dissipation devices based on elastic properties of materials will have rebound forces, therefore design must allow for extra space and the absorption of reaction force after impact. On the other hand, plastic deformation dissipates kinetic energy by transforming it into thermal energy. Such effect can eventually be diminished by a cooling down mechanism, if necessary. Design attempts for energy absorption devices based on plastic deformation of metals have already been examined in the literature review of this thesis, and showed some limitations, especially in terms of system reusability.

A new method to dissipate energy, that combine all the advantages of energy absorption due plastic deformation and total reusability, is the use of deformation thorough constant areas. Figure 3.1 shows the mechanism of a device based upon the principles of such a concept. The main elements are a pushing punch, an exit punch, a bent

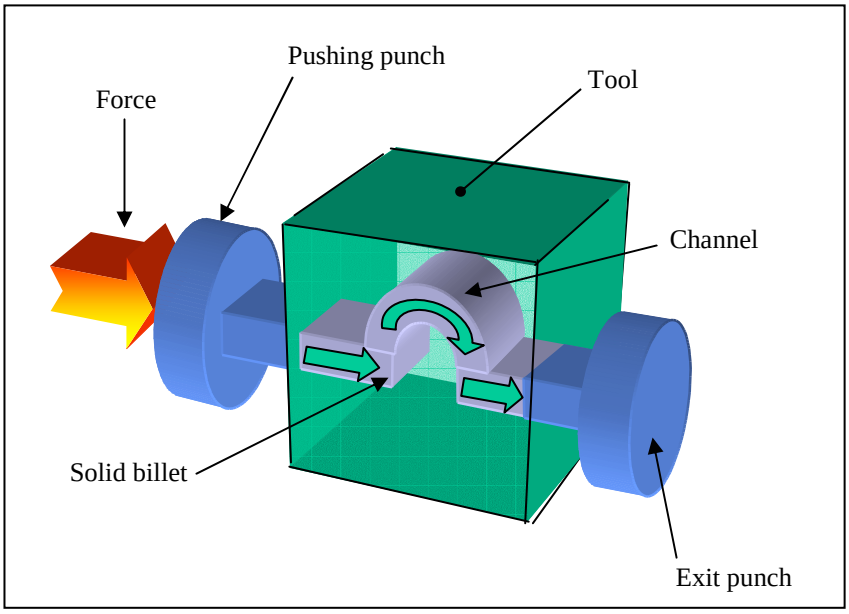

Figure 3.1 A new design to dissipate unwanted energy

channel with constant cross sectional area machined within a tool, and a billet of solid deformable material placed into the channel. When an external force is applied to the pushing punch, the solid billet will be forced to change its moving direction at correspondence of the channel bends, in order to follow the geometry of the channel; hence energy will be dissipated by a plastic deformation shearing process.

This process can be explained by the sketch in Figure 3.2, which shows the plastic deformation mechanism happening on a material when being moved within two intersecting channels, *N* and *J*. In order to achieve the material motion, shear has to happen at the intersection zone. As Figure 3.2 (a) shows, the shearing process is

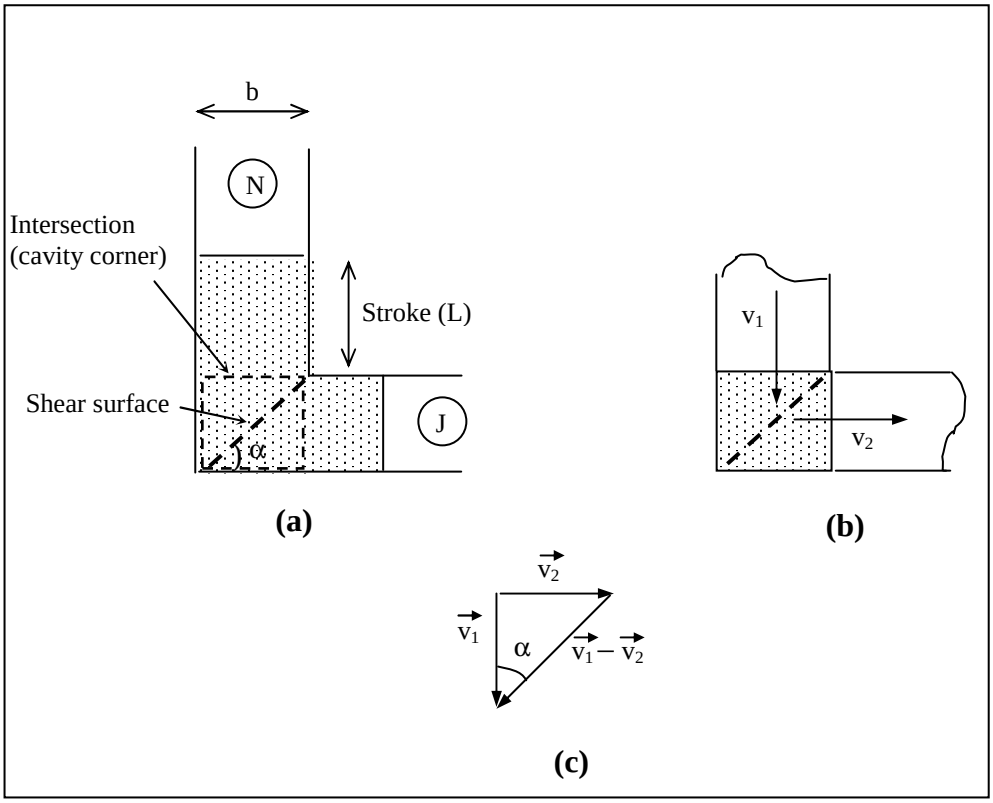

Figure 3.2 Concepts of shearing process of solid materials in a bent channel

modelled to develop on a shear surface, inclined at an angle α. The plastic deformation model for this process is based upon the principles of the Upper Bound analytical technique [85]. In this case, the material in the *N* channel moves with a velocity v_1 , while the material in the *J* channel moves with velocity v_2, as Figure 3.2 (b) shows. The shearing process is therefore demonstrated by the relative velocity (v_1 -v_2) which develops along the shear surface, as shown in the velocity diagram in Figure 3.2 (c).

The intensity of the relative velocity relies upon the inclination angle between the channels.

Because the cross section of the channels is constant, the billet can be moved forward and backwards through the channels, and the device has the potential of infinite reusability. In practice, by forcing a solid material to deform as it passes round a bend in a channel, it is possible to construct a Universal Reusable Energy Absorption Device (UREAD), capable of dissipating unwanted energy. Different channel geometries and deforming material will give different levels of energy absorption, basically by using the same working principles and manufacturing methods. Figure 3.3 (a) and (b) shows

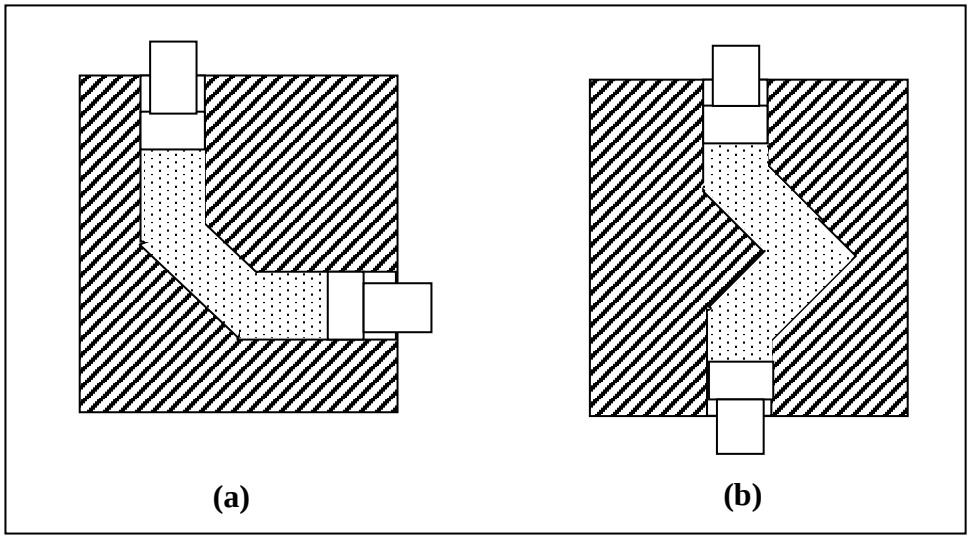

Figure 3.3 Various potential "UREAD" channel designs

some sketches of potential devices characterized by various channels geometries, that have the same basic in design, size and proportions but different shearing mechanisms. The constant cross-sectional area of the channels can be easily manufactured in circular or square forms. However, other geometries can be considered including hexagonal cross-sections.

A tangible example of the potential of accommodating a variety of energy absorption levels is given in Figure 3.4. The figure shows analytical levels of energy dissipation (E), predicted by the Upper Bound technique [85], for an extrusion process similar to the one in Figure 3.2. Details of the analysis will be presented in Chapter 4. The figure

shows the results of channels of equal cross sectional area (A) intersecting at two different angles, 90^0 and 135^0. The geometrical parameter (b) is the channel width and (L) is the total stroke, as in Figure 3.2. Both maximum energy and stroke are represented in terms of the channels parameters and for various frictional conditions; m=0, 0.5 and 1. Also, $(2\tau_k)$ is the material yield stress. The figure demonstrates the potential of UREAD devices to dissipate various energy levels, obtainable for instance by varying the channels inclination angle, the cross-sectional area, the deformable material or the total stroke.

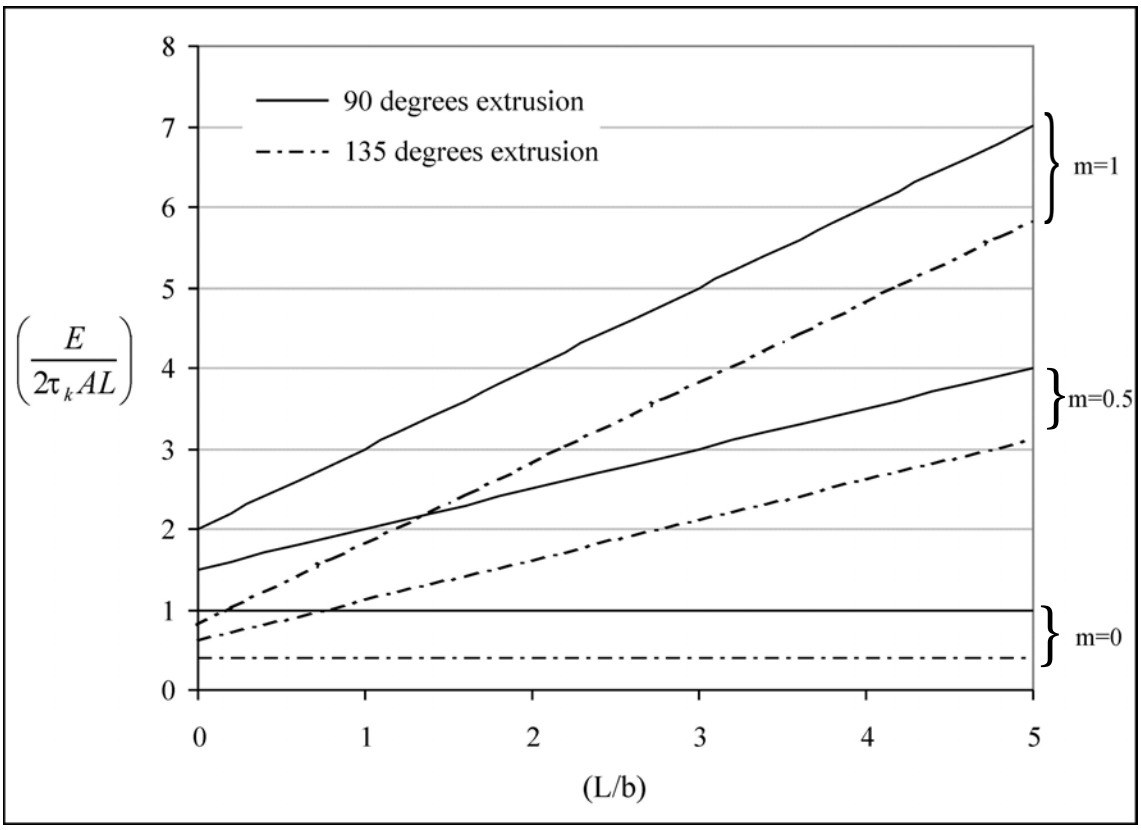

Figure 3.4 Energy absorption levels for UREAD devices

.

This idea of the UREAD device is the invention of Dr. Fayek Osman, lecturer at the University of Bath, and the concept has been recently patented [86]. This new technique represents therefore a new method for energy absorption. It is simple to use, with low cost and easy to manufacture. Devices designed with such a technology are reusable and technically easy to integrate into any structure.

3.3 EQUAL CHANNEL ANGULAR EXTRUSION HISTORY

From the historical point of view, deforming a solid material through equal channels has been used for material refinement, but not to absorb energy. The history of this process dates back to the 1980s, when a Russian researcher, Vladimir Segal, invented and patented a process, commonly known as Equal Channels Angular Extrusion (ECAE) [87]. He claimed that mechanical properties of metallic materials will significantly improve when extruded through inclined channels. This effect is due to the severe plastic deformation, where high effective strain is imposed on the material, with basically no change in billet geometry. The ECAE was studied over the years by a number of researchers [88-93], in order to develop the process and try to relate material final properties to tool shape, geometry and temperature. Rosochowski [94] developed the "2-turns" Equal Channels Angular Extrusion process, which is capable of achieving larger strains in one pass only. In this work, a numerical simulation of the process was carried out and shearing bands identified at the channels intersections, as shown in Figure 3.5 [94].

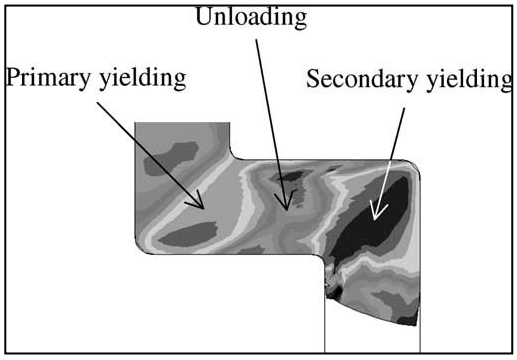

Figure 3.5 Distribution of equivalent stress in 2-turns Equal Channel Angular Extrusion [94]

However, despite the significant research efforts carried out in this area, the ECAE itself never found significant implementations or commercialisations, as an industrial process.

3.4 METHODS OF ANALYSIS

The analysis of the ECAE process is fundamental in order to understand the principles and working mechanisms behind the energy absorption process of devices based on the UREAD technique. In general, when a solid billet is forced to plastically deform within a tool, the following techniques are usually employed in order to provide a solution to forces and stresses.

Force Equilibrium method

This method sets up a force balance on a slab element of differential thickness. This produces a differential equation, where the variation of stresses along the deformation path is predicted.

In this analysis, the following assumptions are usually made:

1) Inertial forces are neglected,
2) The deformation is assumed homogeneous,
3) The effects of surface friction are included in the force balance.

Upper Bound Analysis method

This method calculates the deformation load by equating the internal rate of energy dissipation to the rate of external work applied to the workpiece. Theoretically, it always provides a solution greater than or equal to the exact one. The energy is assumed to be internally dissipated across surfaces of velocity discontinuity. When applying such a method, the following assumptions are made:

1) The force equilibrium is ignored.
2) The material is isotropic and homogeneous.
3) Frictionless or constant shear stress conditions prevail at the tool interface.

The governing formula is given by Equation 3.1, where τ_k is the material shear yield stress, W is the work required to cause the deformation, G is the area of the surface of velocity discontinuity, and v_r is the relative velocity.

$$\frac{dW}{dt} = \tau_k G_i v_{r\,i} \tag{3.1}$$

The Upper Bound technique has been applied to the plain-strain ECAE process by several researchers, Altan [95] and Ivani [96]. Paydar et al [97] developed an upper bound analysis for circular cross sectional channels and provided experimental verification of the results.

Slip Line Field method

This methodology provides a graphical type solution and it is based on an admissible stress field. In practice, a map showing the direction of the maximum shear stresses (sliplines) is constructed inside the deforming material.

Segal [98] has employed a slip lines stress field for the plain strain ECAE process. In his work, equations were developed to predict the material internal and forming stresses when yielding occurs.

Finite Element Analysis method

Finite Element is a generic form of analysis, which is used for obtaining solutions for many engineering problems. It requires all governing equations, usually in differential form, obtained from stress analysis, stress-strain relationships, plastic flow rules and work done. The output of the Finite Element Analysis technique is usually clear and comprehensive, although the accuracy is not always verified. Furthermore, such analysis is rather laborious as it involves complex calculations; therefore it always requires the intense use of computer systems, especially for non-linear problems.

3.5 CONCLUSIONS

An innovative methodology to dissipate unwanted energy in engineering systems was

introduced. This is based upon the working principles of plastic deformation of solid deformable materials through intersecting channels, similar to the process of Equal Channel Angular Extrusion (ECAE). This technique was shown to have the potential of building Universal Reusable Energy Absorption Devices (UREAD). The energy dissipation performance relies upon the relative inclination angle of the channels, the deformable material yield stress, the channels cross sectional area, the channels geometry, the frictional condition at the interface between tool and material and the stroke length.

Chapter 4

THEORETICAL INVESTIGATION

4.1 CAE SLAB METHOD SOLUTION

In order to estimate stress requirements and energy absorption capabilities for the UREAD novel technology introduced in the previous chapter, a plain-strain theoretical analysis is presented. It covers the yielding process of solid materials deforming through intersecting channels and it is based on the force equilibrium method. However, the analysis is generalised by initially considering unequal extrusion channels. For this analysis, the channels intersect at 90-degrees, as sketched in Figure 4.1. The aim of this theoretical study is to estimate the forming pressure p_d against punch displacement y, for a full stroke of length L. Initially, yielding requirements for a deformable solid billet to extrude through intersecting channels will be studied, at various initial strokes L in the vertical channel, but with an empty horizontal channel. Subsequently, the analysis will be extended to include the horizontal channel, and hence achieve a complete analysis of force-pressure behaviour for a full stroke process in UREAD 90^0 devices. In this analysis the tool is assumed to be rigid; punch and channels side walls are in perfect contact with the deforming billet; and the deformation is uniform. In addition, other mechanisms which may contribute to the overall behaviour such as local yielding and general bending effects are assumed to be negligible.

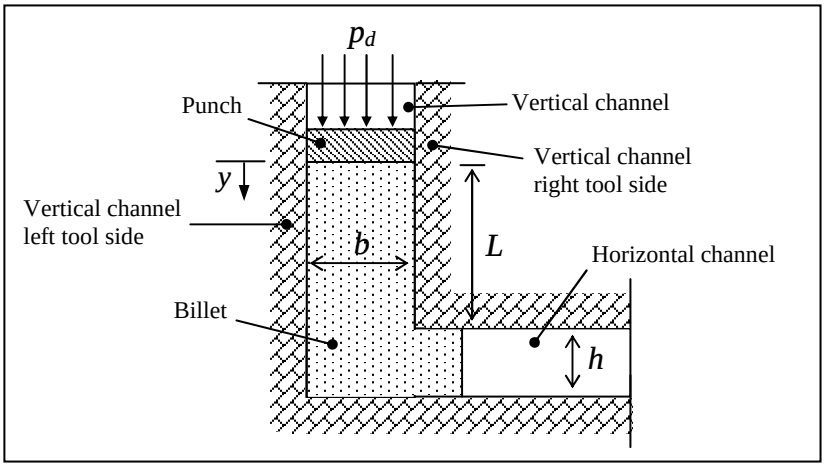

Figure 4.1 Extrusion through intersecting unequal 90^0 channels

4.1.1 Stress analysis in the vertical channel

With regards to this analysis, a billet made of a solid material is positioned into a vertical channel and forced to flow sideways into the horizontal direction. As shown in Figure 4.1, the billet is pushed by a punch, where p_d is the pressure required to yield the material, L is the stroke, b and h are the width of the vertical channel and horizontal exit respectively. When yielding takes place, the material flows through the horizontal direction. In principle yielding occurs and depends upon the flow path available to the material. For example, if the material is forced into an enclosed cavity, a rise to hydrostatic pressure occurs and flow is prohibited by the surrounding tool. Figure 4.2 shows the two extreme cases: fully enclosed cavity and free flow simple compression.

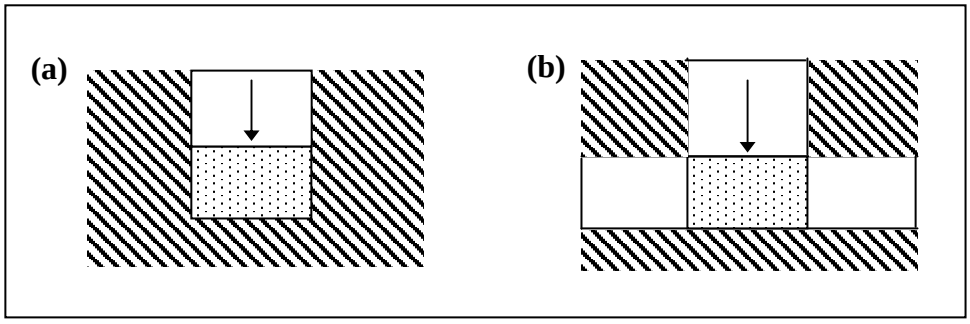

Figure 4.2 a) Fully enclosed cavity. b) Free flow condition

In the approach developed here a local yielding zone will be assumed to evolve according to the dimensions of the exit channel. Therefore, a local yielding zone is assumed to exist, and located nearby the exit channel. The local deformation zone is simulated by a portion of the material in the channels intersection zone (cavity corner),

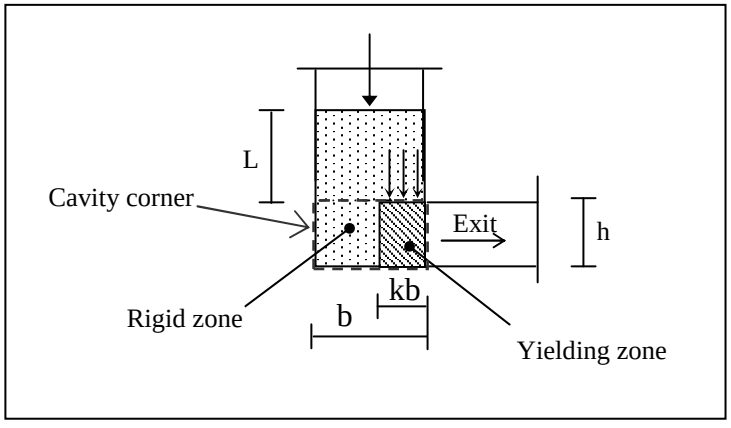

Figure 4.3 Yielding zone location

as Figure 4.3 shows. Yielding will occur due to the intense local pressure. Such pressure acts on a portion of the surface at the entry section of the deforming zone. Hence, a parameter k is introduced, that defines the size of the yielding zone. The assumption is made that the effective yielding zone length is proportional to the width b and represented by kb, where $0 \le k \le 1$. Considering Figure 4.3, a dependence of k may be represented by the following:

When $0 \le L < h$, then $k = \frac{L}{h}$ ⟶ yielding zone length = kb (4.1)

When $L \ge h$, then $k = 1$ ⟶ yielding zone length = b (4.2)

4.1.2 Vertical stress distribution on the cavity corner boundary

The slab method is used in order to calculate the theoretical stresses requirements. Consider an element of material across the cavity corner, as shown in Figure 4.4, μ is the coefficient of friction between the tool and the deforming material. In addition to the general system of forces, $\sigma_x, p, \mu p$, acting on the slab, there is an opposition to the

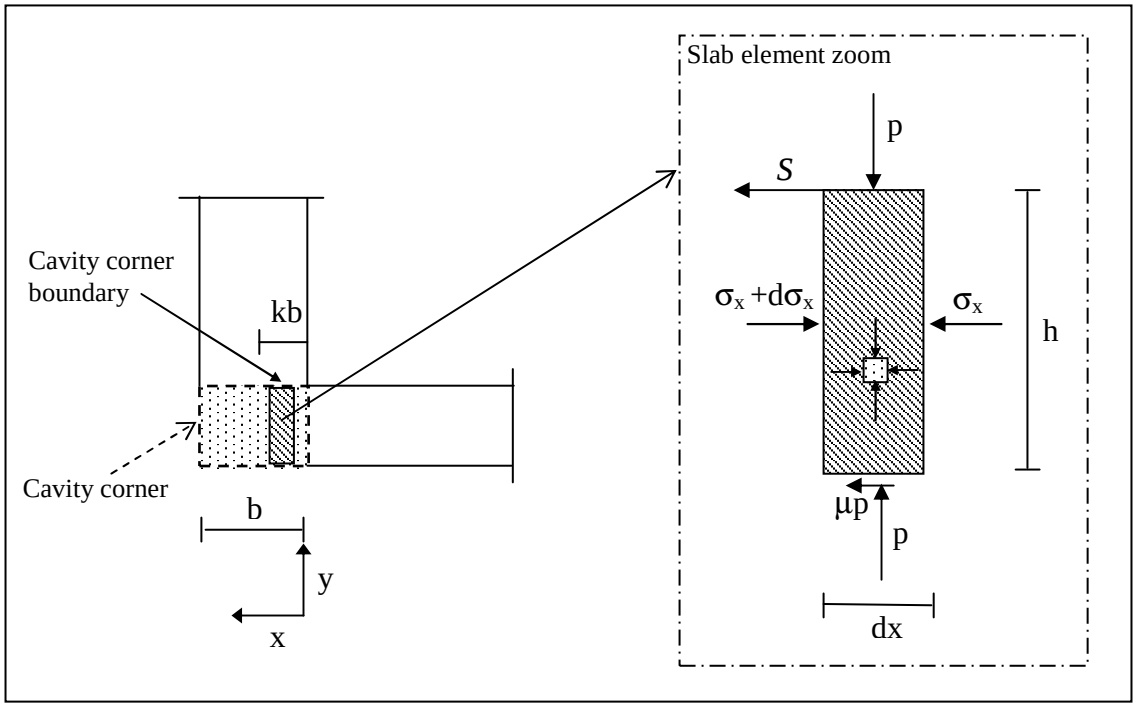

Figure 4.4 Slab element in the yielding zone

material flow, and that is the resistance force S, exerted at the interface between the deforming material and the rigid material in the vertical channel, immediately above the boundary of the cavity corner. When applying the slab method, the following assumptions are made [99,100]:

i) The material is isotropic and incompressible
ii) The inertial forces are small and neglected
iii) Material deformation is homogeneous

Considering the stress system represented in Figure 4.4 (b), the force equilibrium along the X-direction gives

$$-(\sigma_x + d\sigma_x)h + S + \mu p dx + \sigma_x h = 0 \tag{4.3}$$

$$S + \mu p dx = h d\sigma_x \tag{4.4}$$

Assuming that the resistance force S is the maximum possible, such resistance on the slab element is given by

$$S = \tau_k dx \tag{4.5}$$

where τ_k is the material shear stress. Substituting equation 4.5 into equation 4.4, it follows;

$$(\tau_k + \mu p)dx = h d\sigma_x \qquad \text{valid for } [0 \le x < kb] \tag{4.6}$$

As the material deformation is homogeneous and considering that the material can flow only through the horizontal and vertical channels, the principal directions of deformation at any point within the yielding zone must be horizontal and vertical. Hence, when yielding occurs, the Tresca criterion may be defined as

$$p - \sigma_x = 2\tau_k \tag{4.7}$$

and hence

$$d\sigma_x = dp \tag{4.8}$$

By substituting equation 4.7 into equation 4.6 gives

$$(\tau_k + \mu p)dx = hdp \tag{4.9}$$

Equation 4.9 can now be integrated over the horizontal direction

$$\int \frac{dx}{h} = \int \frac{dp}{\tau_k + \mu p} \tag{4.10}$$

$$\frac{x}{h} = \frac{1}{\mu}\ln(\tau_k + \mu p) + C \tag{4.11}$$

Considering that at x=0 the surface is free, i.e. σ_x = 0, equation 4.7 becomes

$$p_{x=o} = 2\tau_k \tag{4.12}$$

Therefore, the value of the constant *C* is obtained from equation 4.12, hence,

$$C = -\frac{1}{\mu}\ln[\tau_k(1+2\mu)] \tag{4.13}$$

By substituting Equation 4.13 into Equation 4.11, the following equation is obtained

$$\frac{x}{h} = \frac{1}{\mu}\ln\left[\frac{\tau_k + \mu p}{\tau_k(1+2\mu)}\right] \tag{4.14}$$

$$\tau_k + \mu p = \tau_k(1+2\mu)e^{\frac{x\mu}{h}} \tag{4.15}$$

re-arranging gives

$$\frac{p}{2\tau_k} = \frac{1}{2\mu}[(1+2\mu)e^{\frac{x\mu}{h}} - 1] \qquad \text{valid for } [0 \le x < kb] \tag{4.16}$$

Equation 4.16 gives the vertical stress distribution on the boundary of the cavity corner, for the material section within the yielding zone.

When considering the remaining part of material in the cavity corner (rigid zone), yielding does not occur and the slab element becomes as shown in Figure 4.5. In this

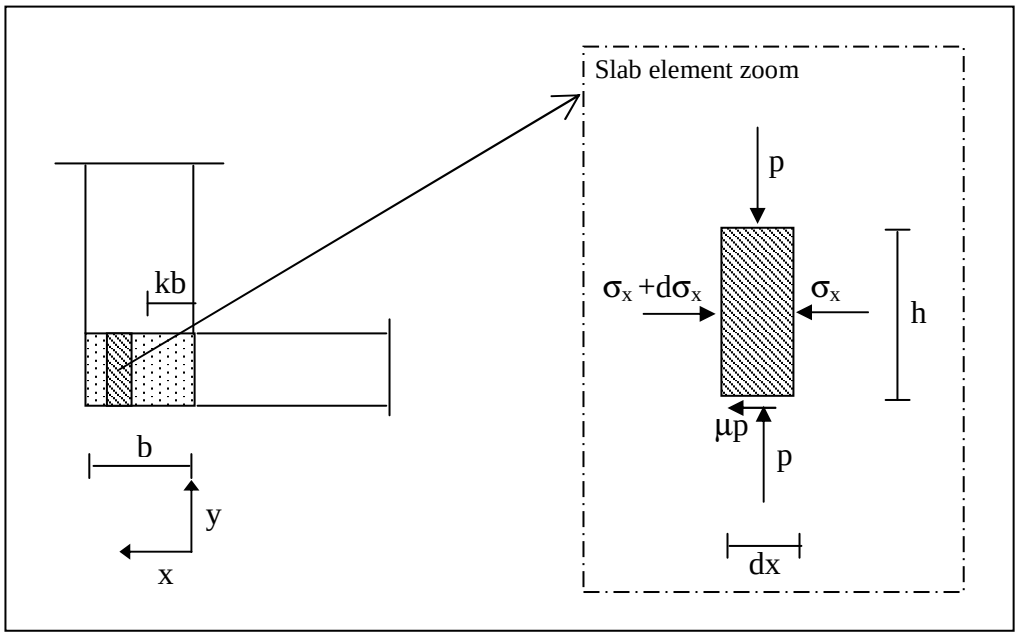

Figure 4.5 Slab element in the rigid zone

case, the resistance force *S* is assumed to diminish, as the material remains rigid. The force equilibrium on the element in Figure 4.5 along the x-direction brings gives the following differential equation

$$-(\sigma_x + d\sigma_x)h + \mu p dx + \sigma_x h = 0$$

$$\mu p dx = h d\sigma_x \qquad \text{valid for} \quad [kb \le x \le b] \tag{4.17}$$

As the principal stresses are in the horizontal and vertical directions and the material across the rigid zone is not deforming, i.e. treated as a rigid body under hydrostatic conditions. Therefore one can write

$$p - \sigma_x = 0 \tag{4.18}$$

and

$$d\sigma_x = dp \tag{4.19}$$

Substituting equation 4.19 into equation 4.17, gives

$$\mu p dx = h dp \tag{4.20}$$

The integration of equation 4.20 gives

$$\frac{x}{h} = \frac{1}{\mu} \ln p + C_1 \tag{4.22}$$

At the interface between the yielding zone and the rigid zone, $x=kb$, the vertical pressure is assumed equal for continuity. Substituting into equation 4.16 and 4.22 with $x=kb$, it gives

$$p = 2\tau_k \left[\frac{1}{2\mu}(1+2\mu) e^{\frac{kb\mu}{h}} - \frac{1}{2\mu} \right] = 2\tau_k \beta \tag{4.23}$$

where $$\beta = \left[\frac{1}{2\mu}(1+2\mu) e^{\frac{kb\mu}{h}} - \frac{1}{2\mu} \right] \tag{4.24}$$

Using Equations 4.23, the parameter C_1 is obtained as it follows

$$\frac{kb}{h} = \frac{1}{\mu} \ln(2\tau_k \beta) + C_1 \tag{4.25}$$

Equation 4.25 gives the value for C_1 , hence by substituting this value into Equation 4.22, the vertical stress distribution can be finally calculated as follows

$$\frac{x}{h} = \frac{1}{\mu}\ln p + \frac{kb}{h} - \frac{1}{\mu}\ln(2\tau_k\beta) \tag{4.26}$$

$$\frac{\mu(x-kb)}{h} = \ln\left(\frac{p}{2\tau_k\beta}\right) \tag{4.27}$$

$$\boxed{\frac{p}{2\tau_k} = \beta \cdot e^{\frac{\mu(x-kb)}{h}}} \qquad \text{valid for} \quad [kb \le x \le b] \tag{4.28}$$

When the stroke L is zero, the material in the cavity corner will not extrude but it will be subjected to simple compression. In this case, the vertical pressure distribution is obtainable from Equation 4.28, using β=1 and k=0. The result is similar to that obtained under the analysis of simple compression [85].

Figure 4.6 gives the vertical pressure curves on the yielding surface against the x-coordinate, for the case of $b=h=10$ mm and μ=0.2. The results are calculated for

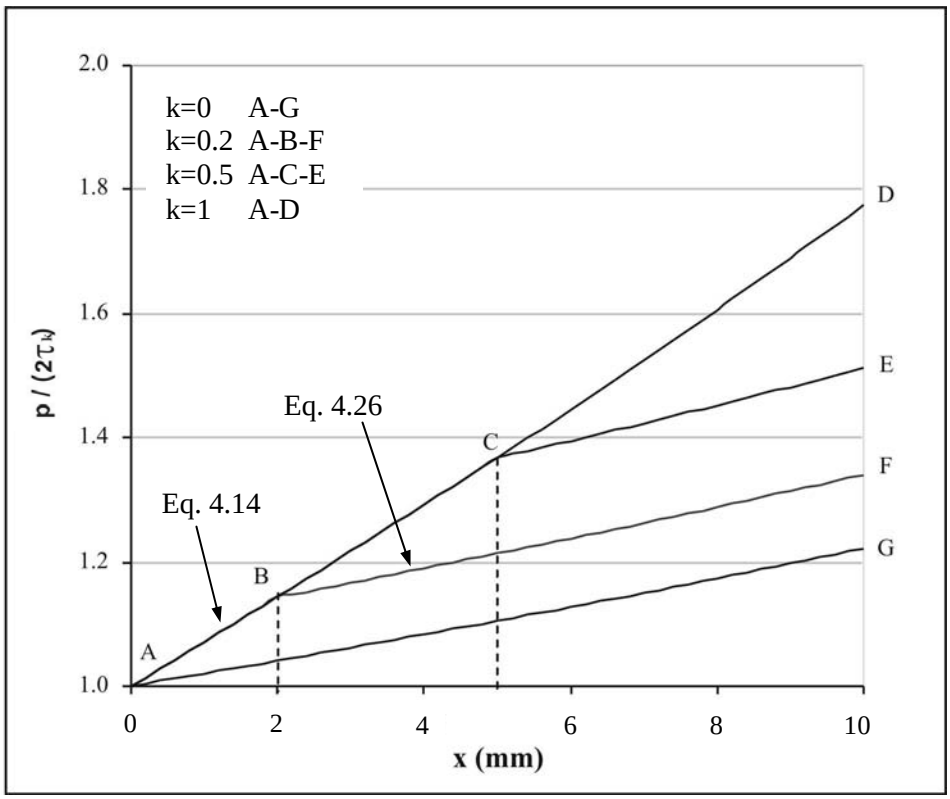

Figure 4.6Vertical pressure p results at different strokes L

different values of the parameter *k*. The distribution shows increasing relative stress values from the material free surface (at x=0) to the channel boundary side (x=b).

4.1.3 Average vertical stress on cavity corner boundary

Equations 4.16 and 4.28 can be now integrated along the x-direction in order to calculate a value of the vertical force along the cavity corner boundary. Figure 4.7 shows a representation of the vertical stress trend given by the equations, where R_1 and R_2 are the areas measured under the curve of the vertical stress distributions for $0 \le x < kb$ and $kb \le x \le b$ respectively.

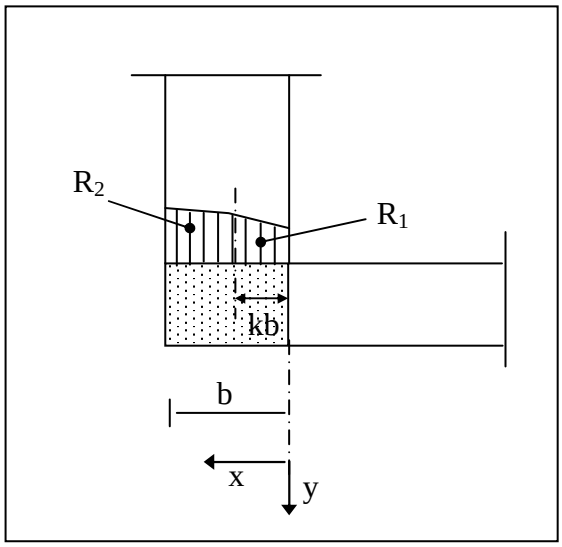

Figure 4.7 Vertical stress on the intersection zone boundary

The integration of equation 4.16 gives

$$R_1 = 2\tau_k \int_0^{kb} \left[\frac{1}{2\mu}(1+2\mu)e^{\frac{x\mu}{h}} - \frac{1}{2\mu} \right] dx = \frac{h}{\mu}\left(\frac{1+2\mu}{2\mu} \right) \cdot \left[e^{\frac{kb\mu}{h}} - 1 \right] - \frac{kb}{2\mu} \qquad (4.29)$$

while the integration of equation 4.28 gives

$$R_2 = 2\tau_k \int_{kb}^{b} \left[\beta \cdot e^{\frac{\mu(x-kb)}{h}} \right] dx = \beta \frac{h}{\mu} \left[e^{\frac{\mu(b-kb)}{h}} - 1 \right] \qquad (4.30)$$

The relative average value of vertical pressure p_{ave} is then calculated in Equation 4.29, by adding equation 4.29 and equation 4.30

$$\frac{p_{ave}}{2\tau_k} = \frac{R_1 + R_2}{2\tau_k}\frac{1}{b} \qquad \text{Hence,} \tag{4.31}$$

$$\boxed{\frac{p_{ave}}{2\tau_k} = \frac{h}{b\mu}\left(\frac{1+2\mu}{2\mu}\right)\cdot\left[e^{\frac{bk\mu}{h}} - 1\right] - \frac{k}{2\mu} + \frac{\beta}{b}\cdot\frac{h}{\mu}\left[e^{\frac{\mu(b-kb)}{h}} - 1\right]} \tag{4.32}$$

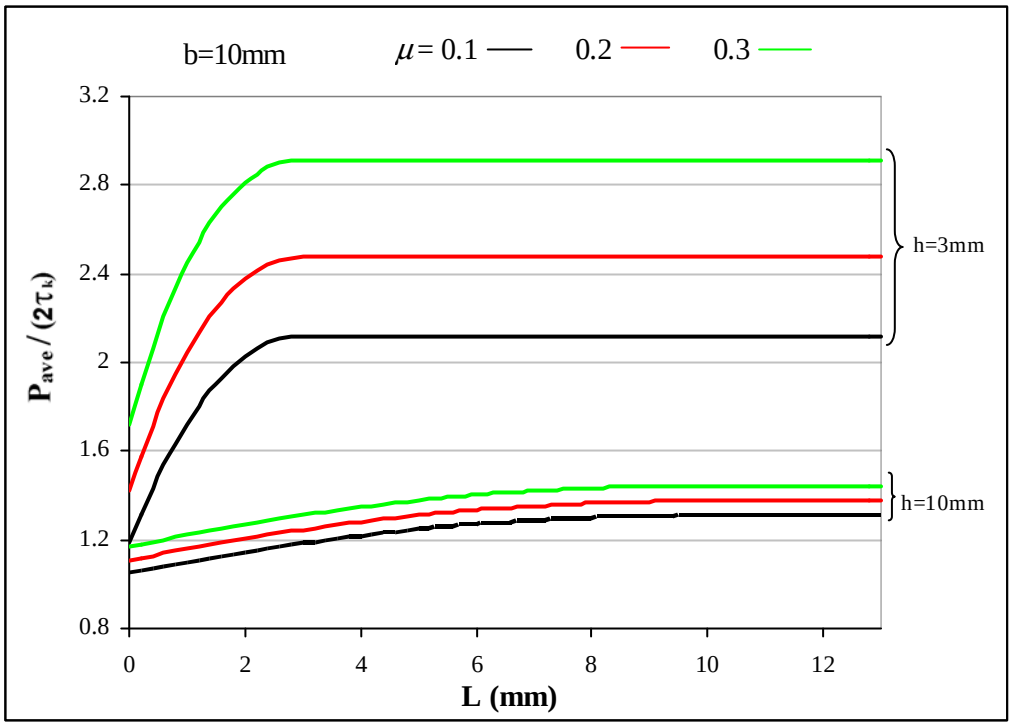

Figure 4.8 Average vertical stress on the intersection zone boundary against the stroke L

Figure 4.8 shows the distribution of the average vertical stress given by Equation 4.30 on the cavity corner boundary for different strokes *L*. In this representation, the friction coefficient μ is set to 0.1, 0.2 and 0.3; and *b* to 10mm. Results are plotted for different values of *h*. The average vertical stress increases with *L*, while a constant distribution is found when *L* is greater then *h*. This means that as *h* decreases, the average vertical stress on the intersection boundary has to increases in order to create the conditions for

the material to flow through the horizontal channel. Also, higher friction coefficients lead to higher levels of vertical stress.

4.1.4 Normal stresses on the vertical channel

The part of the billet inside the vertical channel is not plastically deforming, therefore it can be treated as a rigid body under variable hydrostatic conditions. Hence, the average pressure p_{ave} measured on the cavity corner boundary from equation 4.32 is assumed to act on the billet interfaces in the vertical channel. The forces generated by the pressure p_{ave} on the tool sides in the vertical channel are shown in Figure 4.9(a). F is the force on the cavity corner boundary, F_r and F_l are the forces acting on the right and left hand side of the channel respectively, F_d is the punch force on the top of the billet. In addition to

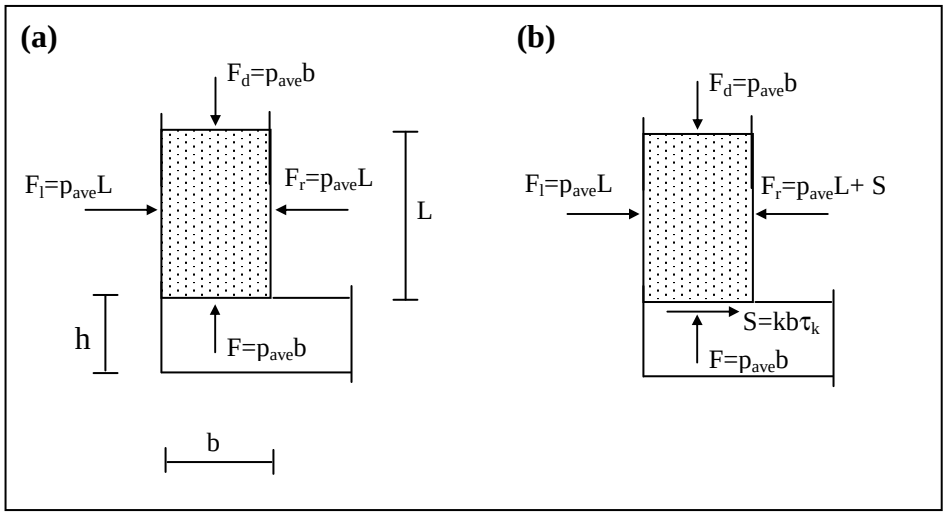

Figure 4.9 Force equilibrium on the material in the vertical channel - frictionless

this, the total tangential shear force S also exists on the cavity corner boundary, as shown in Figure 4.9(b). From equation 4.3, its maximum intensity equals $kb\tau_k$. The force system has to be in equilibrium, therefore it is assumed that the shear force S is balanced by the right hand side of the tool. Equations 4.33, 4.34, 4.35 and 4.36 give a final formulation of the normal forces acting on the billet interfaces.

$$F = F_d = p_{ave}b \tag{4.33}$$

$$F_l = p_{ave} L \tag{4.34}$$

$$S = kb\tau_k \tag{4.35}$$

$$F_r = p_{ave} L + S = p_{ave} L + kb\tau_k \tag{4.36}$$

Normal force formulations can be translated in terms of the normal stress acting on the right and left hand side of the tool, called p_r and p_l respectively

$$p_r = p_l = 0 \qquad \text{for} \quad L=0 \tag{4.37}$$

$$p_r = \frac{F_r}{L} = p_{ave} + \frac{b}{h}\tau_k \qquad \text{for} \quad 0 < L < h \tag{4.38}$$

$$p_r = \frac{F_r}{L} = p_{ave} + \frac{b}{L}\tau_k \qquad \text{for} \quad L \geq h \tag{4.39}$$

$$p_l = \frac{F_l}{L} = p_{ave} \tag{4.40}$$

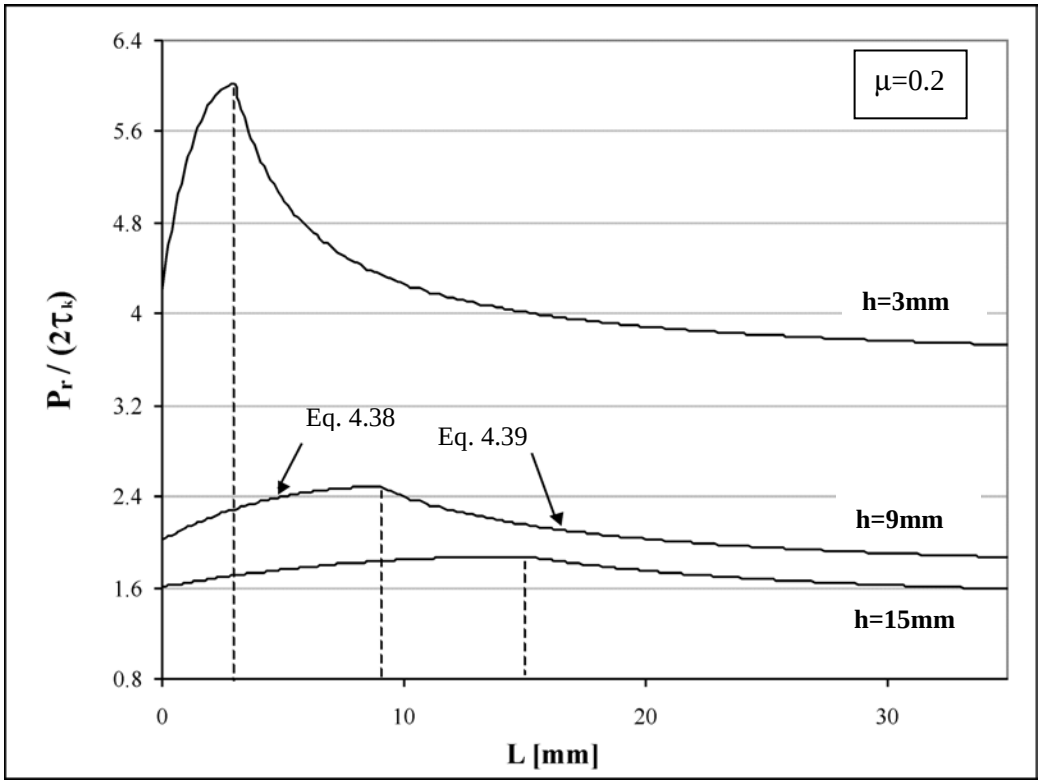

Figure 4.10 Average vertical stress results on the right hand side of the vertical channel

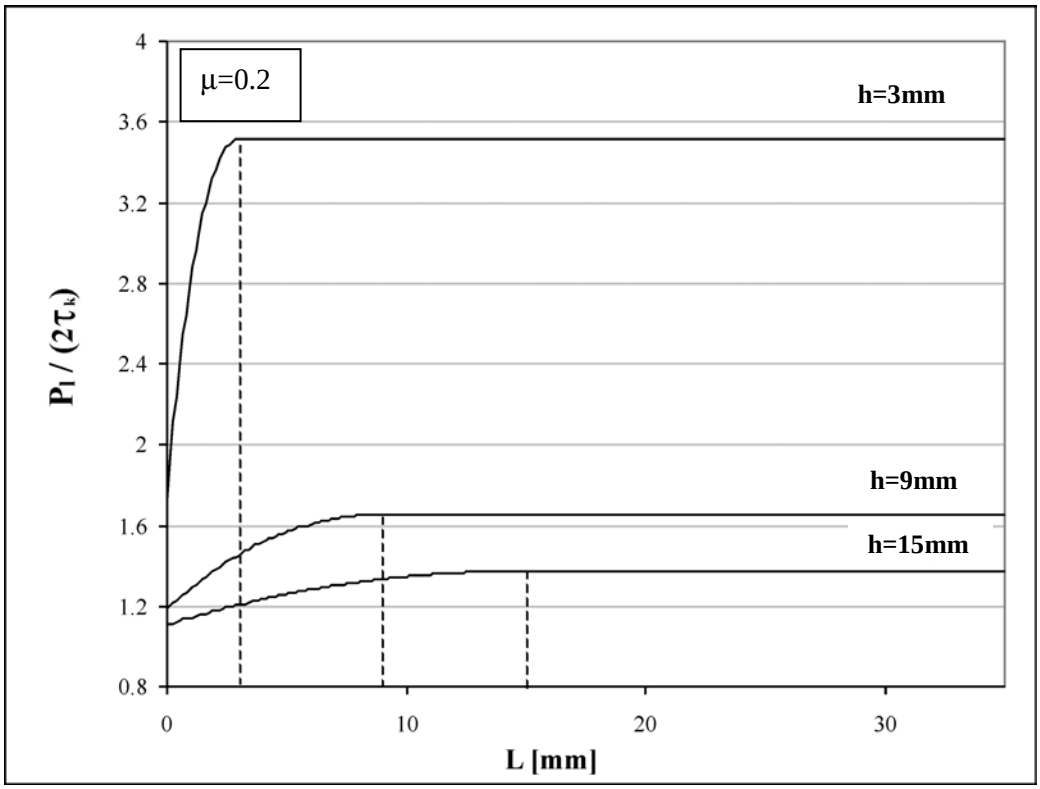

Figure 4.11 Average vertical stress results on the left hand side of the vertical channel

Figure 4.10 and 4.11 give results of the vertical stresses across the right and left hand side of the vertical channel, following Equations 4.37 to 4.40, when b=15mm and μ=0.2, but at different values of the horizontal channel exit *h*. The stress acting on the right hand side increases with *L* until *L* equals *h*, then it decreases to a limiting value.

When friction is considered, the forces acting on the material in the vertical channel are shown in Figure 4.12. The punch force F_d is expected to be higher then *F* due to the

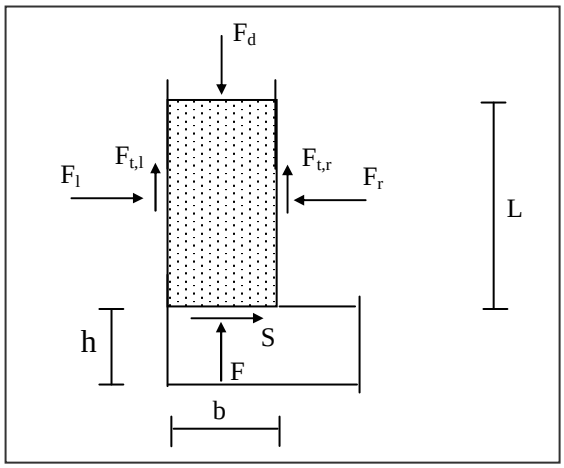

Figure 4.12 Forces action on the vertical channel – with friction

resistance effect of frictional forces $F_{t,r}$ and $F_{t,l}$ acting on the right and left hand side of the billet respectively.

Similar to the analysis with frictionless conditions, the stress system in Figure 4.12 is analysed in two steps. The first is to consider the material enclosed in a closed cavity, and the second is to superimpose the shear force S on it. By following the first step, Figure 4.13 shows the stresses on a slab element of material in the vertical channel of length dy. The material in the vertical channel is stressed within a closed cavity,

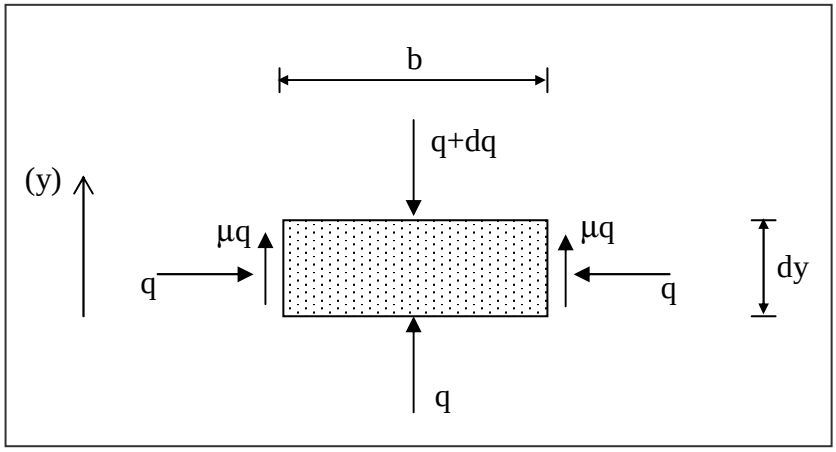

Figure 4.13 Stress system on a slab of material in the vertical channel

therefore a normal stress q acts along the horizontal and vertical directions. The frictional stress along the sides of the slab is μq. Applying the force equilibrium along the y direction gives

$$bdq = 2\mu q dy \tag{4.41}$$

and integrating gives

$$\ln q = \frac{2\mu y}{b} + C \tag{4.42}$$

But at y=0, $q=p_{ave.}$ Substituting into equation 4.42 gives

$$q = p_{ave} e^{\frac{2\mu}{b} y} \tag{4.43}$$

Now, adding the effect of the shearing force S on the extrusion force, gives

$$F_d = qb + \mu S = qb + \mu kb\tau_k \tag{4.44}$$

but $F_d = p_d b$, therefore

$$p_d = q + \mu k\tau_k \tag{4.45}$$

Substituting equation 4.43 into equation 4.45 and noting that the stroke L equals the length y in the vertical channel, gives

$$\boxed{\frac{p_d}{2\tau_k} = \frac{p_{ave}}{2\tau_k} e^{\frac{2\mu}{b}L} + \frac{\mu k}{2}} \tag{4.46}$$

Figure 4.14 gives the relative extrusion pressure p_d from equation 4.46 against the stroke L, for different coefficient μ and horizontal exit h.

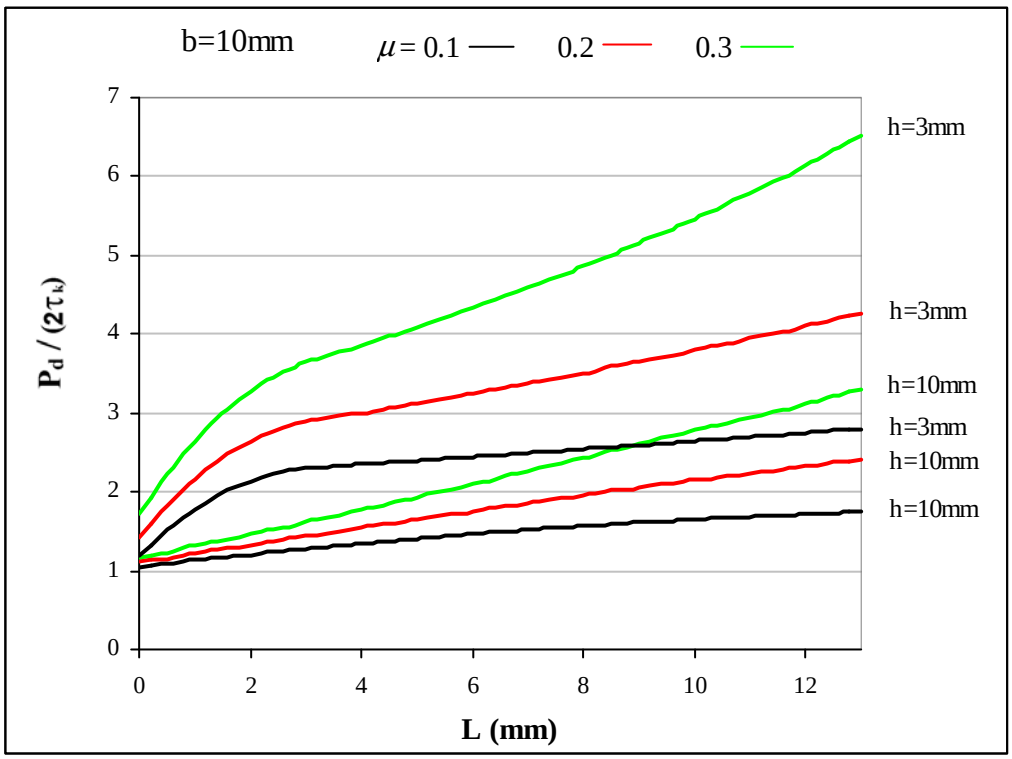

Figure 4.14 Forming stress with friction on channel sides

It is clear that when friction forces are taken into account, the average punch stress increases with the full stroke L. In the case of L=0 the relative stress is higher than 1, because of the friction between the tool and material acting on the bottom boundary of the cavity corner. In general, the effect of increasing the friction coefficient on the forming stress is greater for smaller horizontal channels.

4.1.5 Effect of the horizontal channel on forming pressure

When the deformable material extrudes into the horizontal channel, additional resistance forces plastically and elastically may develop, which would further affect the forming pressure.

Figure 4.15 shows a stress strain characteristic of a deformable material in the general elastic-plastic region. If the material is deformed within the elastic region, up to the strain of ε_1, it will spring back to a final zero strain. In the plastic region the spring back will be from ε_3 strain to ε_2 strain. The ratio between ε_3 and ε_2 depends on the elastic properties of the material being deformed. This behaviour applies to all processes where the material experience plastic deformation.

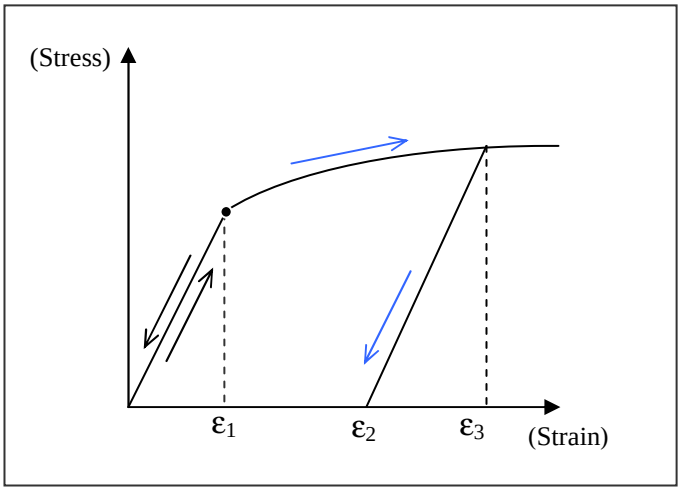

Figure 4.15 Typical stress-strain curve of an elastic-plastic material

In a 90^0 channels extrusion the material exits from the side hole. The extruded material is likely to be slightly bigger then the hole dimensions due to elastic spring back, as

shown in Figure 4.16. Considering now the process of Channel Angular Extrusion (CAE), shown in Figure 4.1, the elastic distortion from the initial hole size to the final material size will be absorbed by the elastic deformation of the horizontal channel walls. This will create an interface pressure between the deformed material and the horizontal channel walls.

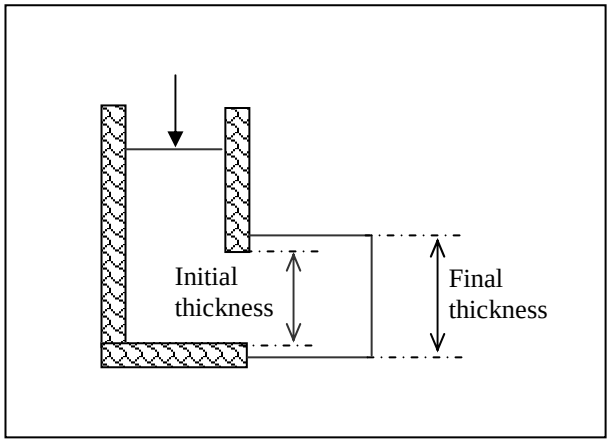

Figure 4.16 Sketch of extrusion through a side hole and back spring effect

The intensity of the contact normal stress, called p_n, imposed by the tool on the material in Channel Angular Extrusion, can be considered to be the pressure required to bring the billet geometry at the exit hole size. The material of the horizontal channel plays an important role in this case. In the limit case of channels walls extremely rigid (exhibiting no elastic deformation), the pressure on the wall be equivalent to the yield strength of the extruded material, therefore

$$p_n = 2\tau_k \tag{4.47}$$

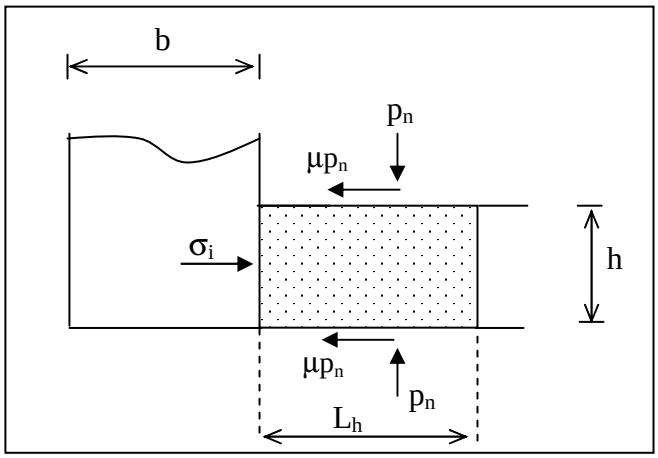

Figure 4.17 Force equilibrium on the billet in the horizontal channel

Figure 4.17 shows possible stresses applied on the extruded billet along a length L_h in the horizontal channel, where μ is the friction coefficient between channel wall and the extruded material. The force equilibrium in the horizontal direction gives

$$\sigma_i = 2\mu p_n \frac{L_h}{h} \tag{4.48}$$

considering the limit case where $p_n = 2\tau_k$

$$\sigma_i = 4\mu\tau_k \frac{L_h}{h} \tag{4.49}$$

Equation 4.49 identifies a new boundary condition to the one already defined in Equation 4.12. In fact, at the location x=0, the value of σ_x would not be zero, but equal to σ_i. With the addition of the horizontal channel, a modified value of average pressure on the cavity corner boundary, ($p_{ave,m}$), can be obtained by re-integrating Equations 4.11 and 4.22 according to the new boundary condition in Equation 4.49.

$$\frac{p_{ave,m}}{2\tau_k} = \frac{2\mu L_h}{h} + \frac{p_{ave}}{2\tau_k} \tag{4.50}$$

In equation 4.50, the value of p_{ave} is obtained from equation 4.32. It can be also considered that during the material movement, from the vertical channel to the horizontal channel, the volume remains constant, therefore

$$L_h = L\frac{b}{h} \tag{4.51}$$

Substituting equation 4.51 into 4.50, and equation 4.50 into equation 4.46, the punch pressure p_d becomes

$$\frac{p_d}{2\tau_k} = \frac{p_{ave,m}}{2\tau_k} e^{\frac{2\mu}{b}L} + \frac{\mu k}{2} \qquad (4.52)$$

Figure 4.18 shows the punch pressure for a material extrusion from a 10mm vertical channel into different horizontal channel sizes; i.e. 10mm and 3mm. The total stroke was set to 13mm, and friction coefficients μ of 0.1, 0.2 and 0.3 were applied. For the smallest horizontal channel (h=3mm) the effect of friction in the horizontal channel is rather high because L_h increases rapidly in relation to the punch displacement. As for the results in Figure 4.14, the effect of increasing friction coefficients on the forming stress is greater for smaller horizontal channels than larger ones.

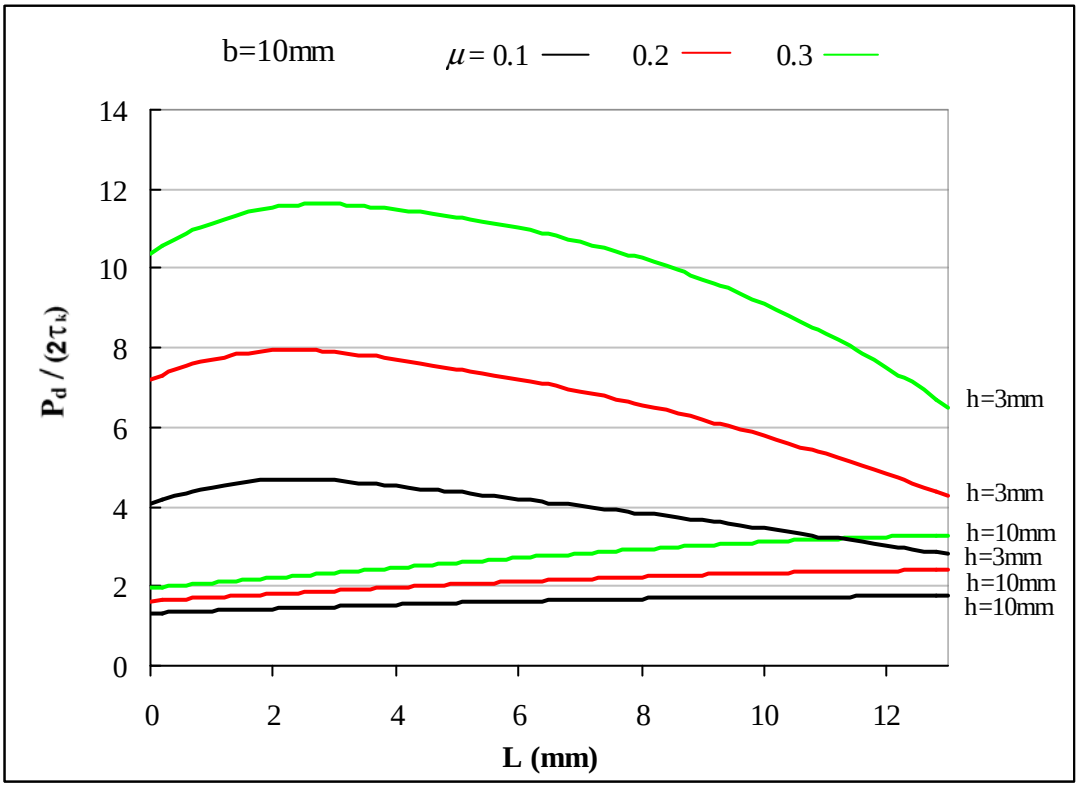

Figure 4.18 Forming stress for the continuous CAE process

In the case of no friction (μ=0) everywhere in the contact zones between tool and material, equation 4.52 cannot be used, as it has been developed by the integration of differential equations with friction forces included in the analysis. Therefore, the procedure from equation 4.3 to 4.52 must be repeated to obtain the forming pressure for

frictionless conditions. Final equations were therefore obtained, showing the relative pressure distribution p on the yielding zone boundary, given by Equation 4.53, and the relative forming pressure p_d, given by Equation 4.54.

$$\frac{p}{2\tau_k} = \frac{x+2h}{2h} \tag{4.53}$$

$$\frac{p_d}{2\tau_k} = \frac{(b-kb)}{b}\frac{p_{x=kb}}{2\tau} + \frac{1+\dfrac{p_{x=kb}}{2\tau_k}}{2b}kb \tag{4.54}$$

4.2 CAE UPPER BOUND ANALYSIS

4.2.1 Channels inclined at 90^0

Figure 4.19 (a) shows an upper bound representation of Channel Angular Extrusion in plain strain. The material is assumed to shear along a surface inclined at an angle α, defined by the edges of the channels intersection. The material moves in the vertical and horizontal channel with velocities v_1 and v_2 respectively. The velocity diagram is given in Figure 4.20 (b), and v_r is the relative velocity along the shearing surface. Assuming m

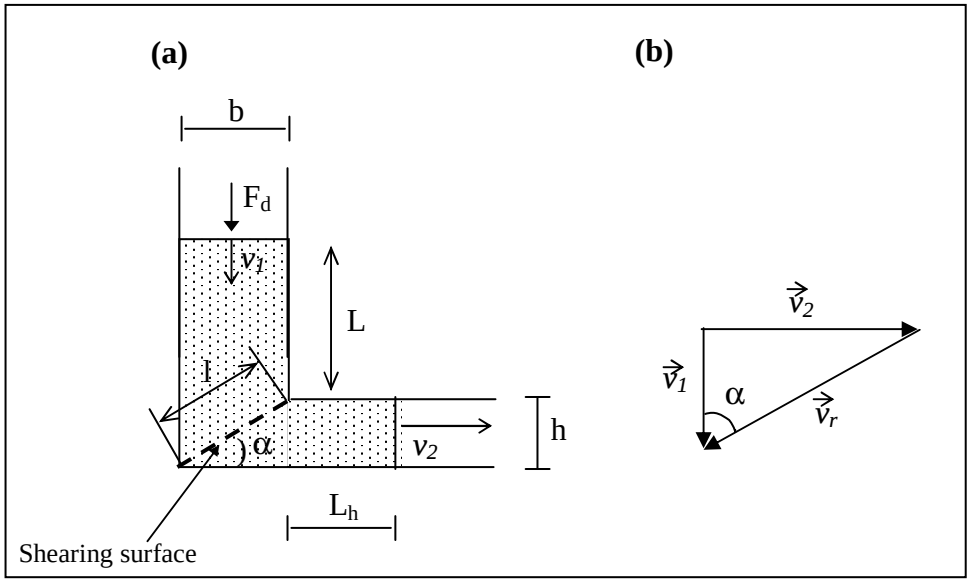

Figure 4.19 Upper bound representation of Channel Angular Extrusion

as the friction factor at the interface between the tool and the billet ($0 \le m \le 1$), the power input by the system, $F_d v_1$, should overcome:

Power due to shearing = $\tau_k l v_r$ (4.55)

Power due to friction on vertical channel:

-right hand surface = $m\tau_k L v_1$ (4.56)

-left hand surface = $m\tau_k (L+h) v_1$ (4.57)

Power doe to friction on the horizontal channel:

-top surface = $m\tau_k L_h v_2$ (4.58)

-bottom surface = $m\tau_k (L_h + b)\, v_2$ (4.59)

Therefore,

$$F_d v_1 = v_1 m\tau_k L + v_1 m\tau_k (L+h) + \tau_k l v_r + v_2 m\tau_k (b + 2L_h) \tag{4.60}$$

Where l is the length of the shearing surface and τ_k is the material shear yield stress of the extruded material. From Figure 4.19 (b),

$$b = l\cos\alpha \tag{4.61}$$

$$v_2 = \frac{v_1}{\tan\alpha} \quad \text{and} \quad v_r = \frac{v_1}{\sin\alpha} \tag{4.62}$$

Substituting equation 4.61 and 4.62 into equation 4.58 gives

$$F_d v_1 = v_1 m\tau_k L + v_1 m\tau_k (L+h) + \frac{v_1}{\tan\alpha} m\tau_k (b + 2L_h) + \tau_k l \frac{v_1}{\sin\alpha} \tag{4.63}$$

The force on the punch becomes

$$F_d = \tau_k m\left[2L + h + \frac{(b+2L_h)}{\tan\alpha}\right] + \tau_k \frac{b}{\sin\alpha\cos\alpha} \tag{4.64}$$

Therefore, if $F_d = p_d\, b$, the relative punch pressure is

$$\boxed{\frac{p_d}{2\tau_k} = \frac{m}{2bh}\left[1 + 2Lh + b^2 + \frac{2b}{L_h}\right]\sin(2\alpha)} \tag{4.65}$$

Figure 4.20 shows the theoretical results from equation 4.63, when the material extruding through the horizontal channel is taken into account. For this representation, the vertical channel width b was set to 10mm, the stroke L to 13mm. Results are plotted at various horizontal channel size and friction factors m values (0.2, 0.4 and 0.6). L_h is calculated by equation 4.51.

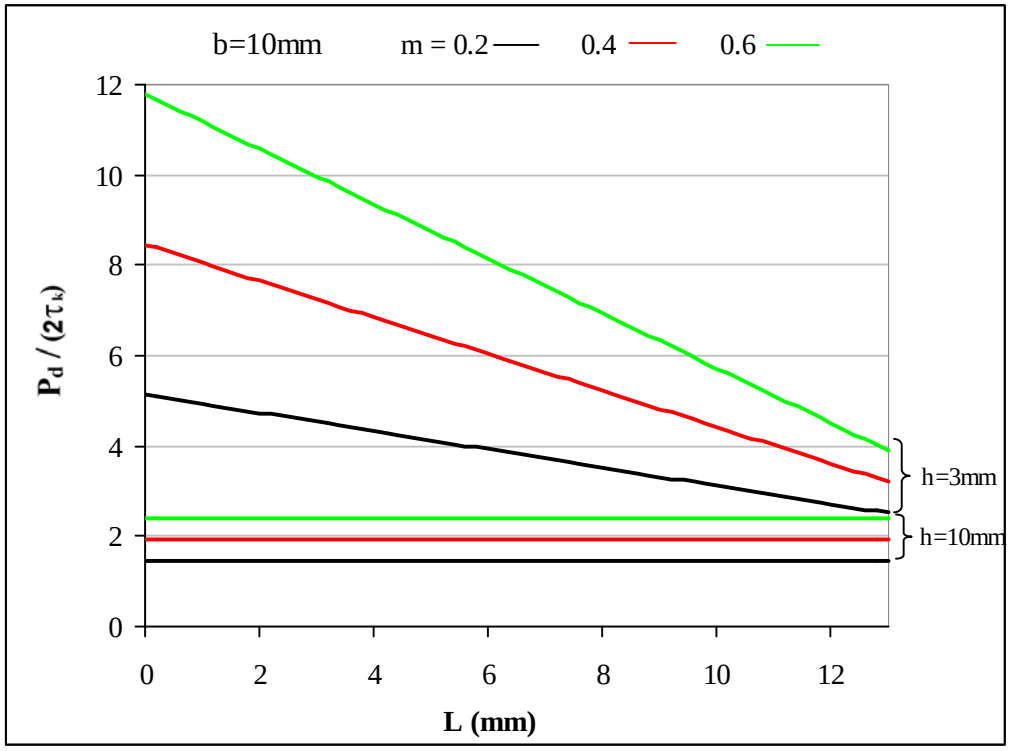

Figure 4.20 Upper bound solution for a continuous CAE process

When the vertical and horizontal channels have exactly the same geometry, i.e. ECAE condition, the forming pressure is shown to remain constant against the punch displacement. However, in the case when the material is forced to flow through smaller channels, the punch stress is shown to linearly increase with the progress of the extrusion, and its maximum value is at the end of the stroke, therefore when L=0.

The Upper Bound method provides a convenient way to calculate the energy dissipated for a full stroke operation. In the special case of Equal Channels Angular Extrusion (h/b=1), the force distribution against the displacement L is constant, therefore the energy dissipated E is the area given by a rectangle. Hence,

$$E = F_d L \tag{4.66}$$

Therefore, by substituting equation 4.64 into equation 4.66, gives

$$\boxed{\frac{E}{2\tau_k AL} = \left[m\left(\frac{L}{b}+1\right)+\frac{1}{2}\right]} \tag{4.67}$$

where A is the cross sectional area of the channels.

4.2.2 General solution for ECAE

Figure 4.21 (a) shows the set-up for an Upper Bound analysis, for the ECAE process (b=h). The angle between the channels is γ. Figure 4.21 (b) gives the velocity field, where v_r is the relative velocity along the shearing surface AB.

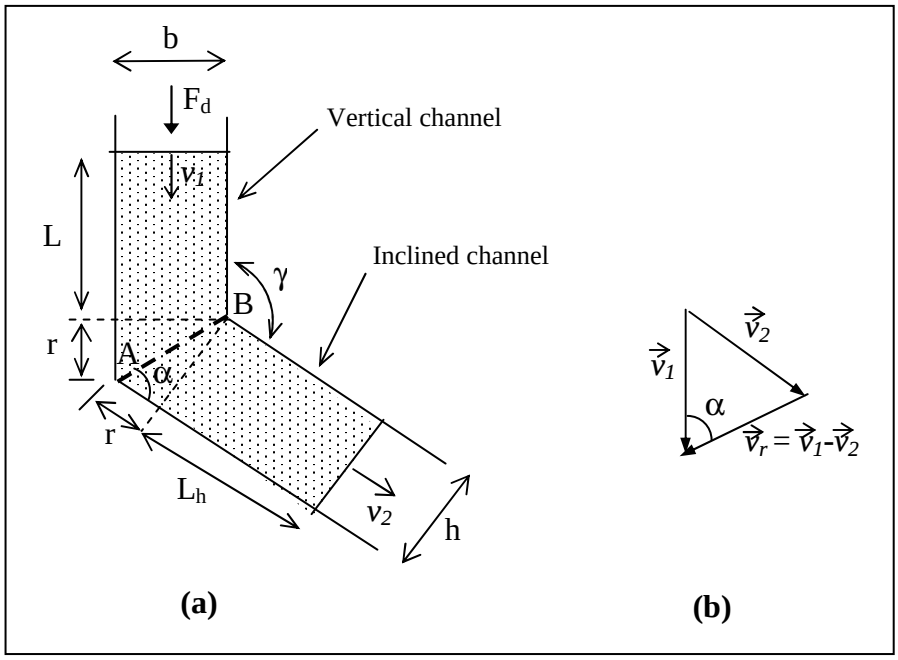

Figure 4.21 ECAE Upper Bound solution

Similar to the CAE analysis in equation 4.60, a solution for ECAE may be written as

$$F_d v_1 = v_1 m \tau_k L + v_1 m(L+r) + \tau_k l v_r + v_2 m \tau_k (2L_h + r) \tag{4.68}$$

As the channels are of equal cross section, the material velocities in the vertical and inclined channels are the same, therefore $v_1 = v_2$. Also, the following relationships may be obtained from figure 4.21.

$$r = \frac{b}{\tan\alpha} \tag{4.69}$$

$$v_r = 2v_1 \cos\alpha \tag{4.70}$$

Substituting equations 4.69 and 4.70 into equation 4.68, gives

$$F_d = \tau_k m\left(2L + \frac{2b}{\tan\alpha} + 2L_h\right) + \tau_k \frac{2b}{\tan\alpha} \tag{4.71}$$

Therefore, the relative punch pressure is given by

$$\frac{p_d}{2\tau_k} = \frac{m}{b}\left(L + L_h + \frac{1}{\tan\alpha}\right) + \frac{1}{\tan\alpha} \tag{4.72}$$

From figure 4.21 it can be considered that $\alpha=\gamma/2$, therefore it follows that

$$\frac{p_d}{2\tau_k} = \frac{m}{b}\left(L + L_h + \frac{1}{\tan\frac{\gamma}{2}}\right) + \frac{1}{\tan\frac{\gamma}{2}} \tag{4.73}$$

The punch pressure p_d given by equation 4.73 is characterized by a constant value for a fixed friction factor m, as the term $(L+L_h)$ remains unchanged due to the constancy of the volume applied to ECAE (see equation 4.51). The energy dissipated can be therefore calculated by substituting equation 4.71 into equation 4.66, therefore

$$\frac{E}{2\tau_k AL} = m\left(\frac{L}{b} + \frac{1}{\tan\frac{\gamma}{2}}\right) + \frac{1}{\tan\frac{\gamma}{2}} \tag{4.74}$$

Equations 4.74 and 4.67 were used in order to obtain the energy distributions in Figure 4.22. This same figure was used in Chapter 3 as part of the introduction of the UREAD technology (see Figure 3.4).

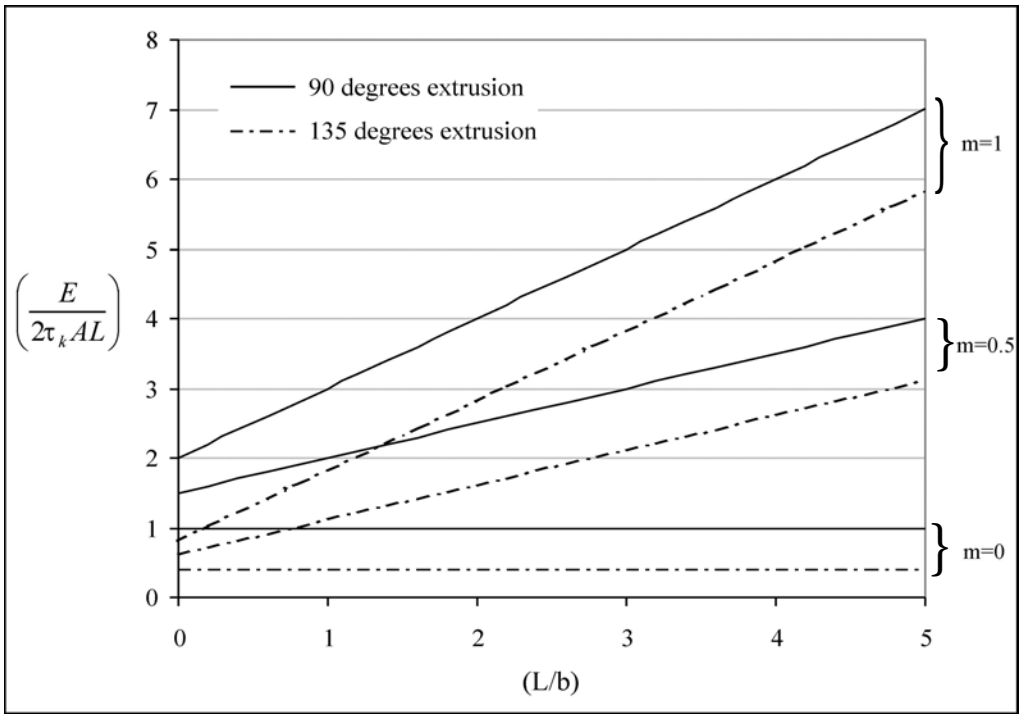

Figure 4.22 Upper Bound solution for energy dissipation in ECAE

4.3 APPLICATION OF NUMERICAL SOLUTION TO CAE

4.3.1 Modelling of the CAE process

A numerical solution, based on non linear analysis of the extrusion process with intersecting channels of 90 degrees was obtained. The geometry of this process is similar to the one shown in Figure 4.1. A two-dimensional model was created and simulated using ANSYS. The aim of this analysis is to explore the initiation of the yielding process in Channel Angular Extrusion, and visualize the internal and contact

stresses. Therefore the numerical analysis only covers the start of the process up to the yielding point. The simulation of the material flowing into the horizontal channels is not considered in this analysis.

The geometry of the model was created in the first instance, as shown in Figure 4.23, where the vertical channel width b is fixed to 10mm. In order to study the effect of the horizontal channel h size, 10mm and 5mm widths were used. Furthermore, the tool was modelled in ANSYS by rigid lines. The billet in the vertical channel was meshed using the mapped meshing criteria provided by the package, and an elastic-plastic material model was selected for the plastic deformation of the billet. Young's modulus and the yield stress for the billet material are 14GPa and 10MPa respectively. A friction coefficient μ at the interface between the tool and the deforming material is taken as 0.2. The initial yielding is examined by a tool displacement of 0.2mm. The command file structure developed for the simulations is given in Appendix (B).

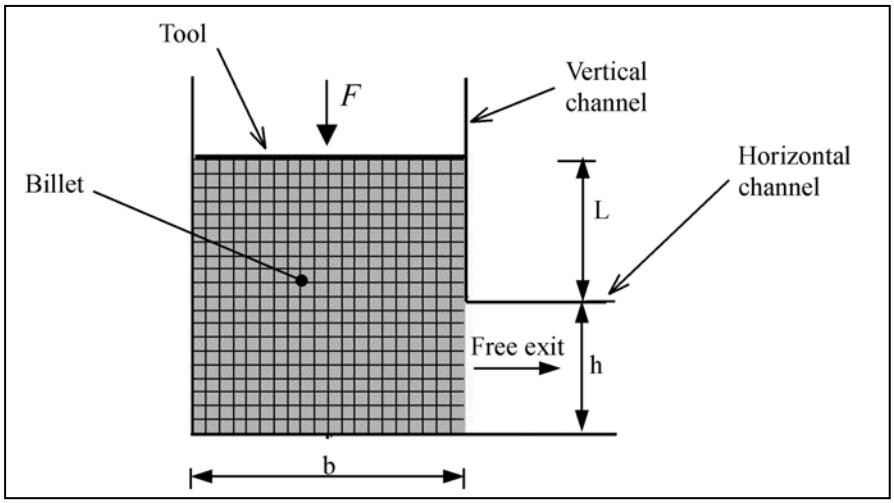

Figure 4.23 Finite Element model and element subdivision

4.3.2 Vertical stresses on the cavity corner boundary

Figure 4.24 shows the results of the numerical analysis in terms of the non dimensional vertical stress distribution ($p/2\tau_k$) along the cavity corner boundary. The stress values were extracted from nodal contour plots at various values of L. The results show that the stresses at the vicinity of x=0 are close to the material yield stress. Also, the values of pressure is shown to increase with increasing values of x. On the other hand, the length L seems to have little effect on the pressure.

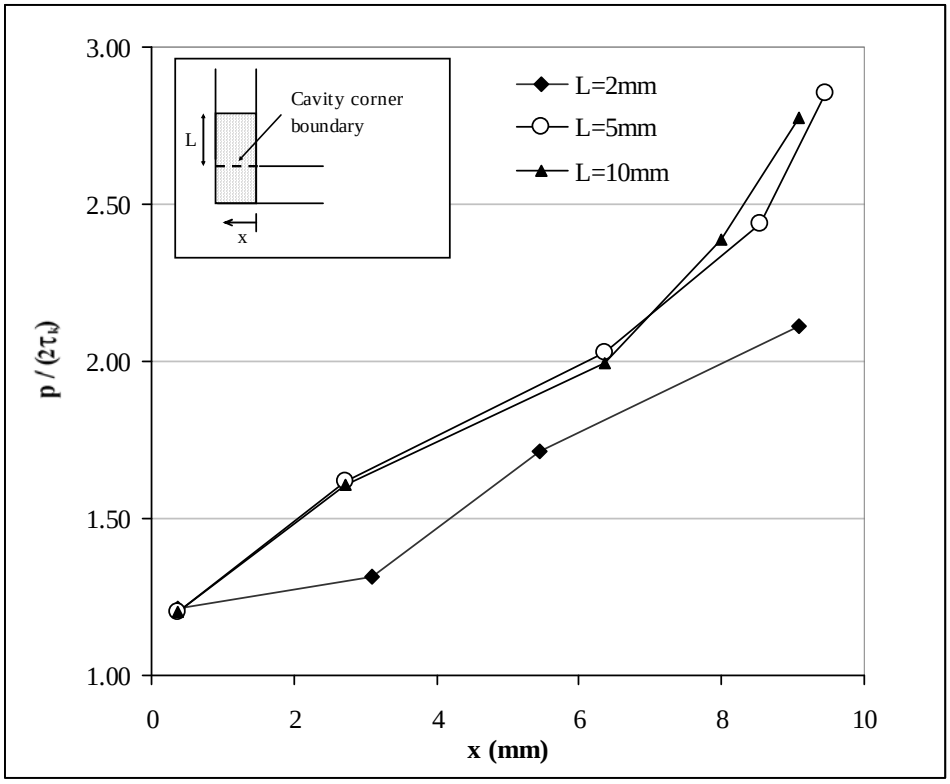

Figure 4.24 Numerical vertical stress curves on the cavity corner boundary

Figure 4.25 shows a comparison between the numerical solution and analytical solution developed in this work by the slab method (Equations 4.16 and 4.28, when *b*=10mm and *h*=5mm for k=1 and k=0.4).

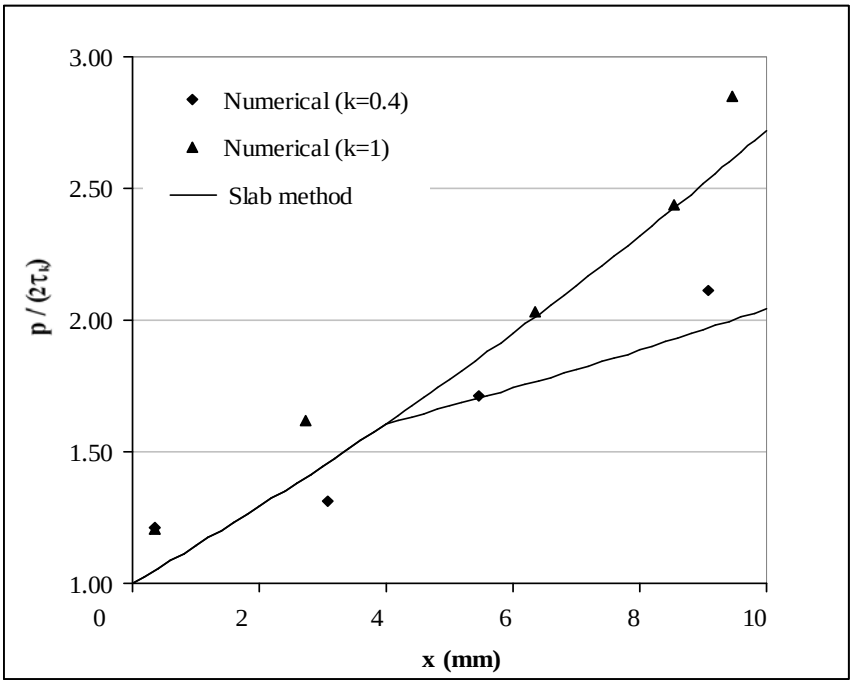

Figure 4.25 Comparison between finite element and slab method for stresses on cavity corner boundary

4.3.3 Shear stress in the deforming material

The results of the internal shear stress distributions in the forming material are shown in the Figures 4.26 (a), (b) and (c). The results are plotted for different lengths *L*, i.e. 0.4mm, 3mm and 10mm, and using vertical and horizontal channels width of respectively 10mm and 5mm. The maximum shear stress is found to be around the cavity corner boundary, and it peaks to a value close to the shear stress of the material at yielding. Also, the length of the yielding zone is shown to increase at higher values of *L*.

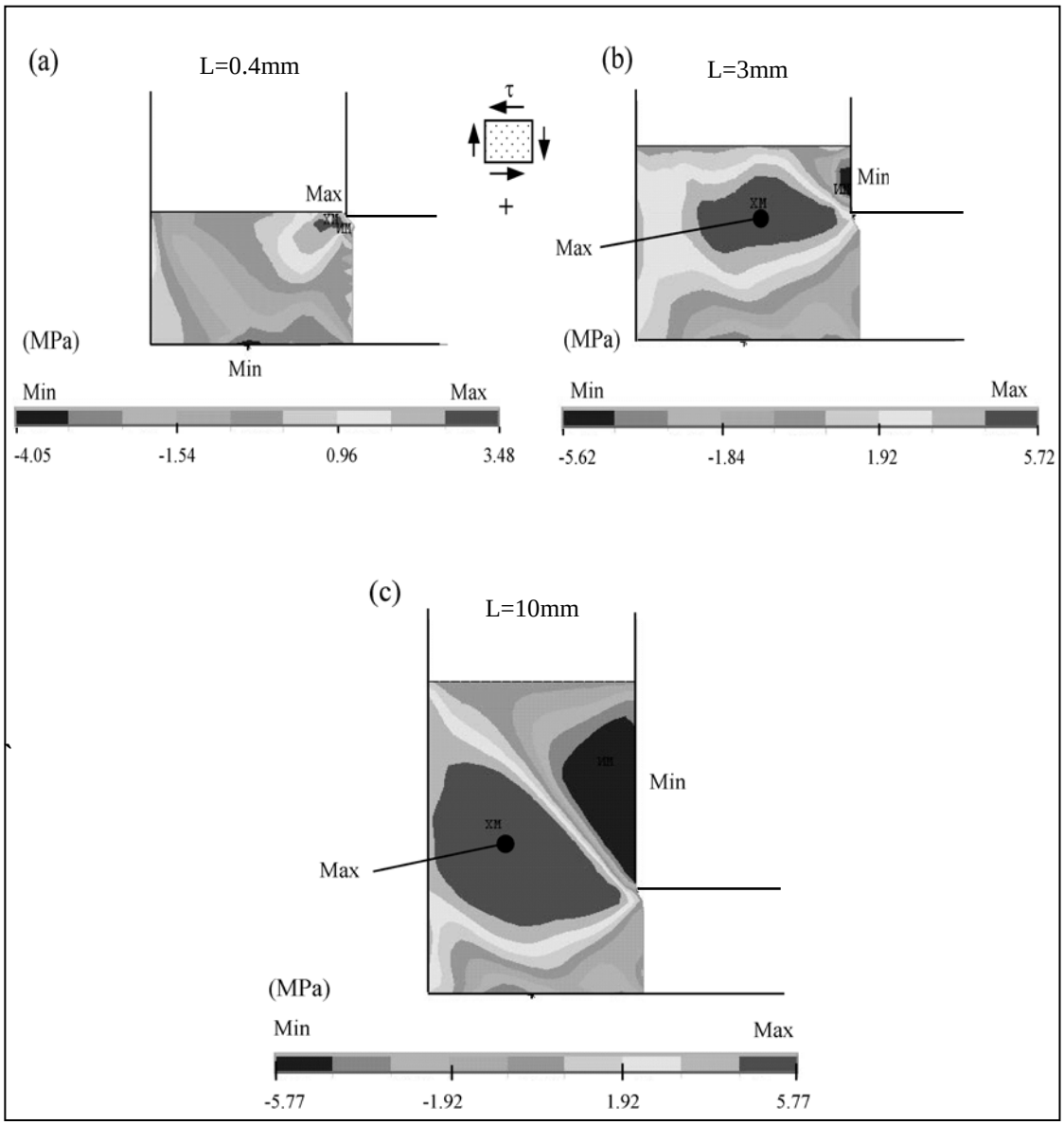

Figure 4.26 Internal shear stress distributions at three different initial lengths *L*

4.3.4 Side pressure

Normal stress distributions results on the side of the vertical channel are presented in Figure 4.27, for different lengths *L*, i.e. 1mm, 3mm, 10mm, 15mm. The results show peak values happening only on the right hand side of the tool exit, where the free tool exit is located. This is well in agreement with the analytical evaluations of normal stress on the tool, described in section 4.1.4.

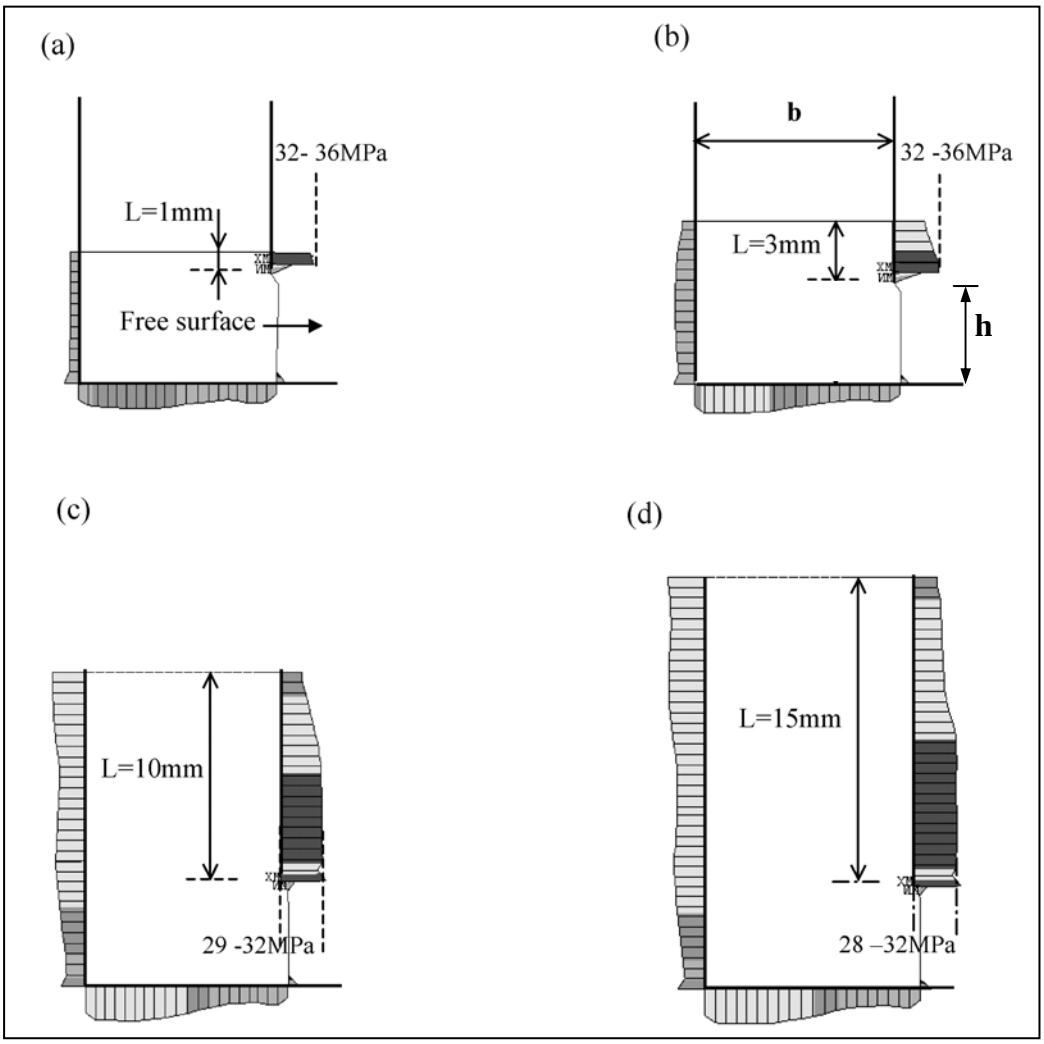

Figure 4.27 Side pressure results at various initial billet lengths L, with b=10mm and h=5mm

Figure 4.28 compares the averaged side pressure results from ANSYS simulations and the slab method, by following equations 4.37, 4.38, 4.39 and 4.40. In the graph, p_r and p_l are the average pressure values on the right and left hand side tool. Results were

obtained for different *L*, i.e. 3mm, 5mm, 7mm and 10mm. The average stress acting on the right hand side of the tool, where the free exit is located, is higher when compared to the values on the left hand side. Numerical and analytical results compare well for *L* greater than 3mm.

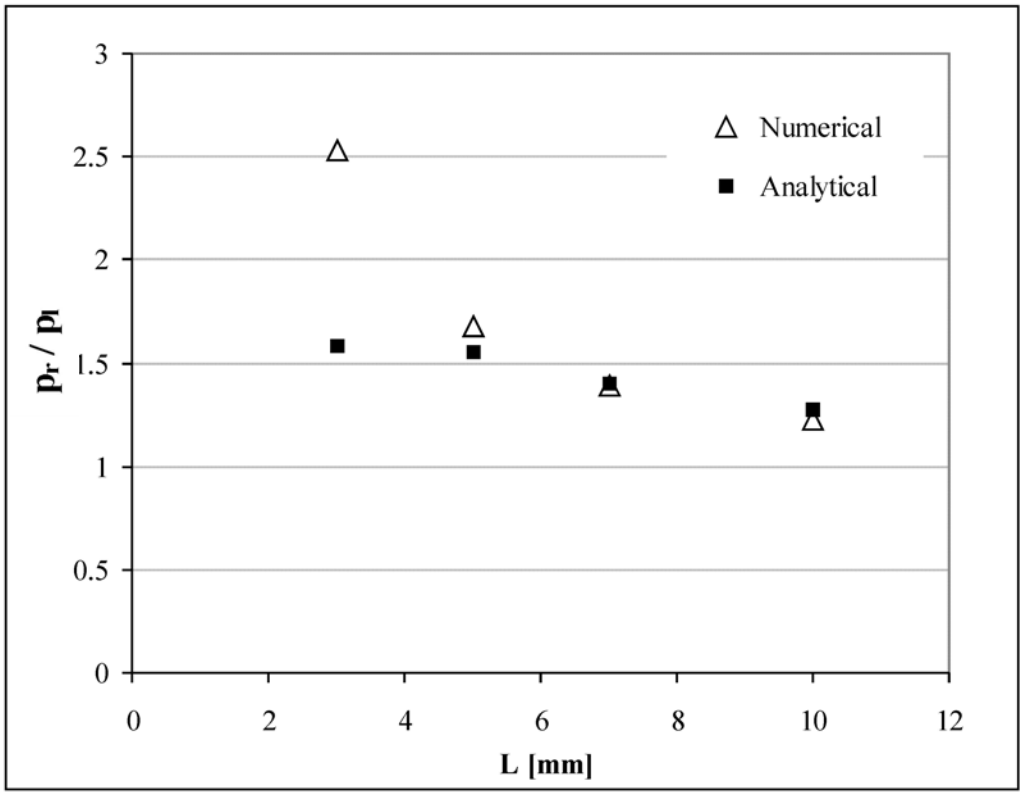

Figure 4.28 Average side pressure results from finite element and slab method solutions

4.3.5 Deformed shape and plastic work

Figure 4.29 shows the numerical results of the deformed billet after the initiation of the extrusion process at *L*= 0.4mm, 1mm, 5mm and for a displacement of 0.2mm. The extent the zone where plastic deformation takes place increases with *L*. At higher values of *L*, plastic deformation becomes more uniform and covers larger areas, in such a way more energy is now required to affect the extrusion.

Figures 4.30 (a), (b), (c) and (d) show the contour plot of the plastic work in J/m, when *L* is 0.4mm, 1mm, 2mm and 5mm respectively. It can be seen that the mechanism of

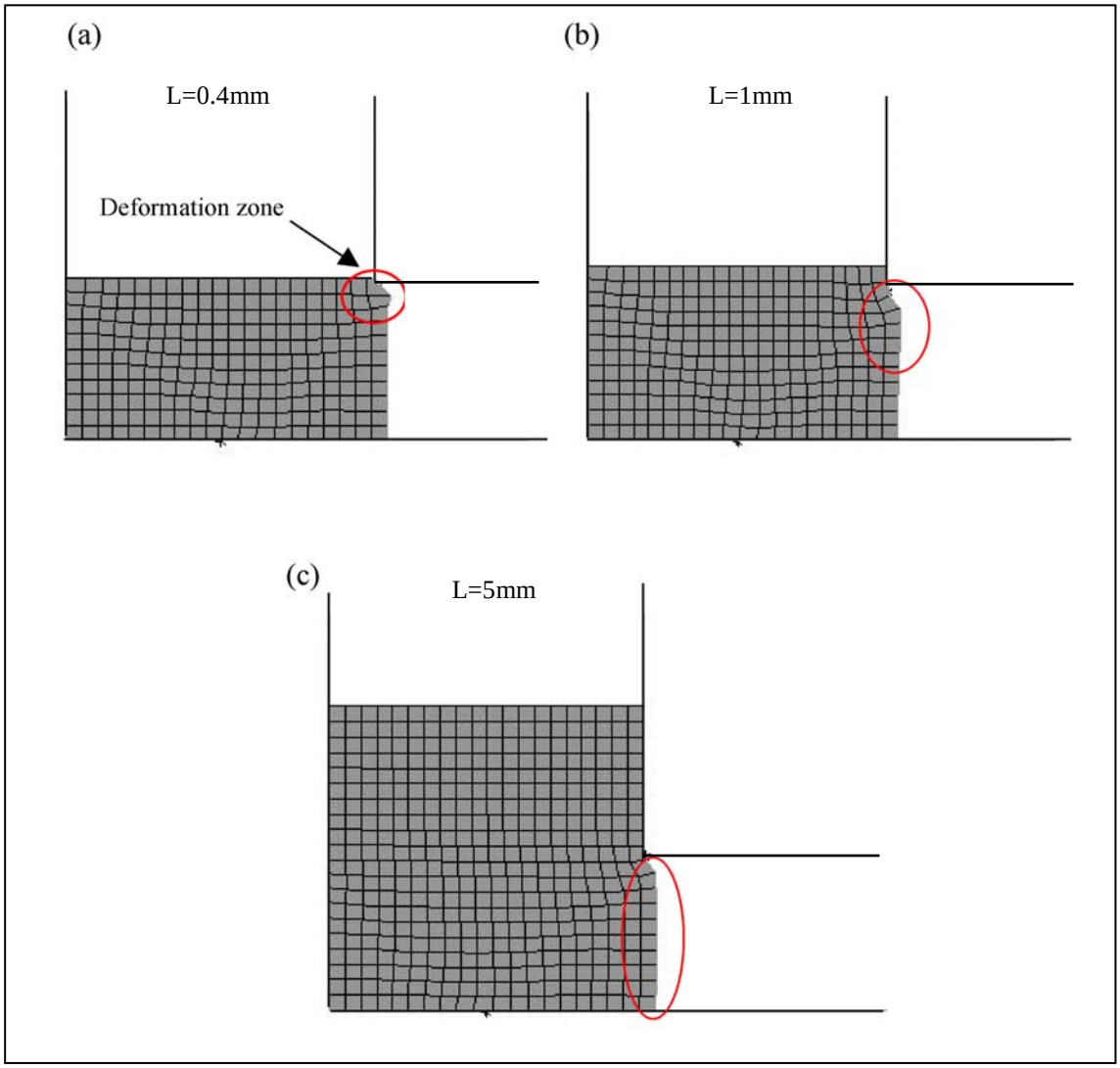

Figure 4.29 Deformed shape results, with b=10mm and h=5mm

deformation is formed through shear layers or bands inclined at an angle of approximately 45˚. The trapped rigid material in the vertical channel would undoubtedly cause an increase in the deformation load in order to overcome the elastic energy exerted on the rigid part of the billet and the elastic energy effected on the container accordingly.

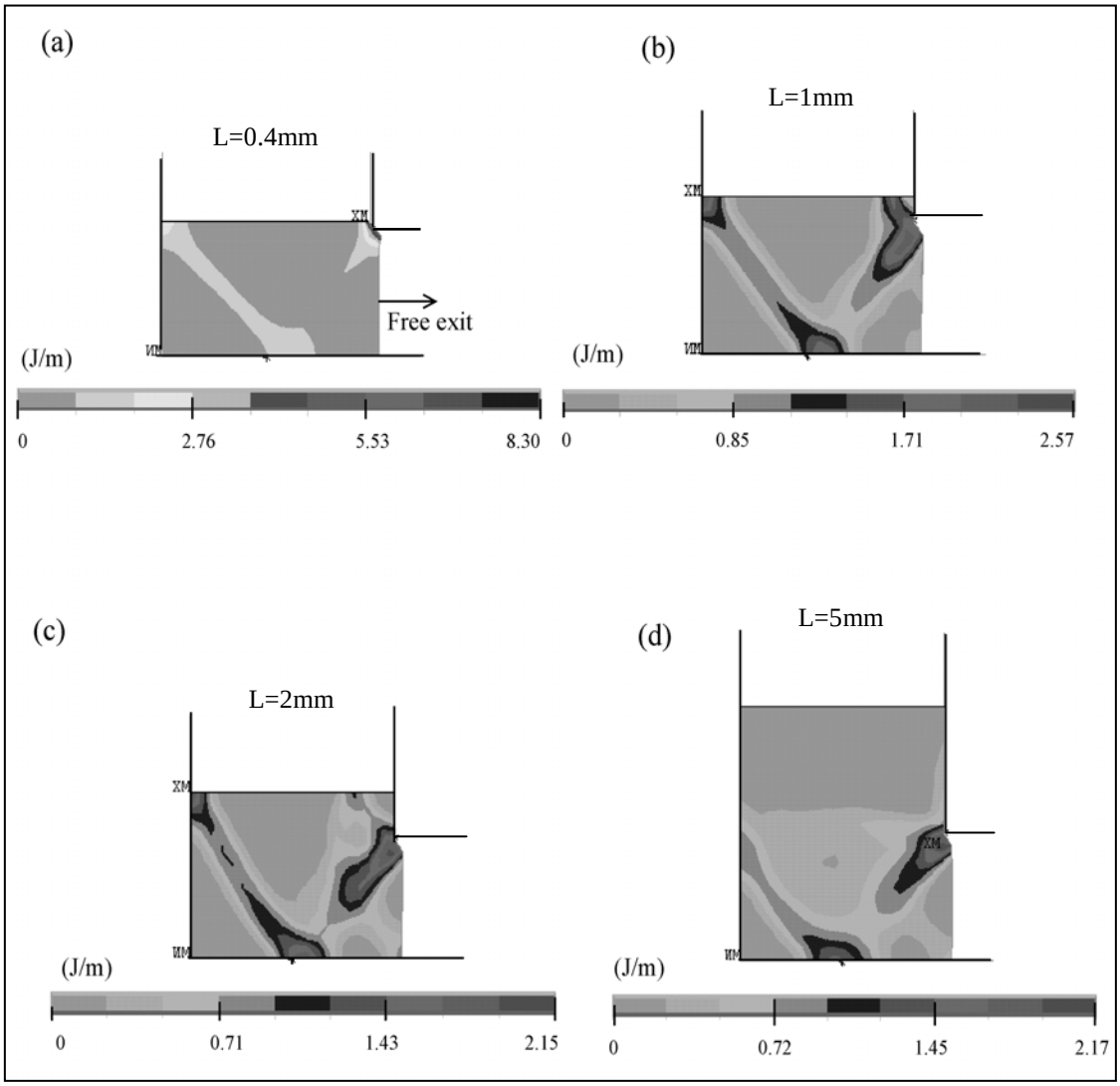

Figure 4.30 Finite element plastic work results with b=10mm and h=5mm

4.3.6 Average forming pressure

The averaged pressing forming pressure p_d required to initiate the yielding process given by the numerical simulations is compared with the one obtained by the slab method in Figure 4.31, given by equation 4.46. The results are plotted for two values of the ratio *h/b*. The analytical results compare well with the numerical solution in both cases, i.e. for *h/b*=1 and *h/b*=0.5; and show that higher loads are required to initiate the yielding process in Channel Angular Extrusion, when the length *L* in the vertical channel increases. Also, when the horizontal channel width decreases, forming stresses

increases, as the extrusion becomes more difficult. *L* seems to be critical to the tool design in this type of forming processes.

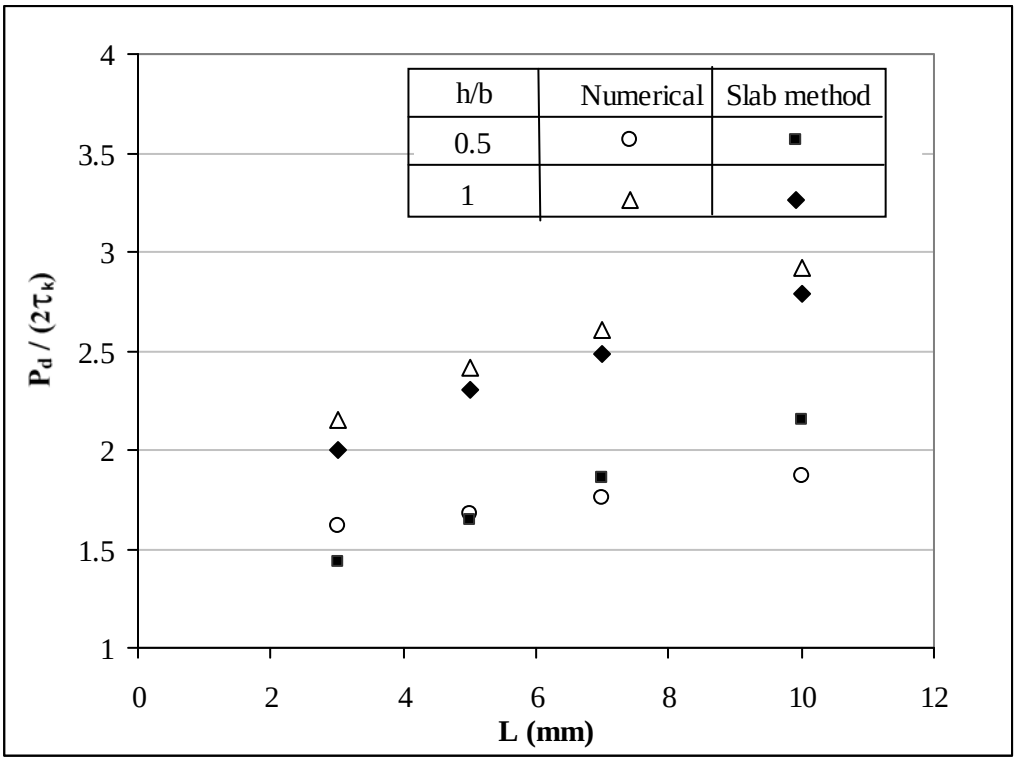

Figure 4.31 Forming pressure by finite element and slab method solutions with b=10mm

4.4 CONCLUSIONS

The process of Channel Angular Extrusion (CAE) was modelled by the Slab Method and Upper Bound analytical techniques, under plain-strain conditions. Parameters such as the width of the vertical and horizontal channel (*b* and *h* respectively), the length of the stroke *L*, the interface condition between tool and material being deformed and the material yield stress were found to be critical for the deformation process. By applying the Slab Method to Equal Channel Angular Extrusion (ECAE) the punch pressure peaks at the starting of the extrusion pressure (when *L*=0), then it is slightly descendent as the extrusion progresses. However, the opposite trend was found for the case of Channel Angular Extrusion (CAE) when the horizontal channel width is relatively small compared to the vertical channel width. This is due to an increasing frictional effect in the horizontal channel. Also, the right hand side tool in the vertical channel experiences

higher levels of pressure than the left hand side tool. The Upper Bound analysis provided similar trends to those obtained by the Slab Method, with respect to the forming pressure.

Results by the finite element analysis by ANSYS showed the deformation pattern in the CAE process. Pressure distributions on the cavity corner boundary, on the side of the tool in the vertical channel and the forming pressure by the numerical analysis were well in agreement with those obtained by the Slab Method.

Chapter 5

EXPERIMENTAL INVESTIGATIONS ON 90^0 "UREAD" DEVICES

5.1 DESIGN AND EXPERIMENTS FOR UREAD DEVICES

The UREAD technique described in Chapter 3, owes its working mechanism and principles to the Channel Angular Extrusion (CAE) process. CAE experimentation has many important parameters, that include contact stresses, the state of contact surfaces between the tool and the workpiece material and the machining accuracy of channels and punches. They are all critical factors, which would affect energy dissipation levels and define the behaviour of the UREAD devices.

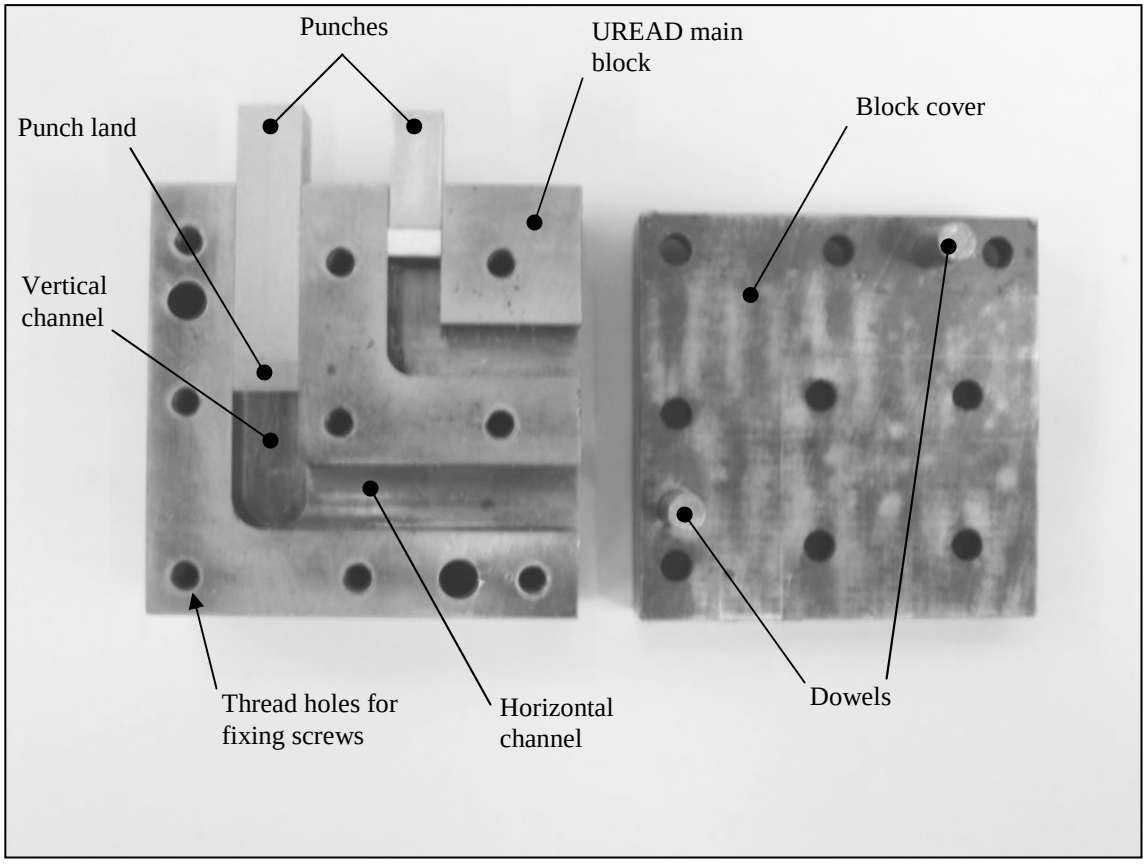

Figure 5.1 UREAD device design with rectangular cross sectional channels

However, two main and independent entities that can be highlighted and investigated are the geometry of channels and the material being deformed. The channels geometry covers different cross sectional areas and inclination angles between the intersecting channels. The experimental set up in this investigation will focus attention on channel geometries compatible with the UREAD technology. Therefore, all channels will be of equal cross sectional area, and the intersection angle is 90^0. The investigation will cover circular and rectangular cross sectional areas, with different effective strokes. Figure 5.1 shows the design of a tool, which comprises UREAD intersecting channels. It is made in two halves for ease of manufacture and testing. Two dowels are used for locating and aligning the two halves. The tool was built with two independent UREAD units, each of which includes two intersecting channels of a constant cross sectional area and with 90^0 angle of intersection. A full set of units that will be investigated are shown in Figure 5.2 and 5.3, for circular and rectangular cross sectional area channels respectively.

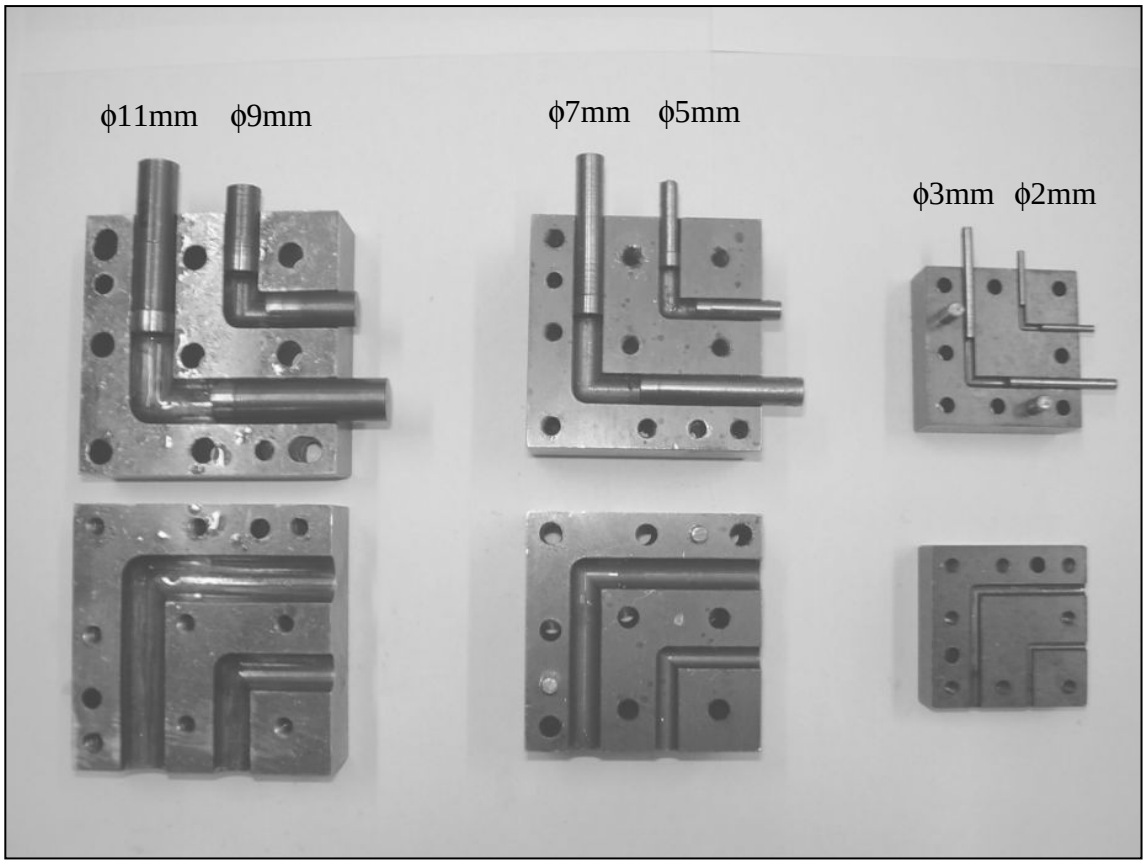

Figure 5.2 Set of UREAD devices with circular cross sectional channels

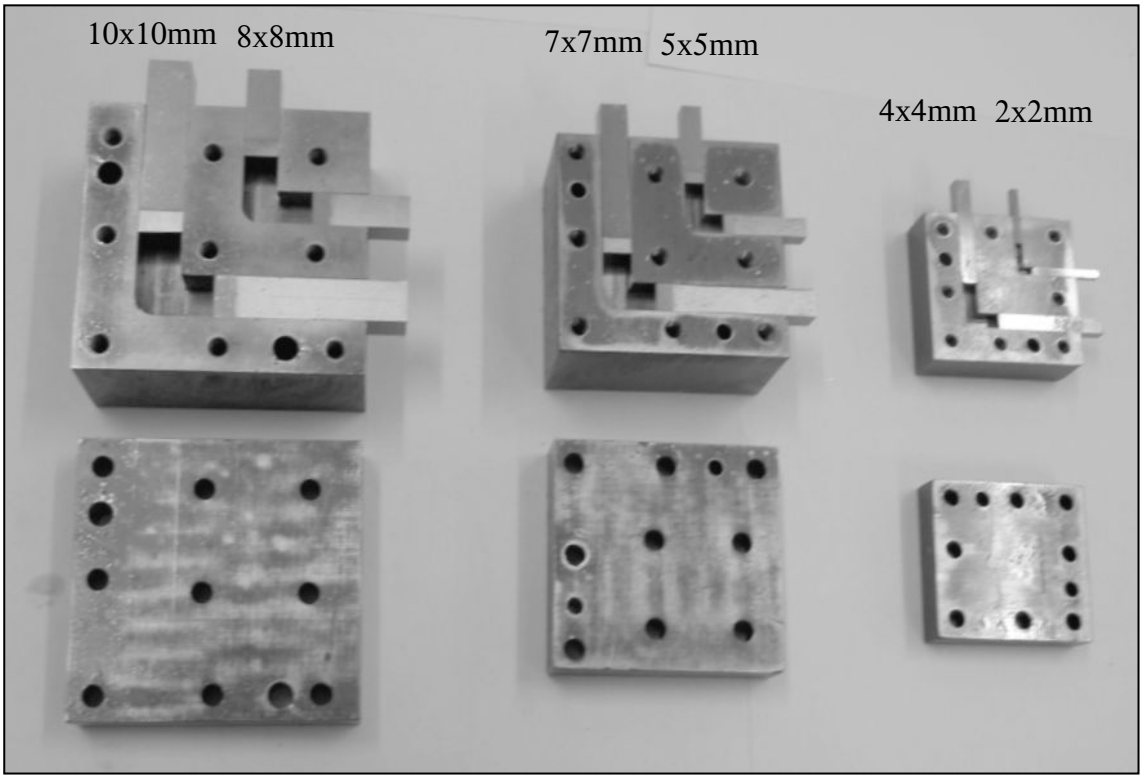

Figure 5.3 Set of UREAD devices with rectangular cross sectional channels

There are three sets of tools for each type, each of which includes two independent intersecting channels. Detailed drawings of the tools, channels and punches are given in Appendix (D). Units with round channels are in the range of 2mm to 11mm in diameter, while the rectangular devices cover cross sectional areas from (2x2)mm to (10x10)mm.

Table 5.1 gives the basic geometry of the devices, length, width and area. Channels and punches were machined from a block of H13 tool steel, using a commercial 5-axis milling CNC machine. The tool and punches were heat-treated to achieve the hardness level of 50HRC. In order to reduce the frictional effects to a minimum, the punches were designed with a small land and the two halves were bolted together in order to form the UREAD devices. For units with rectangular cross section the channels were machined in one half, but for channels with circular cross section the channel is machined in two complementary halves.

	Diameter (mm)	Height(mm)	Cross sectional area (mm^2)
a) Circular	11	41.5	94.98
	9	20.5	63.58
	7	37.5	38.46
	5	19.5	19.62
	3	27.5	7.06
	2	14	3.14
	Length x Width(mm)	**Height(mm)**	**Cross sectional area (mm^2)**
b) Square	10x10	42	100
	8x8	21	64
	7x7	37.5	49
	5x5	19.5	25
	4x4	27	16
	2x2	14	4

Table 5.1 UREAD devices basic geometries

The main aim of the experimental study was to characterize the behaviour of the UREAD units, with respects to performance and energy absorption. Therefore, several extrusion processes were carried out during which the required load against punch displacement was experimentally measured. Such operations were repeated in forward and backward mode for each unit in order to identify the characteristics of both the vertical and horizontal channels.

In addition, the punch velocity was kept low and constant in order to avoid any possible dynamic effects, hence the conditions of static yielding is effected during the deformation process. Lead was used as the main working material for these tests.

5.2 EQUIPMENT AND INSTRUMENTATION

The experimental set up for the static testing of UREAD units comprises a hydraulic bench press, capable of delivering 80kN, and a computerized data acquisition system. The press was designed and built in-house, and was equipped with a load cell and displacement transducer (potentiometer). The forging press and its accessories is shown

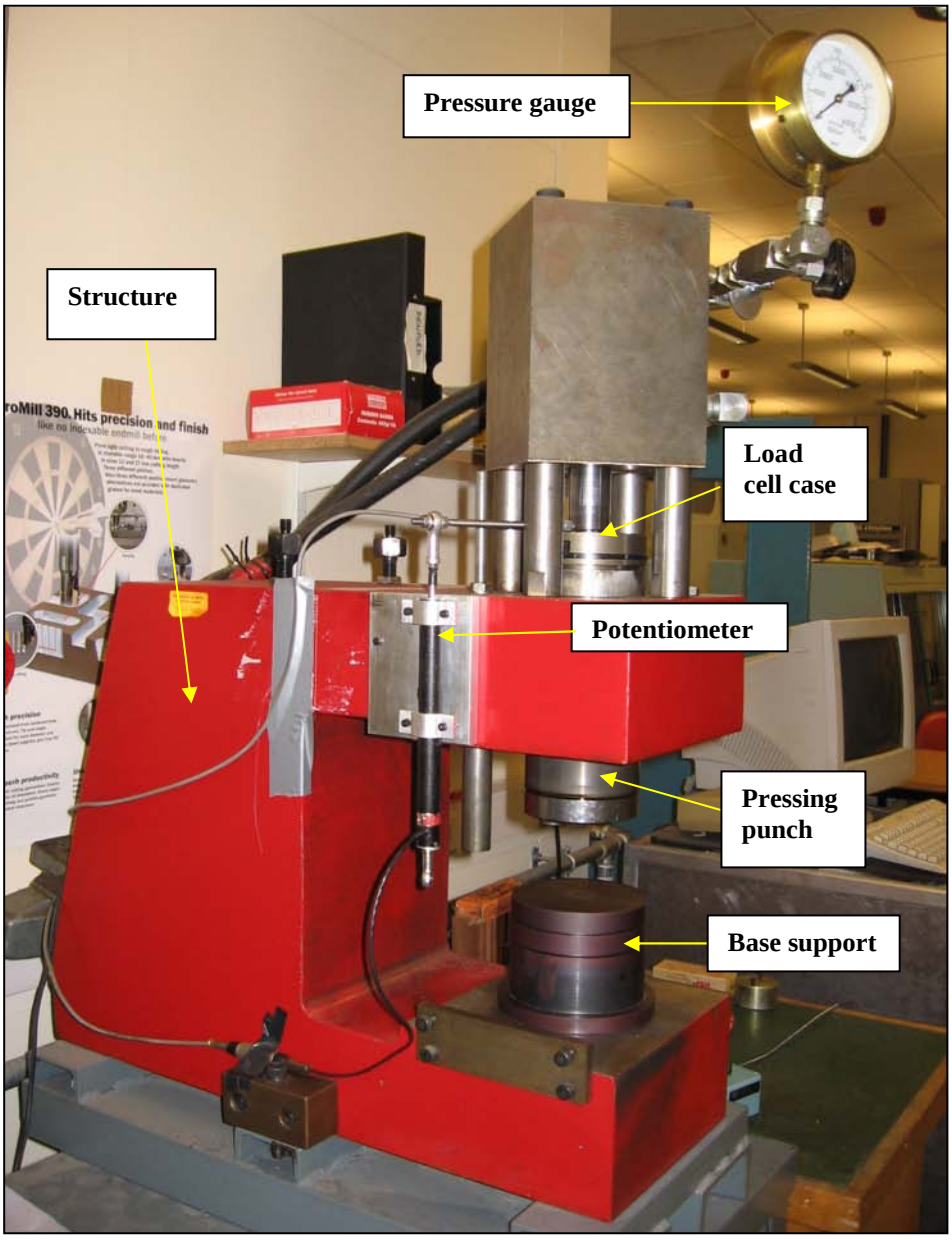

Figure 5.4 Forging bench press (80kN) and instrumentation

in detail in Figure 5.4. The design is of a “C” type of structure. The hydraulic system is fitted with a pressure gauge to display the operating pressure. The power system, which operates the forging press, consists of a pump with an electric single-phase motor capable of delivering 2.2kW at the rotational speed of 2860rpm. The power pack includes a pressure relief valve, to control the maximum pressure on the ram. The maximum pressure of 200bar at the pump gives 80kN force on the ram. The ram speed is controlled by a flow control valve, giving a ram velocity in the range of 0-6mm/s.

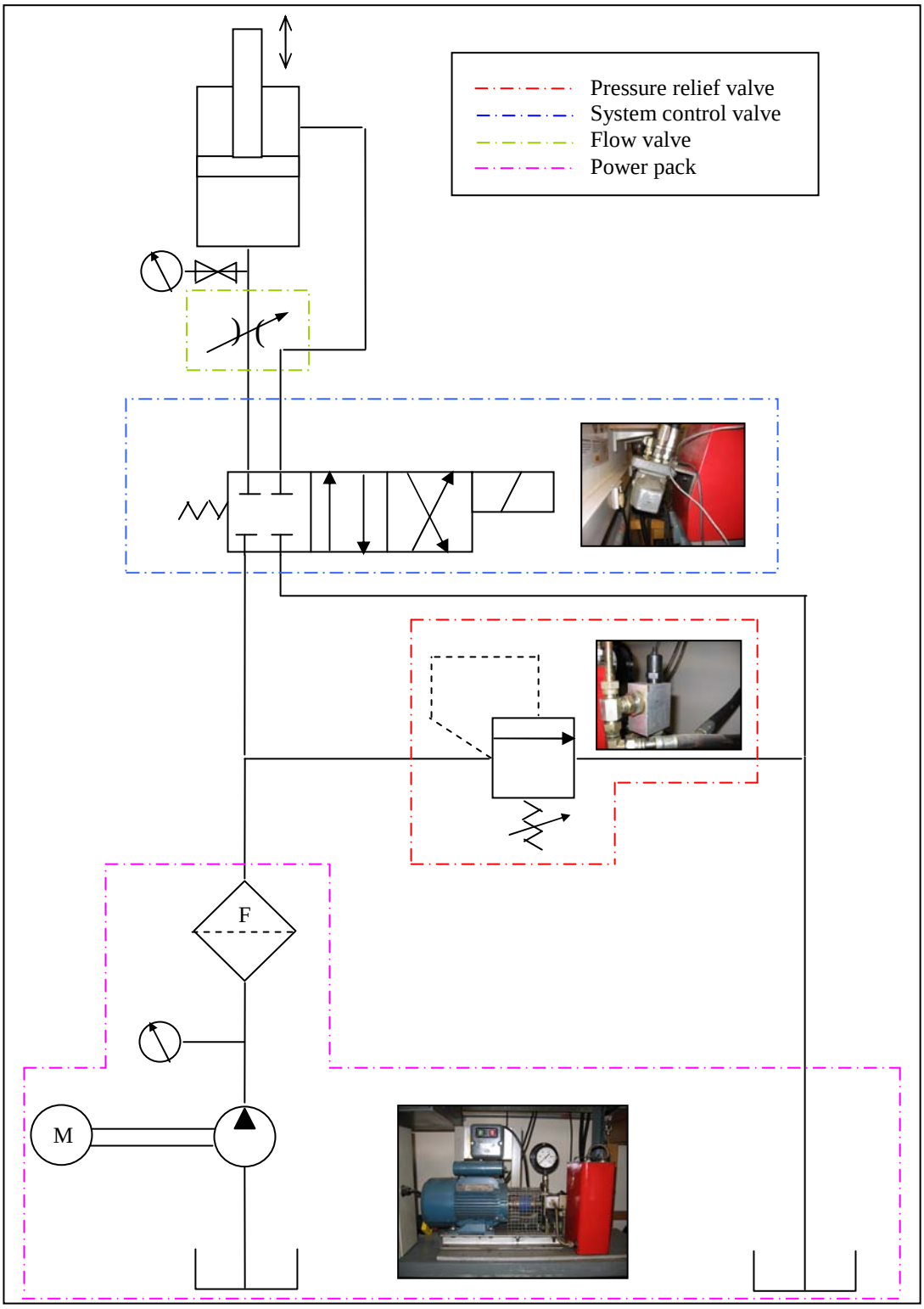

Figure 5.5 Hydraulic circuit of the forging bench press

Press movements and functionalities are controlled by an electronic control station housed within the press surroundings. Figure 5.5 shows the overall hydraulic circuit of

the press in detail. The pressure relief valve, control valves, flow valve and power pack are also highlighted.

Readings from the load cell and the potentiometer are collected by an in-house Data Acquisition System equipped with "PCI230" multi-channel I/O card and a DC instrumentation conditioning/amplifier card for each channel. HP-VEE software was installed and used to acquire the experimental data, at a frequency of 50Hz for all static tests. Figure 5.6 shows an example of the output signal by the load cell and displacement transducer (potentiometer).

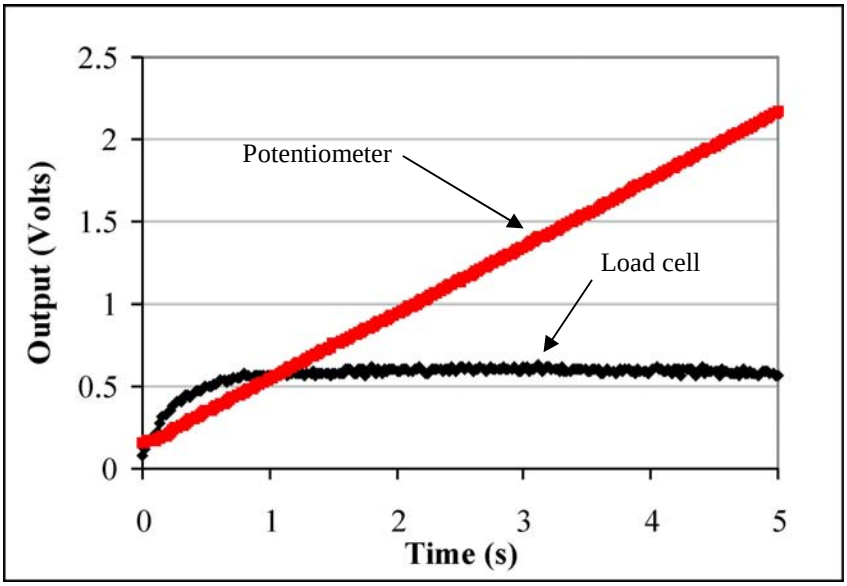

Figure 5.6 Typical output signal by load cell and potentiometer

The load cell and the potentiometer were calibrated before being used for experiments and checked frequently throughout the experimental programme.

5.3 WORKPIECE MATERIAL PROPERTIES

A commercial type of lead alloy was used in the unit static testing experiments. It was produced by following the British Standard BS EN 12588. Lead has excellent plastic deformation behaviour and it recrystallizes at room temperature. It is also easy to cast.

This particular type of lead alloy is characterized by the chemical composition given in Table 5.2.

Element	Composition %
Copper	0,03 to 0,06
Antimony	max. 0,005
Bismuth	max. 0,100
Silver	max. 0,005
Tin	max. 0,005
Zinc	max. 0,001
Other impurities	max. 0,005
Lead	Remainder

Table 5.2 Chemical composition of the lead alloy according to BS EN 12588

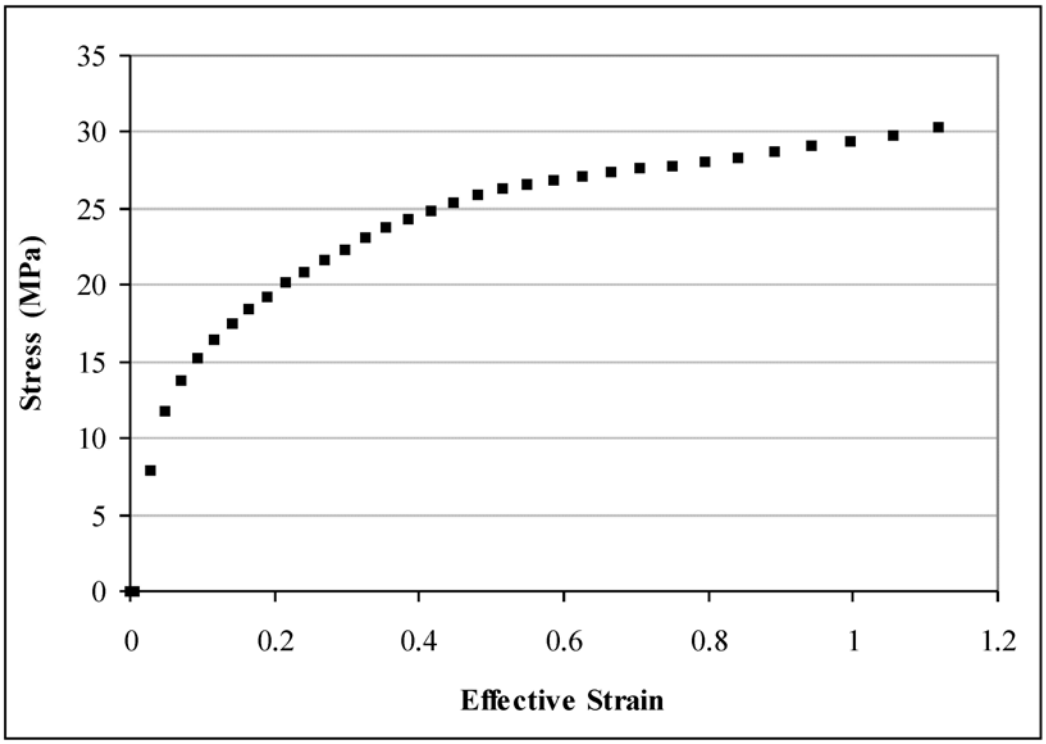

Figure 5.7 Compression test of BS EN 12588 lead

A static compression test was carried out on a cylindrical billet, with an initial diameter and height of 9mm and 24mm respectively. It was axially compressed between two flat dies, using a INSTRON (25kN) testing machine. The stress/strain diagram up to

1.2 strain is given in Figure 5.7, and the yield stress is identified as 11MPa. The bulk material was provided in sheets, and were cast to the dimensions of the UREAD channels using the casting mould, as the one shown in Figure 5.8 for circular cross sections. Another mould was used for the square billets. In addition to the use of lead

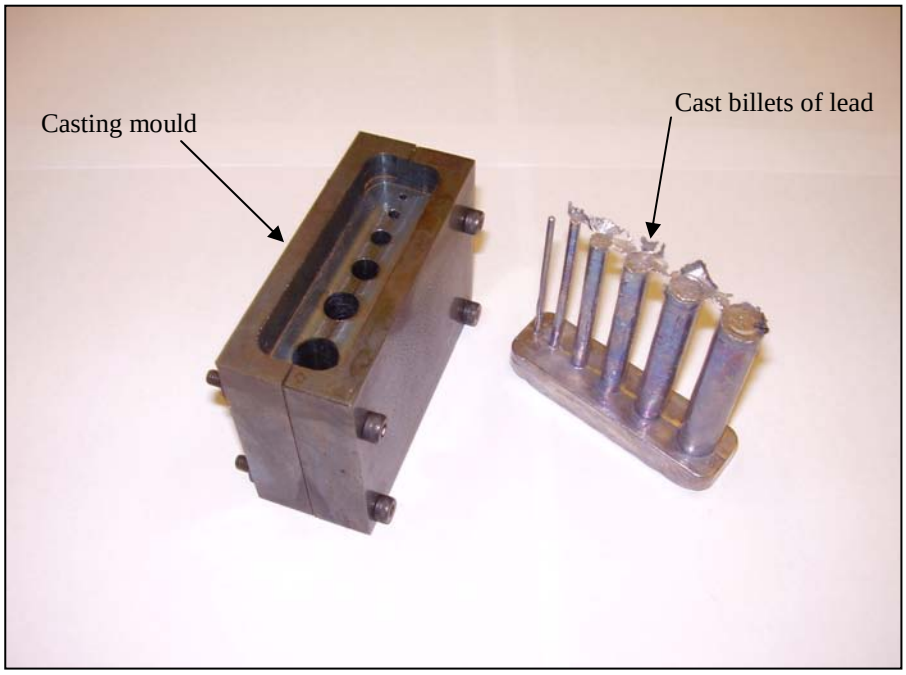

Figure 5.8 Mould for casting lead specimens

in the main experiments, a high performance near-fluid Silicon HCR Gum, with a trade name of RHODORSIL Gum 901, was tested as a deformable material in some of the UREAD energy absorption devices. This material is viscous with a specific gravity of 0.97, and was found to have a yield stress of 60kPa.

5.4 EXPERIMENTS: RESULTS AND ANALYSIS

5.4.1 Sequence of an operational cycle

The behaviour of each channel of the UREAD devices shown in Figure 5.2 and 5.3, with respect to the load and displacement will be characterized by its performance in a full cycle of forward and reverse strokes. Figure 5.9(a) and 5.9(b) show the conventions

used at the beginning of the forward and reverse strokes respectively. Full forward stroke was represented in the direction “x”, while full reverse stroke was represented by the distance “y”.

Billets of different heights were used and deformed under similar conditions. The load cell and the potentiometer were used to measure the forming force and punch displacement. The velocity of the actuator of the press was set to 6mm/s and both billets and channels were lubricated for each test using 10w40 commercial oil.

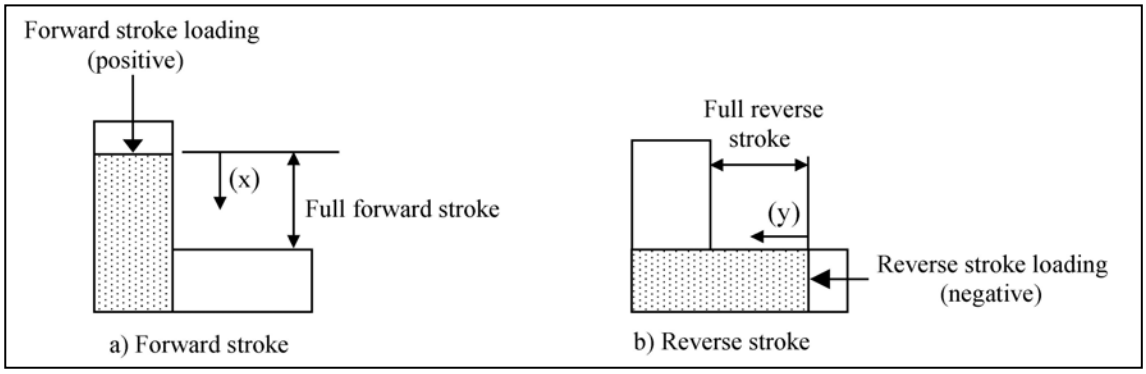

Figure 5.9 Forward and reverse stroke procedure for experiments

The experimental press operates through a vertical ram only, therefore the sequence of operations starts with the material being forced into the vertical channel until the end of the required forward stroke. Then, the punch is removed from the vertical channel and both billet and horizontal channel are lubricated. The unit is then rotated through 90˚ and the billet deformed to the required reverse stroke, i.e full cycle. At the end of the full cycle, the material returns to its original geometry and location if the forward and reverse stroke were equal.

The experimental procedure was repeated for all manufactured channels, and in order to classify experiments, a numbering system was devised and shown in Figure 5.10. It includes information about channel geometry (G), material (M) and displacement (D). As an example, a rectangular channel is defined by GR(a_1,b_1,c_1), where a_1 is the length of the channel, b_1 is its width and c_1 is its height.

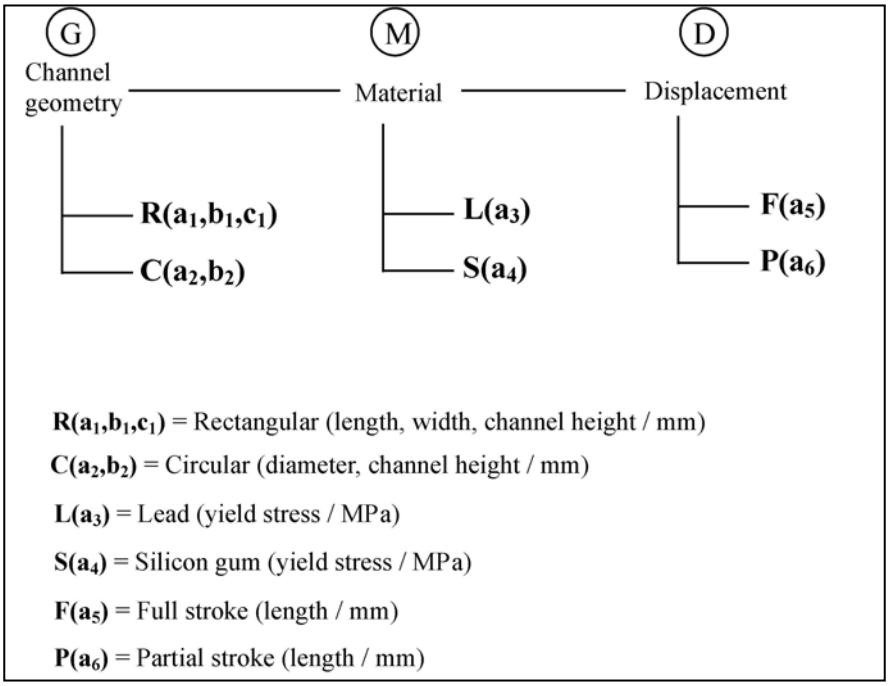

Figure 5.10 Experiments identification nomenclature

5.4.2 Square cross sectional channels with lead

Full stroke experiments were carried out, using the UREAD devices shown in Figure 5.3, with square cross sectional areas, and Figure 5.11 gives the force measurements against punch displacement, for three cycles with three different full strokes (30mm, 22.6mm and 13.8mm) in a unit of a square cross sectional area of 10x10mm. The billet is firstly pushed through the vertical channel (forward stroke), then through the horizontal channel (reverse stroke). Both forward and reverse strokes are presented in a back to back format in Figure 5.11 to show the full cycle. The average load for the longest stroke in this test is in the region of 6kN giving an average extrusion pressure of around 5.5 times the material yield stress. The nature of the deformation process in these channels gives rise to the hydrostatic pressure components before the material starts to yield and extrude through the intersecting channels. Also, the static friction has to be overcome before the deformation commences.

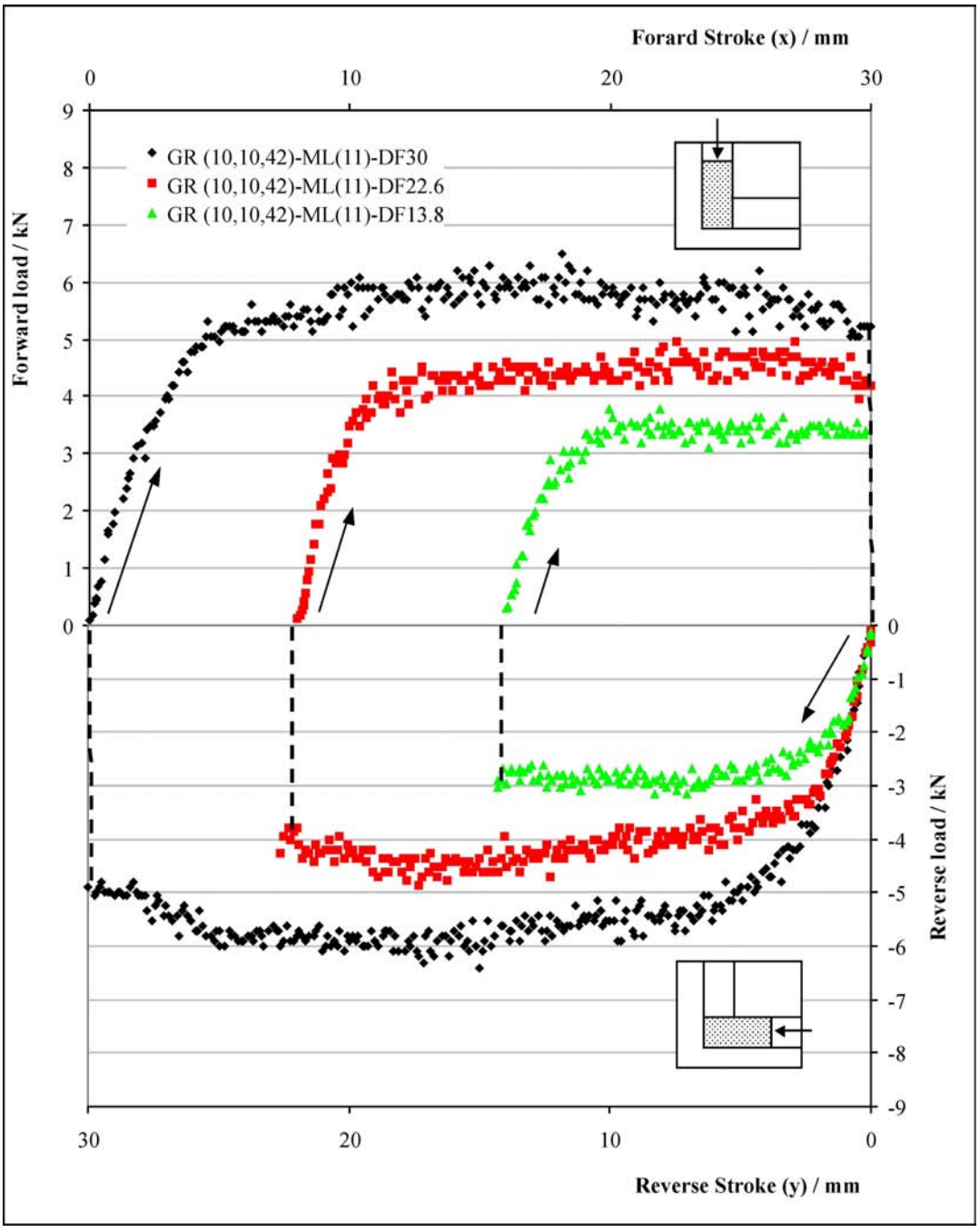

Figure 5.11 Experimental loops with Lead at various full strokes: UREAD - GR (10,10,42)

When the material flow is stabilized, the force is shown to remain almost constant. In this case friction on the vertical channel decreases as the process continues. It is worth mentioning that, during the process wear across the vertical channel diminishes, due to the loss of contact, but friction on the other channel increases. This is the reason of why the force shows a nearly constant trend. Also, the effect of a reducing contact on the

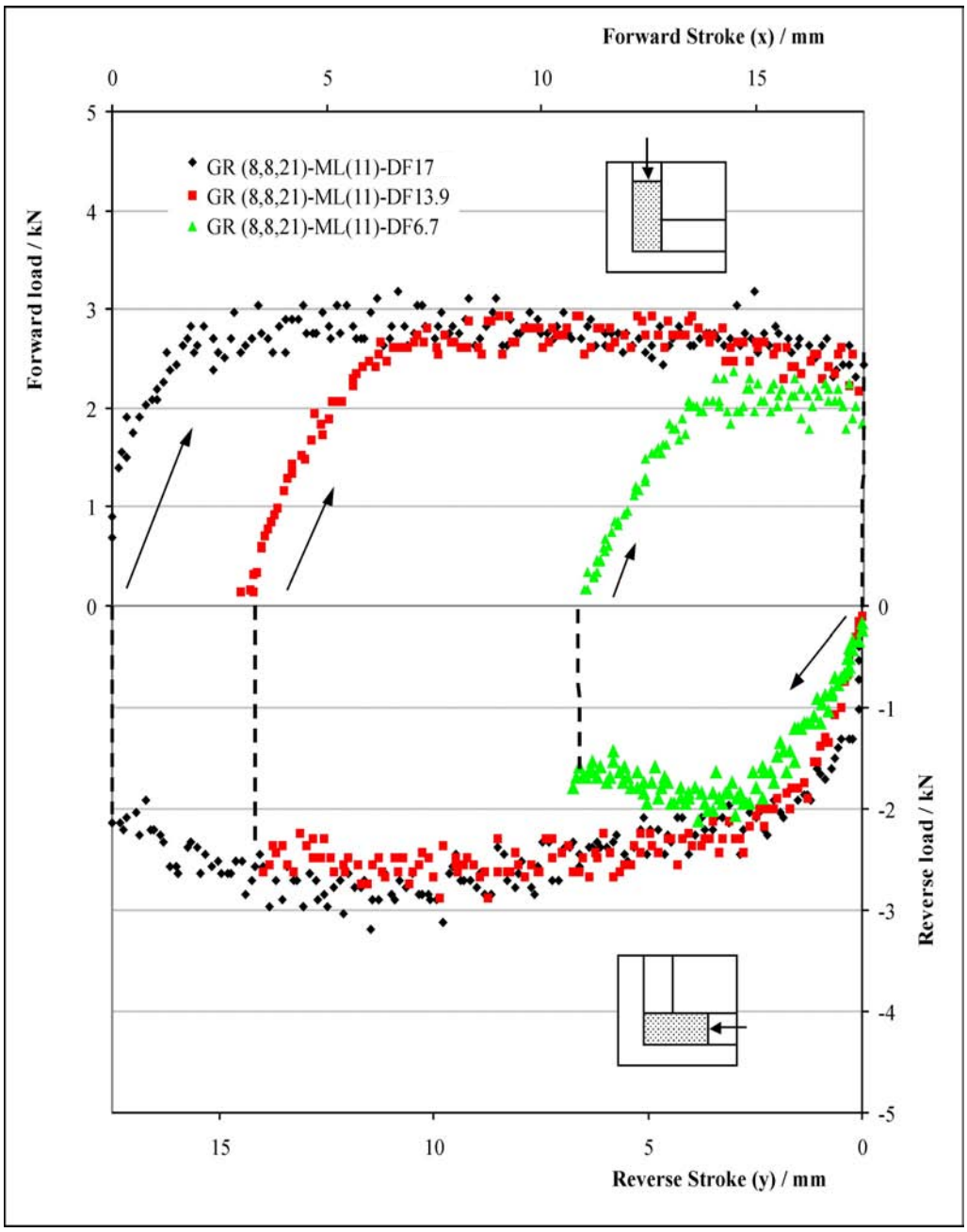

Figure 5.12 Experimental loops with Lead at various full strokes: UREAD - GR (8,8,21)

extrusion force is clear when considering the measurements for smaller full strokes, i.e. smaller billets. The force was measured to be about 40% less for the smaller stroke, when compared to the longest stroke. A similar distribution trend is discovered for square channel with smaller cross sectional area (8x8mm), and results are presented in Figure 5.12. Three different full strokes were performed. The load increases at the beginning of the process, then drops slightly and averages to values in the range

between 2 and 3 kN, giving a pressure of 2.85 and 4.25 times over the material yield stress for the shortest and longest full strokes respectively.

Experimental readings by the in house data acquisition system produced a level of scatter on the experimental distributions, due to the noise created by the instrumentations. A computational method to filter such noise is given in Appendix (C).

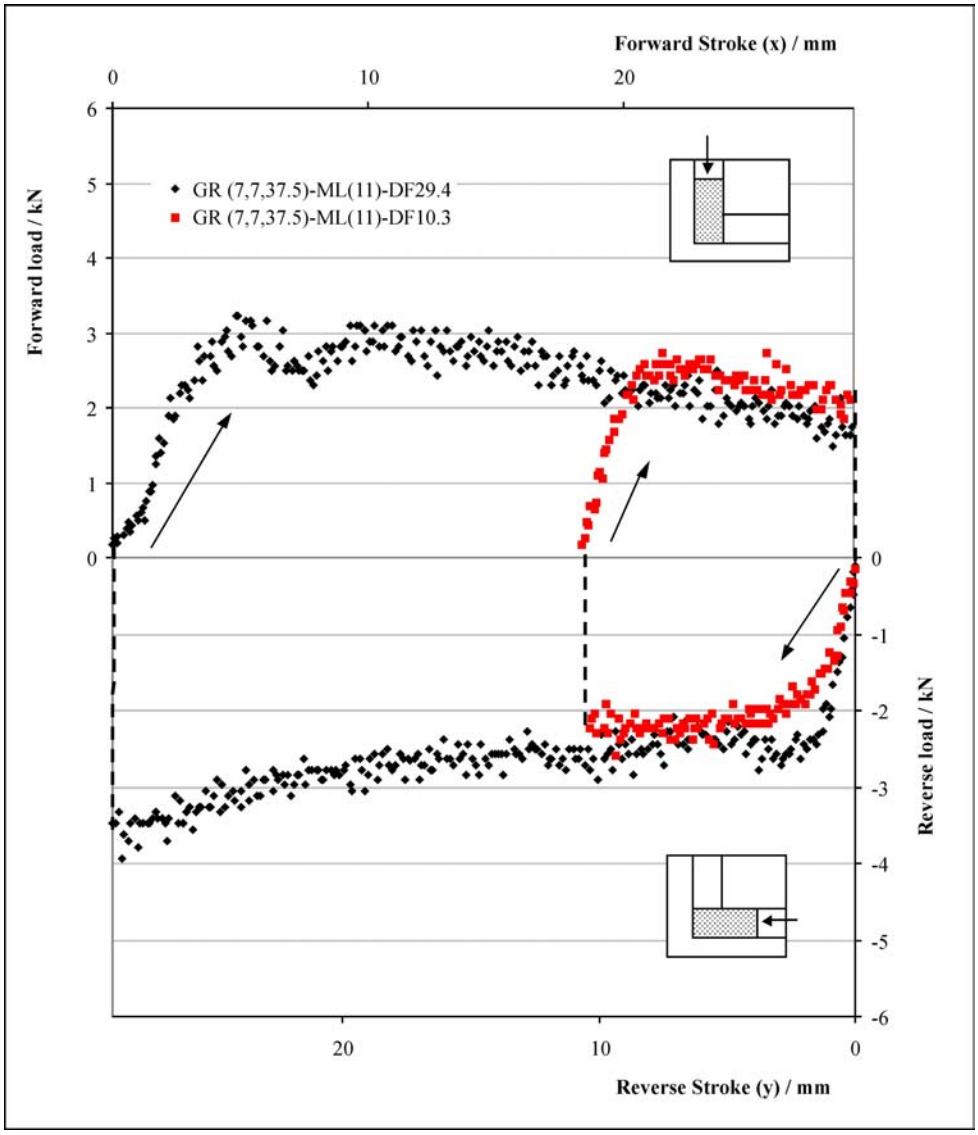

Figure 5.13 Experimental loops with Lead at various full strokes: UREAD - GR (7,7,37.5)

Figure 5.13 shows the experimental results for a square cross sectional channel of 7x7mm. In this case, the representation includes results for two full strokes in the vertical channel, of 29.4mm and 10.3mm. Load against punch displacement curves have

a different trend, when compared to previous results. During the forward stroke, the forming load decreases, after reaching a peak value; while an opposite tendency is found for the reverse stroke. Investigations were conducted, and it was discovered that such behaviour is attributed to the level of machining tolerance in the channels. A layer of “blue paint” was applied on the material interface before the inserting the billet into the channel. Figure 5.14 shows the blue paint trace left on channel 4, when a billet of lead was extruded from channel 3 to channel 4; while Figure 5.15 shows the reverse process, where the material was extruded from channel 4 to channel 3. Channel number

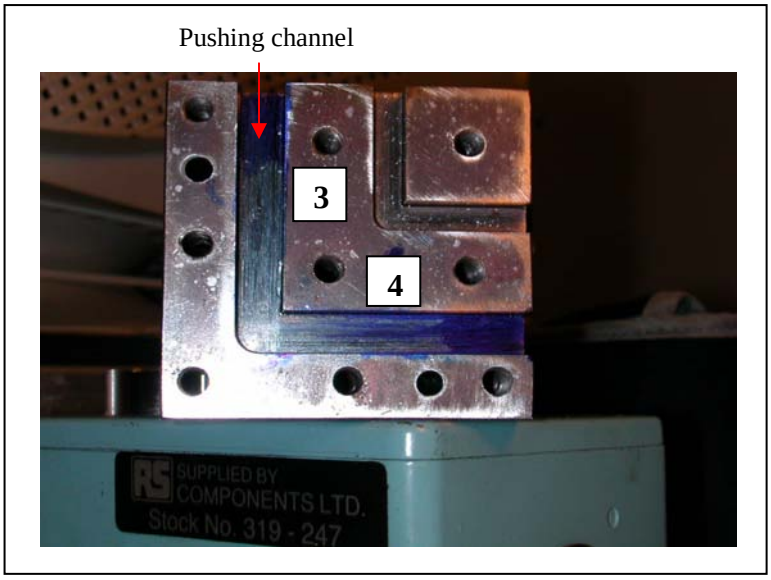

Figure 5.14 Blue paint left on channel 4, when the material is pushed through channel 3

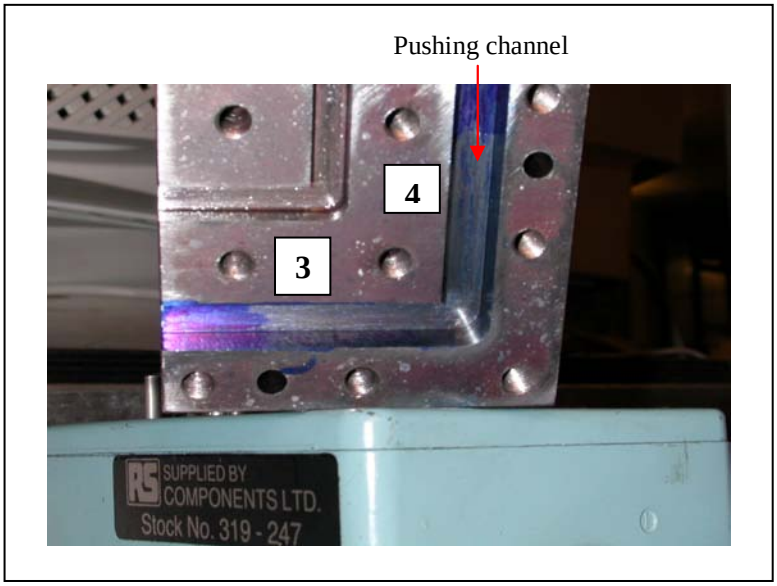

Figure 5.15 Blue paint left on channel 3, when the material is pushed through channel 4

3 was found to tighter then channel number 4. This may explain the results in Figure 5.13, where the forces required to extrude the material from channel 3 to channel 4 show a decreasing trend, while material extruded from channel from channel 4 to channel 3 show an increasing trend.

Figures 5.16 and 5.17 show experimental results using the 5x5mm and 4x4mm square channels, and applying a forward and reverse full stroke of 13.4mm and 19.6mm respectively. The force distribution follows the same trend of the results in Figures 5.11 and 5.12, where after increasing at the beginning of the process the load averages to a constant value.

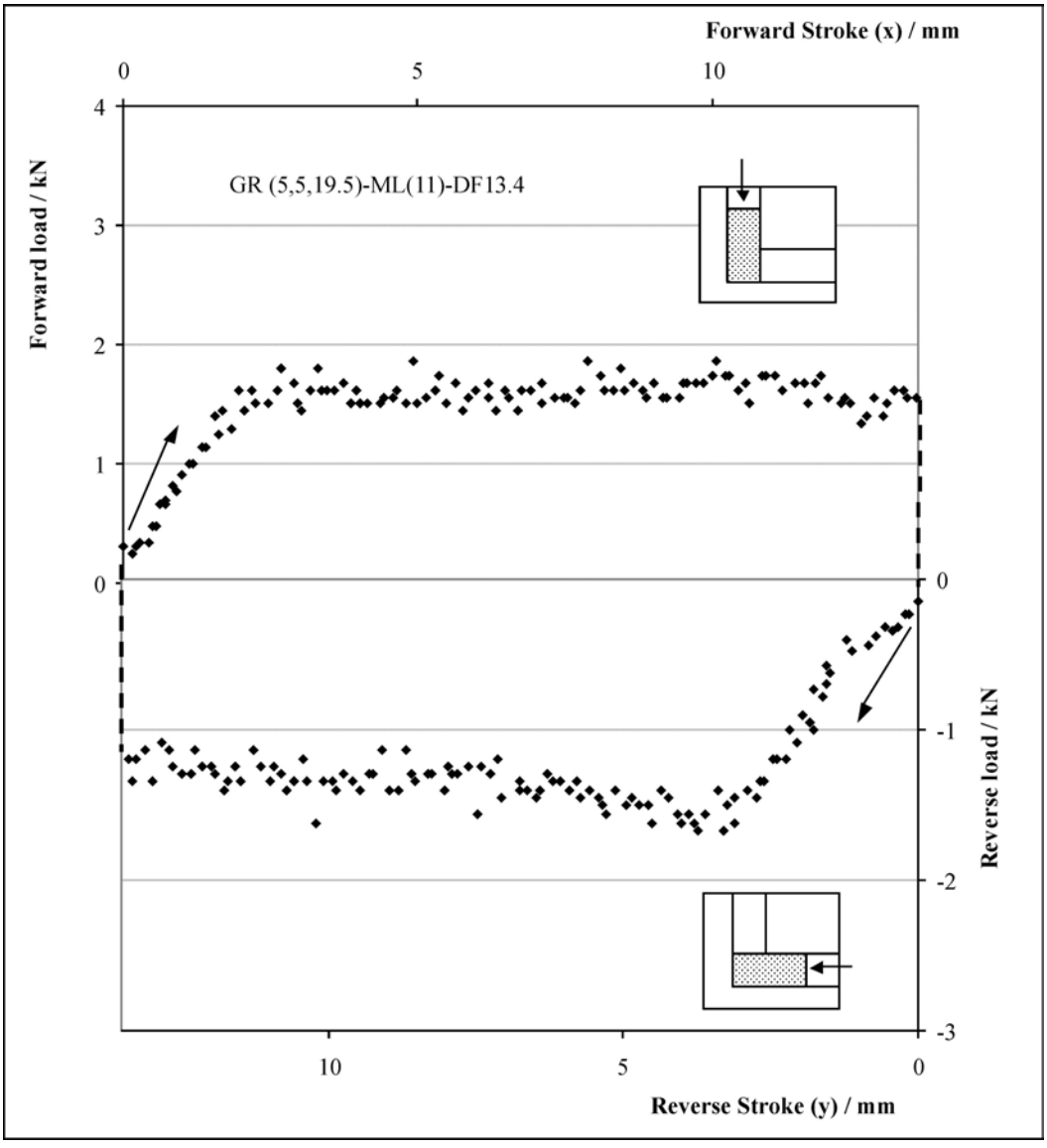

Figure 5.16 Experimental loop with Lead: UREAD - GR(5,5,19.5)

It was not possible to use the square channel of 2x2mm due to their small size and therefore the tolerances required for machining the channels was not achievable within the available facilities.

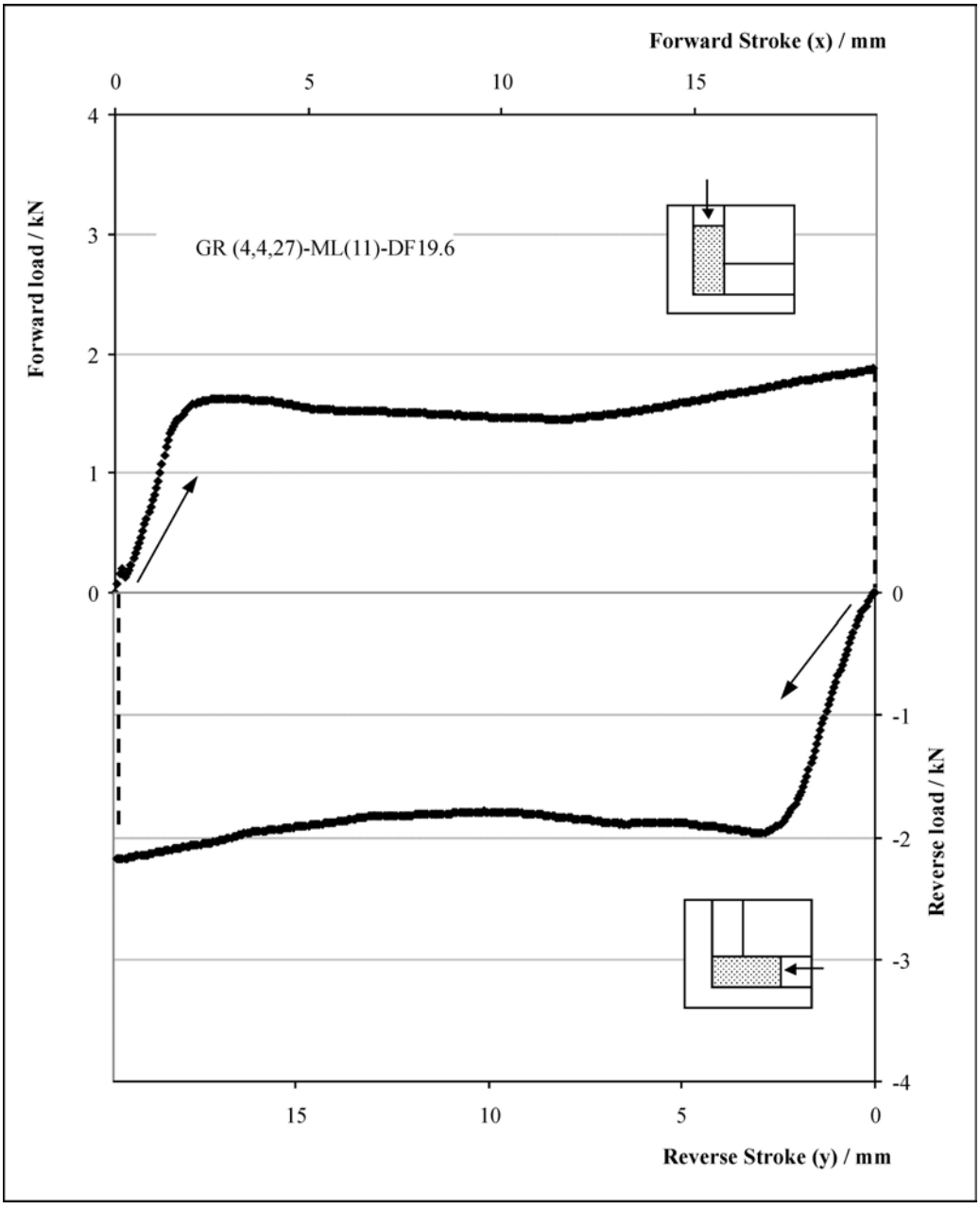

Figure 5.17 Experimental loop with Lead: UREAD - GR(4,4,27)

5.4.3 Square cross sectional channels with silicon gum

Experiments were performed using silicon gum as a plastically deformable material. This is a semi-fluid material, and its properties were given in section 5.3. Figures 5.18

and 5.19 show the experimental results using silicon gum, in the 10x10mm and 8x8mm square channels fro strokes of 25mm and 14mm respectively.

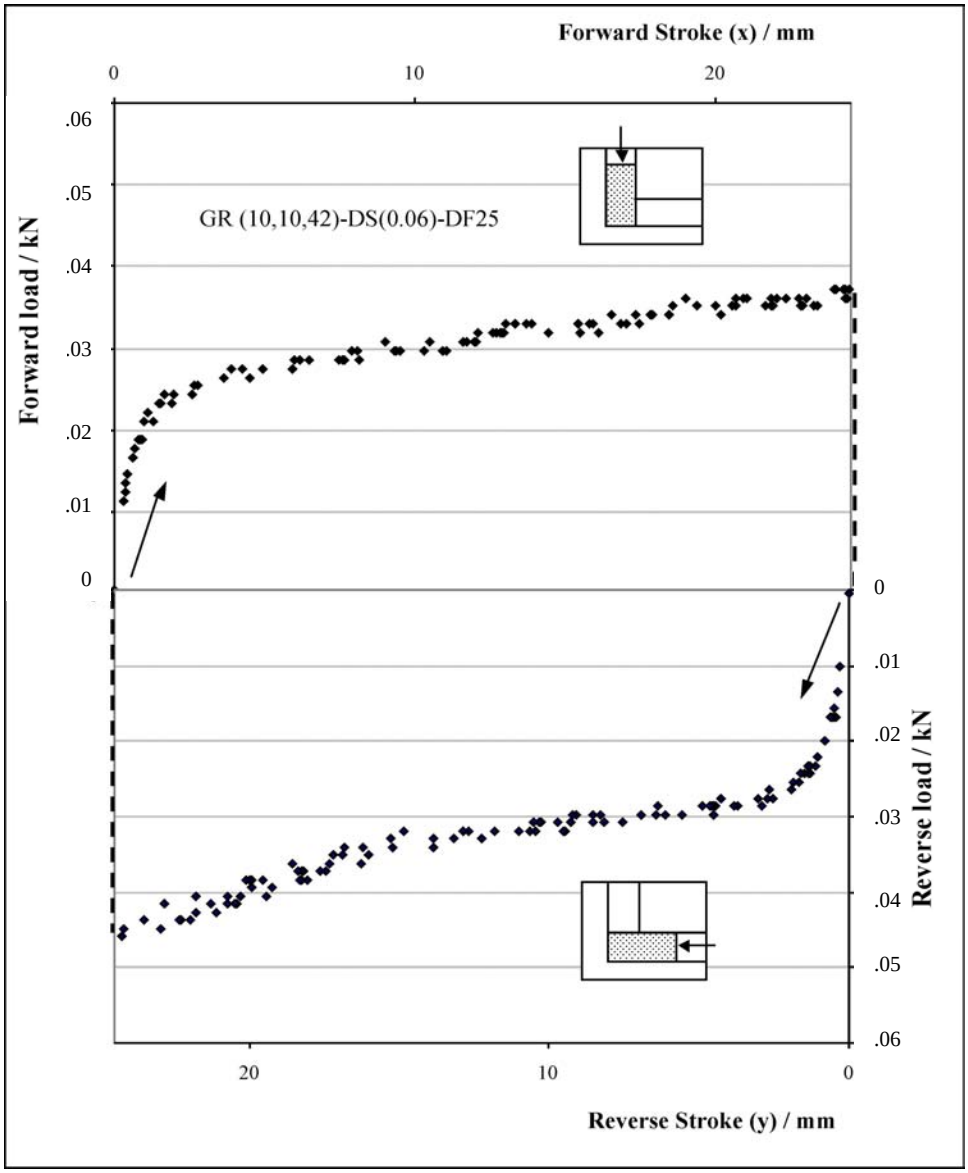

Figure 5.18 Experimental loop with Silicon Gum: UREAD - GR(10,10,42)

The results given by these tests had shown that devices employing the UREAD technology to dissipate unwanted energy are capable of performing different energy absorption levels. In fact, the trend of the results for silicon gum is similar to the ones observed using lead, but the level of measured load is about 70 times lower. However,

for viscous materials the flow characteristics through the channel will depend upon many parameters such as the rate of deformation, the intensity of internal pressure, changes in viscosity due to the shearing mechanism. Such investigation is beyond the research programme of this thesis.

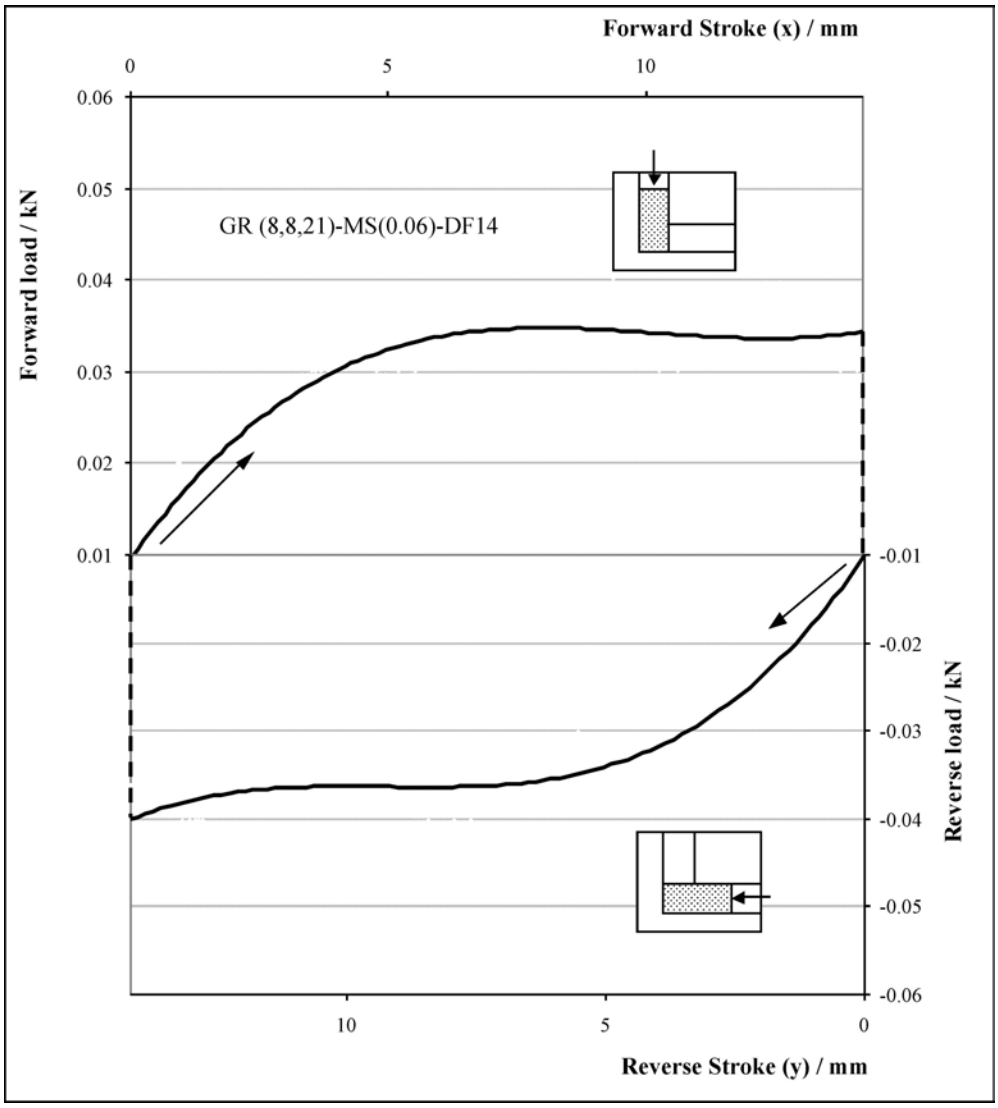

Figure 5.19 Experimental loop with Silicon Gum: UREAD - GR(8,8,21)

5.4.4 Circular cross sectional channels with lead

In this section results obtained using the UREAD devices with circular cross sectional area channels, shown in Figure 5.2, are presented. Figure 5.20 shows the results using a channel of 11mm in diameter, and applying two different full strokes of 33mm and

16.8mm. In both cases, the required force increases at the beginning of the forming process, then it assumes nearly a constant value as the punch displacement progresses. The average load for the longest billet in this case is in the region of 5kN, giving an average extrusion pressure of just under 5 times the material yield stress. For the shorter stroke, the force is in the range of 3kN, this is due to the effect of reduced side contact friction.

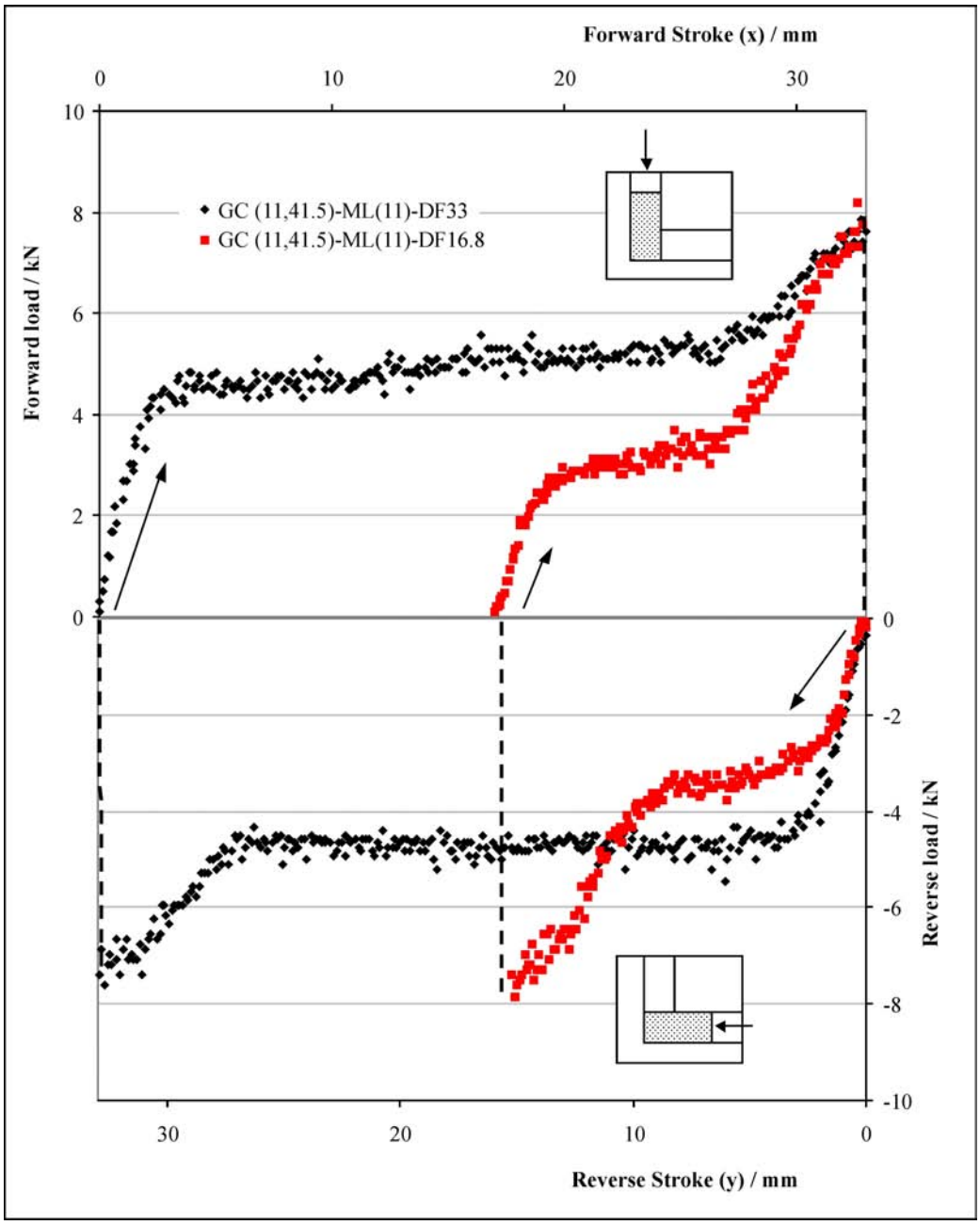

Figure 5.20 Experimental loops with Lead at various full strokes: UREAD – GC(11,41.5)

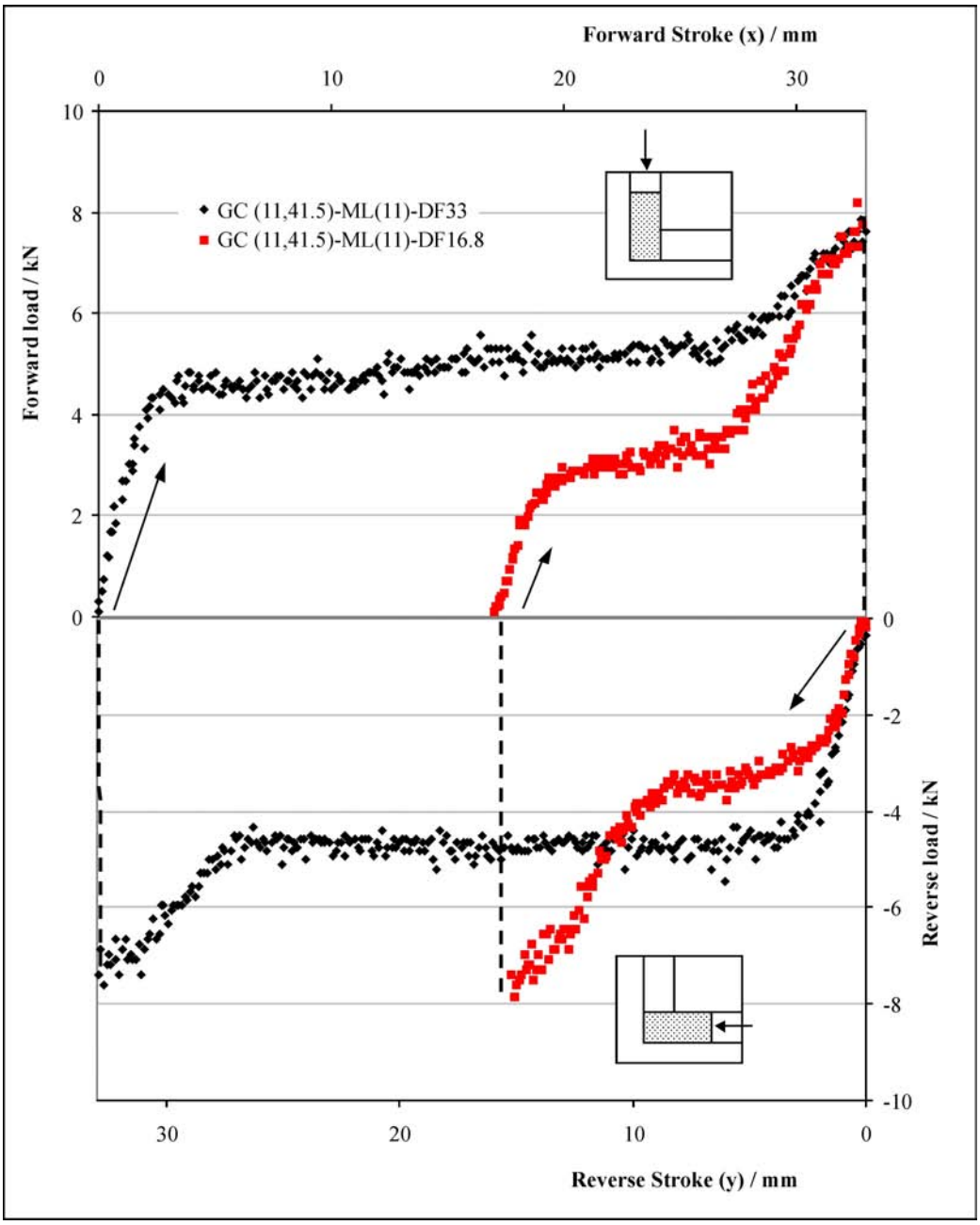

Figure 5.21 Experimental loops with Lead using at various full strokes: UREAD – GC(9,20.5)

Figure 5.21 shows the experimental force-punch displacement distributions for channels of a smaller cross sectional area (9mm diameter). Results were recorded at two different full strokes, of 16.3mm and 33mm. The loading requirement is in the region of just under 3kN for the longest stroke giving an average extrusion pressure of just over 4 times the material yield strength.

It was noticed in these experiments that the punch had experienced very tight roundness tolerance near the end of the stroke. A rapid increase of load at the end of the punch travel was observed.

Figure 5.22 shows force distribution of circular channels with 7mm diameter, at two full strokes of 19.9mm and 9.4mm.

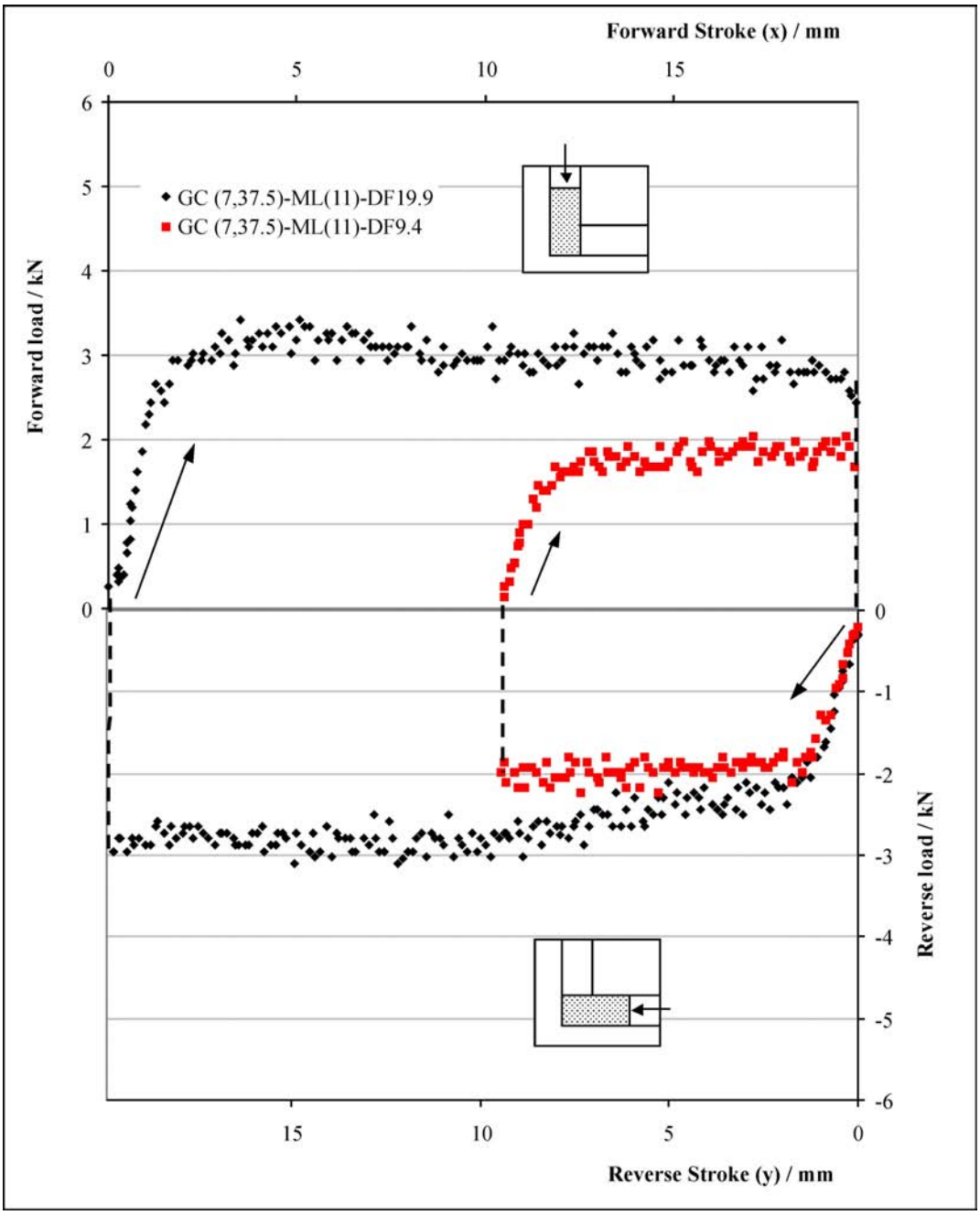

Figure 5.22 Experimental loops with Lead at various full strokes: UREAD - GC(7,37.5)

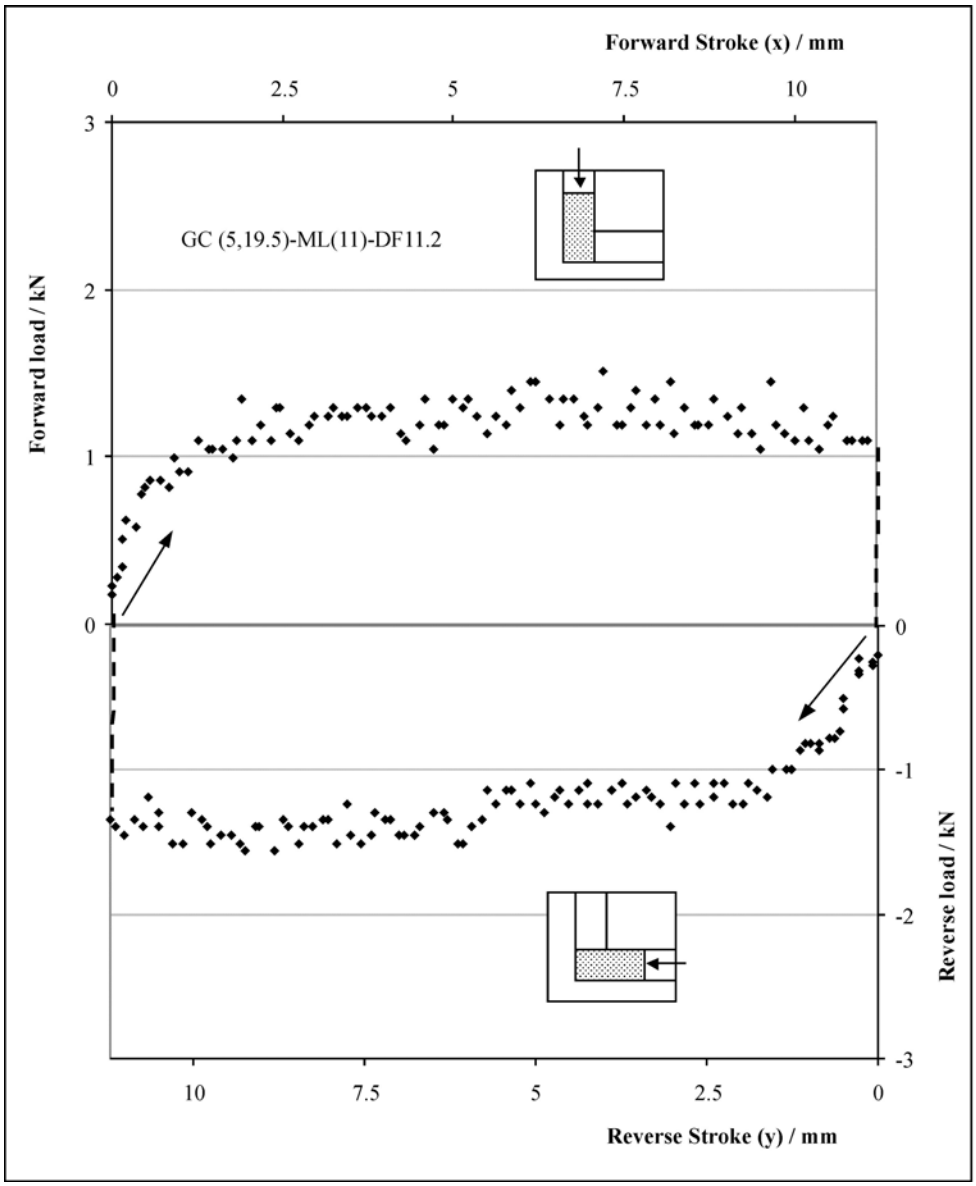

Figure 5.23 Experimental loops with Lead: UREAD – GC(5,19.5)

The experimental load distributions using smaller punches diameters of 5, 3 and 2mm are shown in Figure 5.23, 5.24 and 5.25, and applying a forward and reverse full strokes of 11.2mm, 16.4mm and 7.6mm respectively. For this channel types, a maximum load in the region between 0.35kN and 1.5kN was measured.

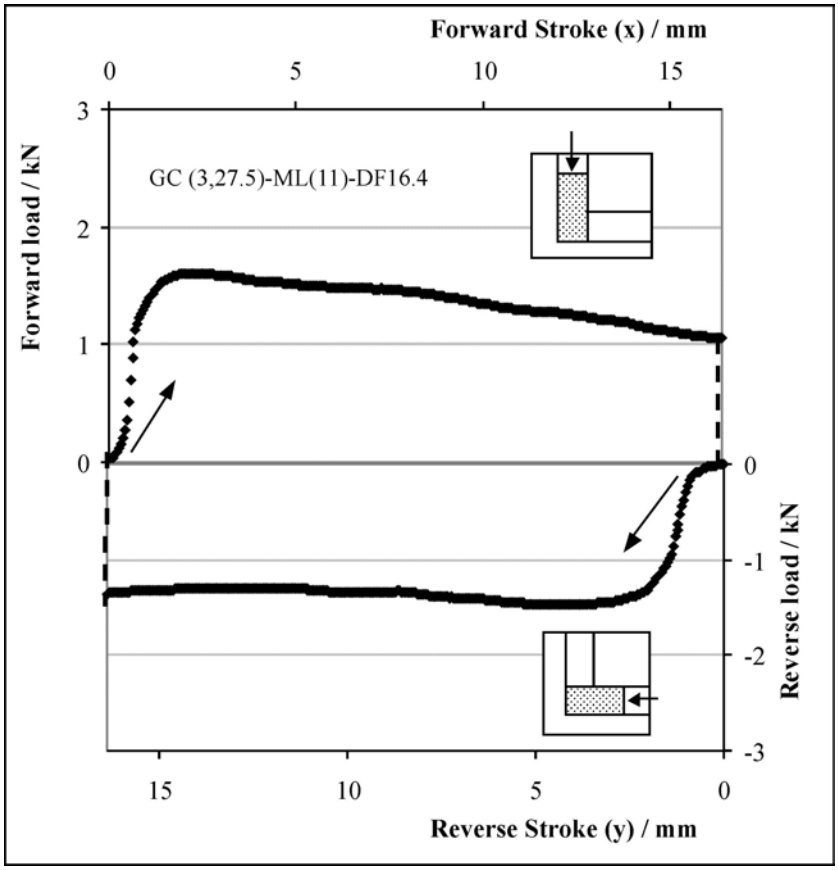

Figure 5.24 Experimental loops with Lead: UREAD - GC(3,27.5)

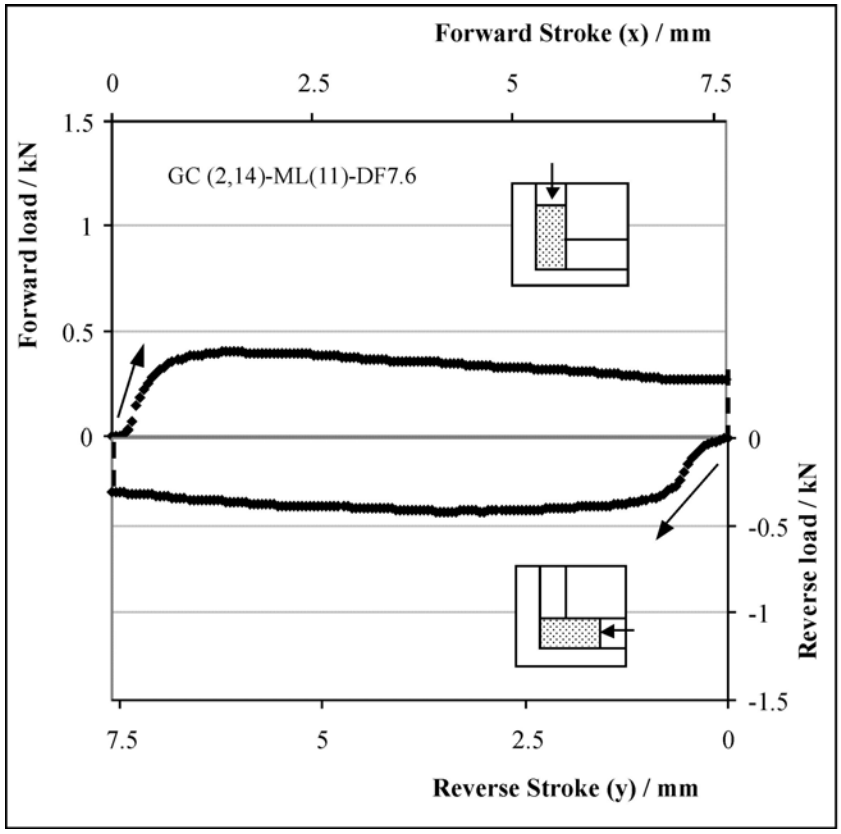

Figure 5.25 Experimental loops with Lead: UREAD - GC(2,14)

5.4.5 Compilation of the UREAD devices results

5.4.5.1 Forming Pressure

Experimental forming pressures using UREAD channels with circular and square cross sections and using lead as a deformable material are shown in Figures 5.26 and 5.27. The figures plot the relative average extrusion pressure p_{ext} with the material yield stress $2\tau_k$, against the ratio of the cross sectional area and full stroke L, for both circular and square cross-sectional channels. The use of relative pressure is convenient as the ratio gives a value that is proportional to the material yield strength obtained from simple tension or compression. Experimental values of average extrusion pressure are

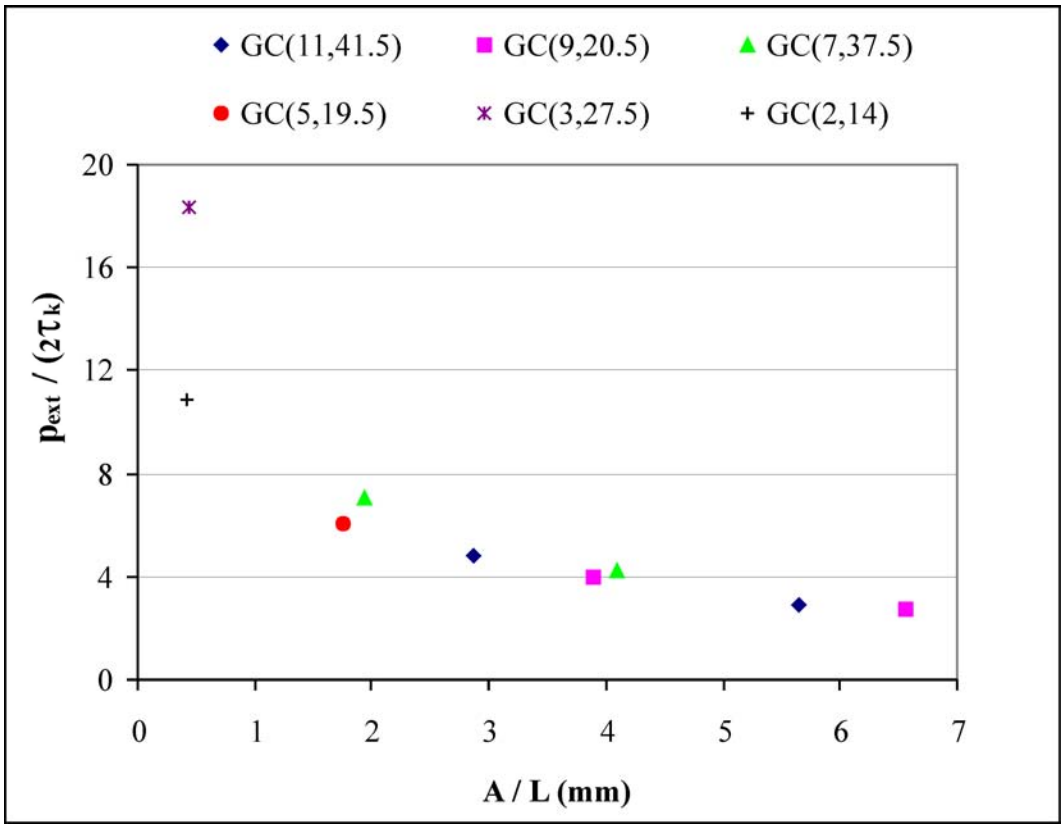

Figure 5.26 Average extrusion pressure against channels geometry - circular cross sections

comparable for both cross sections, and they show a trend similar to an hyperbolic function. Therefore, when small channel cross sectional areas and long strokes are used, the extrusion pressure is high. A pressure value of 18 times the material yield stress was

measured for the GC(3,27.5) geometry. On the other hand for large cross sectional area and small strokes the required extrusion pressure becomes lower.

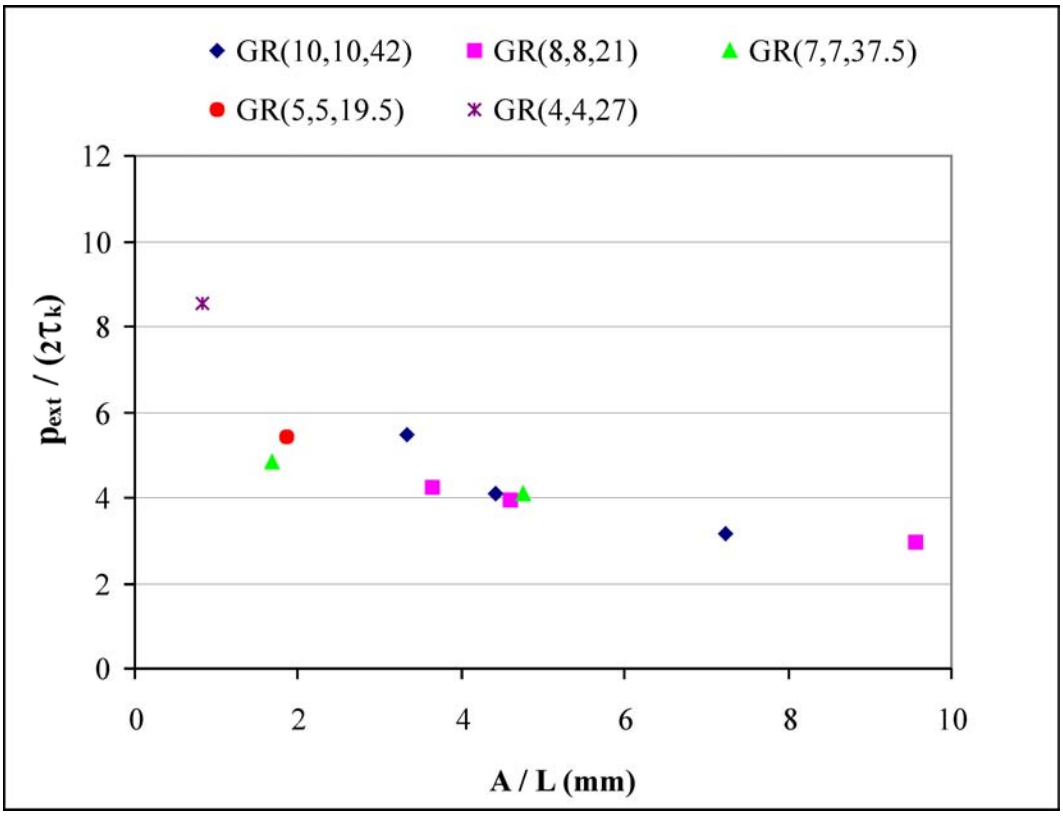

Figure 5.27 Average extrusion pressure against channels geometry - square cross sections

5.4.5.2 Energy dissipation in UREAD devices

The sequence of Figures from 5.28 to 5.38 show the energy dissipated from the tests carried out at various full strokes, therefore by using the UREAD channels with lead as deformable material. The energy graphs correspond to a single stroke only, and it is calculated from the total area under the experimental curves for pressure vs. displacement using the trapezoidal method. Distributions are rather linear, and a maximum value of just under 160J was calculated for the GR(10,10,42) and GC(11,41.5) channels geometry.

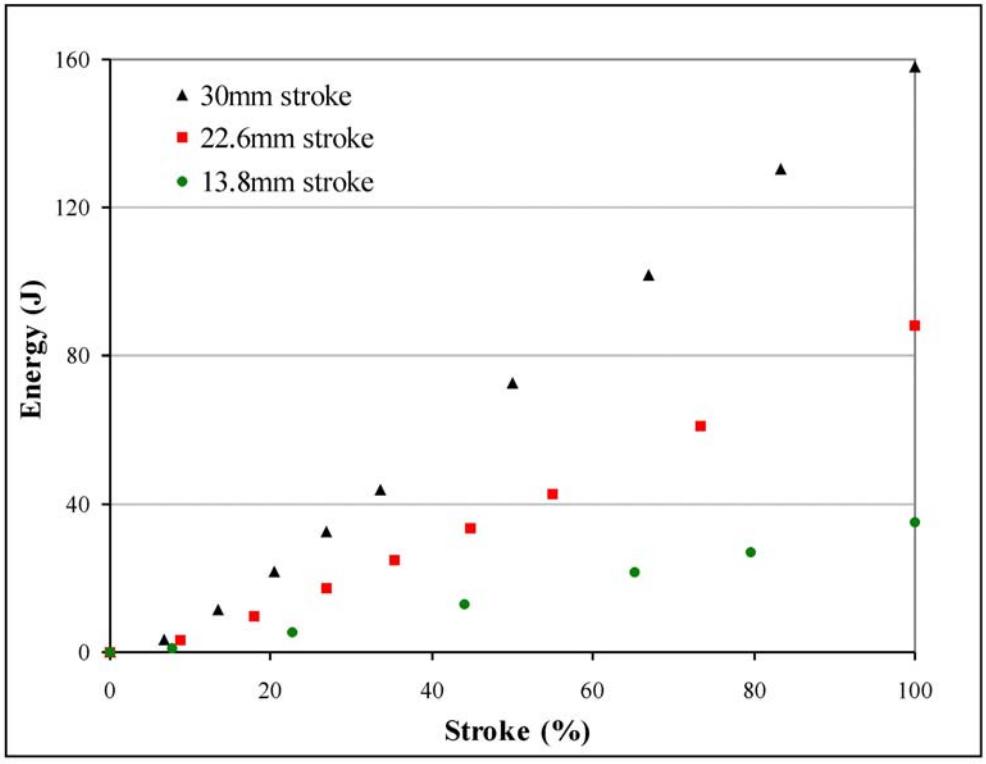

Figure 5.28 Energy dissipation in GR(10,10,42) UREAD channel with lead

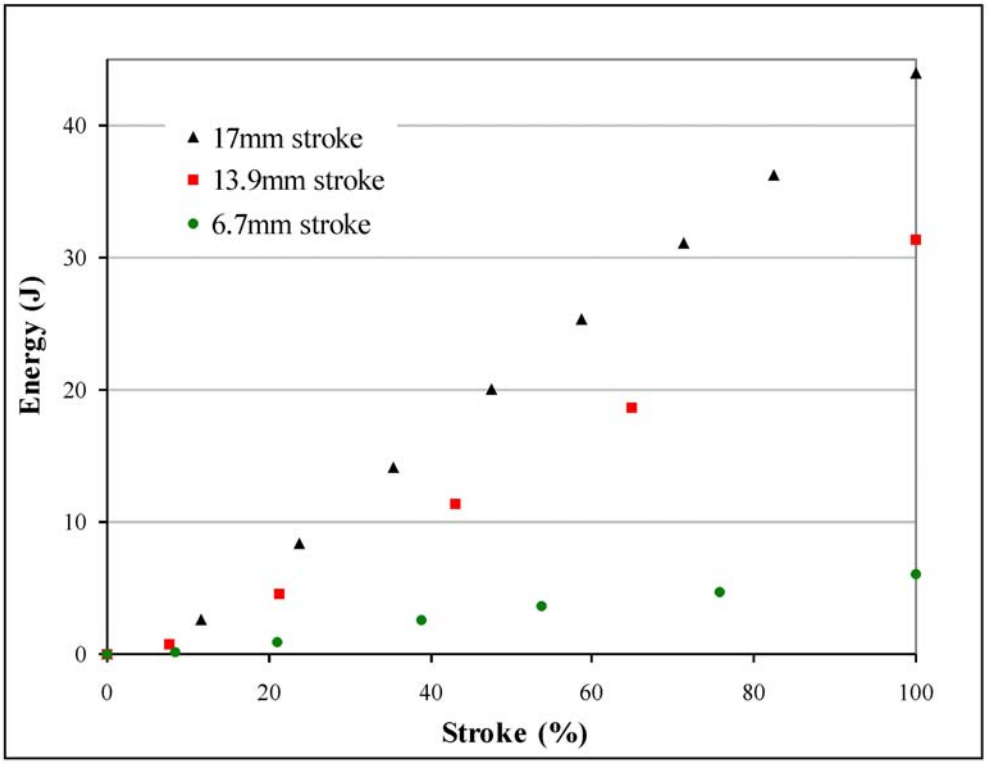

Figure 5.29 Energy dissipation in GR(8,8,21) UREAD channel with lead

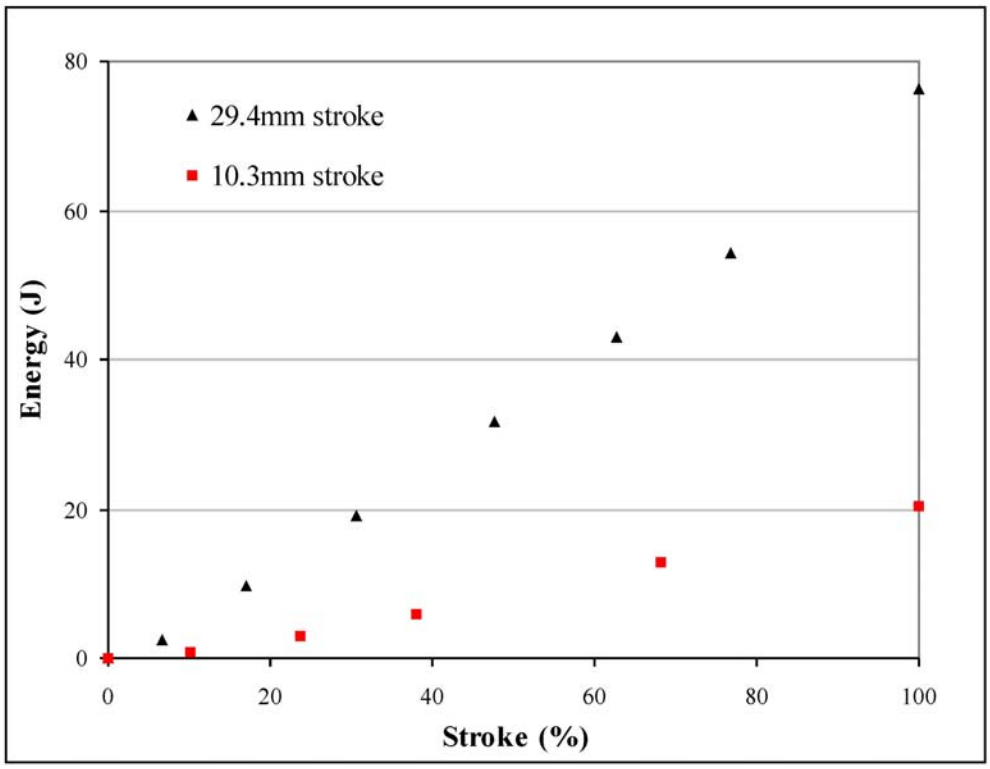

Figure 5 30 Energy dissipation in GR(7,7,37.5) UREAD channel with lead

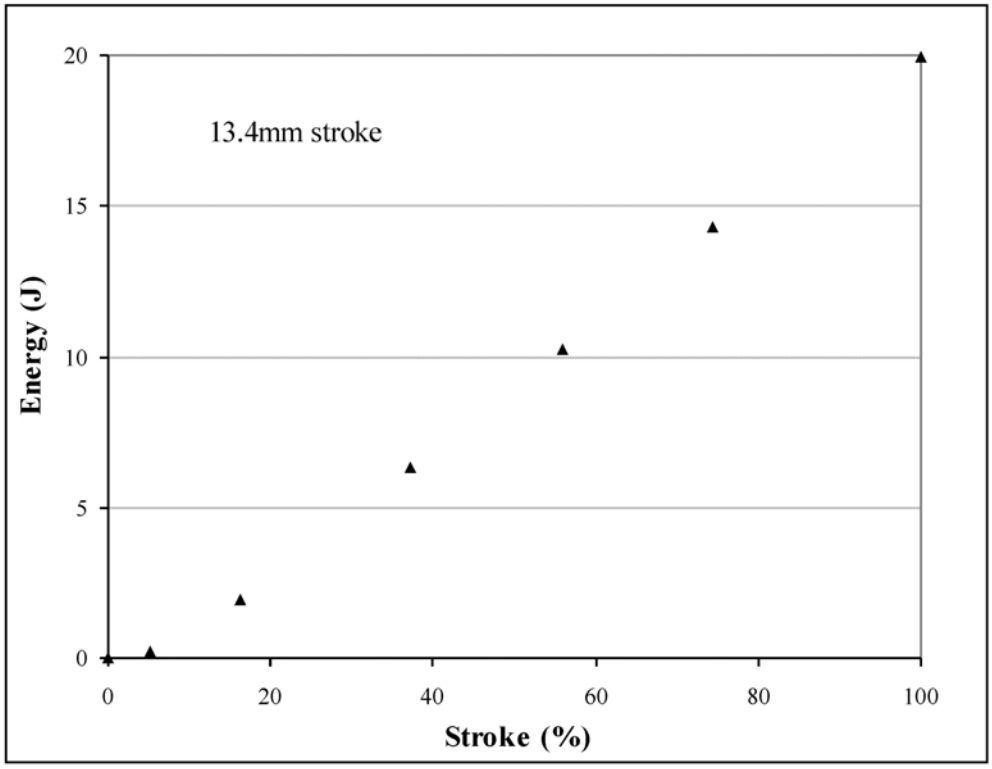

Figure 5.31 Energy dissipation in GR(5,5,19.5) UREAD channel with lead

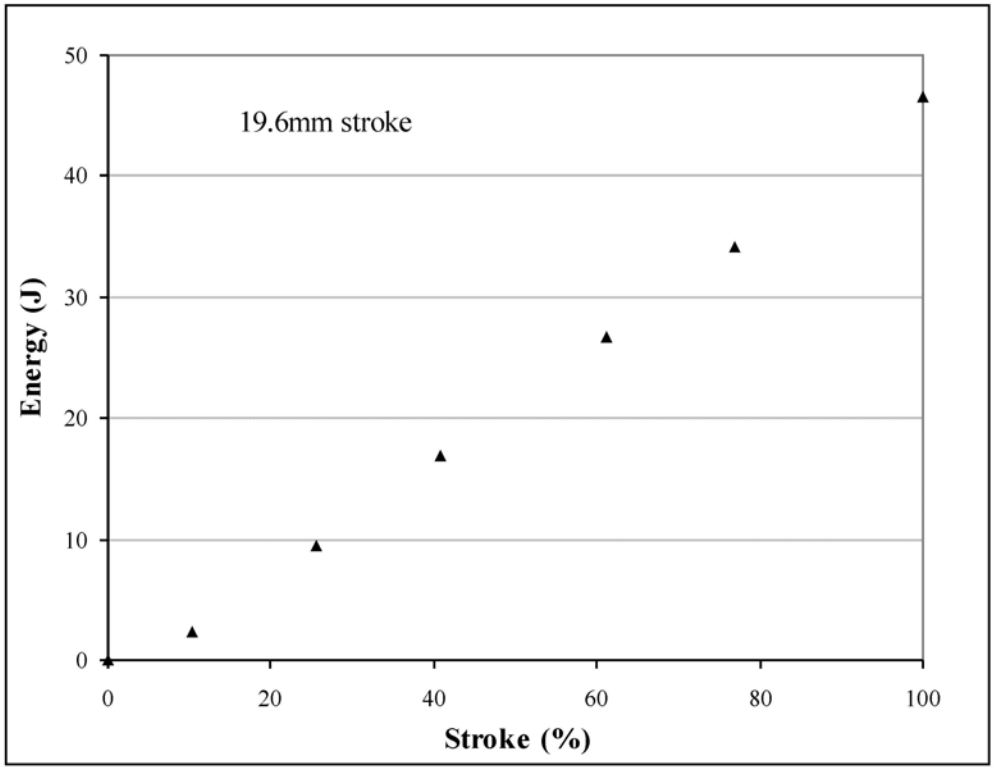

Figure 5.32 Energy dissipation in GR(4,4,27) UREAD channel for with lead

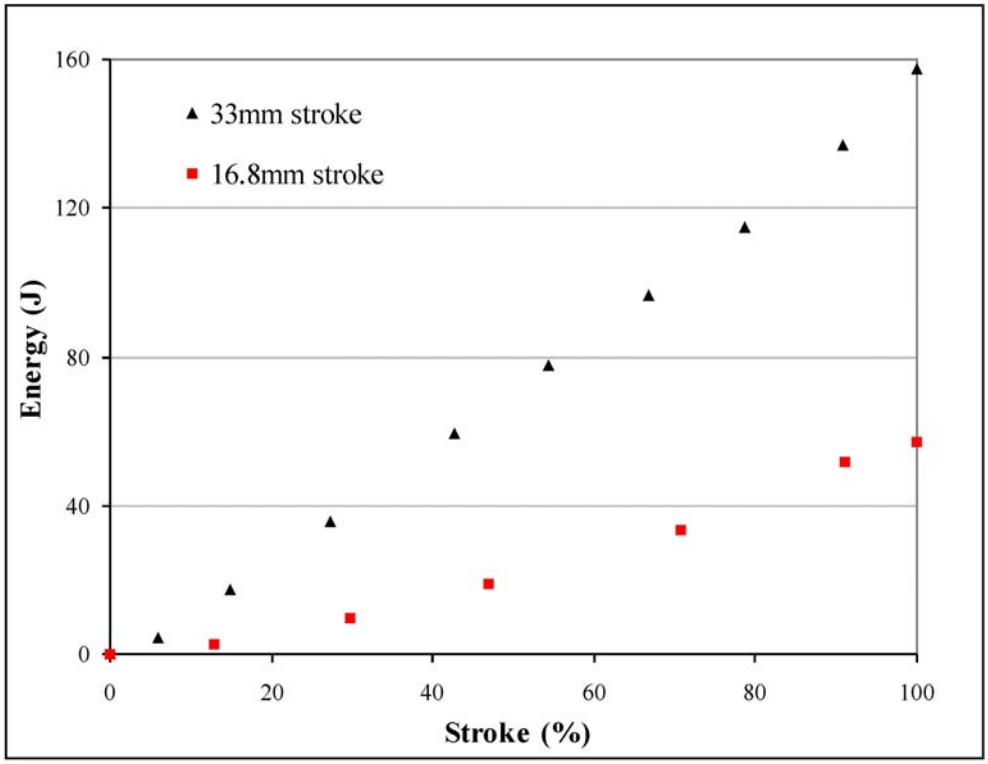

Figure 5.33 Energy dissipation in GC(11,41.5) UREAD channel with lead

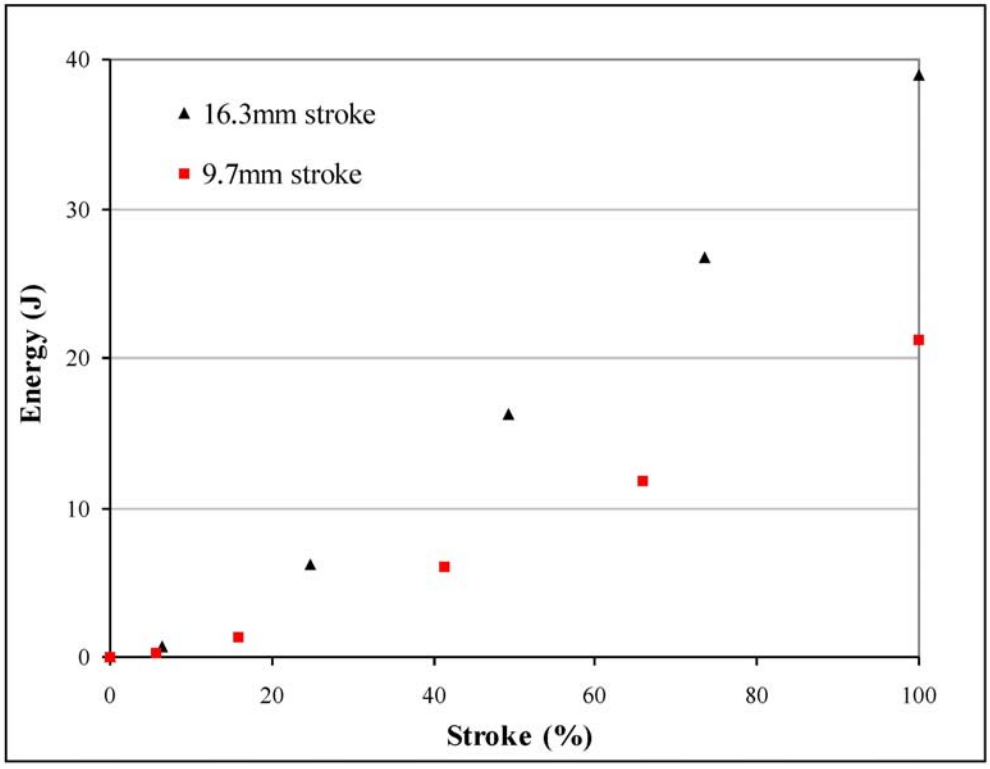

Figure 5.34 Energy dissipation in GC(9,20.5) UREAD channel with lead

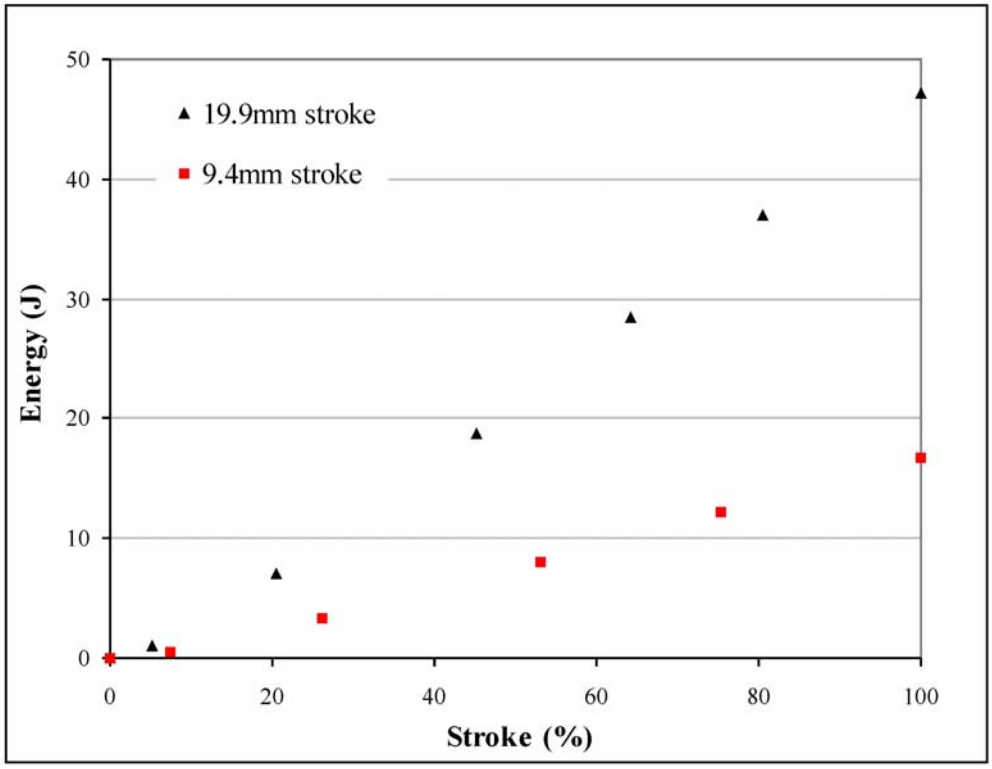

Figure 5.35 Energy dissipation in GC(7,37.5) UREAD channel with lead

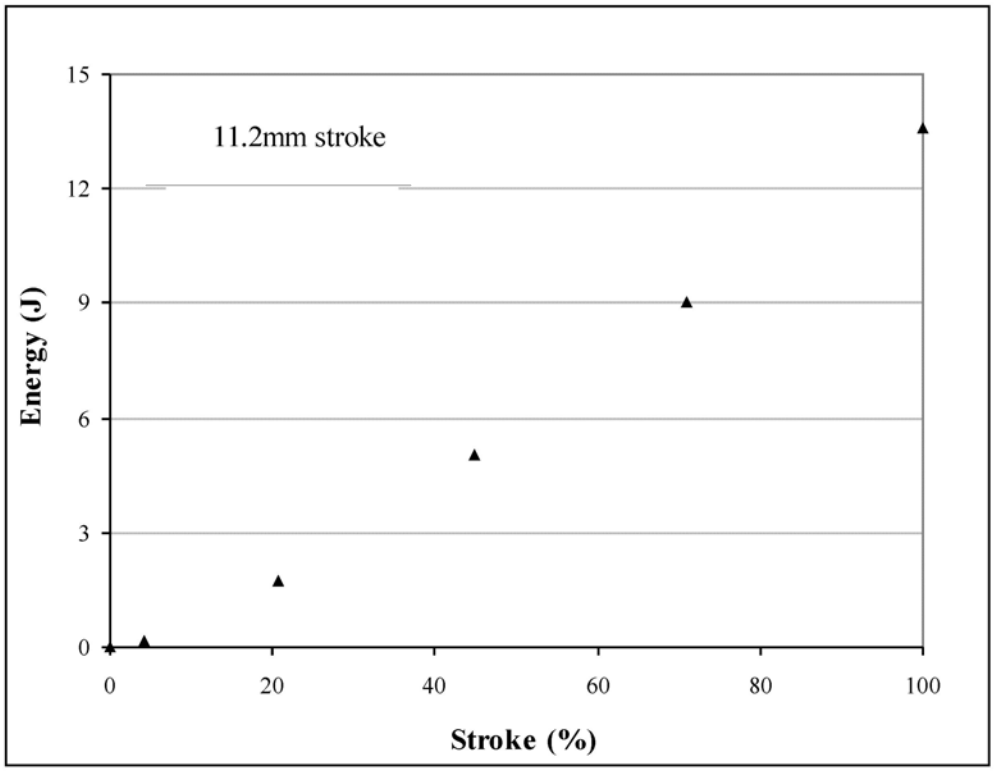

Figure 5.36 Energy dissipation in GC(5,19.5) UREAD channel with lead

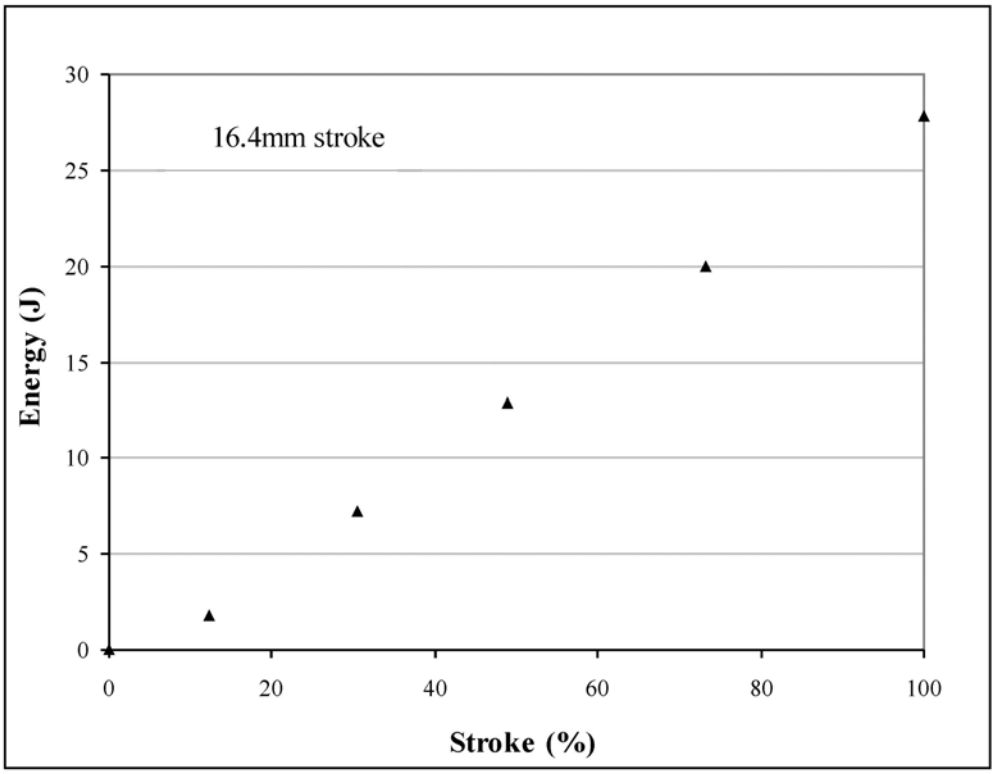

Figure 5.37 Energy dissipation in GC(3,27.5) UREAD channel with lead

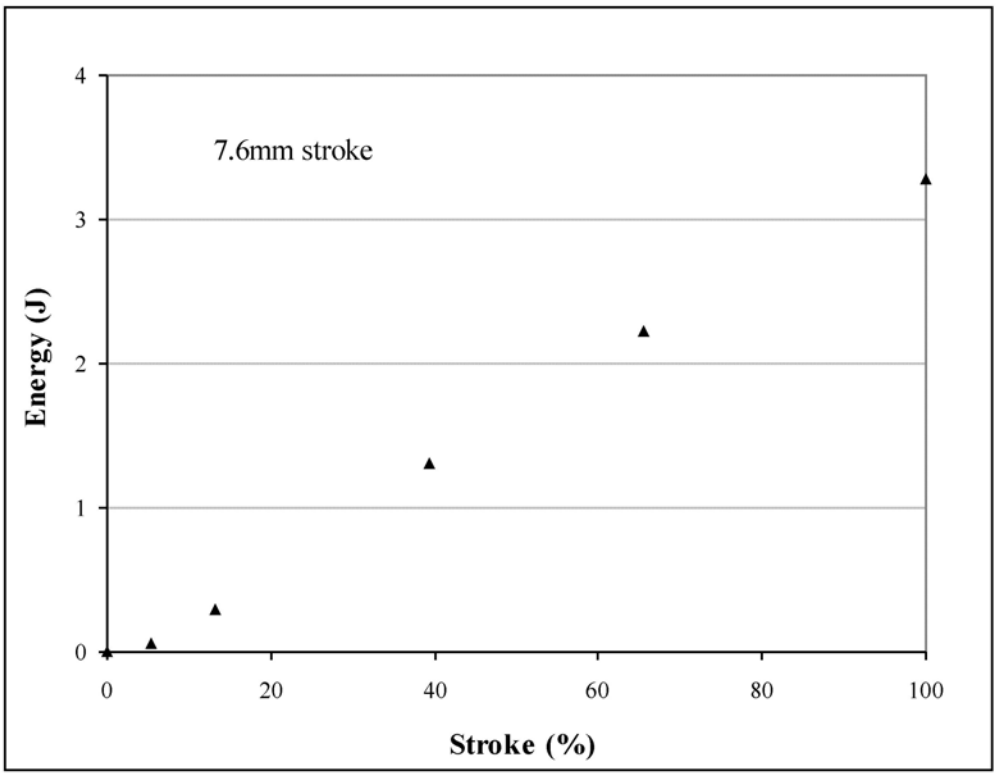

Figure 5.38 Energy dissipation in GC(2,14) UREAD channel for with lead

Energy charts are very useful for sizing and dimensioning of UREAD devises for a particular application. In fact, usually the energy to be dissipated is a known input parameter in the design of engineering systems; therefore the channel type, cross-section, area and full stroke are selected according to the design space and component features.

5.5 COMPARISONS BETWEEN EXPERIMENTAL AND THEORETICAL RESULTS

The process of Channels Angular Extrusion, on which the UREAD technique is based upon, was theoretically studied in Chapter 4, and analytical results were presented. The validation of the theoretical approaches will be through plain-strain comparisons of results against experimental results from square cross sectional area channels.

Figure 5.39 shows analytical results from Figure 4.8 by the slab method (equations 4.16 and 4.28), when the vertical and horizontal channels widths are b=h=10mm. The figure shows the vertical pressure distribution on the yielding zone boundary when yielding occurs, for a full stroke of 5mm (k=0.5) and 10mm (k=1). The experimental average relative pressure is superimposed on the analytical results, for the case of k=0.5. The experimental value was obtained by using lead, with the GR(10,10,42) UREAD channel, and applying a full stroke of 5mm. The billet was well lubricated, and an extrusion process was performed for a displacement of 1mm in order to simulate the yielding conditions.

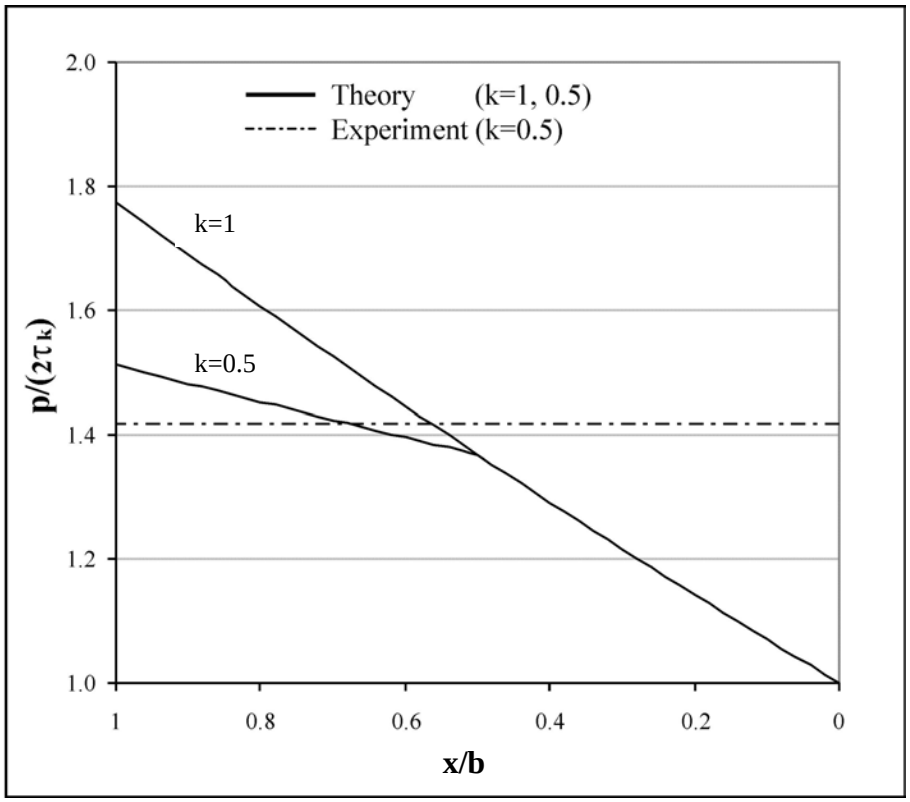

Figure 5.39 Analytical distribution and experimental average pressure on the yielding zone boundary

Figure 5.40 and 5.41 show a comparison between the experimental results from Figure 5.11, for the full stroke of 13.8mm. In this case, the relative experimental average pressure (p_d) is represented. The graph includes several theoretical predictions by the Slab Method and Upper Bound technique, by following Equations 4.52, 4.54 and 4.65. The curves by the Slab Method are plotted at various friction coefficients (μ) between tool and material (0, 0.2, 0.3, 0.4, 0.577); while results by the Upper Bound are

represented at different friction factors (m) at the contact surfaces (0, 0.2, 0.5, 0.8, 1). Results by the slab analysis are shown to be close to experimental distributions for about 70% of the total stroke; however major differences are discovered at the beginning of the process, and at the end. On the other hand, the Upper Bound technique

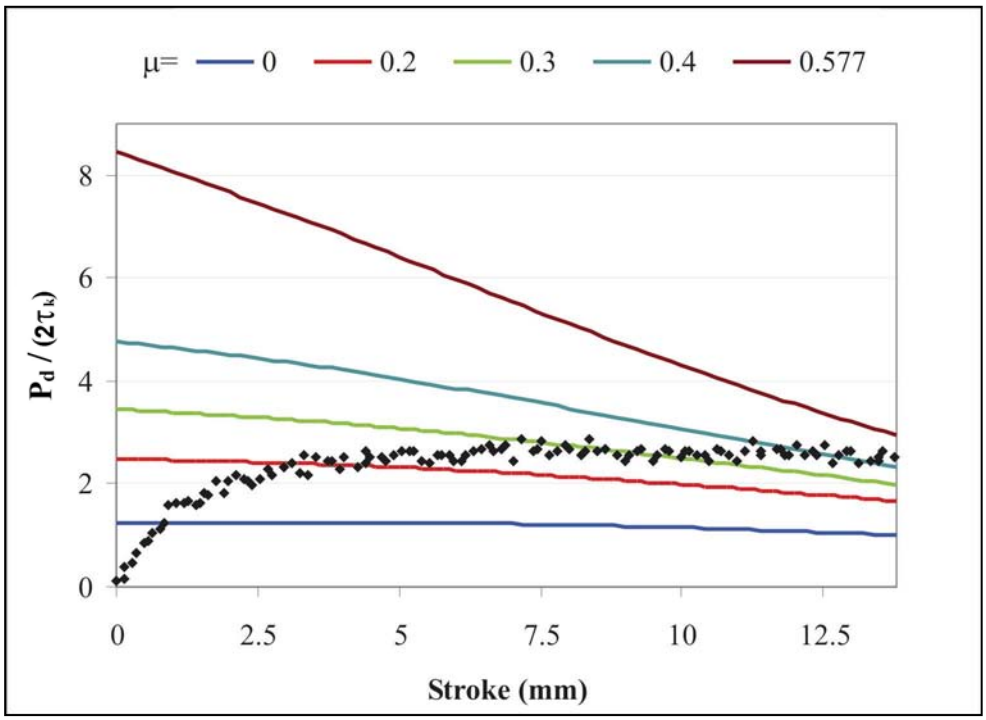

Figure 5.40 Experimental results with analytical distributions by the Slab Method

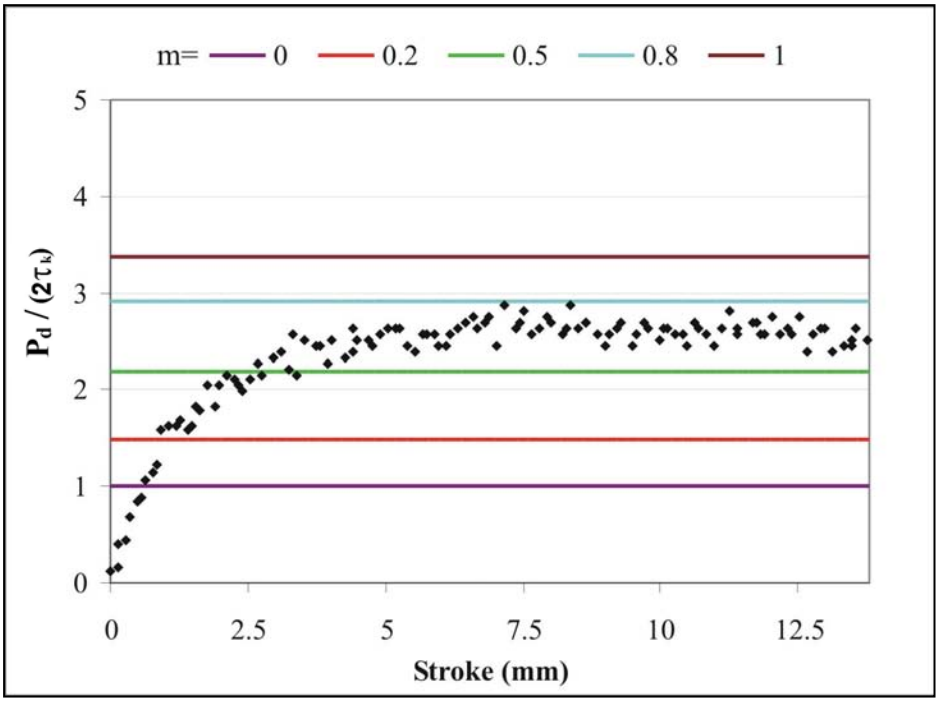

Figure 5.41 Experimental results with analytical distributions by the Upper Bound

provides constant values of forming pressure when vertical and horizontal channels are equal. The experimental results appear to exist between the two limits of friction in both solutions, i.e. $0 \le \mu \le 0.577$ and $0 \le m \le 1$. The results obtained from the Upper Bound technique included in Figure 5.41, show lower stresses when compared to the experimental values. Although the Upper Bound theory would be expected to give higher values [85], the reason for the lower results is most likely caused by the plastic deformation not being uniform in the experiment.

The sequence of Figures 5.42, 5.43 and 5.44 show an example of analytical and experimental energy absorption distributions for full stroke operations.

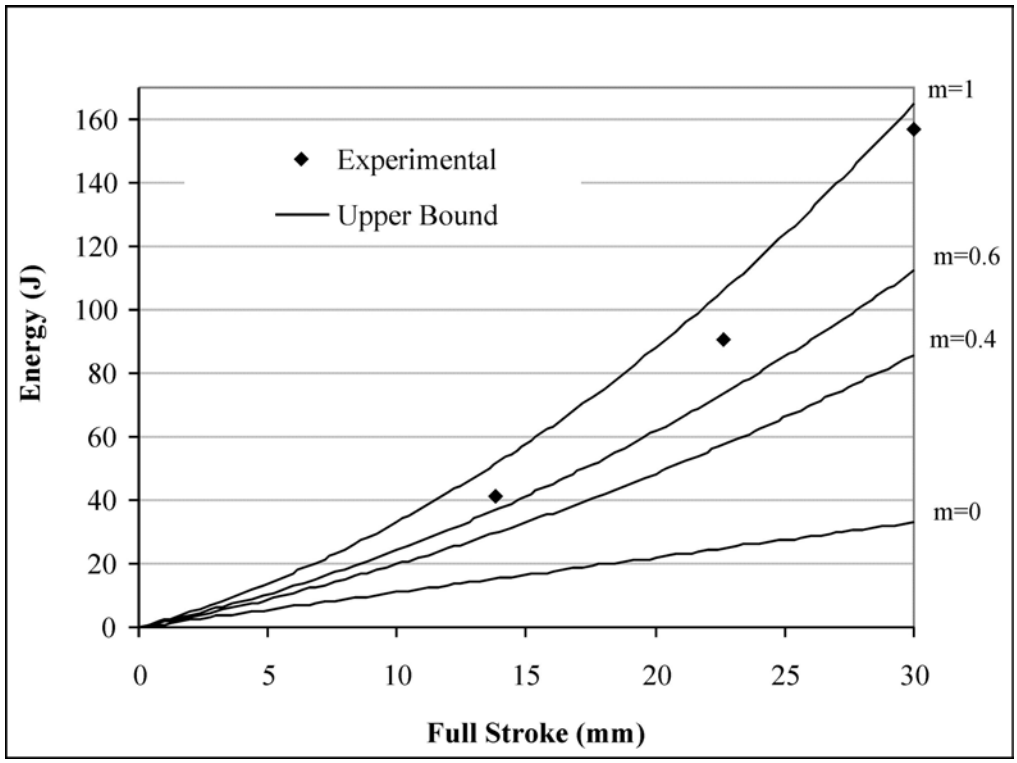

Figure 5.42 Analytical and experimental energy distributions for GR(10,10,42) full stroke with lead

Analytical results are based on the Upper Bound solution for different friction factors *m*. Experimental points, on the other hand, are calculated from the energy distributions in section 5.4.6. Theoretical and experimental results from the channel geometries in the figures are well in agreement, as experimental values exist within the lower and upper limit of the theoretical curves, given by *m*=0 and *m*=1.

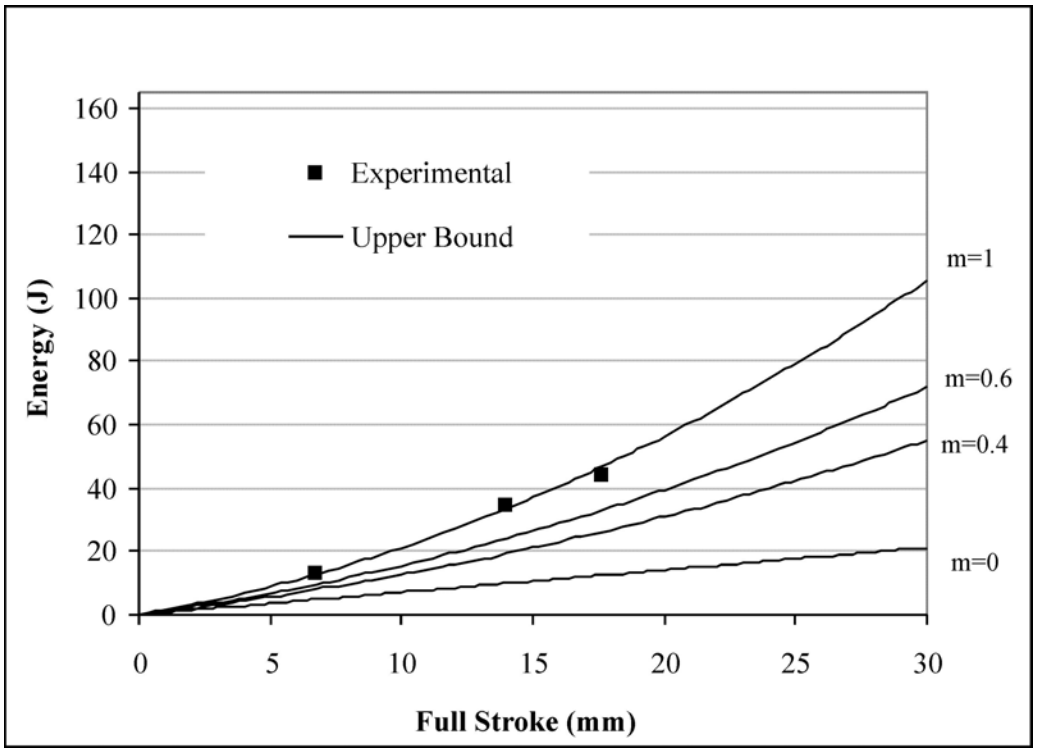

Figure 5.43 Analytical and experimental energy distributions for GR(8,8,21) full stroke with lead

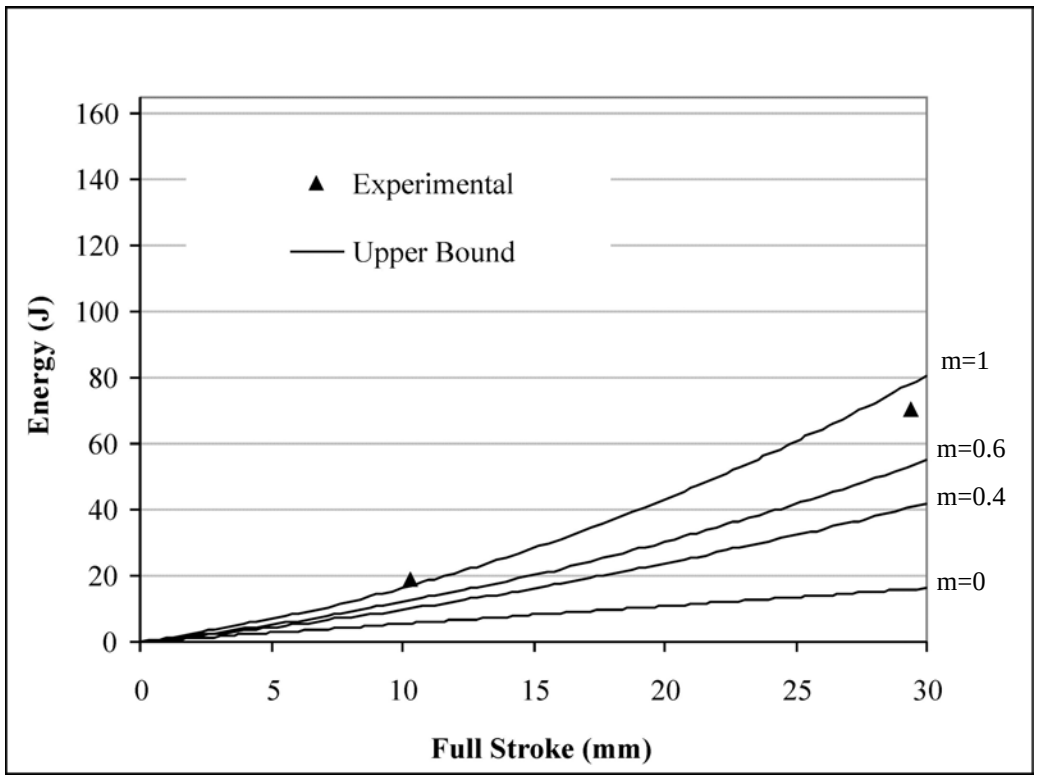

Figure 5.44 Theoretical and experimental energy distributions for GR(7,7,37.5) full stroke with lead

5.6 CONCLUSIONS

Upon loading the UREAD units, the force averages to a constant distribution after an initial increase. The average forming pressure results of the UREAD channels had shown a trend against the size of the channels and the length of the full stroke. Therefore, the channels cross sectional area (A) and stroke length (L) are critical parameters for the extrusion pressure. The experimental energy dissipation distributions are shown to be linear against the progression of the stroke.

The machining tolerance of channels and punches was shown to have some effect on the forming force and the performance of the units.

Analytical results by the Slab Method technique and the Upper Bound analysis gave good prediction of the average extrusion pressure and energy dissipation.

Chapter 6

SIDE CONTACT PRESSURE MEASUREMENTS ON 90^0 "UREAD" DEVICES

6.1 INTRODUCTION

During operations based on severe plastic deformation processes such as Channel Angular Extrusion (CAE), high stresses may develop at the contact surfaces between the pressing tool and the deforming material, therefore damages to the channels or tool failure may occur.

In this chapter, experimental measurements of normal stresses, which develop along the vertical channel during the forward extrusion process in UREAD devices, are presented and analysed. For this aim, special tools were designed in order to incorporate pressure sensors (Pressure Pins) inside the UREAD unit, and obtain stress distributions along the channel wall.

Measurements of contact stresses in metalforming processes are complex to investigate. In fact, stresses that develop at the boundary between forming tools and material being deformed, have a large influence on the quality of the final product and play an important role on the prediction of tool behaviour and tool life. Several experimental methods and techniques have been developed over the last 70 years, all aimed at measuring tool contact stresses during different forming processes. In the early 1950s, Orowan [101] developed the photoelastic pressure sensor, which gave information on the level of pressure at the contact surface. Such a device is shown in Figure 6.1, and it comprises a conical part (pin) which is linked to a pressure sensing element and a photo-sensor to detect changes in a light pattern that gives a measure of the pressure

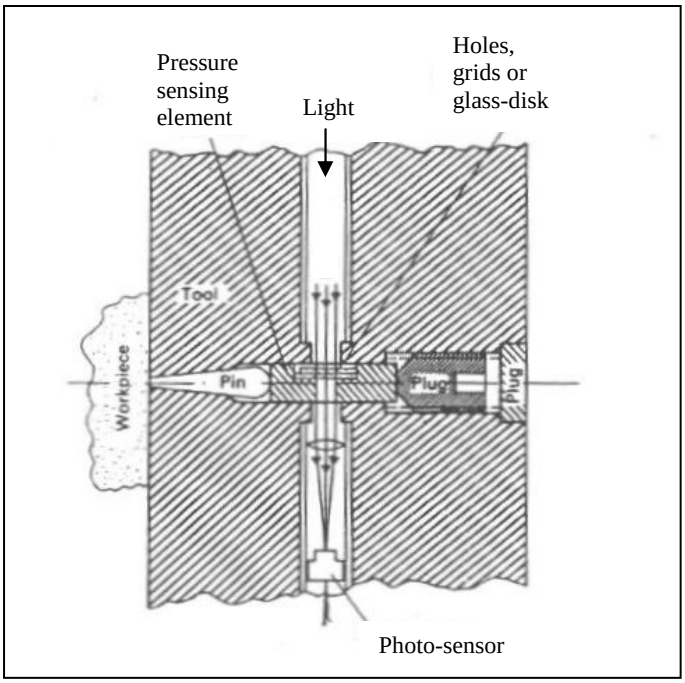

Figure 6.1 The photo-elastic pressure sensor [101]

acting on the pin. Pressure sensitive colour films [102] were used in similar ways, in that a film is positioned between the workpiece surface and tool surface where the colour density of the film varies with the applied pressure. For such a method the film

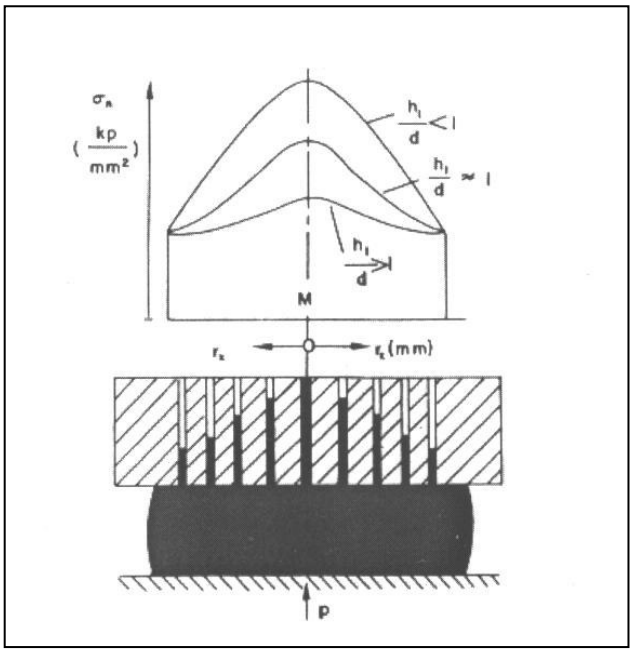

Figure 6.2 Die with orifices to measure contact pressure [104]

can be designed to measure pressures in the range of 60 to 160 MPa, and only provides readings on the maximum levels attained during the forming process. Information on the pressure level acting on the contact surface may be obtained by the employment of the split tools technique [103]. In this method, strain gauges are attached to the vertical interface of the split dies, and away from the actual contact surface. Another experimental method to measure contact stresses was developed by Vater and Nebe [104], in which thin holes (orifices) were machined in the tool as shown in Figure 6.2. Contact stresses are then related to the amount of workpiece material that is forced into the holes.

The Pressure Pin technique [103] was also developed. In this method, a pressure sensor, shown in Figure 6.3, is fitted within the tool at correspondence of the contact surface. A real time recording of contact stresses was achieved through a calibrated strain gauge circuit mounted on the pin. This technique can be applied to several manufacturing processes, and its response is most reliable. Many researchers have used the sensitive pressure pin technique, as a means to measuring the frictional stress distributions in a

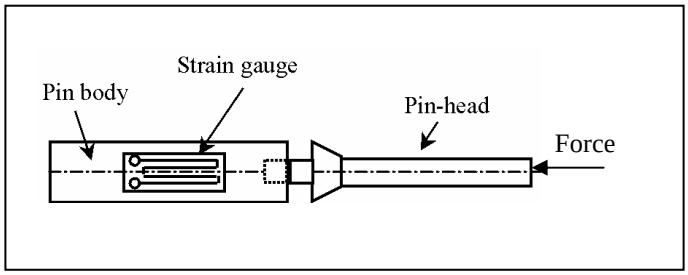

Figure 6.3 Pressure Pin construction

hostile environments, such as interfaces in metal forming processes. It has been widely, applied to contact stresses measurements during various processes such extrusion [105] rolling [106] and forging of axi-symmetrical components [107].

6.2 SENSITIVITY OF PRESSURE PIN POSITION

The position of the pressure sensor relative to the moving material in the pressure pin technique is a critical parameter and strongly linked to the measurements repeatability

and reliability. Figure 6.4[108] shows the possible positions of the pin-head in relation to the interface. It can be positioned flush with the contact surface, as in the case of Figure 6.4 (a) and (d), or below and above the interface, as in Figure 6.4 (b), (c), (e) and (f). In addition, the side gap between the pin-head and the tool side is important. It could invalidate the readings, as the pin-head may get trapped by the material being deformed, as shown in Figures 6.4 (d), (e) and (f). In all cases shown in Figure 6.4 the state of contact between the pin and the deforming material changes throughout the forming process.

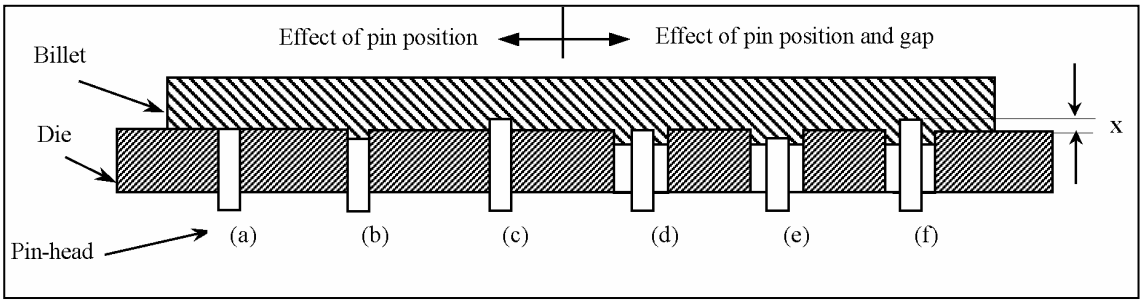

Figure 6.4 Pin position and sliding gap relative to tool surface [108]

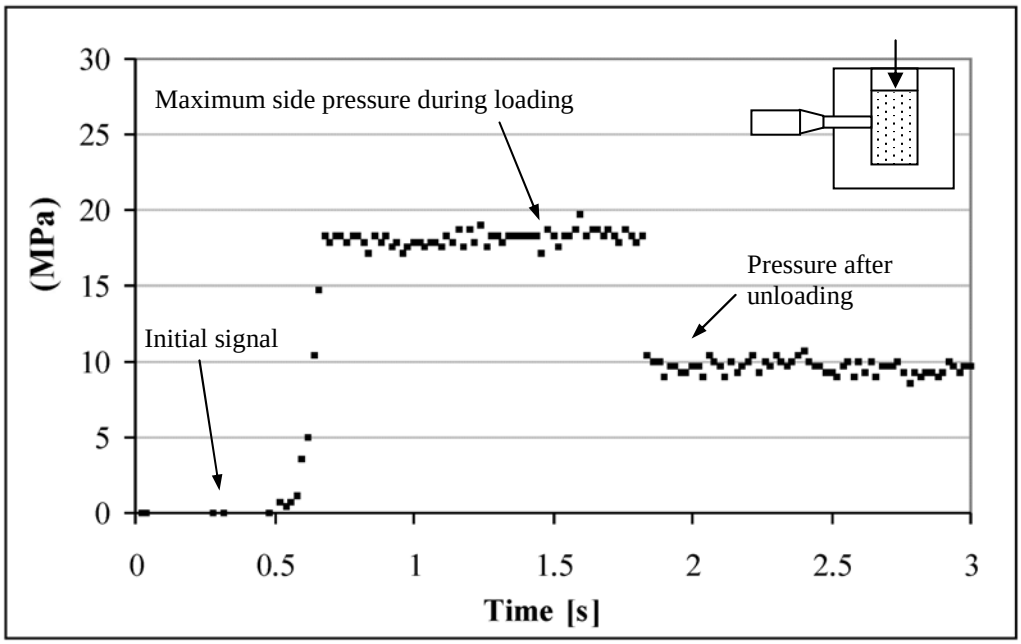

Figure 6.5 Signal by a flush pin for side pressure measurements in closed compression

A tangible example is given by the results in Figure 6.5, where the condition in Figure 6.4 (d) was experimentally reproduced. For this test, a tool with a cylindrical hole of 15mm diameter was produced in tool steel with a side through hole for a pin-head.

A pressure pin was fitted at the side on the tool and a billet was inserted and compressed into the cavity. Figure 6.5 gives the signal trace from the pressure pin before, during and after the compression. When the load is released, the signal given by the pin does not go back to its initial configuration, because the pin-head was trapped in the tool by the material extruding through the large pin-head hole. Such penetration of material is not controllable, and it heavily affects the experimental measurements in terms of repeatability and reliability.

A new strategy for pin design was employed and developed by Lupoi and Osman [108,109], which employ pressure pins concealed within the tool, that are located below the contact surface, at a vertical gap distance form it. Such arrangement provides the advantage of fitting pressure sensors not directly exposed to the severe conditions at the contact surface. Investigations were carried out in order to study the effect of the gap on the pressure measurements. Figure 6.6 shows the pressure readings from a pin, when positioned at various gaps from the contact surface; 1mm, 2mm, 3mm and 4mm. The contact surface was loaded by a constant pressure of 18.7 MPa. A flat forming tool with four holes was used in this experiment. Results clearly show that the readings by the pin load cell reduces as the gap increases. Therefore, experimental readings with small gaps are more sensitive and provide highly accurate readings of the contact pressure.

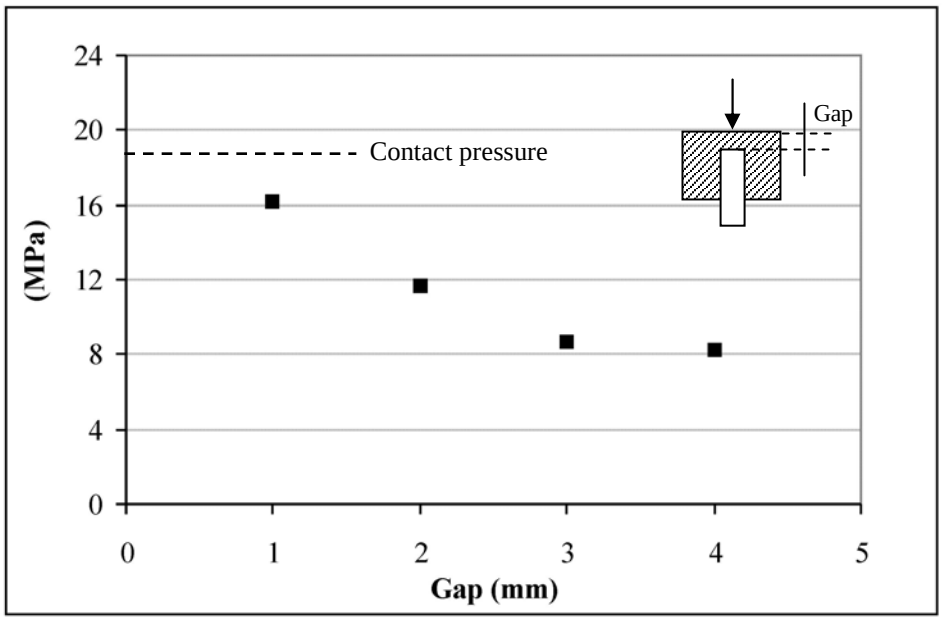

Figure 6.6 Experimental normal pressure distribution within a flat tool

Figure 6.7 and Figure 6.8 show experimental results, from two of the authors publications [108,109] using the concealed pressure pin technique. It was applied for the measurement of contact stresses during compression of cylindrical aluminium billets of 25mm diameter and 30mm height; and aluminium rings with initial inner diameter, outer diameter, height of 13mm, 25mm, 9mm respectively. The pressure pins were fitted within the tools with a gap of 1mm from the contact surface.

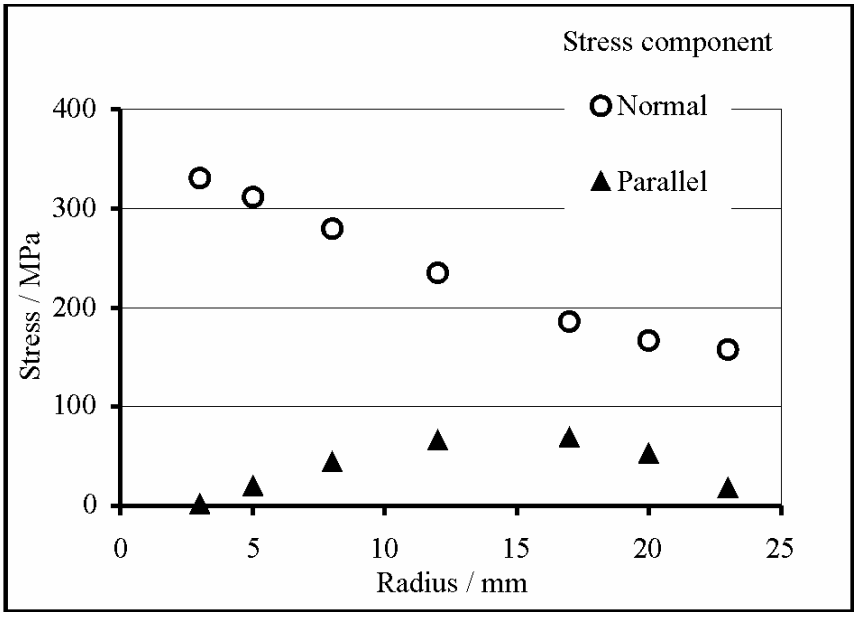

Figure 6.7 Experimental results by concealed pressure pins on cylindrical billet compression [108]

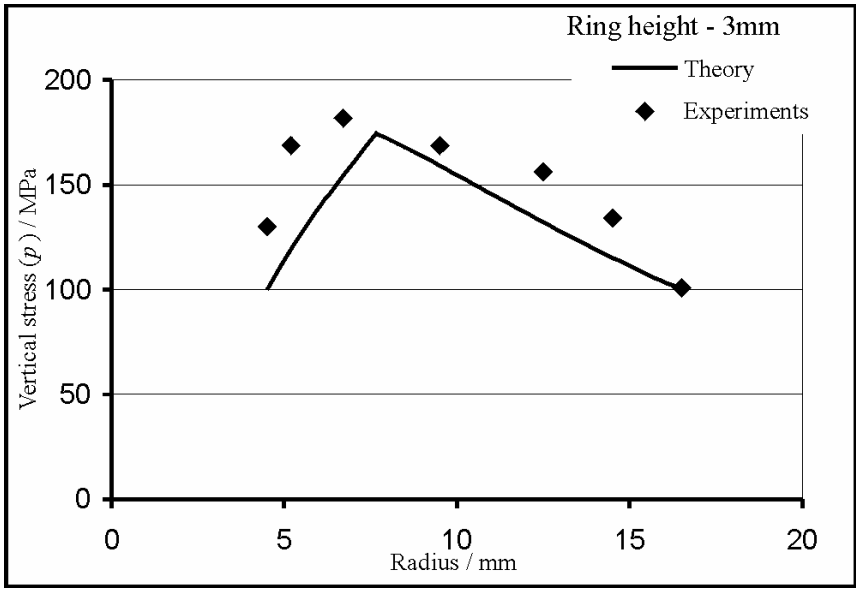

Figure 6.8 Experimental results by concealed pressure pins on ring compression [109]

6.3 SIDE PRESSURE MEASURING DEVICES

An experimental procedure has been built to measure the level and distribution of side contact pressure, which develops on the channels boundary interface during Equal Channel Angular Extrusion (ECAE) process. The concealed pressure pin technique is employed for this activity, and a set of pressure pins was designed and assembled into a new UREAD device.

Measuring the pressure exerted at various locations of contact surfaces requires a flexible tooling arrangement; a device that contains the ECAE channels and a structure to hold the sensitive pressure pins. Figure 6.9 shows a picture of a fully assembled Side Pressure Measuring Device (SPMD). Two intersecting channels at 90^0 are machined inside the device structure, and three concealed pressure pins are accommodated along the side of the vertical channel. They are kept in position by a holder and three locking nuts. All pressure pin heads were concealed inside the device structure with a 1mm gap (see Figure 6.6).

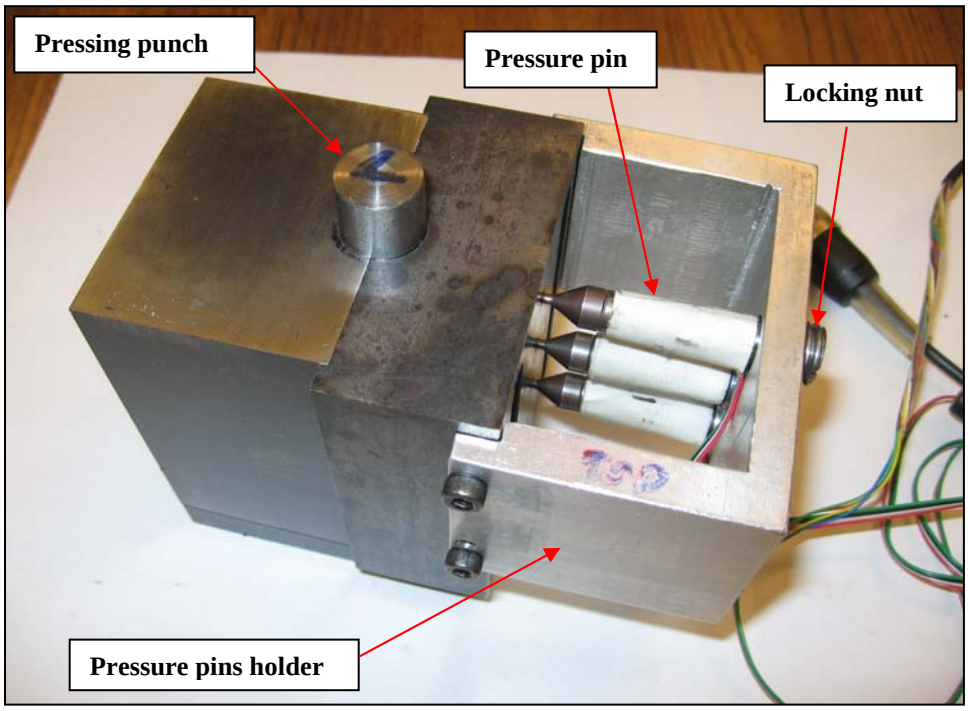

Figure 6.9 The SPMD device with sensitive pressure pins

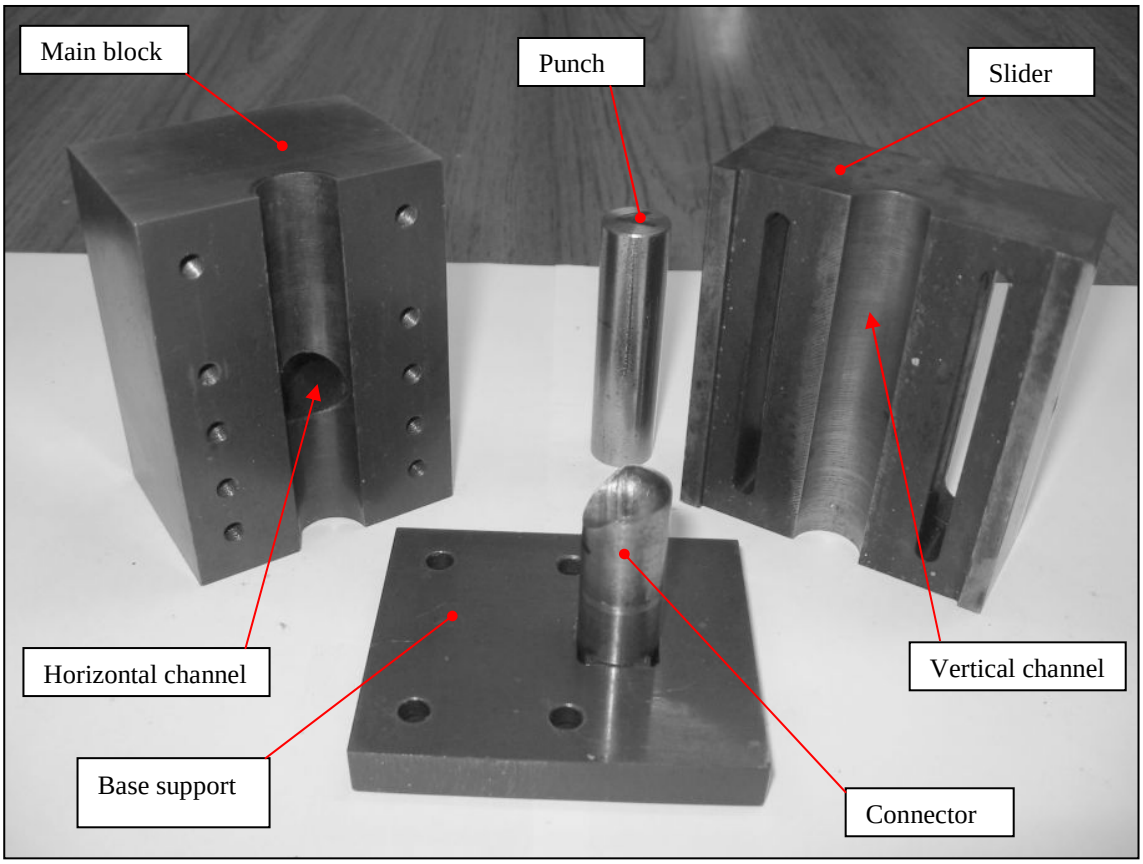

Figure 6.10 The Side Pressure Measuring Device (SPMD) with circular cross sectional channels

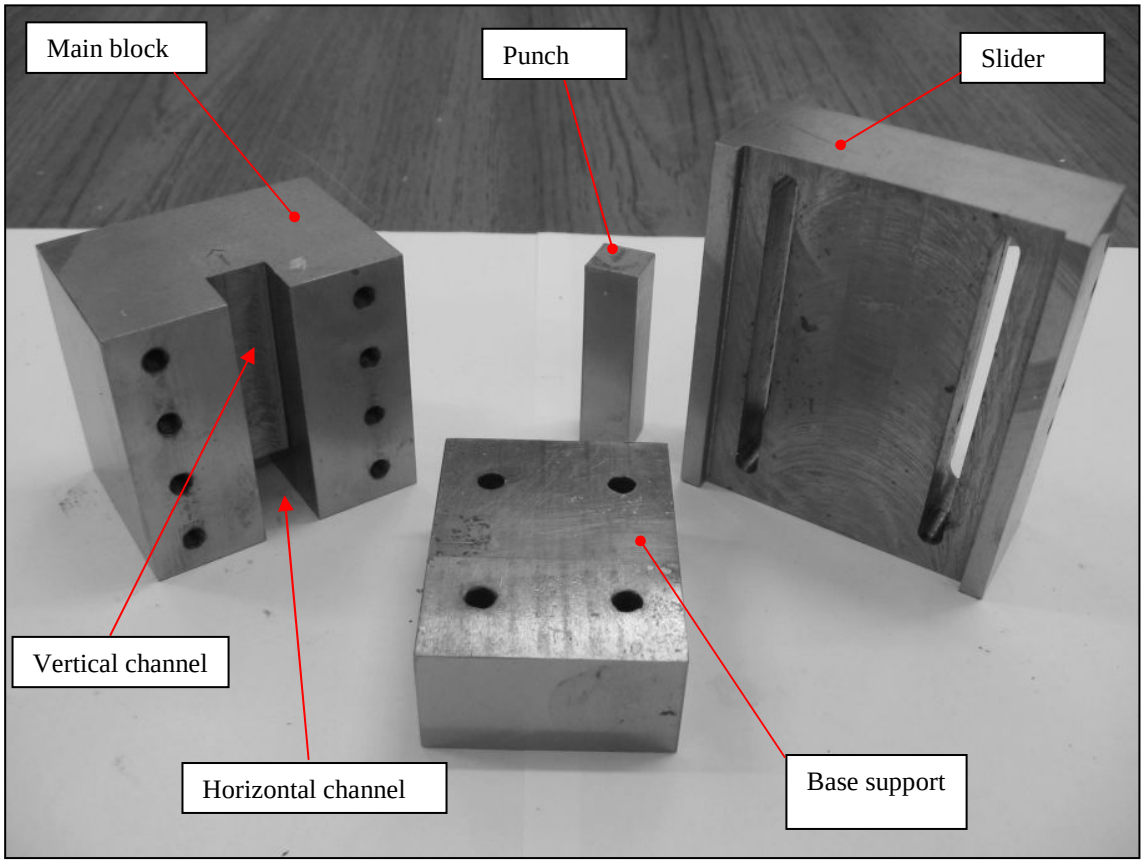

Figure 6.11 The Side Pressure Measuring Device (SPMD) with square cross sectional channels

Figure 6.10 shows the exploded assembly of the Side Pressure Measuring Device (SPMD) given in Figure 6.9. The assembly forms two channels with a circular cross section intersecting together at 90^0. The horizontal channel is machined in the main block; while the vertical channel (pushing channel) is machined in a split tool; two halves, one is in the main block and one in the slider. The slider is attached to the main block, and locked in any required position. Such arrangement gives the advantage of being able to measure the side pressure at many vertical locations. A connector is used to form the 90^0 intersection between the vertical and horizontal channels. Finally, a cylindrical punch is used to force the material through the channels. The main components of the SPMD are manufactured from H13 tool steel and heat-treated, while the punches and connectors are made out of commercial Silver Steel.
Two complete SPMD units with circular cross section channels were produced, with 15mm and 12mm diameter respectively.

A SPMD device was also designed to incorporate square cross sectional channels of 12x12mm, and it is shown in Figure 6.11. For such a geometry, both horizontal and vertical channels are machined in the main block, therefore the slider element and connector can be designed to have flat internal surfaces.

Detailed drawings of the circular and rectangular SMPD devices are given in the Appendix (E).

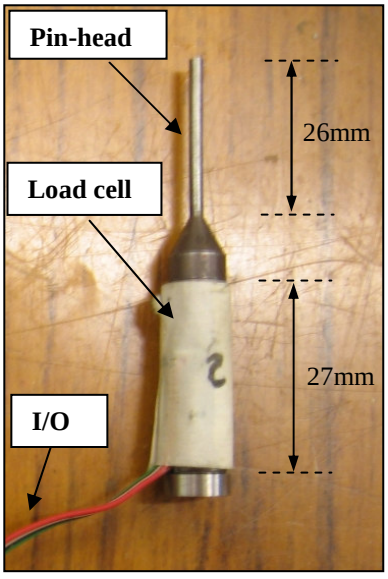

Figure 6.12 The Pressure Pin design

Figure 6.12 shows the design of the manufactured pressure pin. It is made out of H13 tool steel, and it comprises a pin-head and a cylindrical load cell. The load cell measured 8mm in diameter and 27mm in height; while the pin-head diameter is 2mm and its height is 26mm. The pressure pin circuit is equipped with an I/O connection plug. The load cell on the pressure pins were calibrated using an INSTRON testing machine, and connected to the data acquisition system described in section 5.2.

6.4 SIDE PRESSURE RESULTS

6.4.1 SPMD devices with circular cross sections

The experimental procedure used in these experiments was similar to those carried out with the UREAD devices, described in section 5.4. A number of operations were performed using lead, with the pressure sensors positioned at different locations along the vertical channel. A sketch of the SPMD is shown in Figure 6.13 and 6.14, where L is the full stroke length, F_d is the forming load and D is the channel diameter. The position of the pressure pin in each test is identified by the distance s.

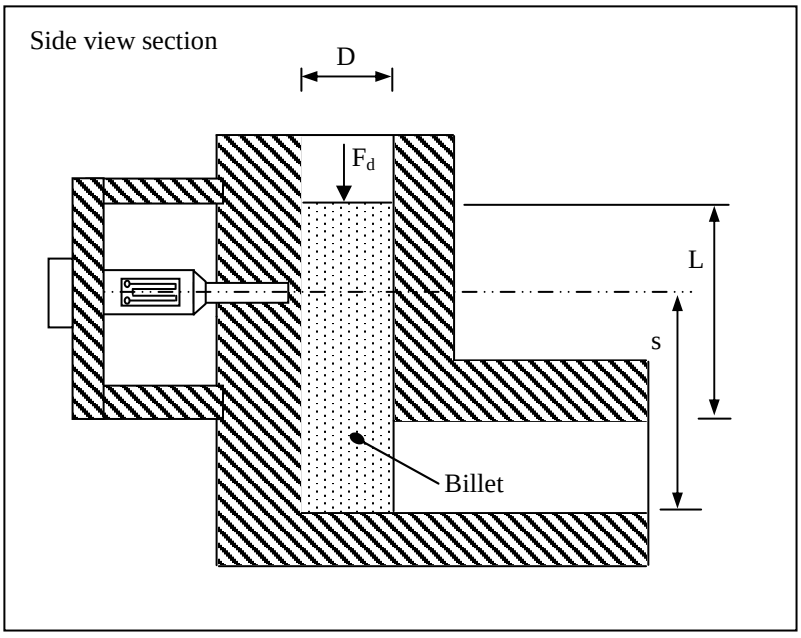

Figure 6.13 Sketch of the Side Pressure Measuring Device (side view section)

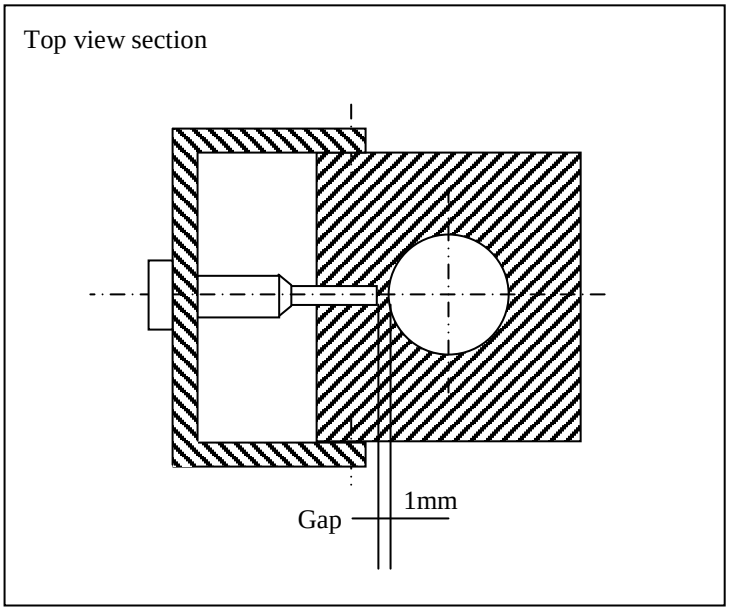

Figure 6.14 Sketch of the Side Pressure Measuring Device (top view section)

Figure 6.15, 6.16 6.17 and 6.18 show the experimental results by the SPMD with a diameter *D* of 15mm. A full stroke *L* of 26.5mm was performed, and readings from the pressure pins positioned at different locations *s* are plotted in the figure, against the progression of the punch stroke. The force readings by the pins load cells were converted into the correspondent pressure p_c acting on the pin-head. The pressure

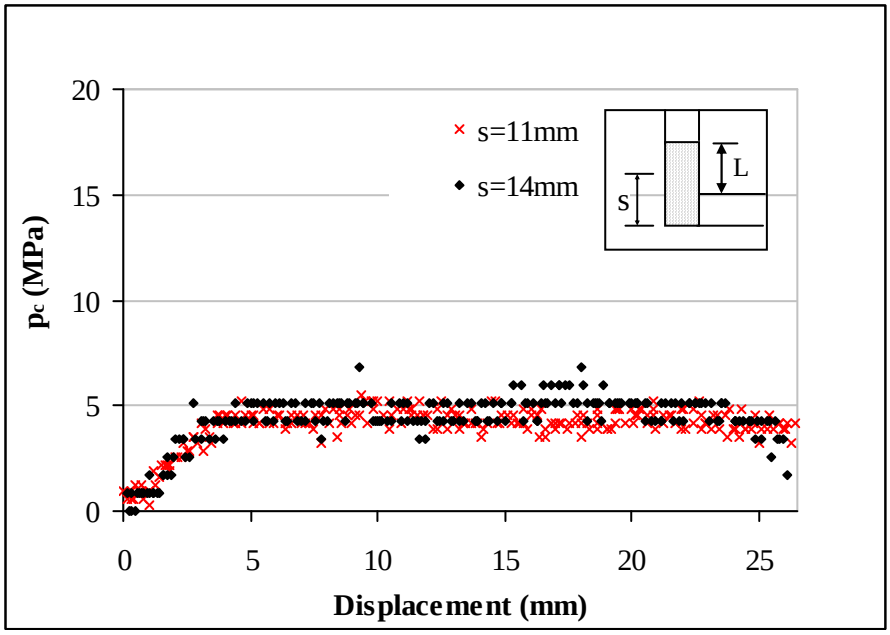

Figure 6.15 Experimental results by the SPMD with D=15mm, L=26.5mm

increases at the beginning of the process, then it averages to a constant trend before dropping. However, it is noted that the pressure signal drops more rapidly when the pressing punch crosses the pressure sensor position.

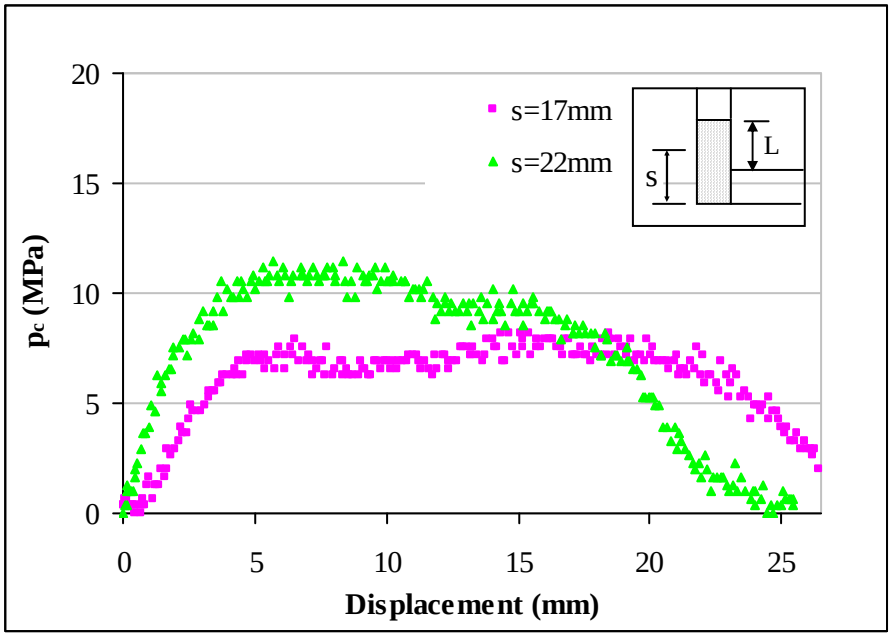

Figure 6.16 Experimental results by the SPMD with D=15mm, L=26.5mm

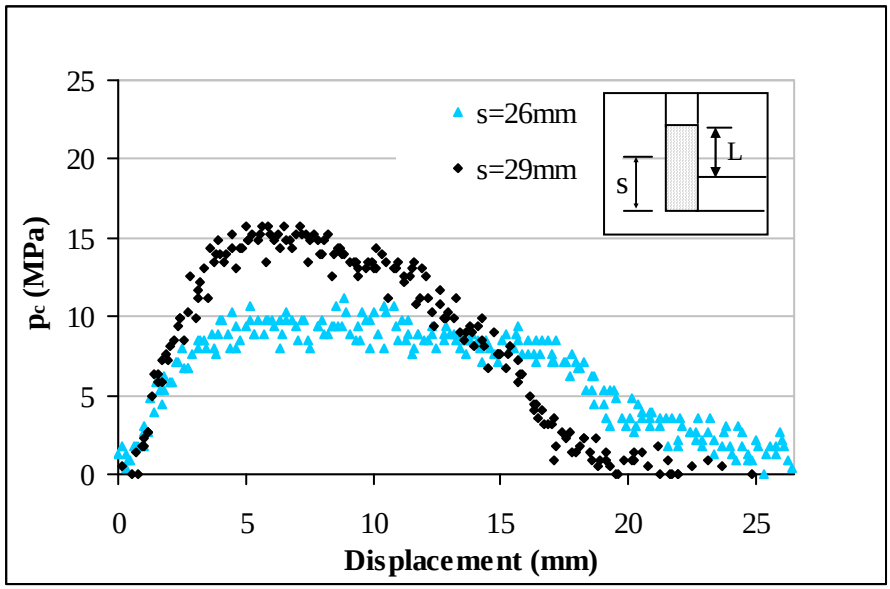

Figure 6.17 Forming load for the SPMD unit with D=15mm, L=26.5mm

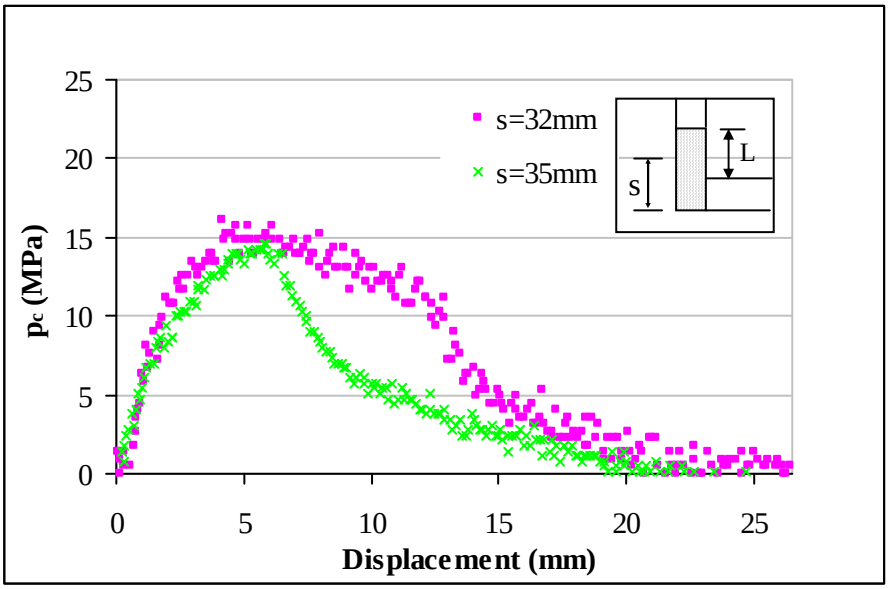

Figure 6.18 Experimental results by the SPMD with D=15mm, L=26.5mm

Figure 6.19, 6.20, 6.21 and 6.22 present side pressure results from the SPMD with circular channels of 15mm diameter, but with a full stroke of 17.3mm was used. The side pressure distributions exhibit the same characteristics to those with the longer stroke of 26.5mm.

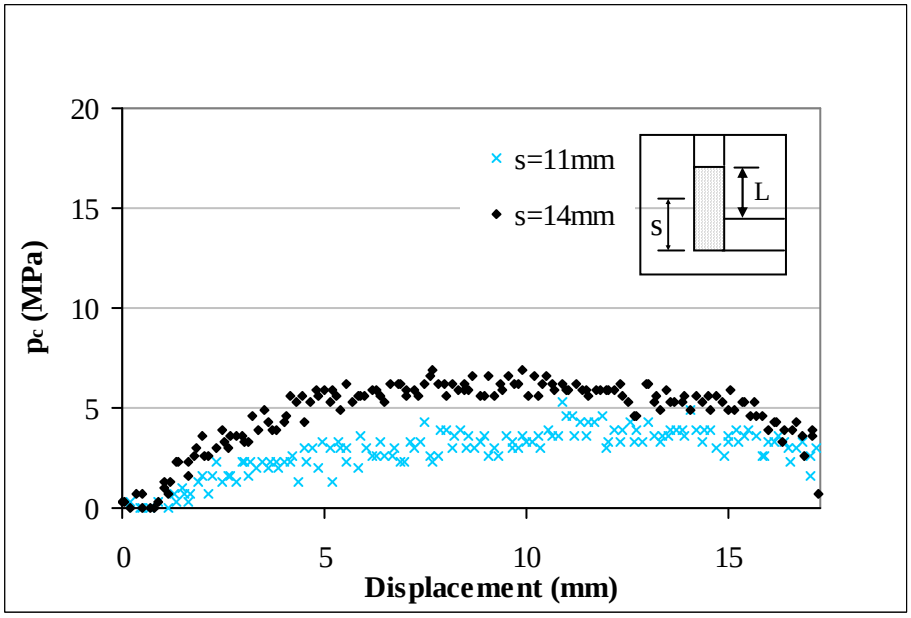

Figure 6.19 Experimental results by the SPMD with D=15mm, L=17.3mm

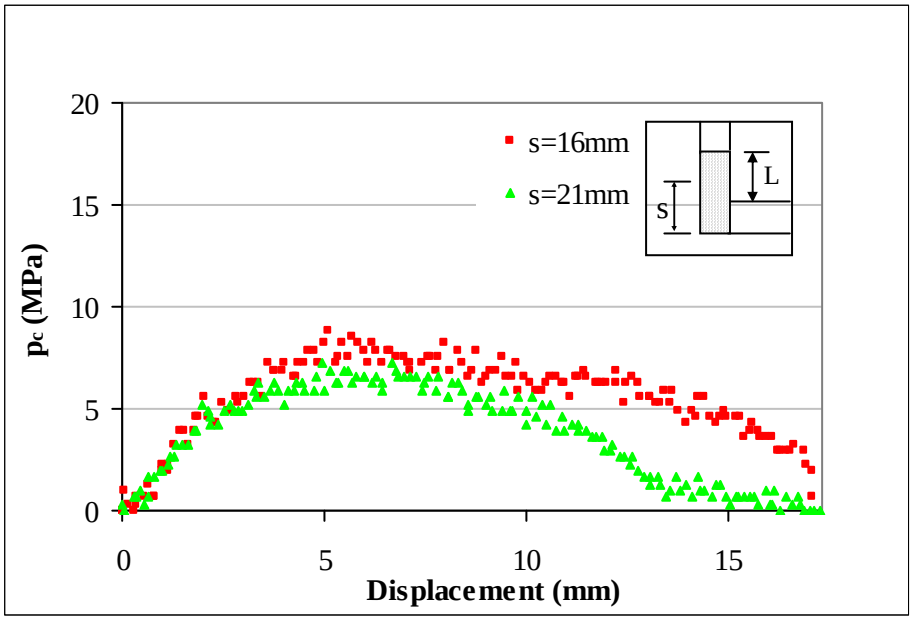

Figure 6.20 Experimental results by the SPMD with D=15mm, L=17.3mm

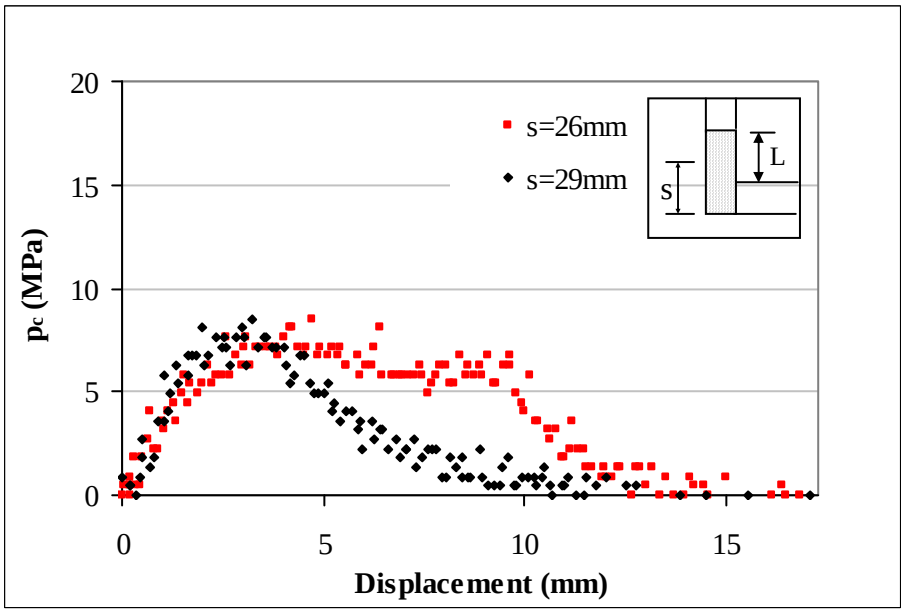

Figure 6.21 Experimental results by the SPMD with D=15mm, L17.3mm

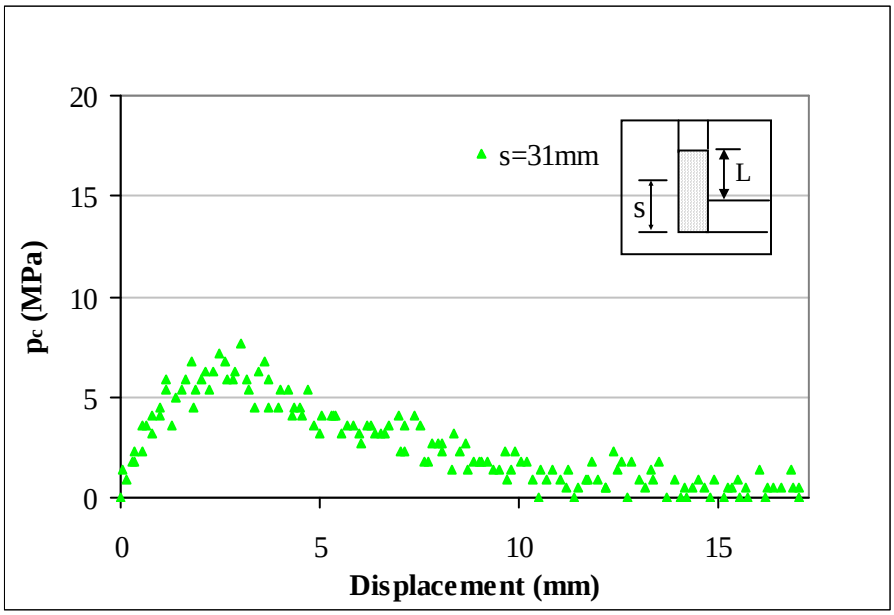

Figure 6.22 Experimental results by the SPMD D=15mm, L=17.3mm, s=31mm

Another set of experiments was undertaken using SPMD with a circular cross sectional area channels of 12mm diameter. Results are shown in Figure 6.23, 6.24, 6.25 and 6.26, with a full stroke of 31mm. Results are similar to the side pressure measured in the SPMD channel of 15mm diameter, however higher levels of pressure are measured and distributions are descendent after reaching a peak value.

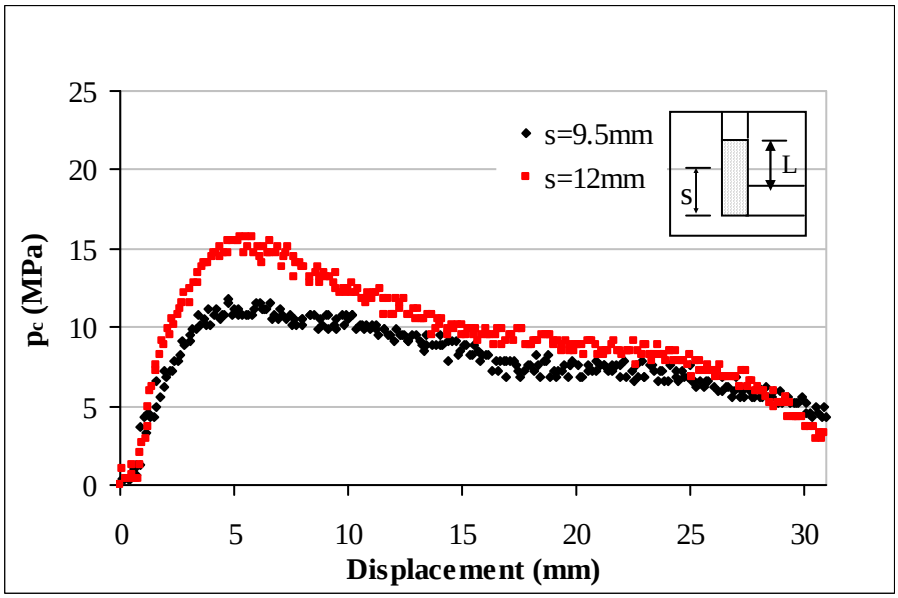

Figure 6.23 Experimental results by the SPMD with D=12mm, L=31mm

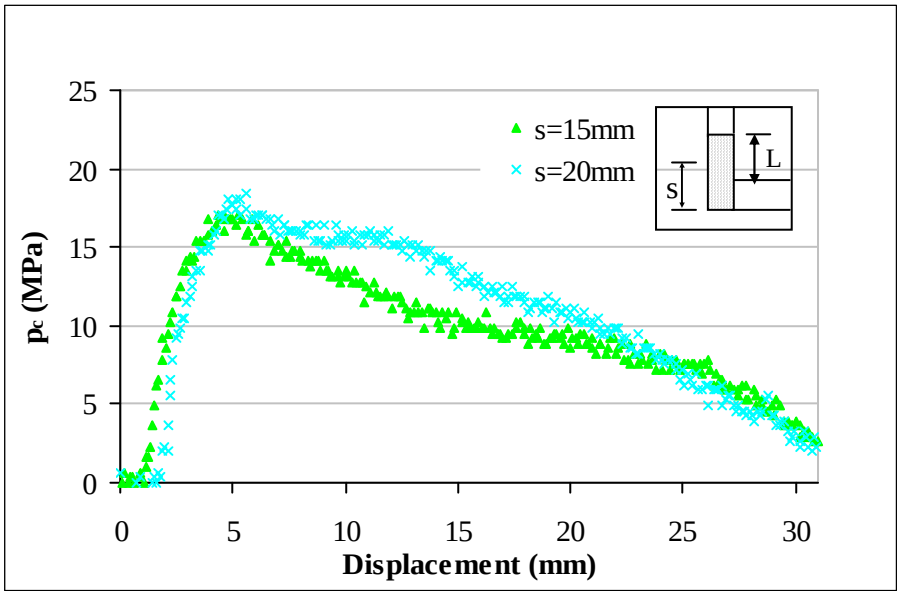

Figure 6.24 Experimental results by the SPMD with D=12mm, L=31mm

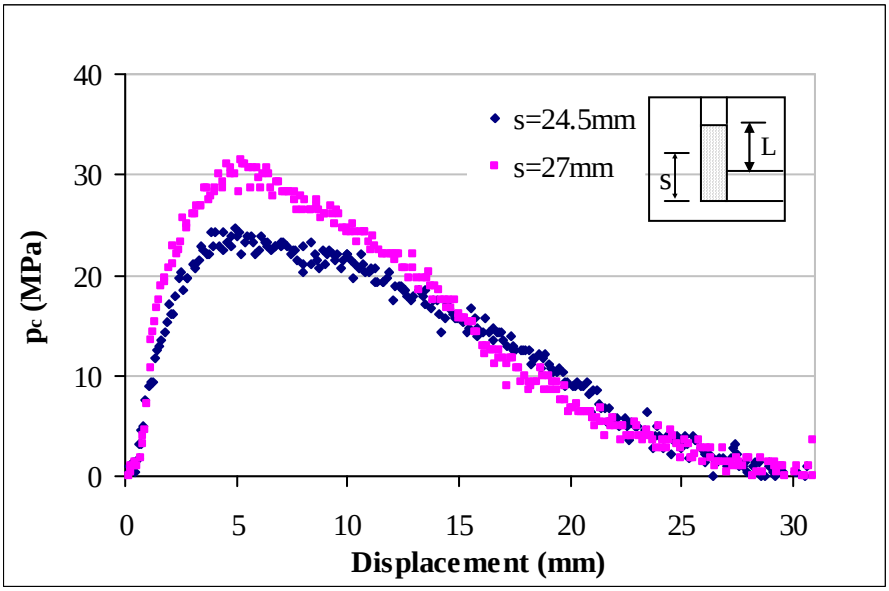

Figure 6.25 Experimental results by the SPMD with D=12mm, L=31mm

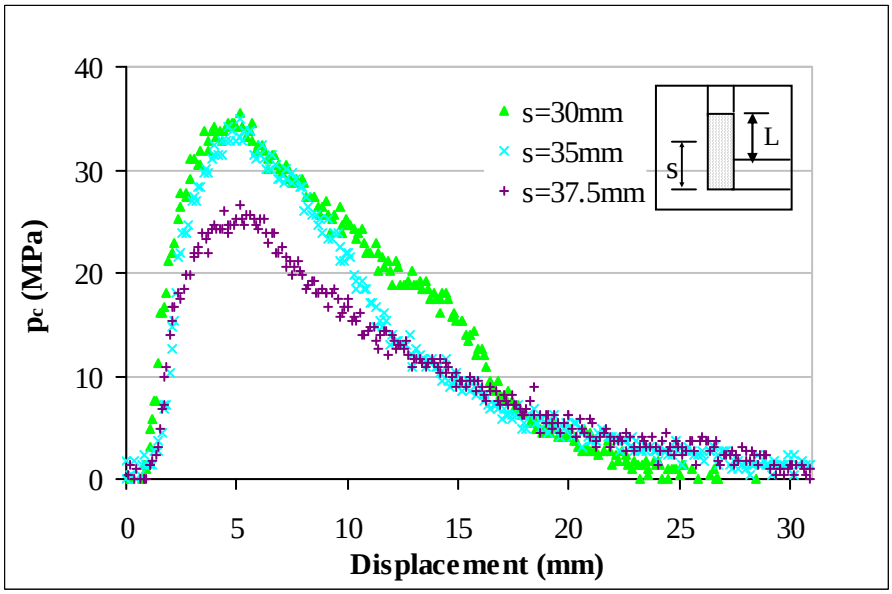

Figure 6.26 Experimental results by the SPMD with D=12mm, L=31mm

Figures from 6.27 to 6.30 show the side pressure experimental results using SPMD with 12mm diameter for a shorter full stroke of 18.2mm.

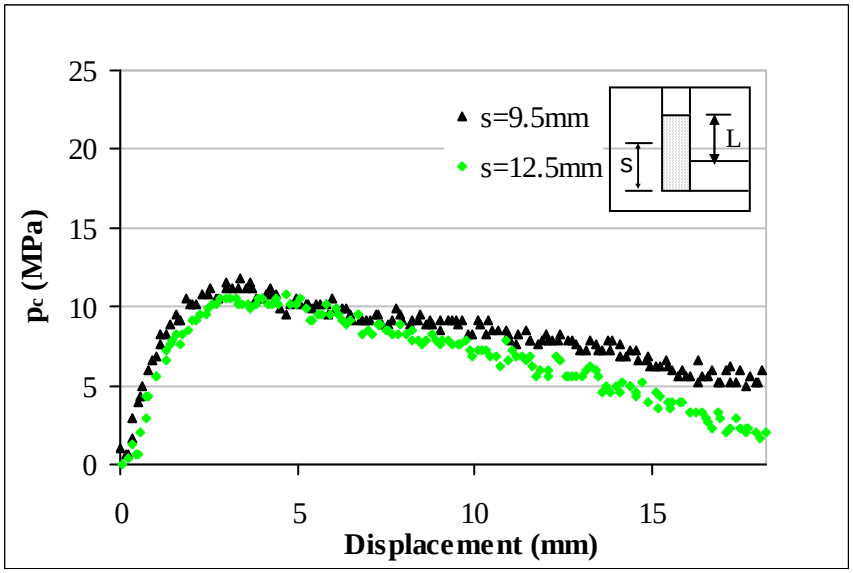

Figure 6.27 Experimental results by the SPMD with D=12mm, L=18.2mm, s=9.5mm and 12.5mm

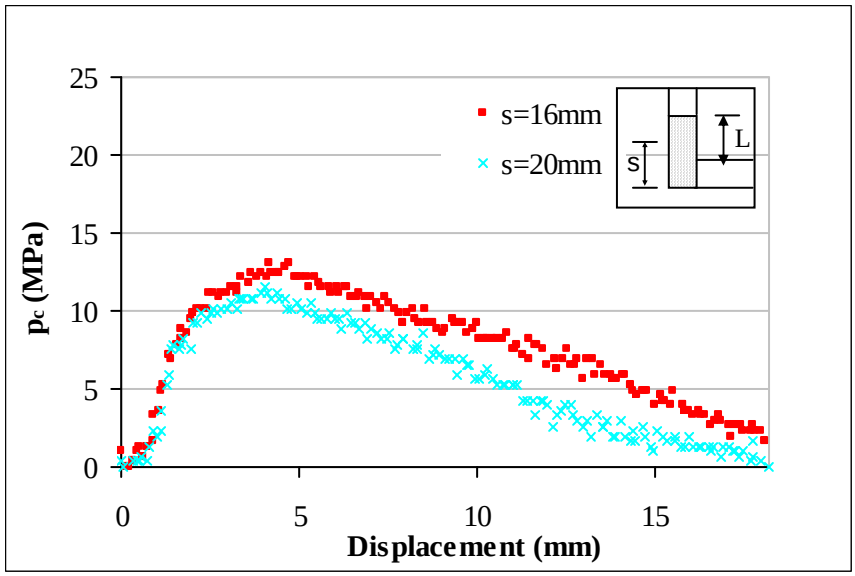

Figure 6.28 Experimental results by the SPMD with D=12mm, L=18.2mm

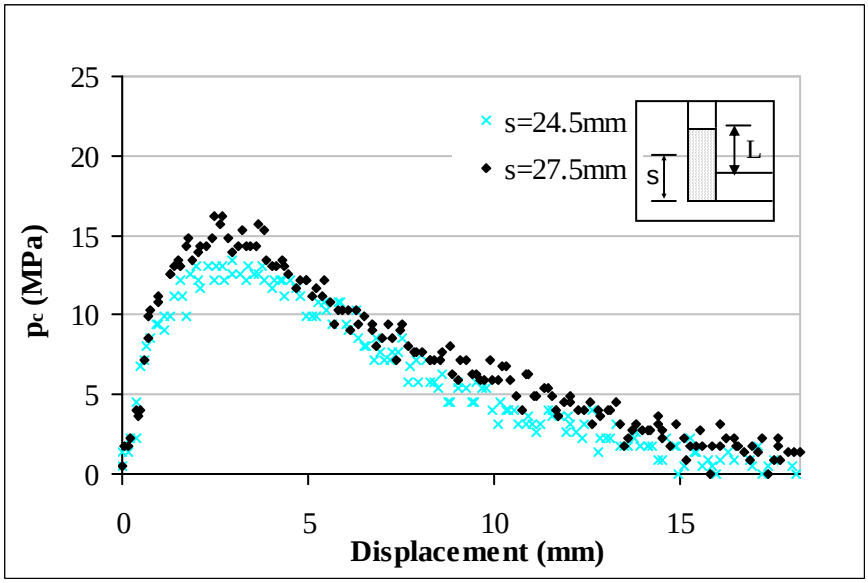

Figure 6.29 Experimental results by the SPMD with D=12mm, L=18.2mm

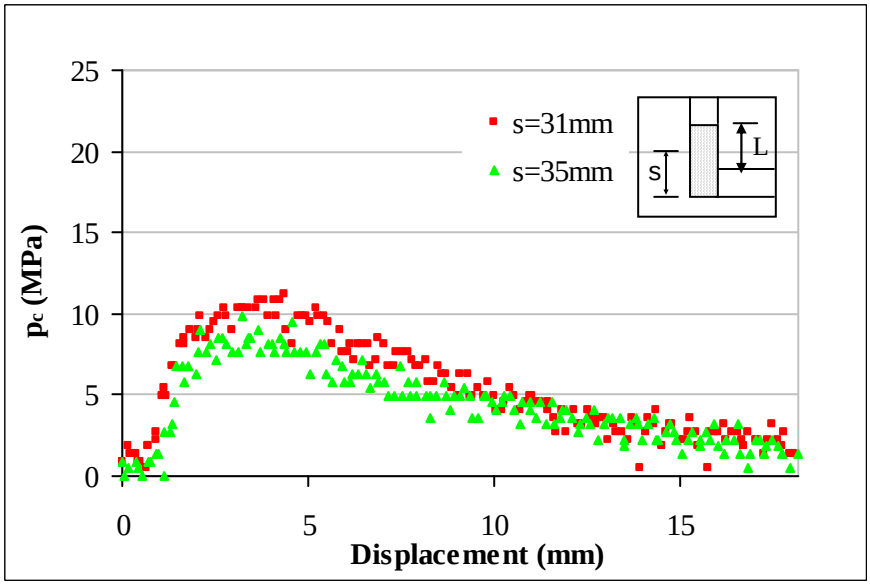

Figure 6.30 Experimental results by the SPMD with D=12mm, L=18.2mm, s=31mm and 35mm

Figures 6.31 and Figure 6.32 show the force against displacement curve for the 26.5mm and 17.3mm strokes respectively using a SPMD of 15mm diameter. Also, figures 6.33 and 6.34 shows the force behaviour of the 12mm diameter SPMD unit, for 31mm and 18.2mm strokes respectively. Distributions by the SPMD devices are characterized by the same trend as the UREAD devices, shown in sections 5.4.

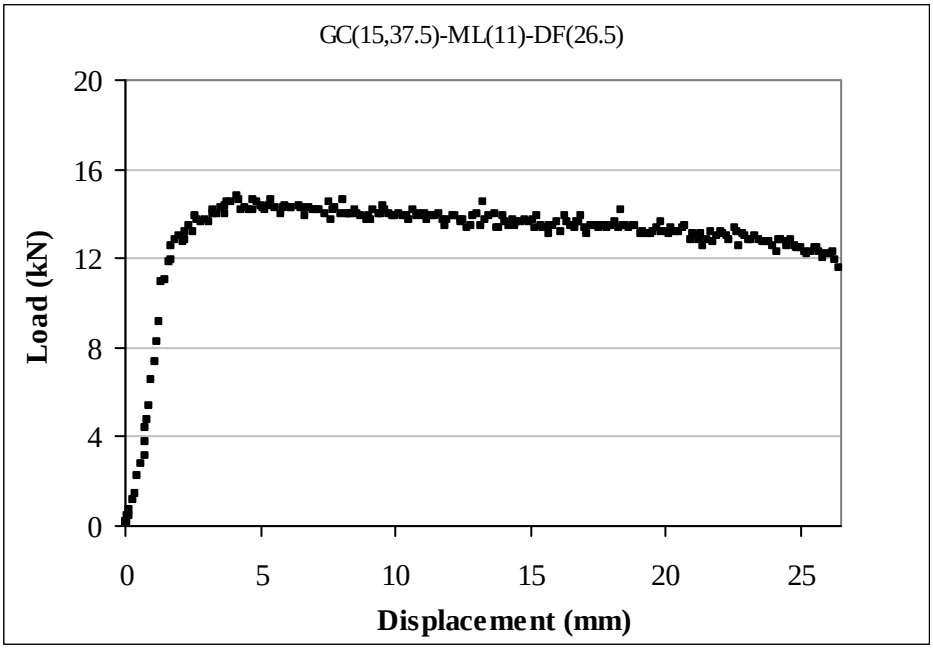

Figure 6.31 SPMD force behaviour against punch displacement, D=15mm and L=26.5mm

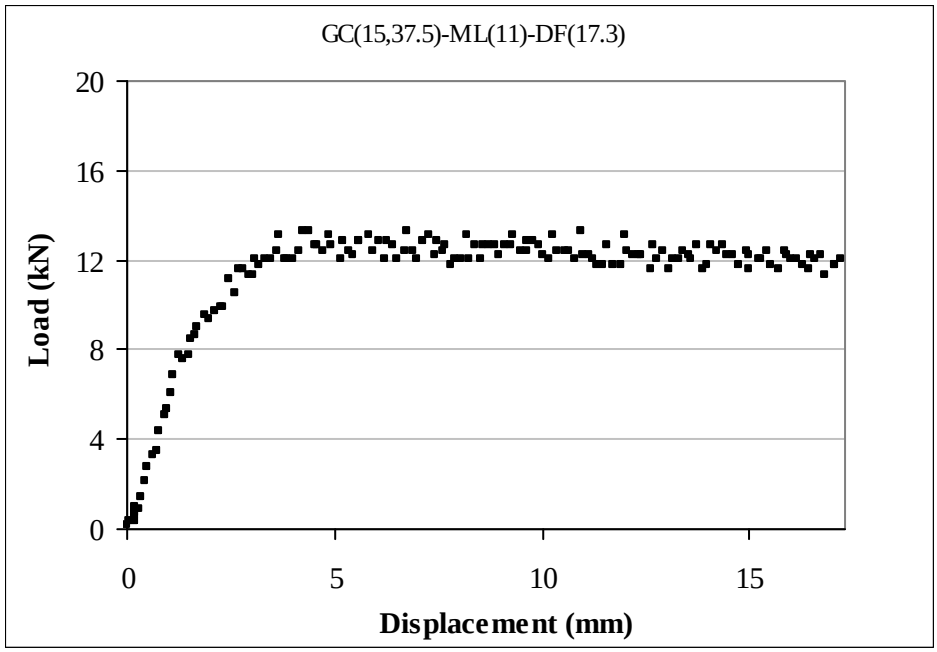

Figure 6.32 SPMD force behaviour against punch displacement, D=15mm and L=17.3mm

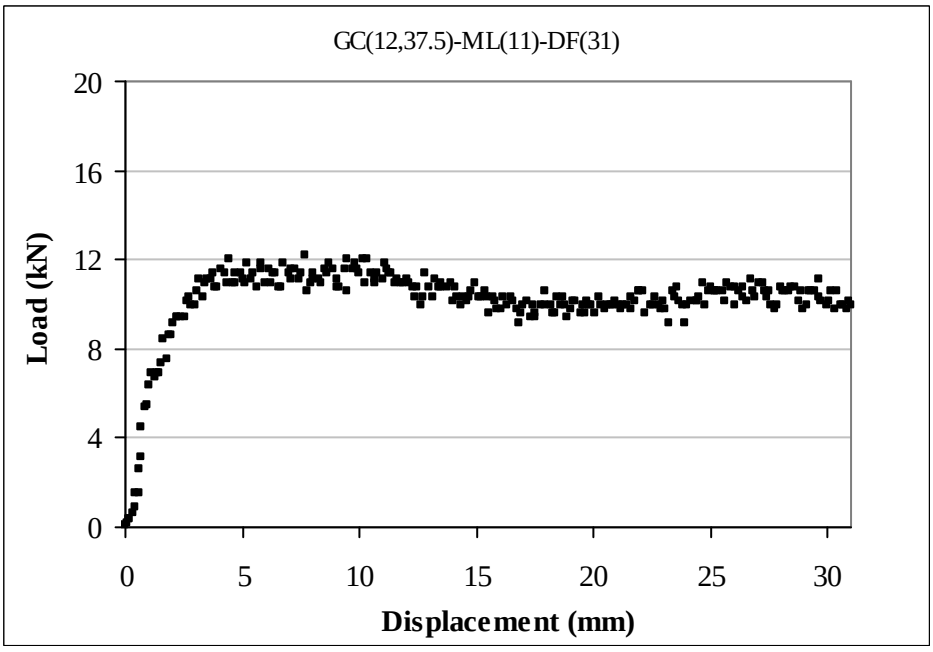

Figure 6.33 SPMD force behaviour against punch displacement, D=12mm and L=31mm

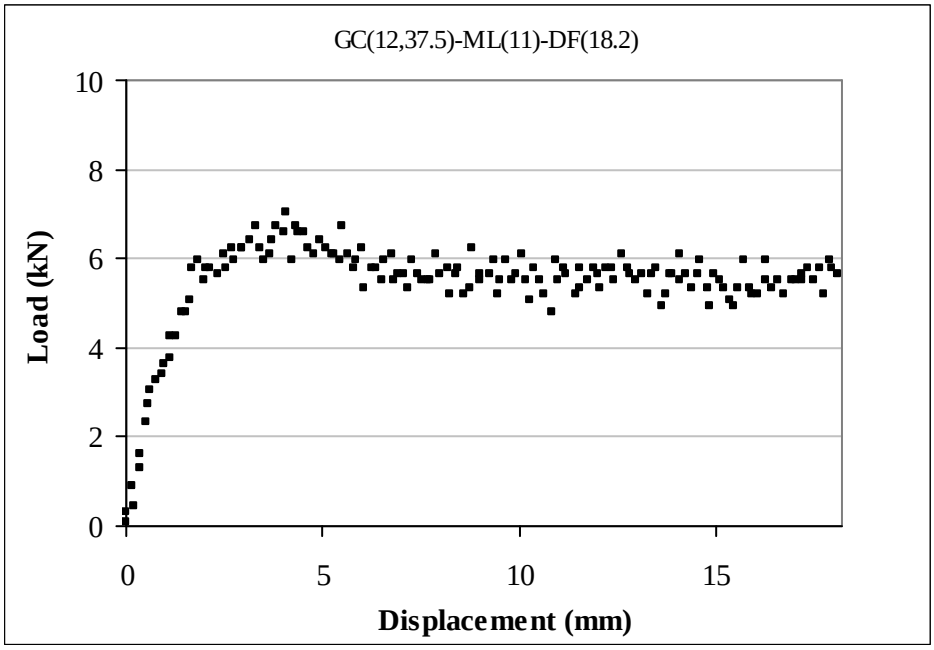

Figure 6.34 SPMD force behaviour against punch displacement, D=12mm and L=18.2mm

6.4.2 SPMD devices with square cross sections

Figure 6.35 and Figure 6.36 show the results obtained using the pressure pins, when positioned at different locations *s*, with the SPMD tool with a square cross sectional area (12x12mm). The full stroke was 24.3mm. The pattern of the pressure distributions is similar to previous tests, where it increases at the beginning of the process to a maximum value; after which a descendent trend occurs. Figure 6.37 shows the forming force against punch stroke.

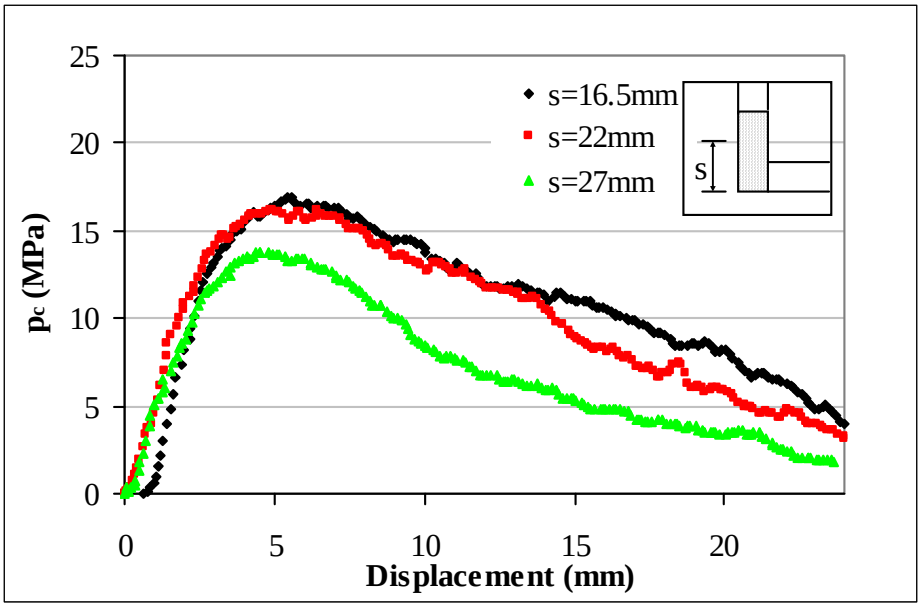

Figure 6.35 Experimental results by the SPMD with 12x12mm, L=24.3mm

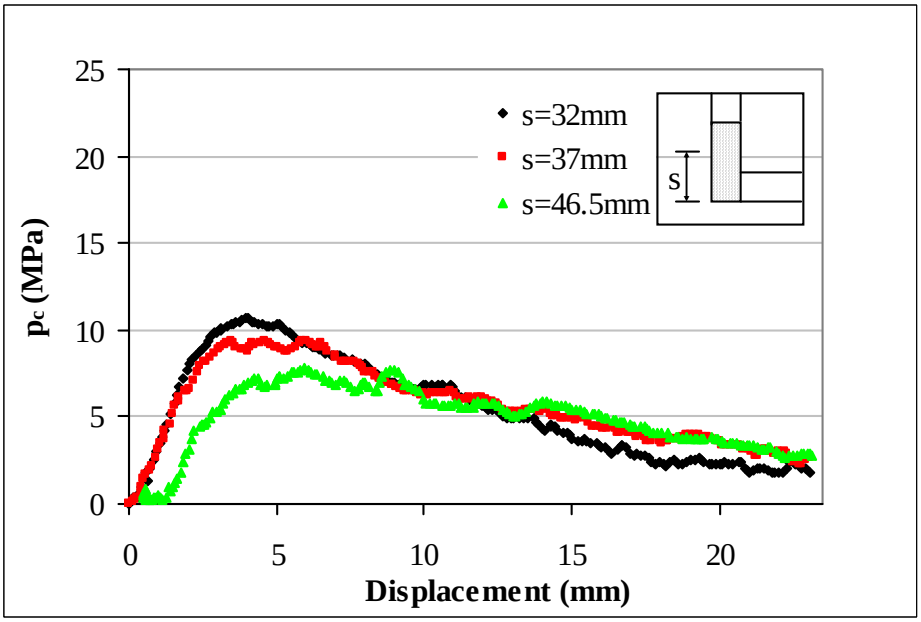

Figure 6.36 Experimental results by the SPMD with 12x12mm, L=24.3mm

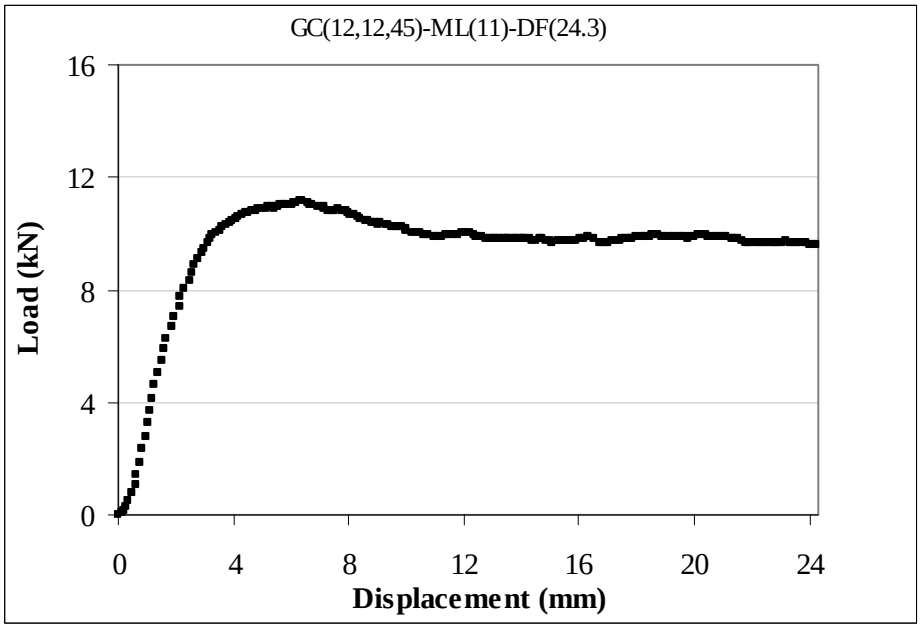

Figure 6.37 Forming load for the SPMD unit (12x12mm), L=24.3mm

6.4.3 Pressure distributions on side wall

The results shown in section 6.4.2 were used in order to produce pressure distributions graphs on the channel wall side where the pins are located, at various stages of the stroke. Figure 6.38 and 6.39 show the pressure distributions by the pins readings in the SPMD with circular cross sectional area and 15mm diameter, for the two strokes of 26.5mm and 17.3mm respectively. Results are plotted at 10%, 20%, 50% and 80% of the full stroke, and the relative location of the punch in the vertical channel is shown at each stage. For 10% and 20% of the stroke, the distributions show a trend characterized by increasing pressure from the bottom to the top side of the channel wall. Also, an higher intensity of pressure is recorded at 20% of the stroke, as the deformation at 10% has not fully developed. As the extrusion progresses (50% and 80%), pressure values assume an increasing trend at the bottom side of the channel, but the pressure starts to drop after the punch had crossed the location of the pressure sensor. In addition, lower levels of pressure are measured for the shorter stroke to those obtained with the longer stroke.

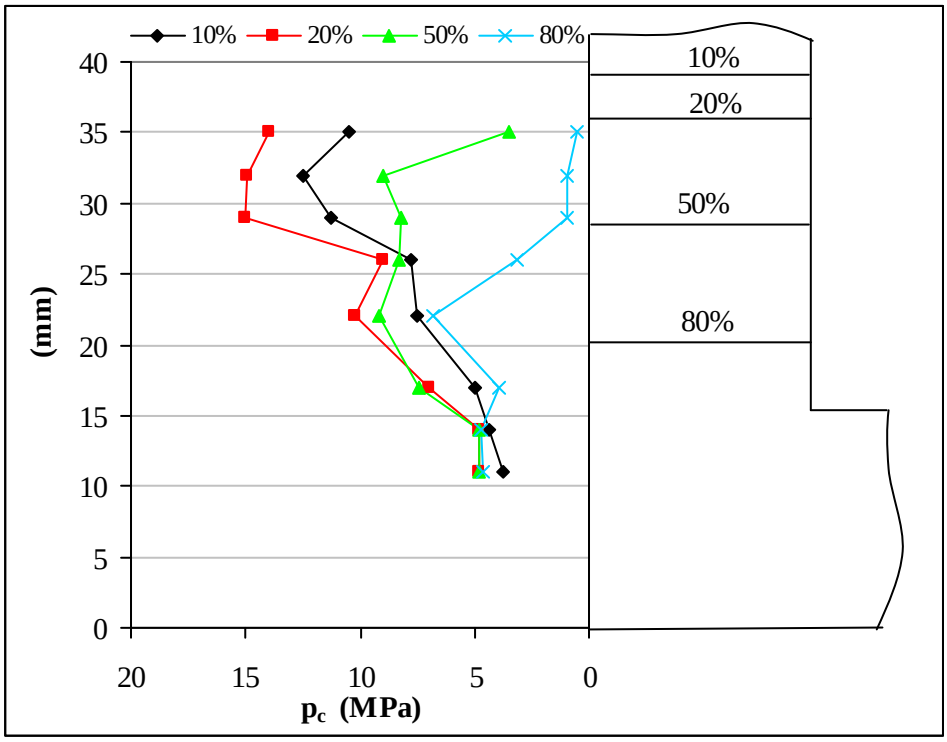

Figure 6.38 Pressure distributions on the channel wall, D=15mm and L=26.5mm

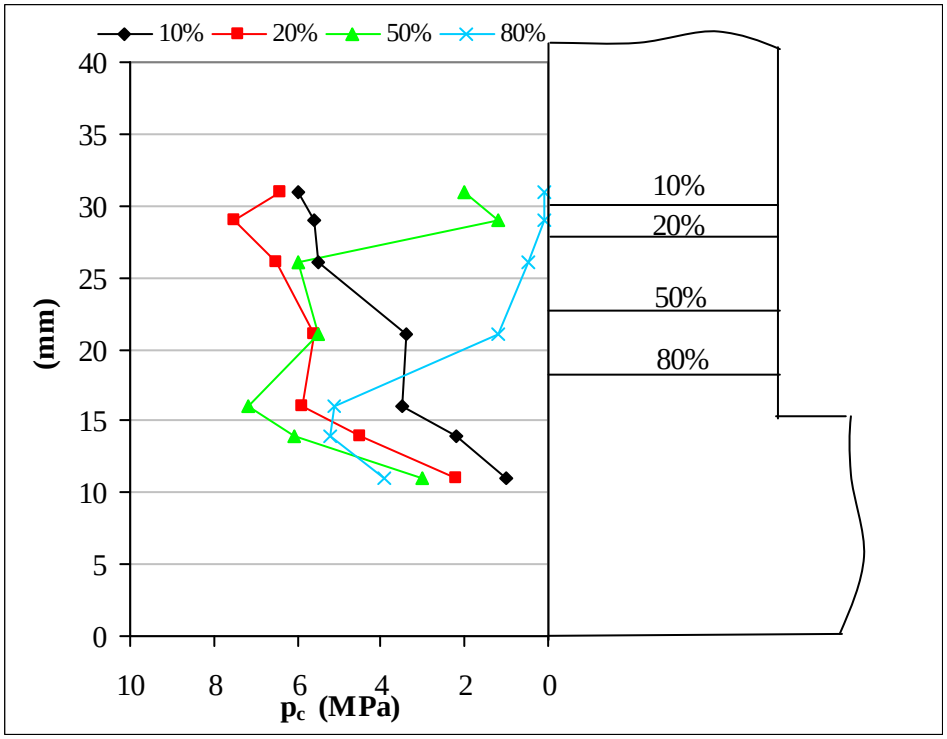

Figure 6.39 Pressure distributions on the channel wall, D=15mm and L=17.3mm

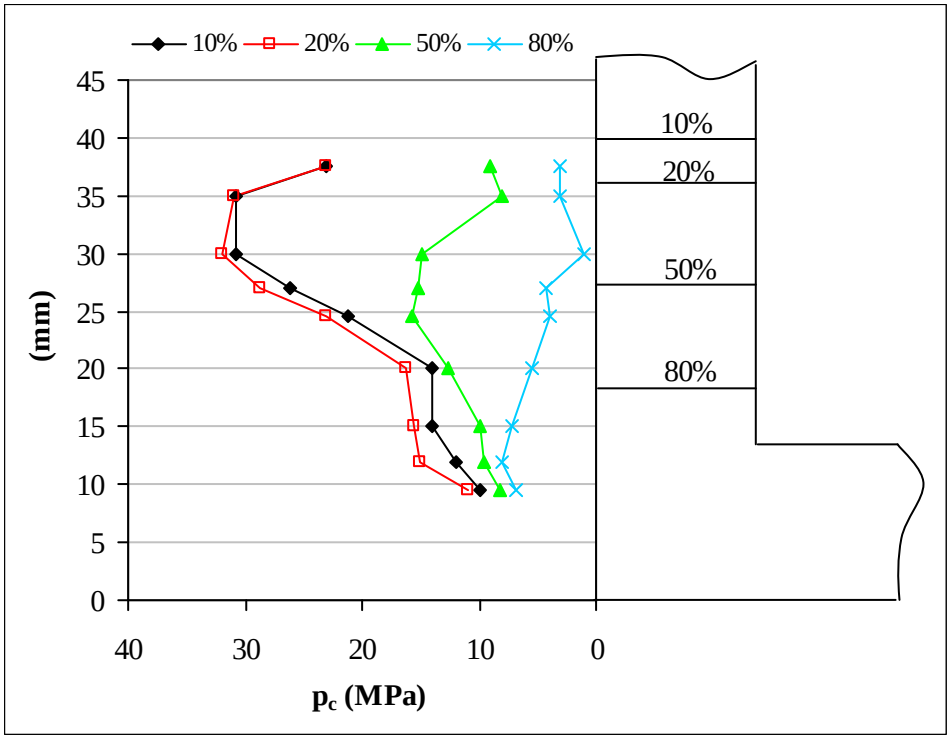

Figure 6.40 Pressure distributions on channel wall, D=12mm and L=31mm

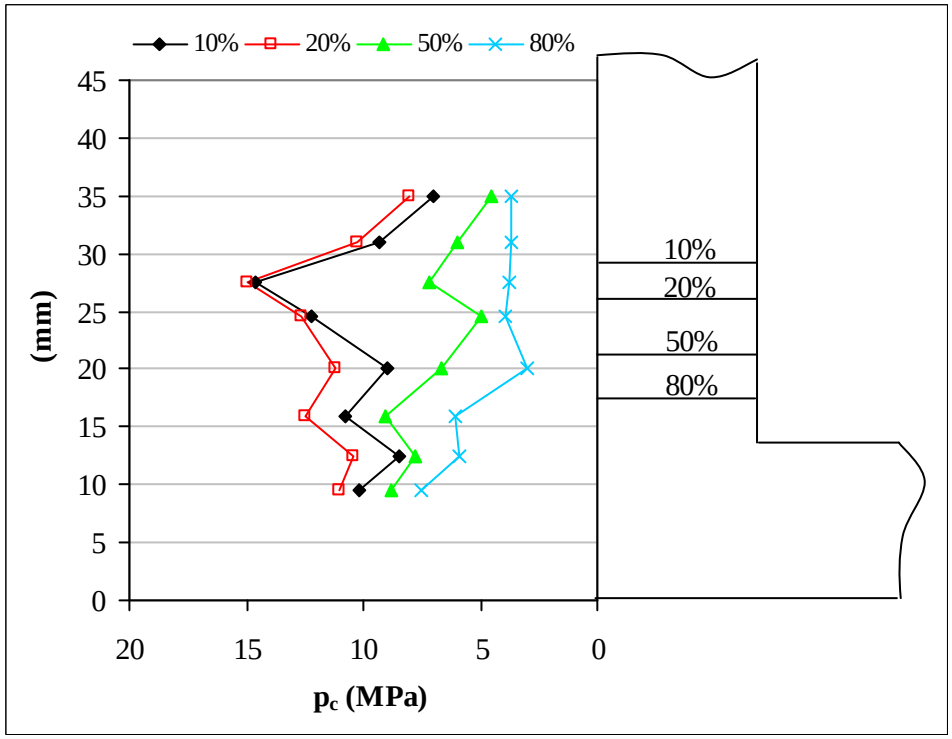

Figure 6.41 Pressure distributions on the channel wall, D=12mm and L=18.2mm

Figures 6.40 and 6.41 show pressure distributions for the SPMD with circular cross sectional area channels of 12mm diameter, using the two full strokes of 31mm and 18.2 mm respectively. Experimental points show a trend similar to those obtained with the larger diameter (15mm), although higher levels of pressure were observed.

Figure 6.42 shows the pressure distribution when SPMD with square cross sectional channels area of 12x12mm is used. The full stroke was 24.3mm. For such channel geometry, a different behaviour is observed from those obtained with circular channels. In fact, the experimental points show a descendent trend, during the progression of the extrusion process, from 10% to 80% of the full stroke.

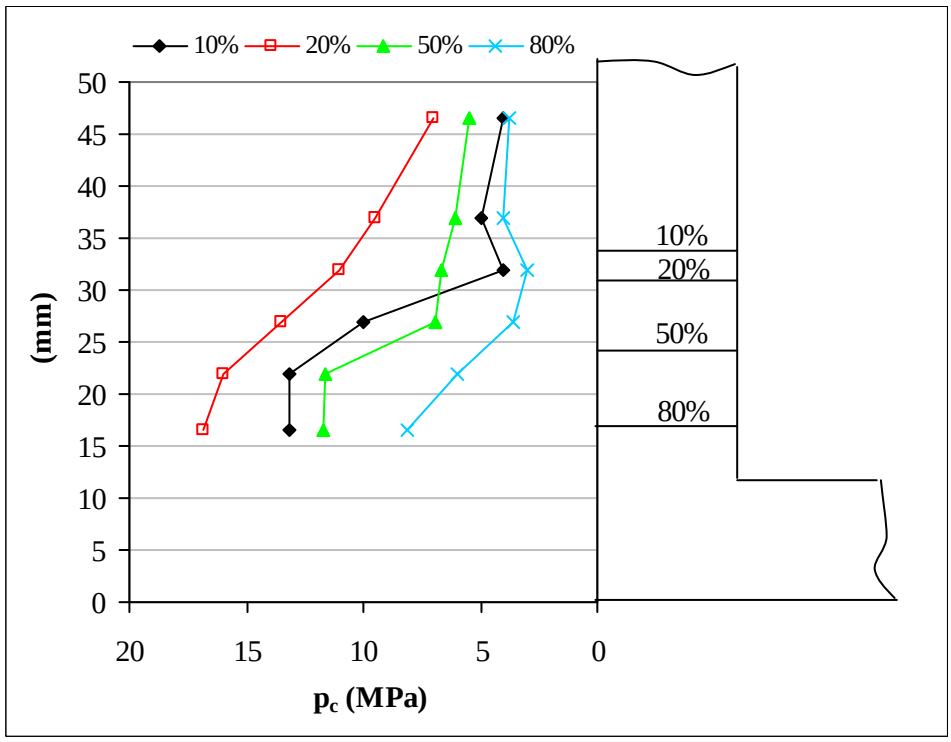

Figure 6.42 Pressure distributions at the channel wall, 12x12mm and L=24.3mm

6.5 CONCLUSIONS

A new tool arrangement, the Side Pressure Measuring Devices (SPMD) was designed and built to measure side contact stresses in the vertical channel which develop during the Equal Channel Angular Extrusion process.

For circular cross sectional area channels, the experimental points had shown a trend characterized by increasing levels of pressure from the bottom of the channel, to the top of it. After the punch crossed the sensor location, the pressure starts to drop. Higher pressure levels in the smaller cross section (D=12mm) were measured in comparison to the larger cross section (D=15mm).

Results by the Side Pressure Measuring Device (SPMD) with square cross sectional channels had shown a different trend to those obtained using the circular cross sectional area channels. Pressure distributions on the tool wall were characterized by descendent trends. This behaviour may be attributed to the difference in geometry and its elastic deformation behaviour.

Chapter 7

SIMULATION OF IMPACT LANDING

7.1 LANDING FRAME DESING

In this chapter, the employment of a UREAD energy absorption device against impacts or heavy landing is investigated. The potential use of UREAD to dissipate excessive energy and its behaviour in circumstances such as impact landing is considered.

The landing of aircrafts is certainly a critical event, during which high forces develop at the instant contact in made with the ground. It is rather difficult to predict the type or level of an impact, as the severity of the landing (soft or heavy) is deeply affected by external parameters such as the weather conditions, the weight of the aircraft and its speed. For this reason, it is important to incorporate into aircraft several landing dampers capable of dissipating the impact energy, for the safety of passengers. Systems are laborious and complex in design, and they basically employ hydraulic and pneumatic arrangements. The idea to incorporate a UREAD reusable device for protection against heavy landings, could certainly provide a large step forward to reducing the complexity of the hydraulic system currently employed in some aircraft. Also, in some cases it could provide extra protection and comfort to passengers.

In order to investigate the use of UREAD in those circumstances, an experimental model was designed and built to simulate impact landings. Figure 7.1 shows an operational sketch of the experimental structure, while Figure 7.2 shows a photo of the laboratory arrangement. The set up comprises a frame that is made out from commercial Aluminium profile bars, a landing platform and a landing unit or carriage. The carriage incorporates the UREAD device, while the landing platform is equipped with a load cell to measure the impact forces. The frame has a descend angle (δ) which is adjustable, and includes a sliding rail for the carriage. In operation, the carriage is driven along the sliding rail by its total weight. A linear sliding bearing was used to guide the carriage and to minimize friction. Upon leaving the sliding rail, the carriage experience free fall,

taking into account the angle of descend and the carriage accumulated speed. The free landing gap is adjusted to suit the angle of descend (δ), so that the carriage lands on the platform.

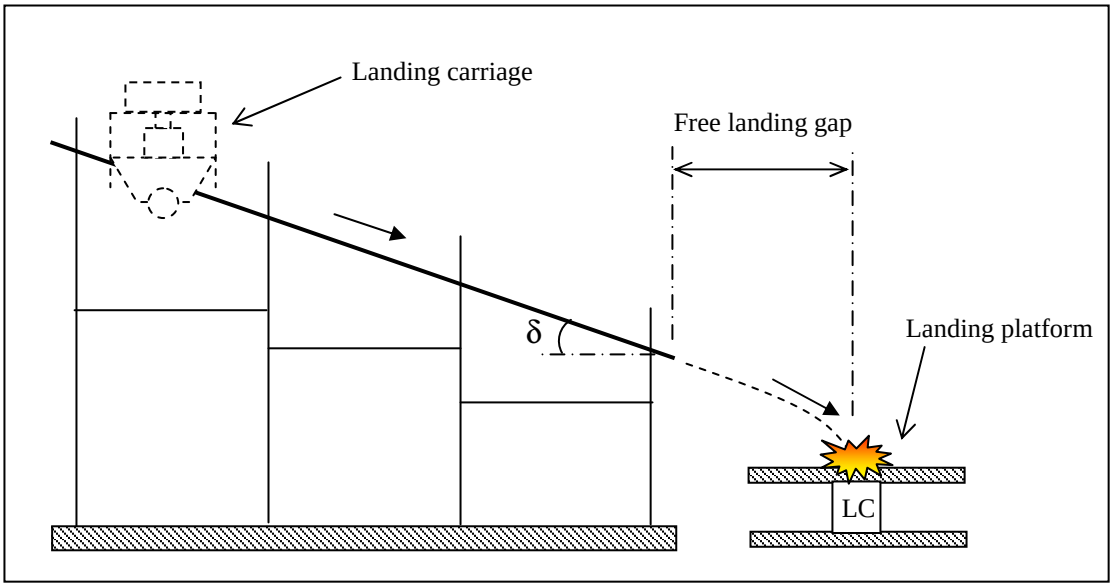

Figure 7.1 Operational sketch of the Landing Frame

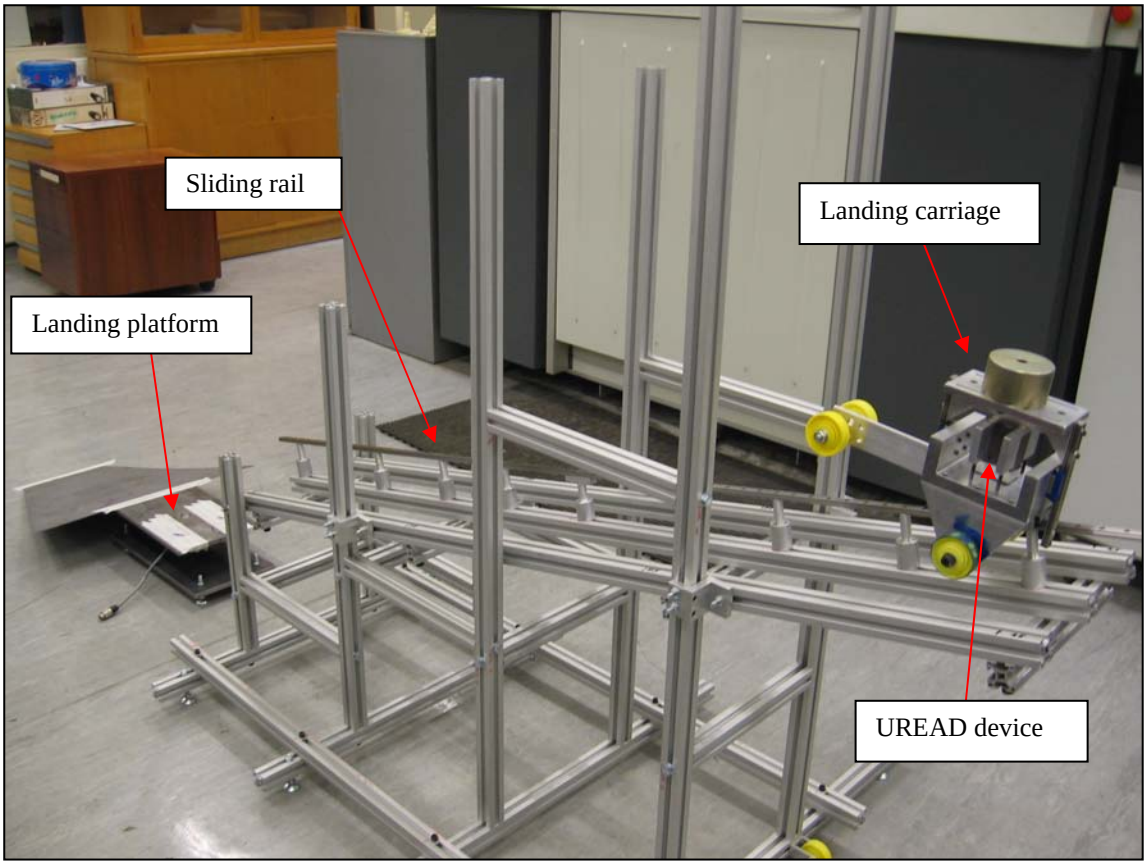

Figure 7.2 Landing Frame and its components

7.2 LANDING FRAME COMPONENTS

7.2.1 Main frame

The frame components are shown in Figure 7.3. The overall dimensions of the frame are 1.5m in length and 0.4m in width. A maximum height "H_1" of 1.5m is achievable at a descend angle "δ" of 45^0. The structure is made of thin extruded sections of aluminium, produced by Bosch-Rexroth. Bars of such a profile were cut to different lengths, then assembled together using brackets and fixing screws, to form a symmetrical structure for stability and rigidity.

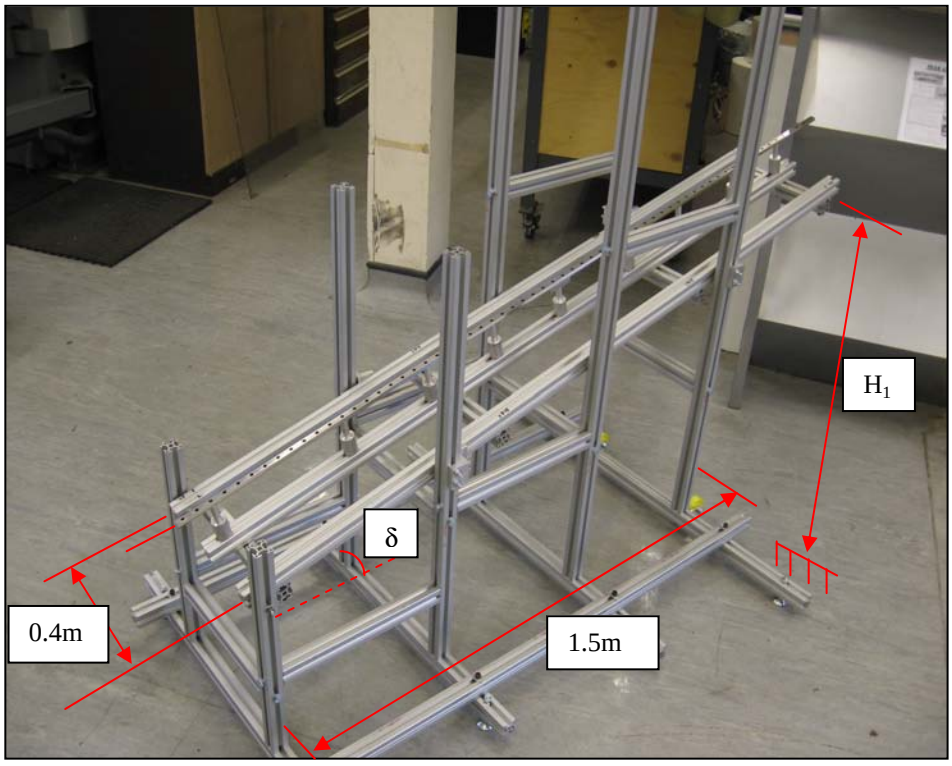

Figure 7.3 The main frame

The frame itself is designed to be composed of two sub structures: a fixed part, and an adjustable part. The adjustable part is the acceleration runner, as shown in Figure 7.4. The angle is adjusted using fixing brackets mounted along the vertical bars, as shown in Figure 7.5. The frame has also adjustable feet, and it is equipped with two wheels for adjusting its position and location. Figure 7.6 shows a close-up picture of the sliding

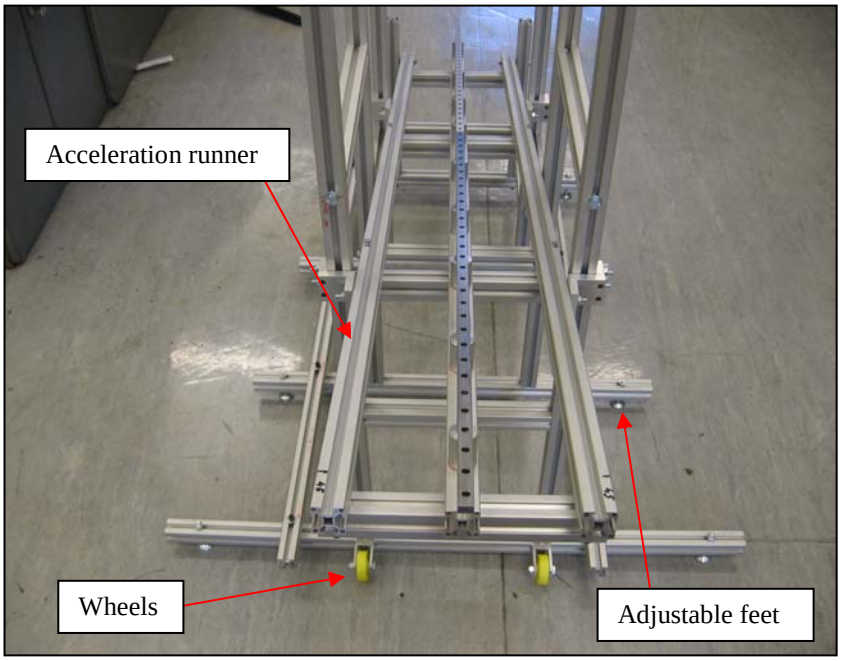

Figure 7.4 The acceleration runner

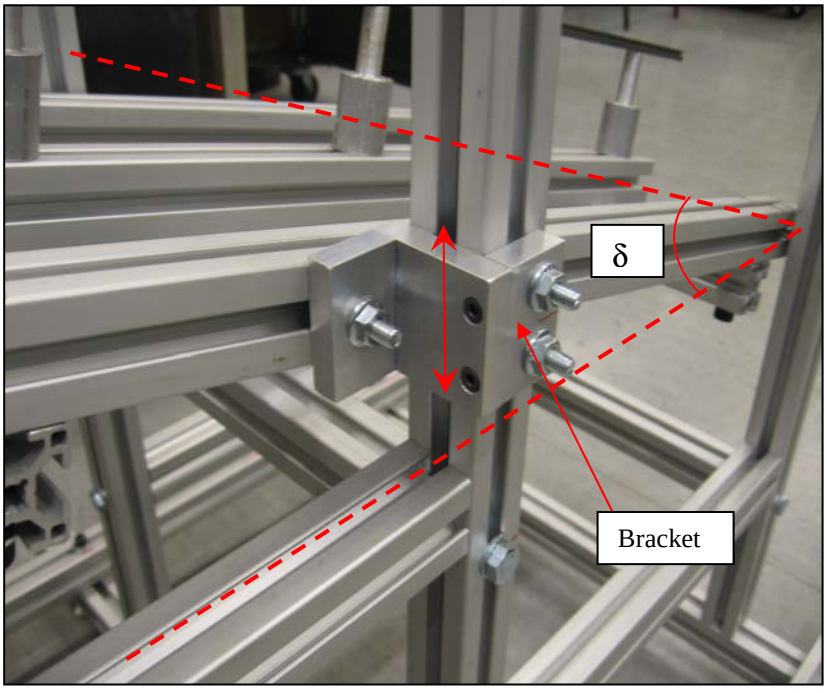

Figure 7.5 Fixing bracket

rail, produced by NSK. It is made out of stainless steel and measures 12mm in width, 1.6m in length. As the figure shows, it is fixed to the acceleration runner through a

number of cylindrical aluminium supports. The end of the sliding rail is fitted with a linear ball plastic sliding connector. It is used to keep in position the elements of the linear bearing during the free fall of the landing carriage, and it is located in its initial position by an elastic band. In operation the plastic connector is released with the carriage as it enter the free fall zone.

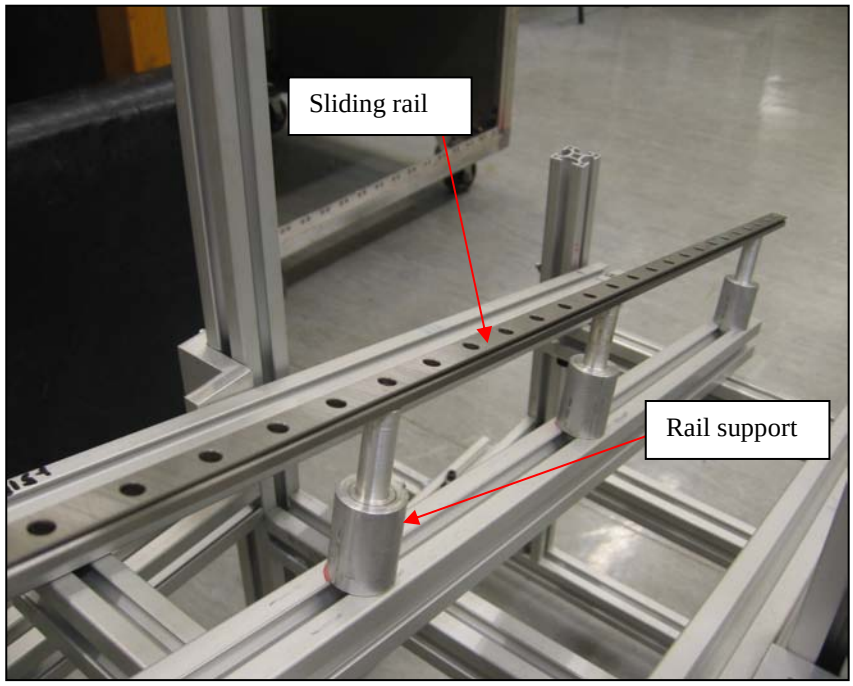

Figure 7.6 Sliding rail and supports

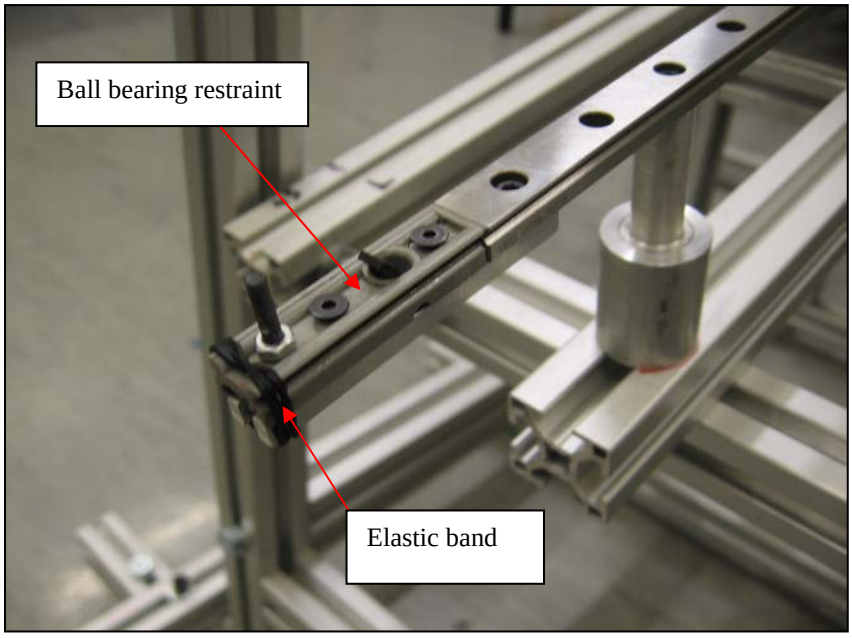

Figure 7.7 Ball bearing restraint mechanism

7.2.2 The landing carriage

Figure 7.8 shows the working mechanism of the landing carriage. This unit comprises two sub-structures: a sliding sub-structure of mass m_1 and a main block with a UREAD device of mass m_2; m_1 and m_2 measure 1.61 Kg and 1.8 Kg respectively. The sliding structure is free to move along the vertical direction, therefore at the instant of landing it will transfer its impact energy to the UREAD energy absorption device, according to the weight of mass m_1.

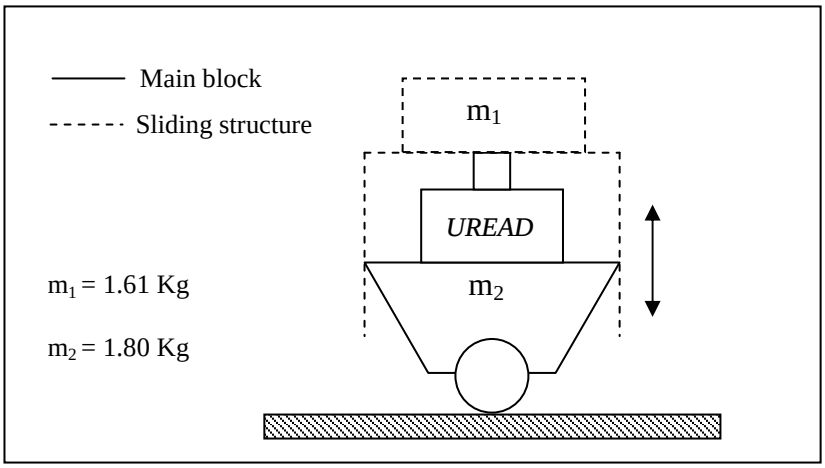

Figure 7.8 Landing carriage working mechanism

Figure 7.9 shows a close up picture of the landing carriage parts. The main elements were machined from HE30 aluminium alloy. Figure 7.10 shows an exploded picture of the landing carriage. The main block comprises a UREAD unit GR(4,4,27), two linear bearings (bearing 1 and bearing 2 - NSK P1U series), two landing wheels and a tilting mechanism. The connection with the sliding rail is achieved through another linear bearing (bearing 3) in the tilting mechanism. The sliding structure comprised of two linear guides, a calibrated weight, weight support and supporting wheels. It is connected to the main block through the linear guides fitted in bearing 1 and bearing 2. The weight position X on its support is changeable. The carriage is designed to impact on the landing wheels, while the supporting wheels are there to provide stability after landing. Figure 7.11 shows a close up picture of the tilting mechanism. It is used to change the tilting angle of the landing carriage.

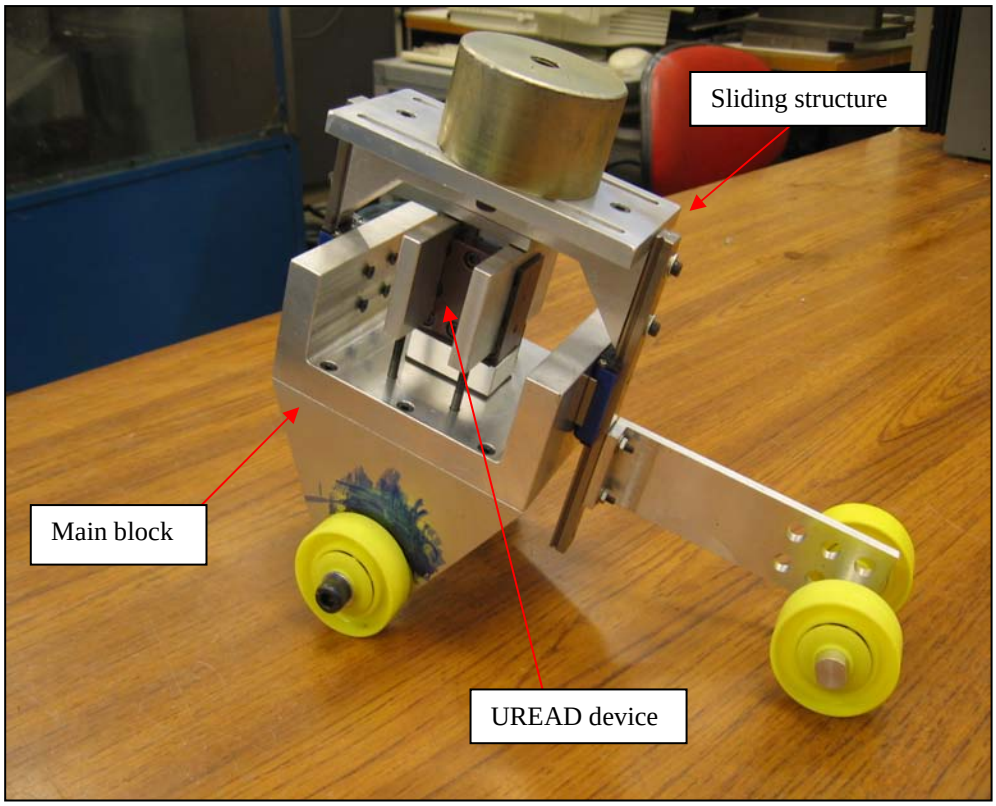

Figure 7.9 The landing carriage

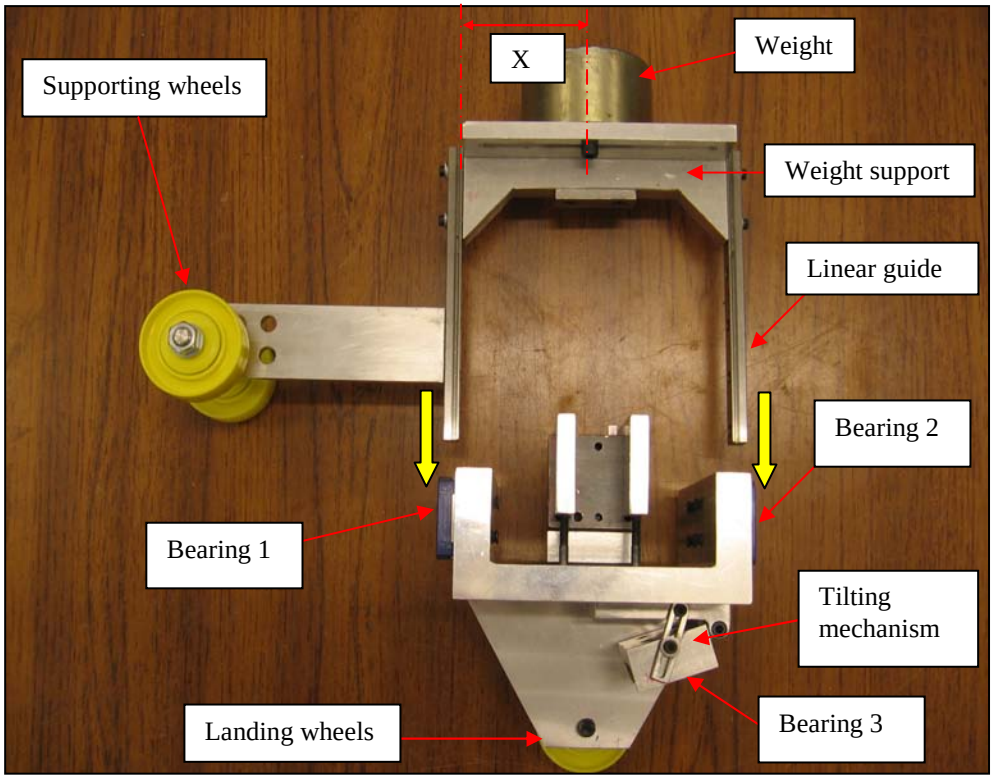

Figure 7.10 Exploded picture of the landing carriage

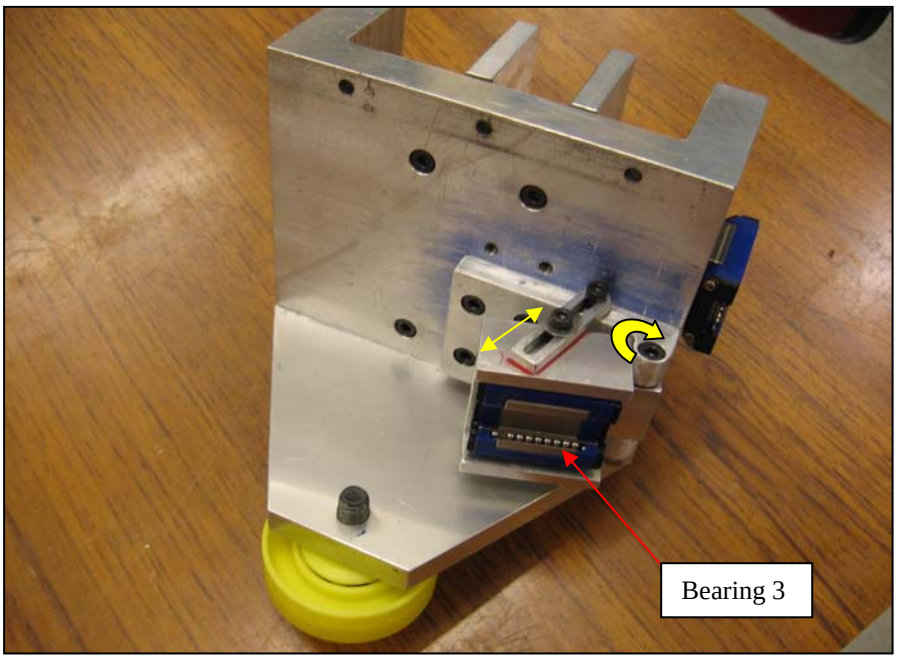

Figure 7.11 The tilting mechanism

7.2.3 The landing platform

Figure 7.12 shows a picture of the landing platform. It is made of two rectangular steel plates (lower and upper plates), with a 22.3 kN (5000 lb) cylindrical load cell fixed

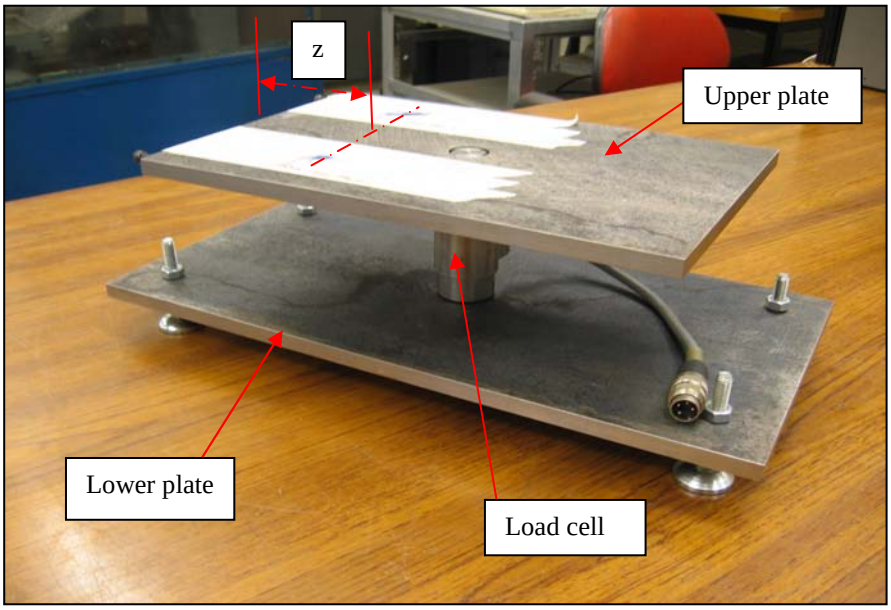

Figure 7.12 The landing platform

between them. The lower plate stands on four adjustable levelling feet, while the upper plate is linked to the load cell by a fixing screw. The landing unit is supposed to impact on the upper plate, at a distance ***z*** from its external edge, as shown in Figure 7.12. The impact point can be visualized by the marks left by the wheels of the carriage. The wheels were painted with "blue liquid" before the test, while the platform was covered with white tape for this purpose. The load cell is connected to the data acquisition system thorough an I/O connection plug.

Detailed drawings of main parts of the landing frame are reported in Appendix (F).

7.3 EXPERIMENTS: IMPACT LANDING SIMULATION

7.3.1 Impact force measurement

Experimental tests were carried out by using the landing frame shown in Figure 7.2. The aim of the experiments presented in this chapter, is to compare force measurements results when the UREAD absorber is operational (active) and not-operational (not active) at the instant of impact. Commercial plasticine was used as working material in the UREAD unit. Commercial types of plasticine have a yield stress in the region 0.08 to 0.175 MPa [110]. The commercial plasticine used in these experiments had shown a yield stress of 0.08 MPa, when subjected to a compression test. The frame was set to a descend angle δ of 14.6^0, while the landing unit was adjusted parallel to the horizontal, by using the tilting mechanism shown in Figure 7.11.

Impact landing results were recorded at two different configurations: the first when the UREAD is active, the second when the UREAD device is not active. This second configuration was achieved by removing the pressing punch of the UREAD device.

The load cell was calibrated inside the platform before the experiments. The distance ***z*** from the landing point (see Figure 7.12) was measured to be 73.5mm, and the calibration was performed on an INSTRON (5kN) testing machine at the corresponding distance ***z*** on the landing platform.

Figure 7.13 shows the readings by the load cell during the impact testing. It includes the results of two different landings; when the UREAD device is active and when it is not. In both cases, readings were acquired at a frequency of 1000Hz. When the UREAD

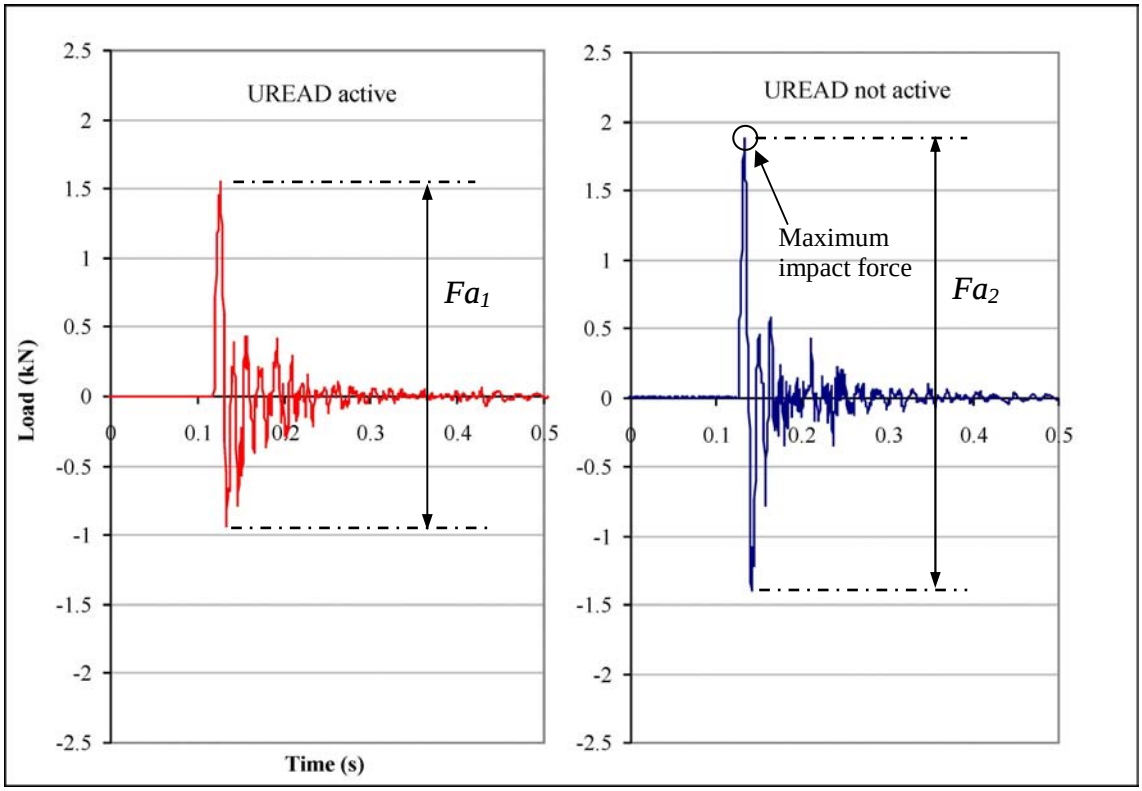

Figure 7.13 Force measurements at landing instant - test 1

absorber is not active, the load cell measures a maximum impact (positive) force of approximately 1.8 kN. Due to the severity of such impact, the landing platform continues to elastically vibrate for about 0.3 seconds before the measured load can come back to zero again. On the other hand, in the case when the UREAD device is active, the load is 1.5 kN, giving a total impact reduction of 16.6%. Also, when the UREAD is active the landing platform experiences vibrations for a reduced time then in the previous case (about 0.25 seconds). Attention is given to the maximum force amplitude Fa, which is interpreted as an indication of comfort during impact landing. The maximum force amplitude Fa_1 when the UREAD is active reduces to 71.5% of the force amplitude Fa_2 measured when the energy absorber is not active. The vertical pressing punch displacement in this test was measured to be 4mm, after impact. Figure 7.14 shows a repetition of the impact experiments in Figure 7.13, and gives a confirmation that results are repeatable.

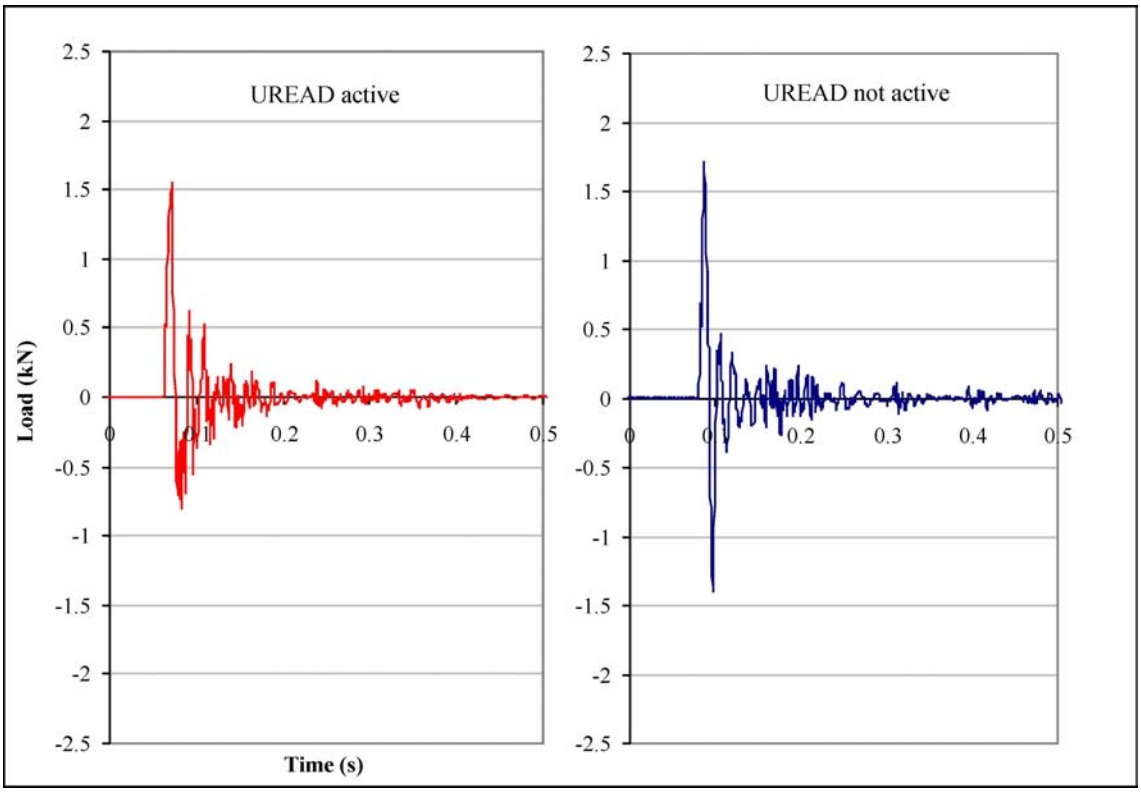

Figure 7.14 Force measurements at landing instant – test 2

7.3.2 Impact energy analysis

Figure 7.15 shows a sketch of the landing frame. The landing unit is initially placed on the top of it, then it is released to travel under its own weight from the height H_1 to the

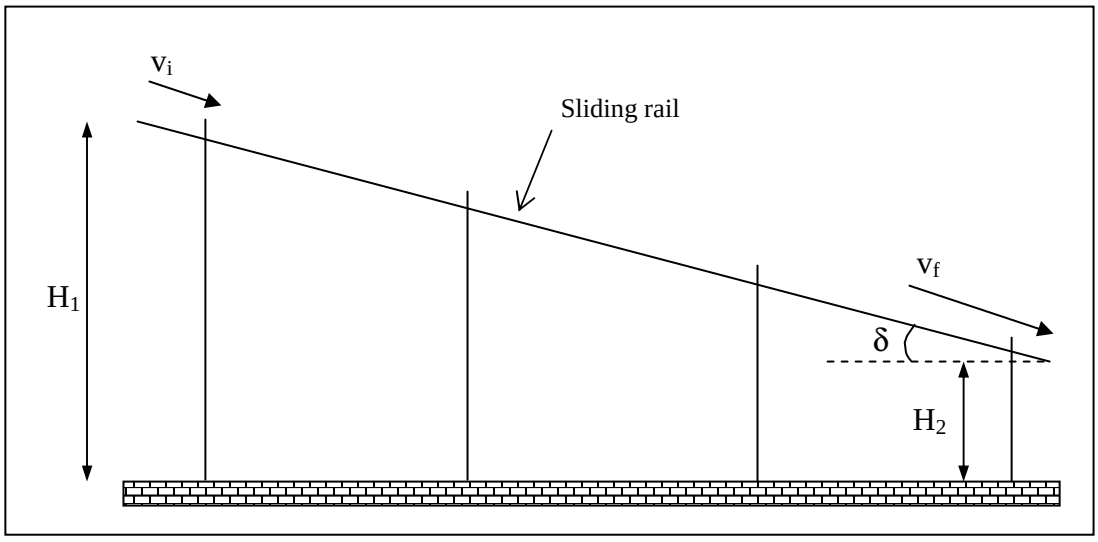

Figure 7.15 Acceleration of the landing carriage

height H_2. The landing carriage will accelerate on the sliding rail from the velocity v_i (initial velocity) to the velocity $v_{f,}$ (exit velocity) under the effect of the gravitational acceleration g. The initial velocity equals zero, therefore the exit velocity v_f is calculated by following equation.

$$v_f = \sqrt{2g(H_1 - H_2)} \tag{7.1}$$

For a descend angle δ of 14.6^0, the distances H_1 and H_2 are 0.835m and 0.435m respectively. Therefore, the exit velocity from equation 7.1 becomes

$$v_f = 2.8m/s \tag{7.2}$$

After leaving the frame, the landing carriage is under "free fall" conditions, and will impact on the landing platform by following a parabolic path, as Figure 7.16 (a) shows.

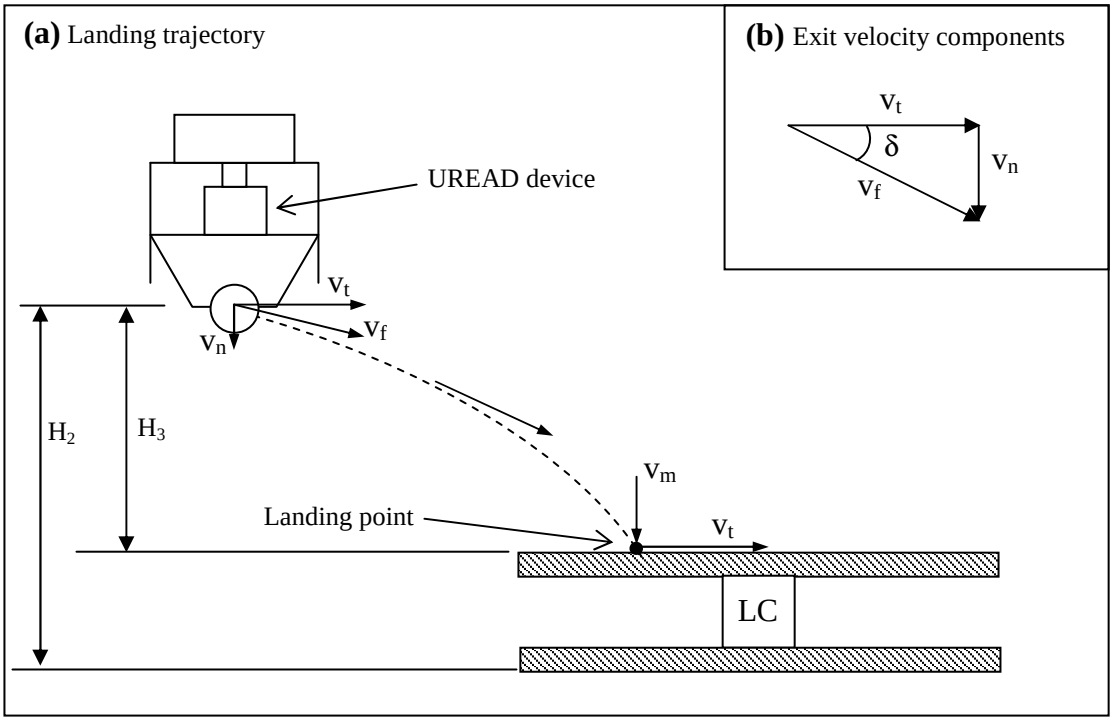

Figure 7.16 Landing unit free fall path and impact on the landing platform

Figure 7.16 (b) shows the velocity components at the moment the carriage exits from the main frame. If air resistance is neglected, the horizontal component v_t will not

change its value during the free fall [111]; on the other hand the vertical component will increase from the exit value v_n of 0.7m/s, to the impact value v_m. The vertical component v_m at the instant of landing is calculated from

$$v_m = v_n + gt_c \tag{7.3}$$

The time t_c is the total free fall time, given by the following equation [112]

$$0.5gt_c^{\,2} + v_n t_c - H_3 = 0 \tag{7.4}$$

As the distance H_3 is 0.4225m, the time t_c equals 0.23s from Equation 7.4. The vertical component of the velocity at impact is calculated from Equation 7.3

$$v_m = 2.95 m/s \tag{7.5}$$

The intensity of the total impact energy E_t of the landing carriage along the vertical direction is then given by the following equation, where the mass m_1 and m_2 are defined in section 7.2.2.

$$E_t = \tfrac{1}{2}(m_1 + m_2)v_m^{\,2} \tag{7.6}$$

Therefore, the total impact energy equals 14.79J by Equation 7.6. However, the UREAD device can only dissipate the energy from the mass m_1, therefore a value of 7J is obtained from Equation 7.7

$$E_{UREAD} = \tfrac{1}{2} m_1 v_m^{\,2} = 7J \tag{7.7}$$

The impact energy reduction $E_{re}(\%)$ is therefore given in Equation 7.8, and equals the value of 47.3%.

$$E_{re}(\%) = \left(1 - \frac{E_t - E_{UREAD}}{E_t}\right)100 = 47.3\% \tag{7.8}$$

An experimental indication of the reduction of energy transmitted to the ground during impact landing when using a UREAD device can be calculated from the results in Figure 7.13 or 7.14, by analysing the elastic deformation imposed to the landing platform at the instant of impact. A simple sketch of the landing platform is given in Figure 7.17 (a), where η is the elastic displacement by the generic impact force ***Fi***. When the UREAD is not active, the impact force ***Fi,a*** produces a displacement η_1; while when the UREAD device is active the reduced force "***Fi,b***" will produce a displacement η_2 in the landing platform. The two cases are represented in Figure 7.17 (b), which shows a sketch of the force-displacement behaviour of the landing platform, when loaded. The residual impact energy, for both cases, is the energy transmitted to the platform which, that is the area under the graph respectively in Figure 7.17 (b).

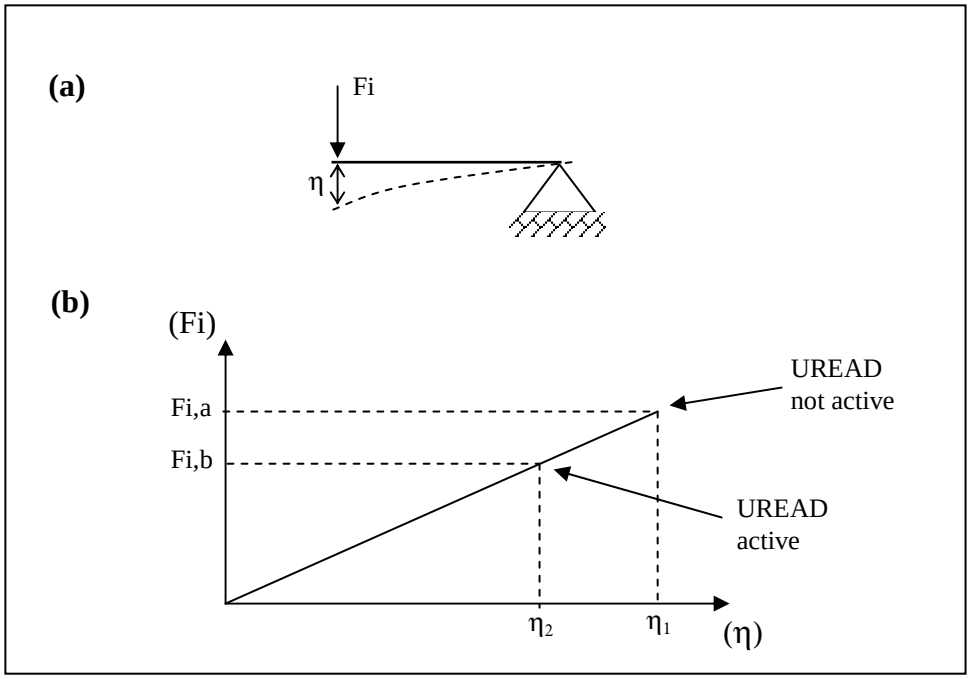

Figure 7.17 Impact loading of the landing platform

The following equations are therefore obtained for the impact energy and the impact energy reduction E_{re}***(%)***, if E_1 and E_2 are the energy transmitted to the platform when UREAD is not active and when it is active respectively.

$$E_1 = \frac{1}{2} Fi,a \cdot \eta_1 \tag{7.9}$$

$$E_2 = \frac{1}{2} Fi,b \cdot \eta_2 \tag{7.10}$$

$$E_{re}(\%) = \left(\frac{E_1 - E_2}{E_1} \right) 100 \tag{7.11}$$

Values for *Fi,a* and *Fi,b* are obtained from the experimental readings in Figure 7.14, they are 1.8kN and 1.5kN respectively. It is therefore assumed that only the region between zero and maximum load is relevant to the impact energy provided to the platform, as the rest represents its reaction. The correspondent elastic displacements are in the same ratio of the forces, as given by

$$\frac{\eta_2}{\eta_1} = \frac{Fi,b}{Fi,a} = 0.83 \tag{7.12}$$

By substituting Equations 7.9, 7.10 and 7.12 into Equation 7.11 a value for the impact energy reduction $E_{re}(\%)$ is obtained and equals 31.1%. This value is comparable with the one from Equation 7.8, of 47.3%.

A static full stroke test on plasticine of 4mm at the punch speed of 6mm/s was carried out in the UREAD GR(4,4,27). Experimental results showed an energy absorbed of 0.1J, at a constant force of 25N. The static dynamic force was therefore 80 times higher then the static force. However, the resistance of materials depends on the strain-rate or deformation velocity [112]. The relation between strain rate and material properties is beyond this research programme.

7.4 CONCLUSIONS

The UREAD technique was successfully implemented into a landing structure. The experimental tests demonstrated the effectiveness of the UREAD device as an energy absorber against landing impacts. An impact force reduction of 16.6% was experimentally obtained when using a GR(4,4,27) unit and plasticine as material being deformed. Also, the reaction force amplitude of the landing platform after impact was

shown to considerably reduce when using the UREAD absorber. An impact energy reduction of 31.1% was calculated from experimental results.

Chapter 8

CONCLUSIONS AND FUTURE WORK

8.1 CONCLUSIONS

The research presented in this thesis has investigated a novel technique to dissipate energy in engineering systems.

With regards to energy absorption, a literature review was undertaken on current energy dissipation devices. Application fields such as structures, personal protection and transport were explored. For structures, dissipation devices based on friction, plastic deformation and viscoelasticity were shown to be in use against severe earthquakes, while for personal protection the market offers a range of helmets, body armour and leg protectors. Although the capabilities of these devices in energy absorption were demonstrated, further analysis gave insight on some significant disadvantages that may exist in such protective systems. Dissipative devices attached to buildings and based on friction are highly affected by wear; on the other hand devices based on plastic deformation are not reusable, and energy absorbers based on viscoelasticity are not reliable at changeable climatic conditions. In the field of personal protection, the way energy is absorbed in body armour may still cause “blunt-traumas” across crucial zones, such as the chest, as a consequence of the impact. In addition, the area of transport was investigated, with respect to aircraft landing energy absorbers. It was discovered that current devices are complex in design, as they are based on oleo-pneumatic mechanisms.

An innovative technique to dissipate energy was therefore introduced, capable of providing the base for the design of Universal Reusable Energy Absorbers Devices (UREAD). The principle of such methodology is based upon the plastic deformation of a solid material in a tool and made out of intersecting channels of equal cross sectional area, similar in principle to Equal Channels Angular Extrusion (ECAE).

In order to understand the nature of the process, an analytical approach to the extrusion process was carried out, following the Slab Analysis method and the Upper Bound technique. In both cases, the deformable material yield stress, channels cross sectional area, channels geometry, level of friction at the tool/material interface and stroke length had shown to be critical for the forming pressure. The energy absorption performance was shown to be also dependent on the relative channels inclination angle. The Finite Element Analysis was also performed, using the ANSYS software package. Favourable comparisons with the analytical approach were obtained.

A number of UREAD devices were manufactured with intersecting channels at 90^0 and tested. Force-displacement behaviours were presented at different geometrical conditions. Lead and Silicon Gum were used as deformable materials in the experiments, and channels geometries covered circular and square cross sectional area. Upon loading the UREAD units, the force averages to a constant distribution after an initial increase. Also, the average forming pressure results of the UREAD channels had shown a trend against the geometry of the channels and the length of the full stroke. Therefore, the channels cross section geometry, stroke length and material yield stress were identified to be critical with respect to the forming pressure, and Figures 5.26 and 5.27 provide conclusive channels characterization graphs. However, the machining tolerance of channels and punches was shown to have some effects on the forming force and the performance of the units. The energy dissipated during the extrusion processes was estimated from the load-displacement characteristics, and had shown a linear distribution against the progression of the stroke. Experimental measurements using the square cross sectional geometries favourably compared against analytical results obtained in plain-strain conditions, by the Slab Method and Upper Bound techniques.

Experimental investigations were performed to measure the pressure that is developed on the side wall of the extrusion channel. Measurements were acquired by the employment of Pressure Pins. The design of special tools was required in order to incorporate the sensors into the body structure of the UREAD devices. For circular cross sectional area channels, the side pressure increased from the bottom side of the channel to the top of it. However, it drops when the punch had crossed the sensor location. Higher levels of pressure were measured for smaller cross sectional area channels. For square cross sectional area channels, the measured pressure was shown to

peak near the bottom side of the channel. Such trend was opposite to those obtained by the circular geometry channels. This may be attributed to the difference in geometry and its elastic deformation behaviour.

A possible application of the UREAD technique was presented. The potential implementation of UREAD devices against heavy impacts was investigated. An experimental apparatus, the Landing Frame, was designed and built in order to test the effectiveness of UREAD absorbers, when incorporated into a landing carriage. Experimental results had shown that the impact ground force, at a fixed lading angle, was reduced by 16.6% due to the action of the energy absorber, and hence effecting an impact energy reduction of 31.1%. Energy dissipation capabilities were therefore verified for a real potential application, with all the advantages of such technique in being reusable and relatively simple to incorporate into structures.

8.2 RECOMMENDED FUTURE WORK

Experimental and theoretical work carried out and presented in this thesis, opened new areas for future investigations:

1. Development of 3-D theoretical models of Channel Angular Extrusion (CAE) and Equal Channel Angular Extrusion (ECAE), in order to improve the forming pressure prediction.

2. Investigate the static characterization of UREAD devices with channels inclined at various inclination angles, along with the use of other possible deformable materials as an alternative to lead.

3. Extend the research carried out in this project on side pressure measurements to cover a variety of channels geometries.

4. Development of a Side Pressure Measuring Device (SPMD) that incorporates pressure sensors positioned at an angle with the contact surface, in order to measure friction forces.

5. Development of the Landing Frame to improve the measuring system by fitting a load cell and a potentiometer, capable of measuring the impact force exerted directly on the UREAD device and the punch displacement respectively. This will allow the energy absorbed by the UREAD unit to be experimentally measured, under any landing angle and impact speed condition.

6. Expand the research field to include investigations on the dynamic behaviour of the UREAD devices.

REFERENCES

[1] Sharratt Michael, "Galileo decisive innovator", *Cambridge University Press*, 1996.

[2] Guicciardini, "Reading the Principia : the debate on Newton's mathematical methods for natural philosophy from 1687 to 1736", *Cambridge University Press*, 1999.

[3] L. T. C. Rolt and J. S. Allen, "The Steam Engine of Thomas Newcomen", *Landmark Publishing*,1997.

[4] Dickenson, H. W., "James Watt: Craftsman and Engineer", *Cambridge University Press*, 1935.

[5] "Le fardier de Cugnot", Source S.I.A. - *Société des Ingénieurs de l'Automobile*, April 1989.

[6] Enrico Fermi, Edoardo Amaldi, Bruno Pontecorvo, Franco Rosetti, Emilio Segre,"Process for the production of radioactive substances", *US Patent*, 2.206.634, 1935.

[7] "Proceeding of the Apollo 11 lunar science conference in Huston", *Pergamon*, 1970.

[8] "Energy for the world, why uranium?", educational paper of the *World Nuclear Association* (www. world-nuclear.org).

[9] "Basic carriage gear horse drawn vehicle", *Great Northern Livery Company Inc.*

[10] Gloag, John, "Victorian Comfort: A Social History of Design, 1830-1900", *A&C Black*, 1961.

[11] Charles E. Sorensen, "My 40 years with Ford", *Wayne State University Press*, 2006.

[12] "How products are made", *Volume 6, Springs* (http://www.madehow.com).

[13] Dixon, John C, "The shock absorber handbook", *John Wiley*, 2007.

[14] Wai-Fah Chen, E. M. Lui, "Handbook of Structural Engineering", *CRC Press*, 2005.

[15] "Earthquake engineering", *by Consortium of Universities for Research in Earthquake Engineering (CUREE)*, San Francisco (US), April 2006.

[16] Allen Breed, "Airbag restraint system with venting means", *US Patent*, 5,071,161, 1991.

[17] D. Cadogan, C. Sandy and M. Grahne, "Development and evaluation of the mars pathfinder inflatable airbag landing system", *Acta Astronautica*, Vol. 50 (2002), 10, 633–640.

[18] T.T Soong, G.F Dargush, "Passive energy dissipation systems in structural engineering", *Wiley*, 1996.

[19] "New technologies in earthquake engineering", Technical brochure, University of Buffalo, *CSEE center*, Buffalo (US), 2001.

[20] G.F. Dargush, T.T. Soong, "Behaviour of metallic plate dampers in seismic passive energy dissipation systems", *Earthquake Spectra*, 4 (1995), 545-568.

[21] Juan Enrique Martý´nez-Rueda, "On the Evolution of Energy Dissipation Devices for Seismic Design", *Earthquake Spectra*, Volume 18, No. 2, pages 309–346.

[22] William Henry Robinson, "Energy Absorber", *US Patent*, (6,141,919), 2000.

[23] William Henry Robinson, "Cyclic energy absorber", *US Patent*, (3,833,093), 1974.

[24] "Robinson Seismic Limited", *Technical papers*, (www.robinsonseismic.com).

[25] Douglas K Nims, Philip J. Richter, Robert E. Bachman, "The use of energy dissipation restraint for seismic hazard mitigation", *Earthquake Spectra*, 9 (1993), 467-489.

[26] H. Mualla, Borislav Belev, "Performance of steel frames with a new friction damper device under earthquake excitation", *Journal of Engineering Structure*, 24 (2002), 365-371.

[27] G. Anagnostides, A.C. Hargreaves, T.A. Wyatt, "Development and applications of energy absorption devices based on friction", *J.Contruct. Steel Research*, 13 (1989), 317-336.

[28] Ronald Darby, "Viscoelastic fluids", *Marcell Dekker*, 1976.

[29] Zhao-Dong Xu, Hong-Tie Zha, Ai-Qun Li, "Optimal analysis and experimental study on structures with viscoelastic dampers", *Journal of Sound and Vibration*, 273 (2004), 607–618.

[30] S.W. Park, "Analytical modelling of viscoelastic dampers for structural and vibration control", *International Journal of Solids and Structures*, 38 (2001), 8065-8092.

[31] Ngai Yeung, Austin D.E. Pan, "The effectiveness of viscous-damping walls for controlling wind vibrations in multi-story buildings", *Journal of Wind Engineering and Industrial Aerodynamics*, 77&78 (1998), 337-348.

[32] Douglas P. Taylor, "History, design and applications of fluid dampers in structural engineering", *TAYLOR Devices Inc.*, on-line technical paper.

[33] Nishimura, Yamada, Sakamoto, Kobori, "Control performance of active–passive composite tuned mass damper", *Smart Material Structures*, 7 (1998) 637–653.

[34] P. Wang, R. Fung, C. Huang "Dynamic analysis of a tall building with s tuned mass damper device subjected to earthquake excitations", *Journal of Sound and Vibration*, (2001), 244(1), 123-136.

[35] R. Collins, B. Basu, B. Broderick "Optimal design of multiple tuned mass dampers (MTMDS) for wind turbine towers using SSA", *SECED Proceedings*, 21-22 March (2005), University of Bath.

[36] Jacob Pieter Den Hartog, "Mechanical Vibrations", *Courier Dover Publications*, 1985.

[37] H.F. Bauer, "Oscillations of immiscible liquids in a rectangular container: a new damper for excited structures", *Journal of Sound and Vibration*, 93(1)(1984), 117-133.

[38] Duerig T W, "Engineering aspects of shape memory alloys", *Butterworth Heinemann*, 1990.

[39] Ian D. Aiken, Douglas K. Nims, Andrew S. Whittaker, James M. Kelly, "Testing of passive energy dissipation systems", *Earthquake Spectra*, 9 (1993), 335-370.

[40] E.J.Graesser and F.A.Cozzarelli, "Shape memory alloy as new materials for aseismic isolation", *Journal of Engineering Mechanics*, Vol. 117, No. 11, November 1991, 2590-2608.

[41] Davide Fugazza, "Shape memory alloy devices in earthquake engineering: mechanical properties, constitutive modelling and numerical simulations", *Master degree dissertation*, University of Pavia, September 2003.

[42] M. Reinhorn, T.T. Soong "Active bracing systems", *Modern Steel Construction*, 33 (1993), 28-33.

[43] Kazuto Seto, Yukito Matsumoto, "Active vibration control of multiple buildings connected with active control bridges in response to large earthquakes", *Proceedings of the American Control Conference*, San Diego, California (US), June 1999.

[44] Michael Bruneau, Andrew Whittaker, Andrei Reinhorn, "Overview of damage to buildings near ground zero", *MCEER Special reports series*, Volume 1, March 2002.

[45] Yi Li, Jian Bao Li, RouQi Zhang "Energy-absorption performance of porous materials in sandwich composites under hypervelocity impact loading", *Composite Structures*, 64 (2004) 71–78.

[46] **"**Foreign impact and energy and energy absorbing structure", *ImechE Seminar Publication*, 1998.

[47] M. R. Edwards, A. Mathewson "The ballistic properties of tool steel as a potential improvised armour plate", *International Journal of Impact Engineering*, 19 (1997), 4, 297-309.

[48] Morril K.B., Malvar L.J., Crawford J.E., Ferritto J.M. "Blast resistant design and retrofit of reinforced concrete columns and walls", *Proceeding of the 2004 Structures Congress*, American society of civil engineers, Reston (USA), 1471-1478.

[49] Eduardo Moreno Almansa, Manuel Fernández Cánovas "Behaviour of normal and steel fiber-reinforced concrete under impact of small projectiles", *Cement and Concrete Research,* 29 (1999) 1807–1814.

[50] Jeffrey Hanks, "Protective wall panel assembly", *Patent*, W0 2004/065729 A1, 2004.

[51] Sarah Tomas Cleevely, "Safe and sound-new developments in body armours", *Material World*, September 2002, 13-15.

[52] D.P. Gonc¸alves, F.C.L. de Melo a, A.N. Klein, H.A. Al-Qureshi, "Analysis and investigation of ballistic impact on ceramic/metal composite armour", *International Journal of Machine Tools & Manufacture*, 44 (2004) 307–316.

[53] John Joseph Holloway, "A garment having pockets to contain protective body armour", *Patent*, GB 2418832 A, 2006.

[54] Z. Fawaz , W. Zheng, K. Behdinan, "Numerical simulation of normal and oblique ballistic impact on ceramic composite armours", *Composite Structures*, 63 (2004) 387–395.

[55] Seshadri Ramkumar, "Body armour composite fabrics: an overview", *International Textile Bulletin*, 48(2002), 16-22.

[56] V.P.W. Shim, C.T. Lim, K.J. Foo, "Dynamic mechanical properties of fabric armour", *International Journal of Impact Engineering*, 25 (2001), 1-15.

[57] Luca Di Landro, Giuseppe Sala, Daniela Olivieri, "Deformation mechanisms and energy absorption of polystyrene foams for protective helmets", *Polymer Testing*, 21 (2002), 217–228.

[58] R. Willinger, D. Baumgartner, T. Guimberteau, "Dynamic characterization of motorcycle helmets: modeling and coupling with the human head", *Journal of Sound and Vibration*, (2000) 235(4), 611-625.

[59] S.K. Hui, T.X. Yu, "Modelling of the effectiveness of bicycle helmets under impact", *International Journal of Mechanical Sciences*, 44 (2002), 1081–1100.

[60] A S McIntosh, D Janda, "Evaluation of cricket helmet performance and comparison with baseball and ice hockey helmets", *British Journal of Sports Medicine*, 37(2003), 325-330.

[61] De-Shin Liu, Chia-Yuan Chang, Chin-Ming Fan, Shu-Lin Hsu, "Influence of environmental factors on energy absorption degradation of polystyrene foam in protective helmets", *Engineering Failure Analysis*,10(2003), 581–591.

[62] E.C. Chirwa, " Structural crashworthiness simulation of a rear end collision of a small European car", *International Journal of Crashworthiness*, 1996 (1),1, 21-35.

[63] J. Latchford, E.C. Chirwa, "Airbag head restraint system", *IMechE*, 214(2000), 229-241.

[64] Taian Chen, E.C. Chirwa, M. Mao, J. Latchford, "Rollover far side roof strength test and simulation", *Proceedings of the ICRASH 2006 Conference*, Athens, July 2006.

[65] Grzegorz Adamczyk, Ukasz Luboiński, "Epidemiology of football, related injuries" ***Epidemiologia urazów*****,** tom 2 (2002), number 3, 236-250.

[66] Anthony C. Francisco, Roger W. Nightingale "Comparison of soccer shin guards in preventing tibia fracture", *The American Journal of Sport Medicine*, 28 (2000), 2, 227-233.

[67] Shinichi Sakamoto "Research history of motorcycle leg protection", *SAE Transactions*, 99 (1990), 6, 1032.

[68] Donald E. Godshaw, "Knee pad construction", *US Patent*, 2006/0041986 A1, 2006.

[69] Noaki Hotta, "Knee protection airbag apparatus", *US Patent*, 2005/0062265 A1, 2005.

[70] A.A.A. Alghamdi, “Collapsible impact energy absorbers: an overview”, *Thin-Walled Structures*, 39 (2001), 189–213.

[71] A.A.A. Alghamdi, “Reinversion of aluminium frustra”, *Thin-Walled Structures*, 40 (2002), 1037–1049.

[72] A.A.N. Aljawi, A.A.A. Alghamdi, T.M.N. Abu-Mansour, M. Akyurt, “Inward inversion of capped-end frusta as impact energy absorbers”, *Thin-Walled Structures*, 43 (2005), 647–664.

[73] H. Hamada, K. Kameo, M. Sakaguchi, H. Saito, M. Iwamoto, “Energy-absorption properties of braided composite rods”, *Composites Science and Technology*, 60 (2000), 723-729.

[74] Shun Yi Jin, William Altenhof, “Comparison of the load/displacement and energy absorption performance of round and square AA6061-T6 extrusions under a cutting deformation mode”, *Proceedings of the ICRASH 2006 Conference*, Athens, July 2006.

[75] Guoxing Lu, Tongxi Yu, “Energy absorption of structures and materials”, *Woodhead Publishing Limited*, 2003.

[76] A. Kim, M.A. Hasan, S.H. Nahm, S.S. Cho, “Evaluation of compressive mechanical properties of Al-foams using electrical conductivity”, *Composite Structures*, 71 (2005), 191–198.

[77] E.C. Chirwa, J.Latchford, P. Clavell, “Carbon skinned aluminum foam nose cones for high performance circuit vehicles”, *International Journal of Crashworthiness*, 2003(8), 1, 107-114.

[78] L.R. Jenkinson, P. Simpkin, D. Rhodes, “Civil jet aircraft design”, *Butterworth Heinemann*, 1999.

[79] John D. Anderson, “Aircraft performance and design”, *McGraw-Hill*, 1999.

[80] Richard S. Shevell, ”Fundamentals of flight”, *Prentice Hall*, 1989.

[81] Daniel P.Raymer, “Aircraft design: a conceptual approach”, *American Institute of Aeronautics and Astronautics*, 1999.

[82] Norman S.Currey, “Aircraft landing gear design: principles and practice”, *American Institute of Aeronautics and Astronautics*, 1988.

[83] Denis Howe, “Aircraft loading and structural layout”, *Professional Engineering*, 2004.

[84] Gerhard Mellmann, “Aircraft comprising a rescue device”, *International Patent*, W0 03/099656A1.

[85] Hosford William, "Metal Forming Mechanics and Metallurgy", *Prentice Hall*, 1993.

[86] Fayek Osman, "Reusable Energy Dissipation Device", *Patent*, W0 2004/044450 A1, 2004.

[87] Vladimir Segal, "Apparatus for Strengthening Metals by Plastic Deformation", *SU Patent*, SU902884, 1982.

[88] L. R. Cornwell,K. T. Hartwig,R. E. Goforth, S. L. Semiatin "The Equal Channel Angular Extrusion Process for Materials Processing", *Materials Characterization*, 37 (1996), 295-300.

[89] Zubear Ahmed Khan, Uday Chakkingal, P.Venugopal "Analysis of forming loads, microstructure development and mechanical property evolution during equal channel angular extrusion of a commercial grade aluminium alloy", *Journal of Material Processing Technology*, 135(2003), 59-67.

[90] V.M. Segal, "Materials processing by simple shear", *Materials Science and Engineering A*, 197 (1995),157-164.

[91] J.R. Bowen, A. Gholinia, S.M. Roberts, P.B. Prangnell, "Analysis of the billet deformation behaviour in equal channel angular extrusion", *Materials Science and Engineering A*, 287 (2000) 87–99.

[92] V.M. Segal, "Equal channel angular extrusion: from macromechanics to structure formation", *Materials Science and Engineering A*, 271(1999), 322-333.

[93] V.M.Segal, K.T.Hartwig, R.E. Goforth, "In situ composites processed by simple shear", *Materials Science and Engineering A*, 224(1997), 107-115.

[94] A. Rosochowski, L. Olejnik, "Numerical and physical modelling of plastic deformation in 2-turn equal channel angular extrusion", *Journal of Materials Processing Technology*, 125–126 (2002), 309–316.

[95] B.S. Altan, G. Purcek , Miskioglu, "An upper-bound analysis for equal-channel angular extrusion", *Journal of Materials Processing Technology*, 168 (2005), 137–146.

[96] A.R. Eivani, A. Karimi Taheri, "An upper bound solution of ECAE process with outer curved corner", *Journal of Materials Processing Technology*, 182 (2007), 555–563.

[97] M.H. Paydara, M. Reihaniana, R. Ebrahimia, T.A. Dean, M.M. Moshksara, "An upper-bound approach for equal channel angular extrusion with circular cross-section", *Journal of Materials Processing Technology*, 198(2008), 48–53.

[98] V.M. Segal, "Engineering commercialization of equal channel angular extrusion", *Materials Science and Engineering A*, 386(2004), 269-276.

[99] R.Hill, "The mathematical theory of plasticity", *Clarendon Press*, 1985.

[100] T. Altan, R.J. Fiorentino, "Prediction of loads and stresses in closed die forging", *Journal of Engineering for Industry*, May 1971, 477-483.

[101] Orowan E., Scott F.H., Smith C.L., "A photoelastic dynamometer for rapidly varying forces", *Journal of Scientific Instruments*, 27 (1950), 117-122.

[102] Mori K., Osakada K., Fukuda M., "Measurement of contact pressure in metal forming by pressure sensitive film", *Journal of Engineering Materials and Technology*, 106 (1984), 127-131.

[103] Tuncer C., Dean T.A., "Surface stress measurement techniques in metal forming", *International Journal of Machine Tools Manufacture*, 1988, 28(4), 417-428.

[104] Cole I.M., Sandsome D.H., "A review of the application of pin-load cell pressure measurements techniques to metal deformation processes", *Proceedings of the 9th International MTDR conference*, 1968, 271-286.

[105] El-Behery, A.M. Lamble, Jhonson W., "The mesurement of container wall pressure and friction coefficient in axi-symmetric extrusion", *4th International MTDR Conference*, 1963, 319-335.

[106] Van Rooyen, Backofen W.A., "Friction in cold rolling", *Journal of the Iron and Steel Institute*, 1957 (186), 235-244.

[107] F.H. Osman, E.W. Merrygold, M.S. Loveday, "Stress distribution at contact surfaces in forming operations", *The 1st ESAFORM Conference on Metalforming*, 1998.

[108] R.Lupoi, F.H.Osman, "Under surface pressure sensing technique for the evaluation of contact stresses", *Journal of Material Processing Technology*, 2005, 164-165, 1537-1543.

[109] R.Lupoi, F.H. Osman, "Use of concealed pressure pins to determinate contact stresses in ring compression", *The 8th ESAFORM Conference on Metalforming*, Cluj- Napoca (RU), April 2005, 519-522.

[110] Hasan Sofuoglu, Jahan Rasty, "Flow behaviour of plasticine used in physical modelling of metalforming processes", *Tribology International* , 3 (2000), 523–529.

[111] P.Mazzoldi, M.Nigro, C.Voci, "Fisica Volume 1", *Edises*, 1998.

[112] Kenji CHIJIIWA, Yotaro HATAMURA, Nobuki HASEGAWA, “Characteristics of Plasticine Used in the Simulation of Slab in Rolling and Continuous Casting”, *Transactions of the Iron and Steel Institute of Japan*, 21, 3(1981), 178-186.

APPENDIX A: Overview of energy absorption devices

In the structural field, energy absorption devices are basically implemented to provide protection against earthquakes and high impact loads. When considering protection against earthquakes, dampers based on dry friction can be employed, such as the EDR device, the Sumitomo energy absorber or the Gregorian friction damper. Also, special designs to retrofit old structures were discovered, aimed at reducing a damper invasivity. However, arrangements based on plastic deformation provide alternatives, such as general metallic dampers and lead extrusion devices. Furthermore, the structural protection can also be improved by the employment of devices based on viscoelasticity and other techniques that lead to the design of tuned mass/liquid dampers and active bracing systems. In the chart, devices were categorized to be more suitable or more commonly used for different applications, such as buildings and bridges. On the other hand, when impact loads are considered, the design of armoured walls or protective shelters is the most common solution. For those methods, different material are usually employed, such as steel, concrete and composites, or a combination of them in order to enhance properties and performance. Buildings can be also locally reinforced by the employment of external retrofits, such as steel spiral or bars, in order to enhance the ductility of the structure, therefore to increase earthquake resistance.

In the transports field, energy absorption devices commonly employed for airplanes landing were searched in literature. Arrangements and designs, for such application, are usually complex and laborious as they usually incorporate fragile internal mechanisms, and absorb high amounts of energy during landing operations. On the other hand, such absorbers must be also capable to ensure the damping of low energies, in order to increase the comfort of passengers during taxiing motions. However, dissipation techniques were identified to be mainly through devices based on steel springs, rubber, air, liquid spring and ole-pneumatic springs.

In the personal safety field, devices discovered in literature were categorized upon the part of the body to be protected. For chest protection, different types of body armours are reported, such as Ceramic/metal armours, fabric armours, armours made from Twaron-Kevlar-Spectra and innovative designs such as the Lorica and Sali vests.

Helmets are also used to provide head protection in risky industrial environments and in sport (i.e. in rugby, hockey, football, baseball, cricket, cycling and motorcycling). On the other hand, head restraints are usually employed to provide protection against rear car accidents. To protect legs and knees, in sport external shin guards are normally employed, commonly made out from Fibreglass, Kevlar and plastic in general. When motorcycle accidents are considered, protection can be achieved by devices attached to the motorbike chassis. Side protection devices, hard leg protectors and crush bars are an example. Also, a list of devices is tabulated in order to protect the month, hands and eyes for any loading condition. Furthermore, for preventing foot injuries, different types of shoes are used, either in sport (i.e. running, tennis, soccer, ski, climbing, skating) or for general safety in industrial environments, such as shoes with a reinforced toecap.

Common material such as rubber mats, rubber caps, polystyrene chips and wrapping paper are practical energy dissipators, usually simple in design and cheap in price.

To complete the overview, also other dissipation methodology and ideas that may find application across several fields are considered. Techniques such as the axial deformation of a conical element or axial cutting of a hollow cylinder can be used in order to inspire the design of energy absorption devices suitable for many applications.

APPENDIX B: ANSYS (8.0) log file

(1)

```
fini
/sys,rm *.jpg
/sys,erase *.jpg
/clear
/prep7

mu=.2              !friction coefficient

! Define Body 1    !MATERIAL: LEAD
/triad,off ! turn off the global triad display
/pbc,f,1

k,1,-10,0,0
k,2, 0,0,0
k,3, 0,5.4,0
k,4,-10,5.4,0

a,1,2,3,4
aesize,1,.5

! Create rigid target element 1

et,2,169
type,2
r,2
real,2
mat,2
mp,mu,2,.2

n,1,-20,0,0
n,2, 0,0,0
n,3, 0,23,0
n,6, -5,0,0

tshap,line
e,2,1
tshap,line
e,3,2

tshap,pilot
e,6

! Create rigid target element 2

et,6,169
type,6
r,3
real,3
mat,2
mp,mu,2,.2

n,4, -10,23,0
n,5, -10,5,0
```

(2)

```
tshap,line
e,5,4
tshap,pilot
e,5

! Mesh Body 1

et,1,106
type,1
mp,ex,1,14000
mp,nuxy,1,.45
tb,biso,1
tbdata,1,10,0
mat,1
real,1
mp,ex,1,14000
mp,nuxy,1,.45
tb,biso,1
tbdata,1,10,0

real,1
amesh,1

! Create flexible contact 1

esel,none
nsel,none
et,3,171
type,3
real,2              ! same as rigid target
mat,2
esel,s,type,,1
nsle,s
nsel,r,loc,y,0
nplot
esln,s,0
esurf

*get,emax,elem,,num,max

! Create flexible contact 2
esel,none
nsel,none
et,4,171
type,4
real,2              ! same as rigid target
mat,2
esel,s,type,,1
nsle,s
nsel,r,loc,x,0
nplot
esln,s,0
esurf

*get,emax,elem,,num,max
```

(3)

```
! Create flexible contact 3
esel,none
nsel,none
et,5,171
type,5
real,3              ! same as rigid target
mat,2
esel,s,type,,1
nsle,s
nsel,r,loc,x,-10
nplot
esln,s,0

esurf

*get,emax,elem,,num,max

! Apply The Displacement

nsel,s,loc,y,5.4
d,all,uy,-.2
allsel
eplot
time,200
nsubst,100,10000,10
lswrit,1

save

/solu
solcontrol,on,on
nlgeom,on

lssolve,1
```

APPENDIX C: Filtering of experimental results

Static UREAD loading behaviours, shown in Chapter 5, had revealed a level of scatter. It may be coming from a certain magnitude of noise, self-created by the in-house instrumentation (load cell and data acquisition system). In order to obtain a final confirmation of such hypothesis, an extrusion process was performed by using the R7x7 channel, in this case for a full stroke 24.7mm. The hydraulic forging press was used, but load readings were obtained by employing both the press load cell and a 5kN commercial load cell, which was positioned between the UREAD device and the punch

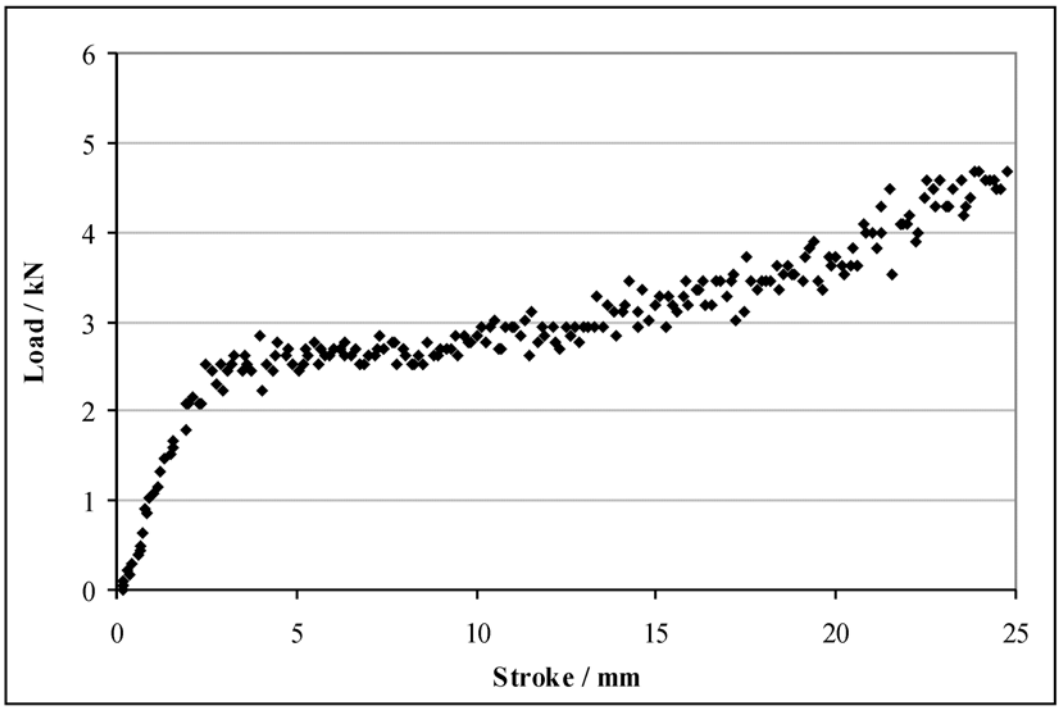

Figure C 1 Experimental results with by the press load cell - GR (7,7,37.5)-ML(11)-DF(24.7)

of the press. Such load cell works by the same principles as the in-house arrangement, but strain gauges include further developments such as temperature compensators. Results of such extrusion process, by the press load cell, are shown in Figure C1. On the other hand, Figure C2 shows results for the same extrusion process in Figure C1, but using the commercial load cell. The two trends are very similar and force values compare well, but results by the commercial load cell do not reveal scatter. As a result,

it can be concluded that such uneven distributions are caused by instrumentation noise, and they do not rely upon the nature of UREAD channels behaviours.

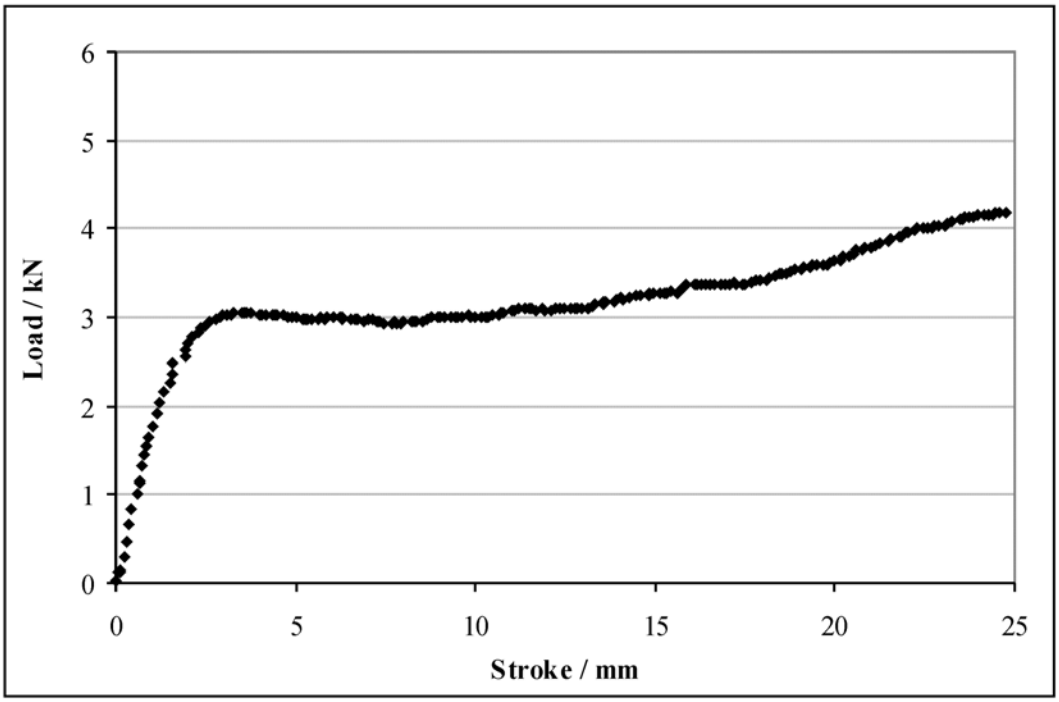

Figure C 2 Experimental results with by the external load cell - GR (7,7,37.5)-ML(11)-DF(24.7)

Therefore, experimental distributions can be filtered from the instrumentation noise. For such a work, the software MATLAB can be used, through the commands “butter” and “filter”. The first one creates a filter function, while the second one uses such function to filter a set of data points. Figure C3 shows an example of the filtering operation. The graph reports the experimental results in Figure 5.11, for the GR (10,10,42)-ML(11)-DF(30) test; along with a representation with filtered points by MATLAB. It can be seen from the graph that a substantial reduction of scatter is therefore achieved.

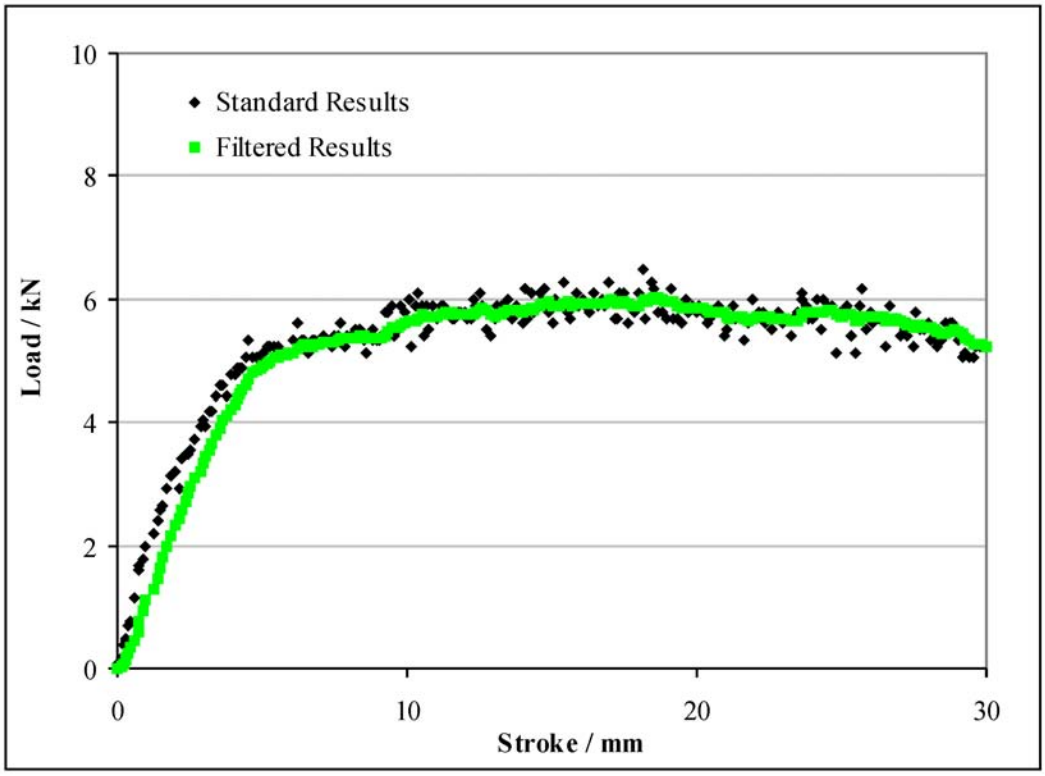

Figure C 3 Filtered experimental distribution - GR (10,10,42)-ML(11)-DF(30)

APPENDIX D: UREAD devices technical drawings

- Devices with circular cross-sectional channels (Tools Number 1, 2, 3)
- Devices with square cross-sectional channels (Tools Number 4, 5, 6)

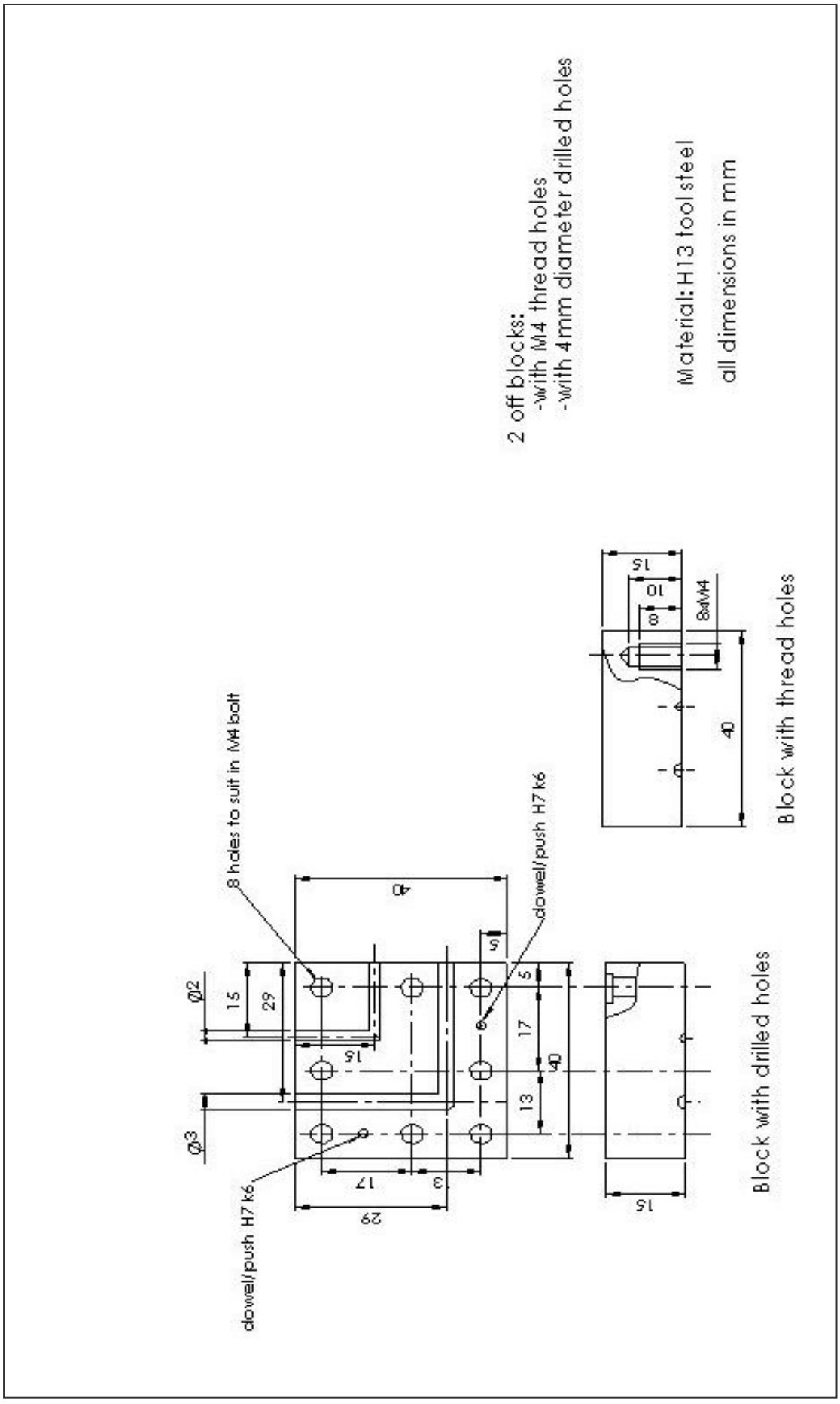

Figure D 1 Tool Number 1

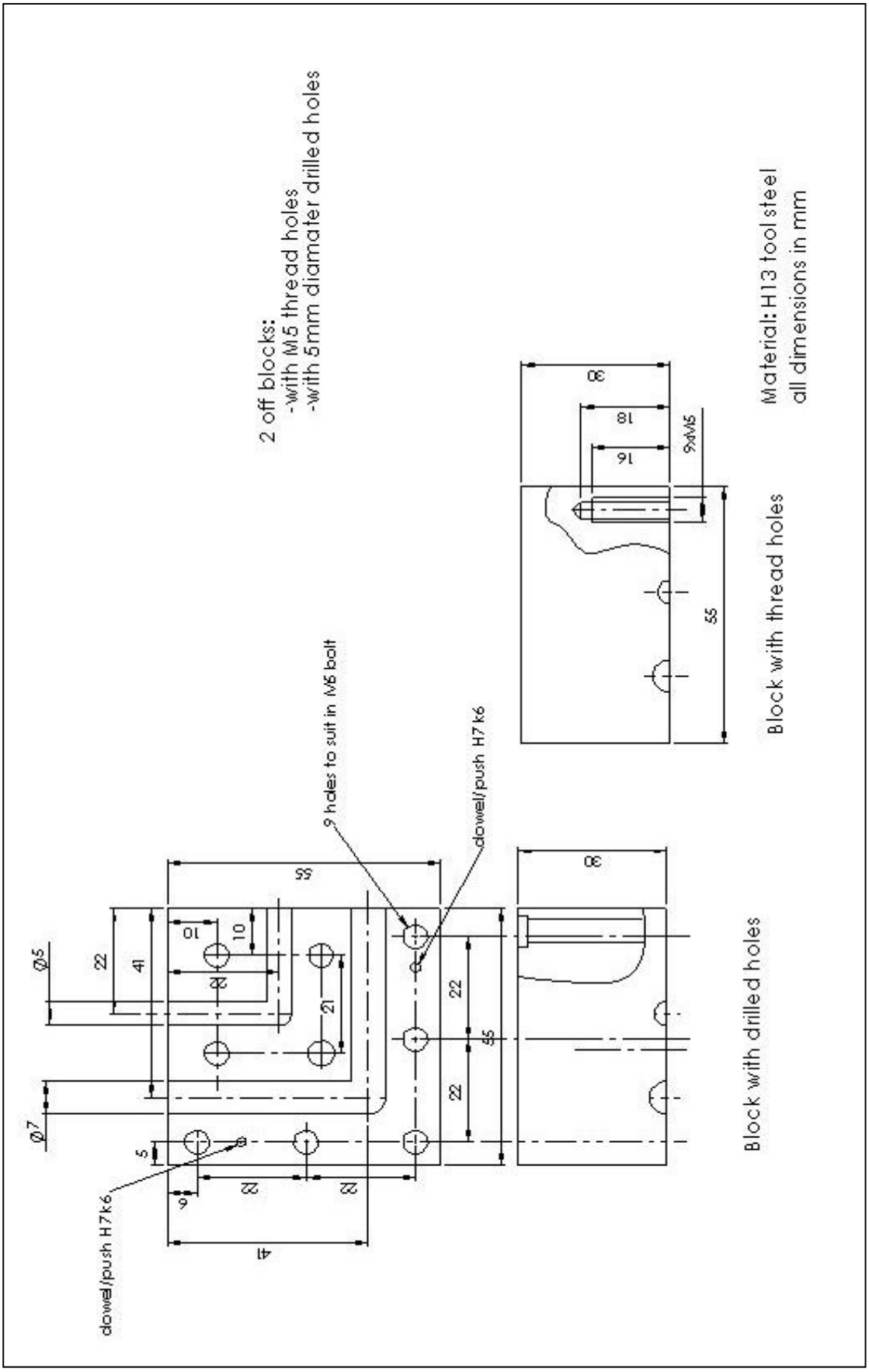

Figure D 2 Tool Number 2

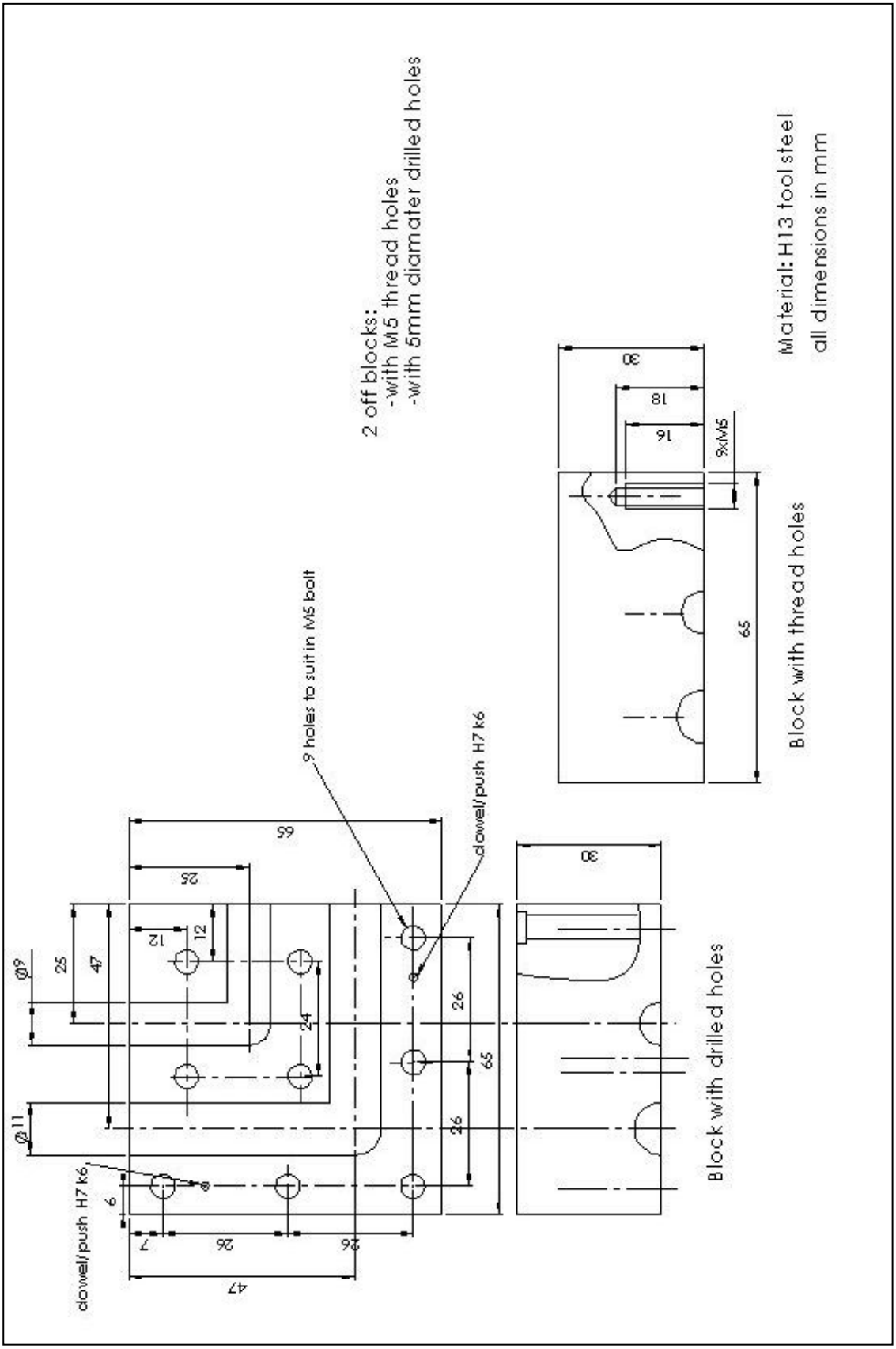

Figure D 3 Tool Number 3

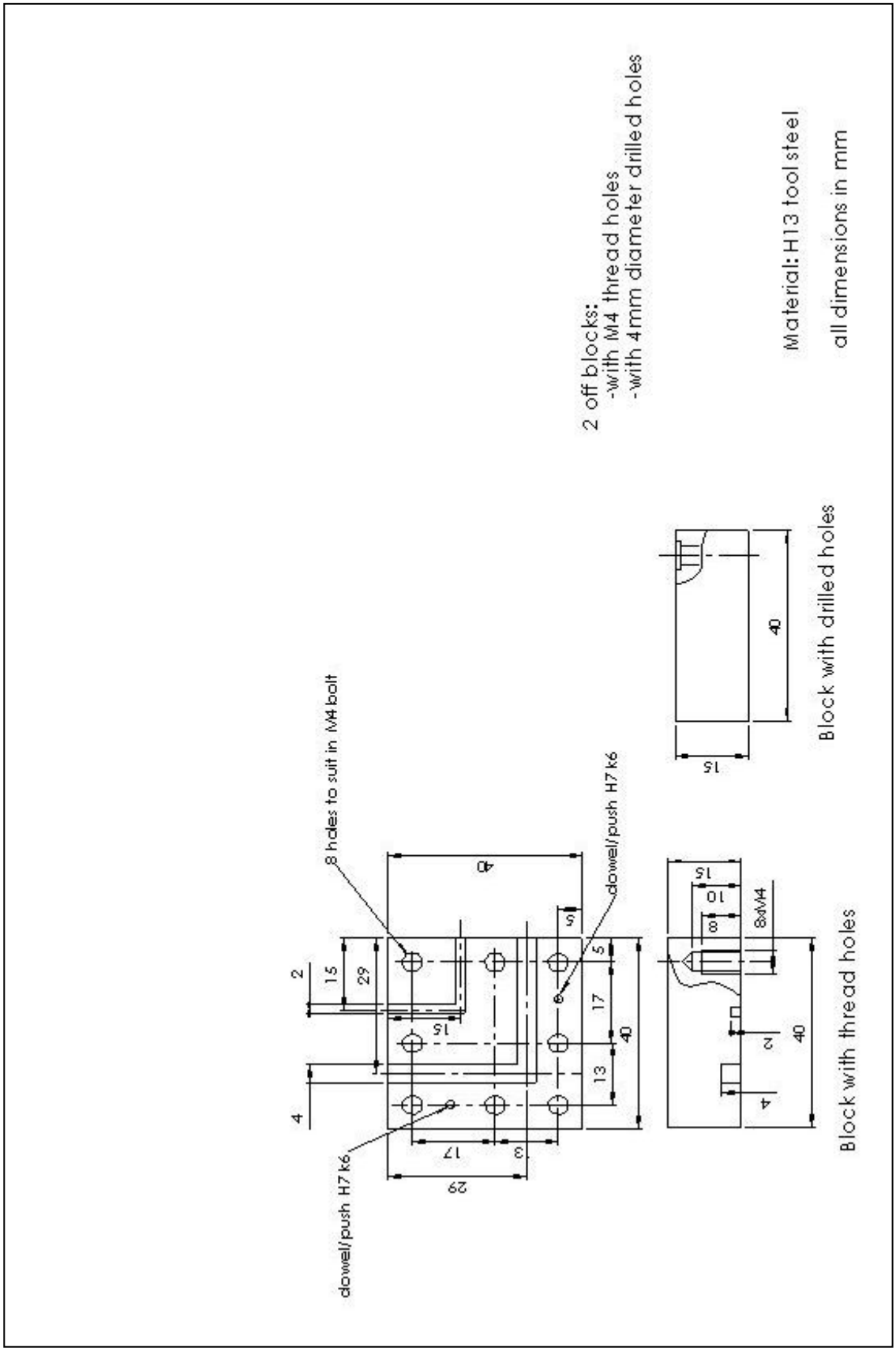

Figure D 4 Tool Number 4

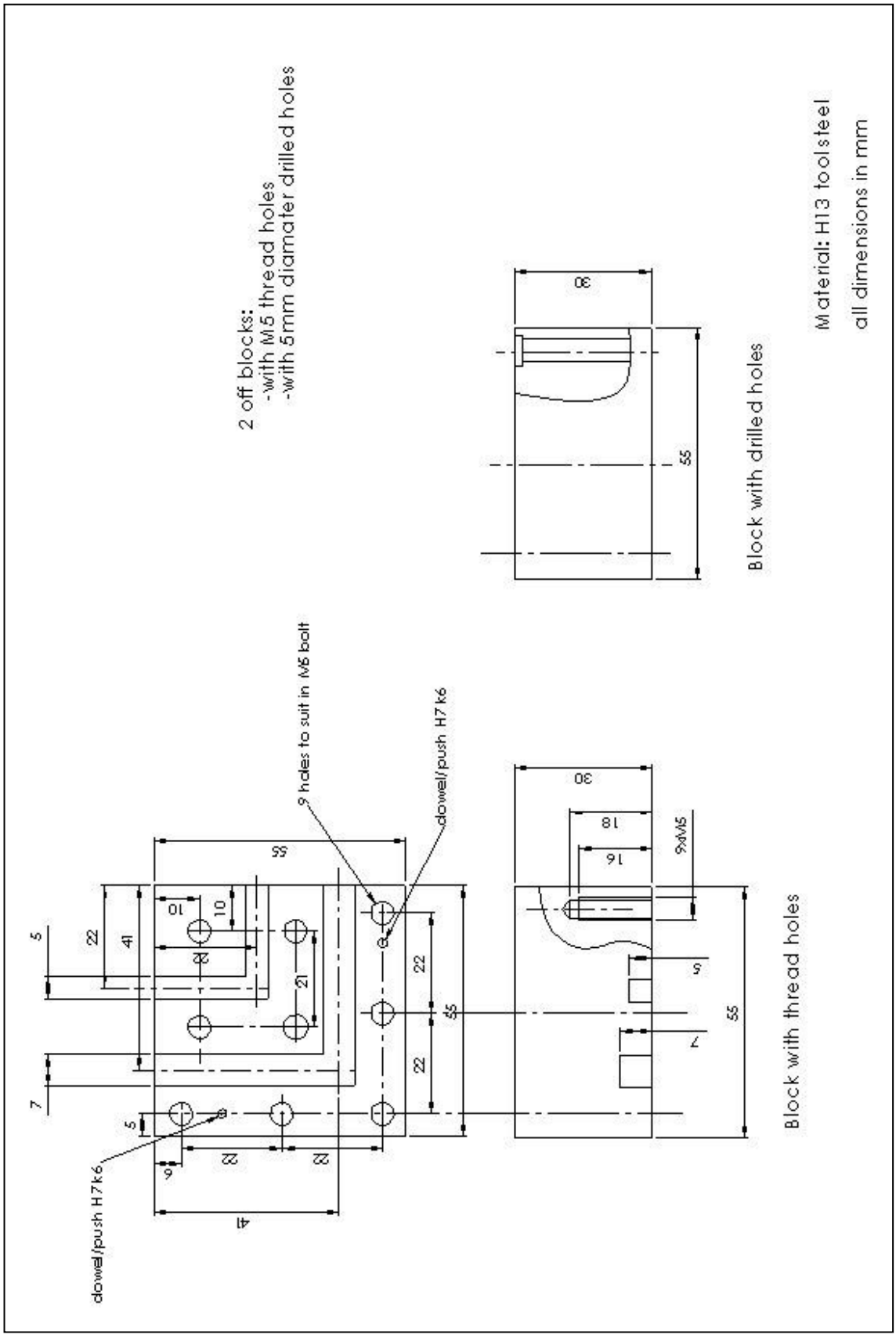

Figure D 5 Tool Number 5

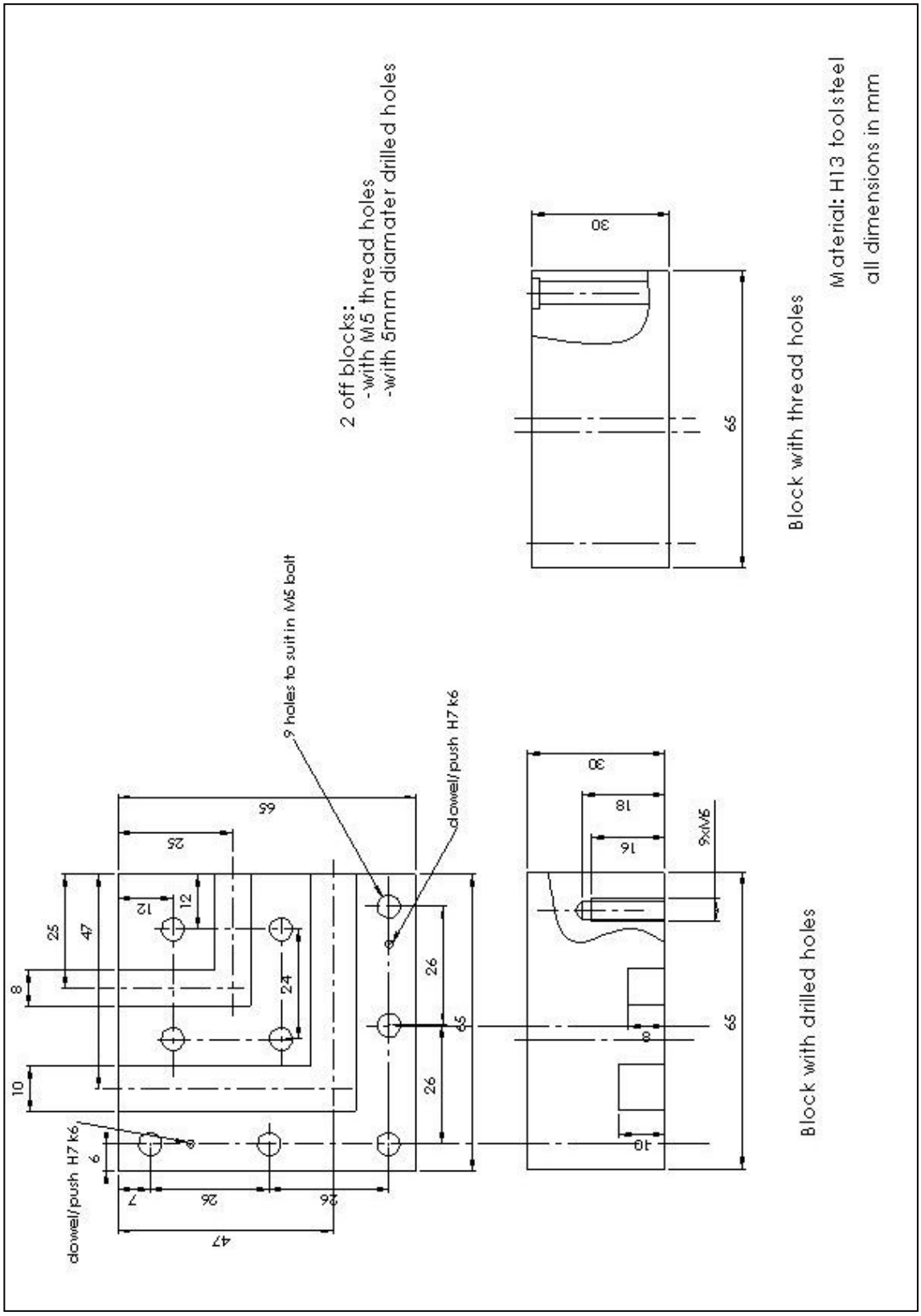

Figure D 6 Tool Number 6

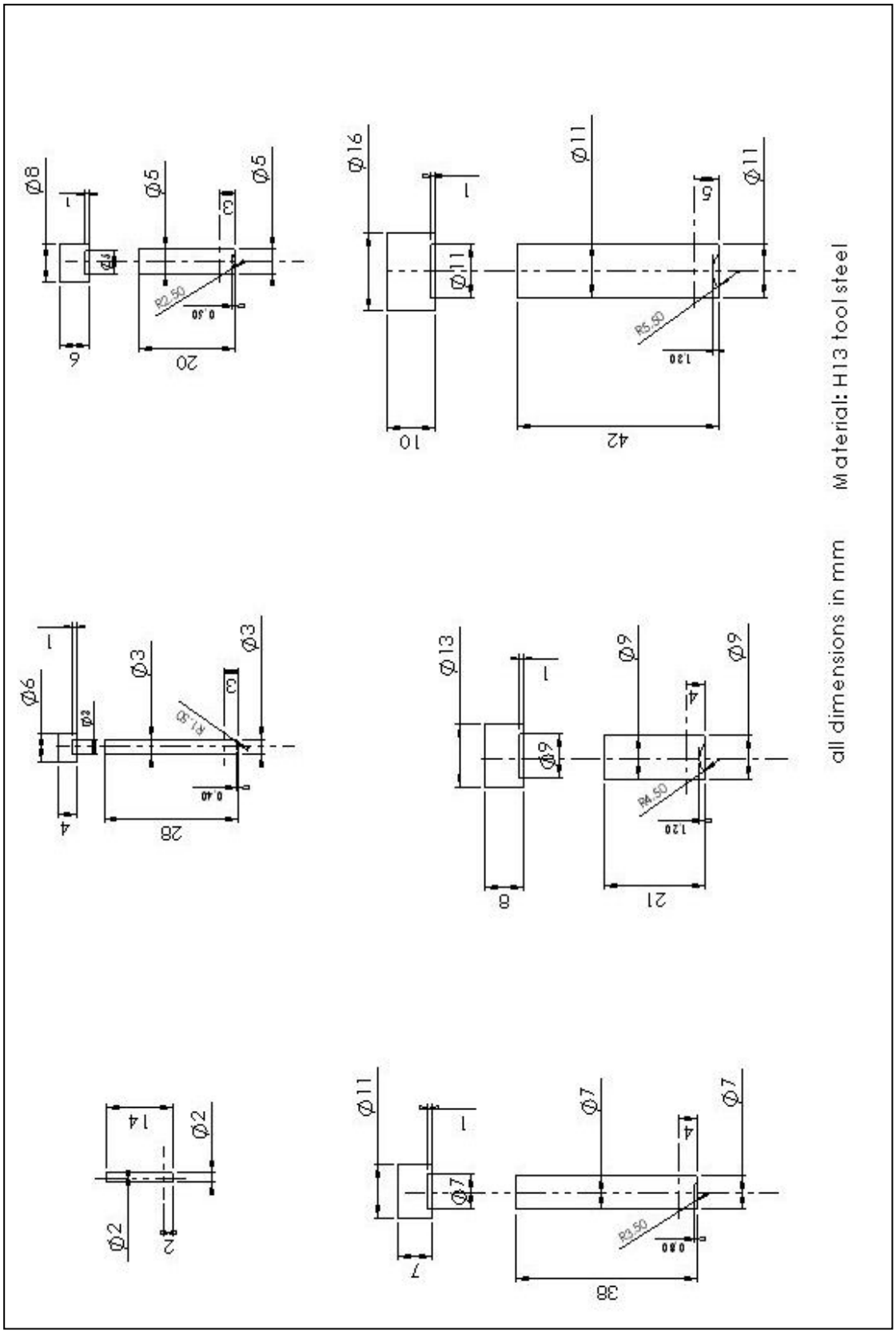

Figure D 7 Circular cross sectional area punches

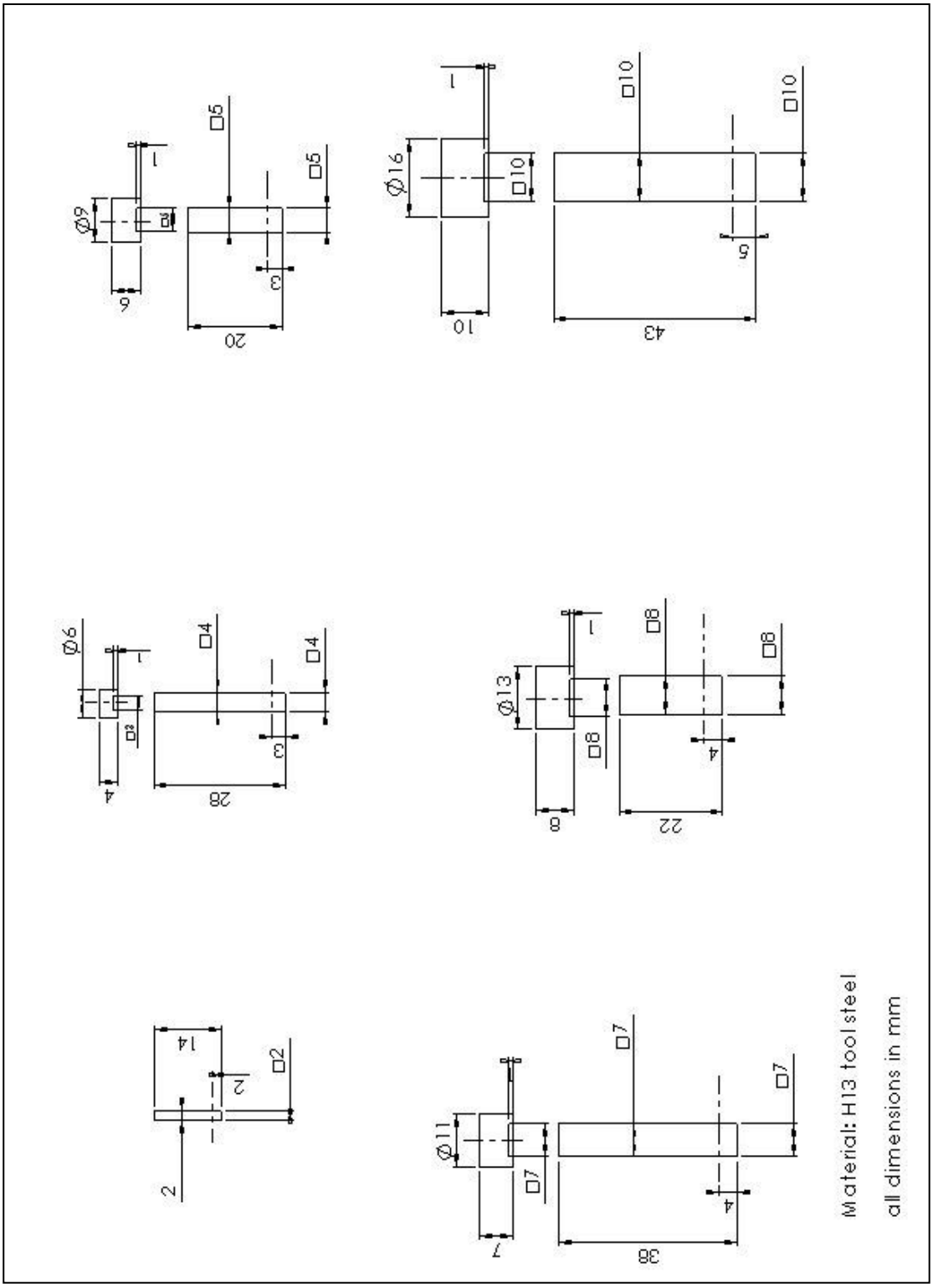

Figure D 8 Square cross sectional area punches

APPENDIX E: SPMD technical drawings

- Device 1 (SPMD with circular cross-section channels, D=15mm)
- Device 2 (SPMD with circular cross-section channels, D=12mm)
- Device 3 (SPMD with square cross-section channels, 12x12mm)

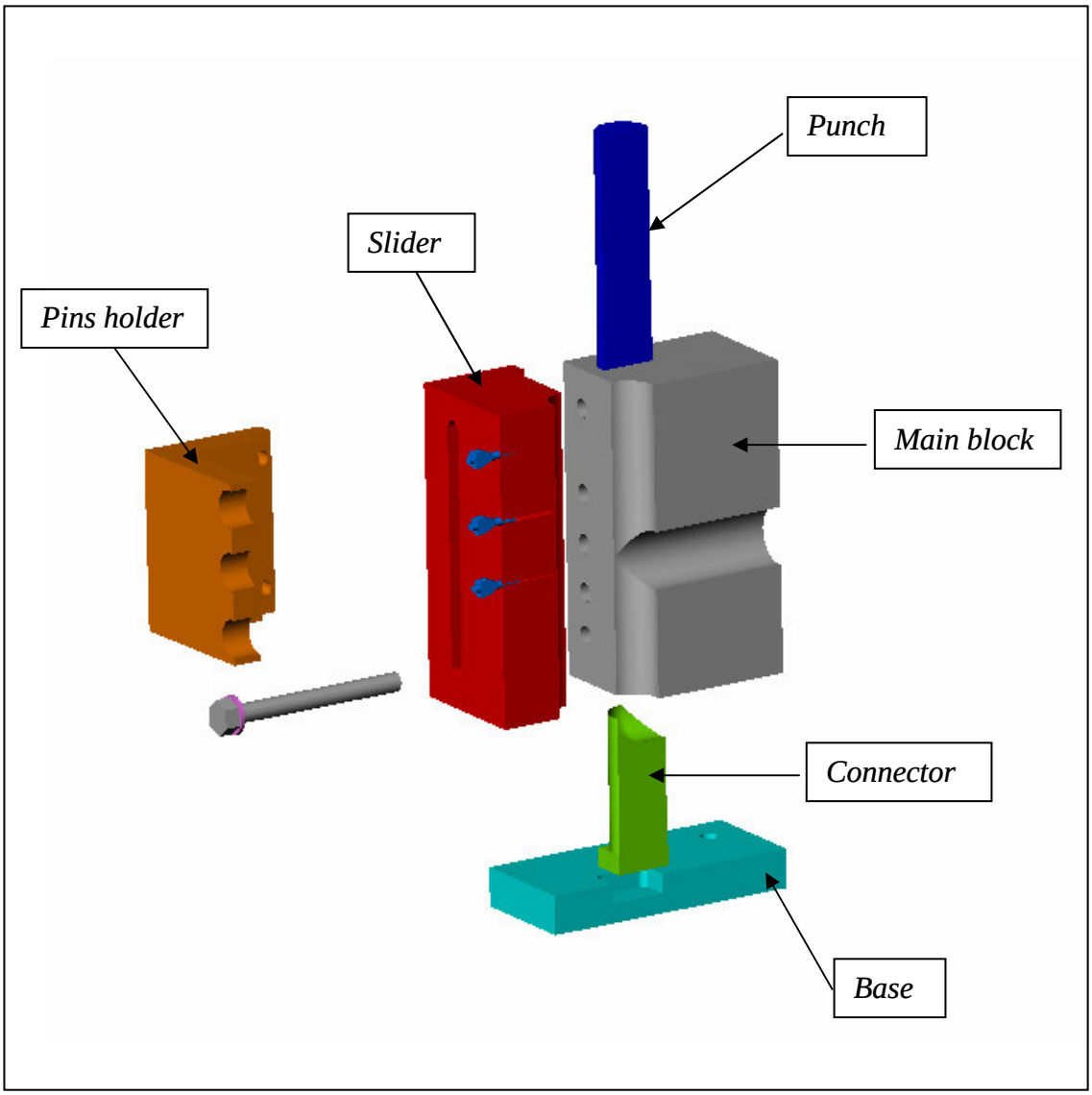

Figure E 1 Side Pressure Measuring Device - exploded view

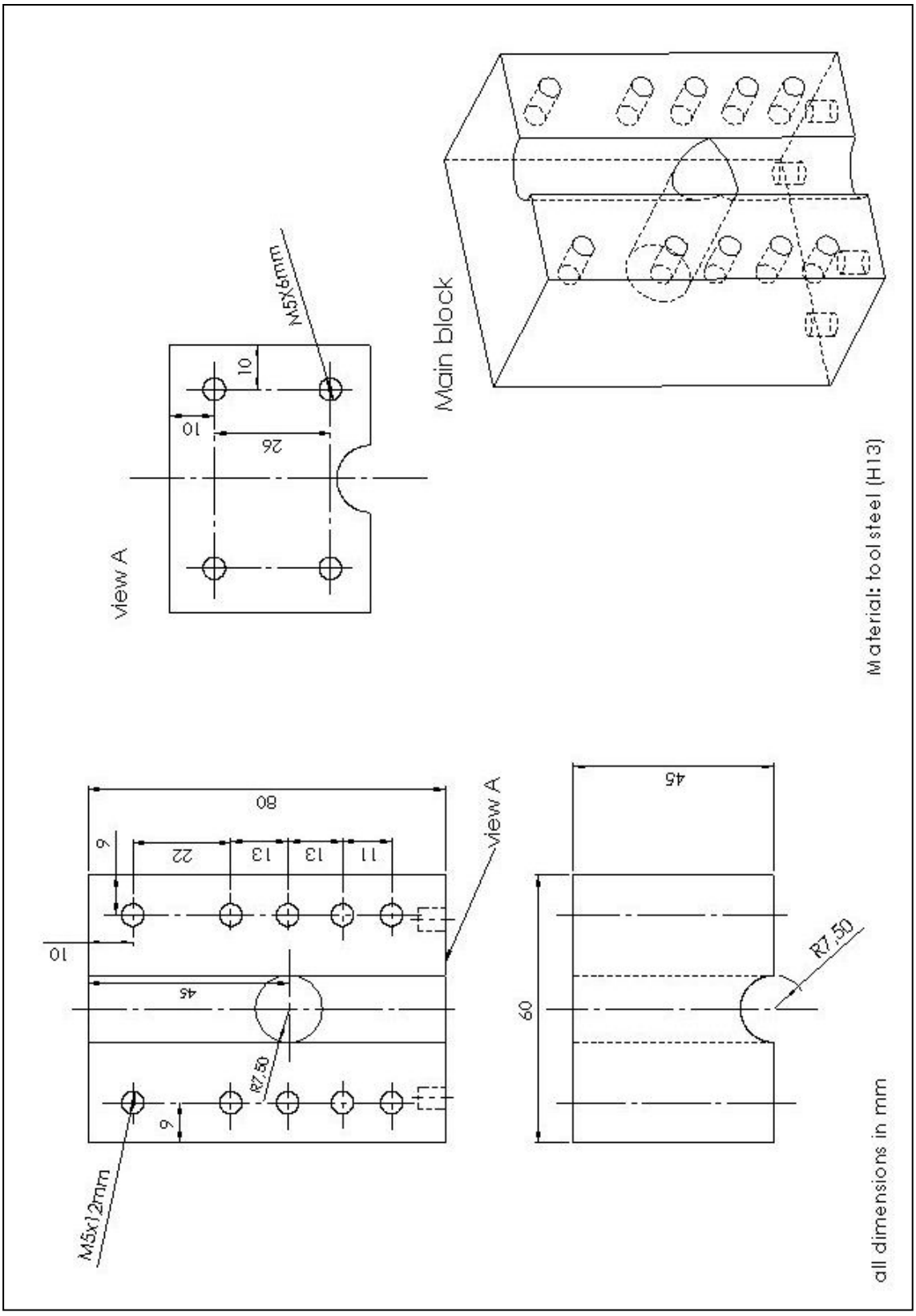

Figure E 2 Main block - device 1

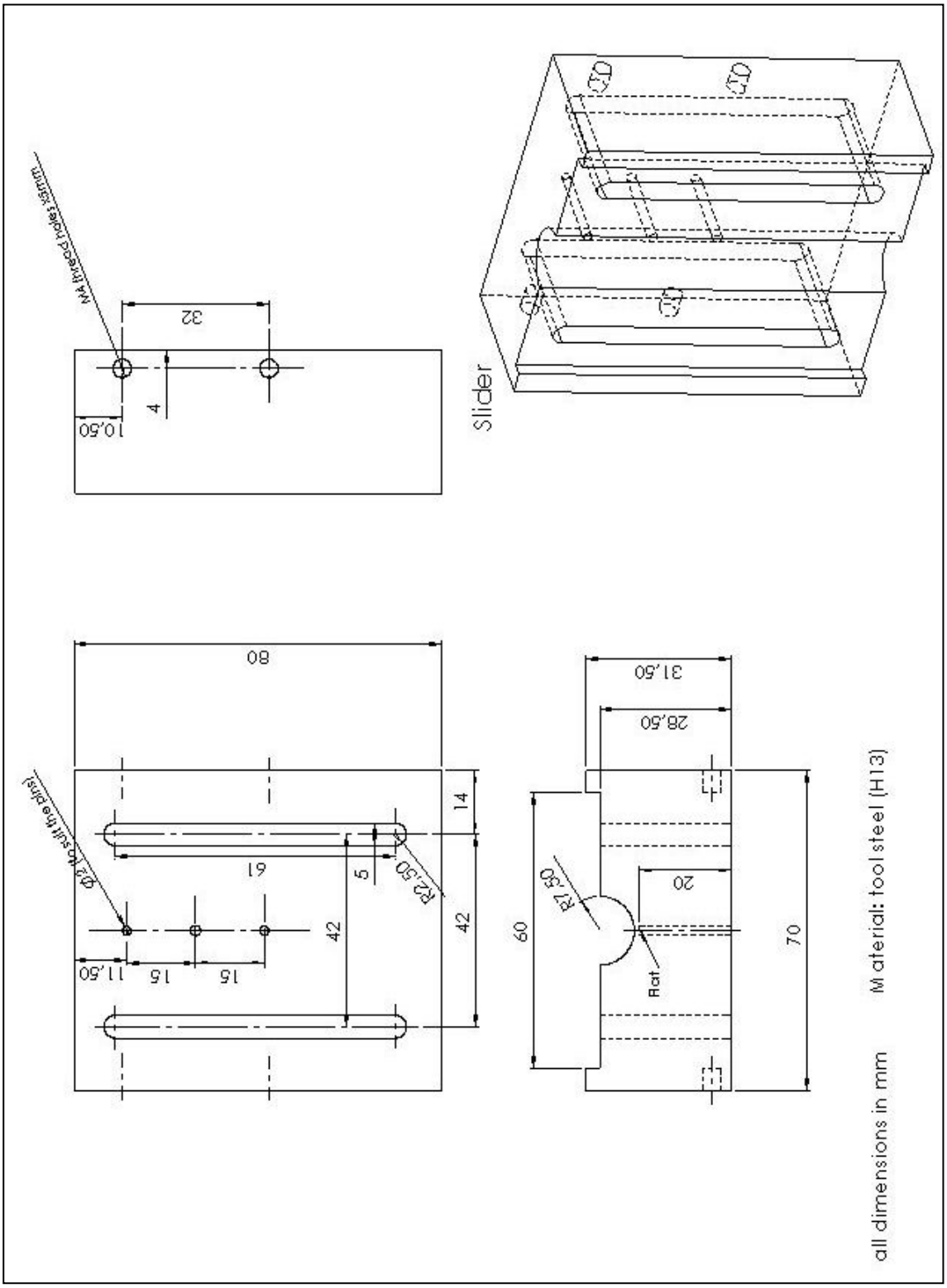

Figure E 3 Slider - device 1

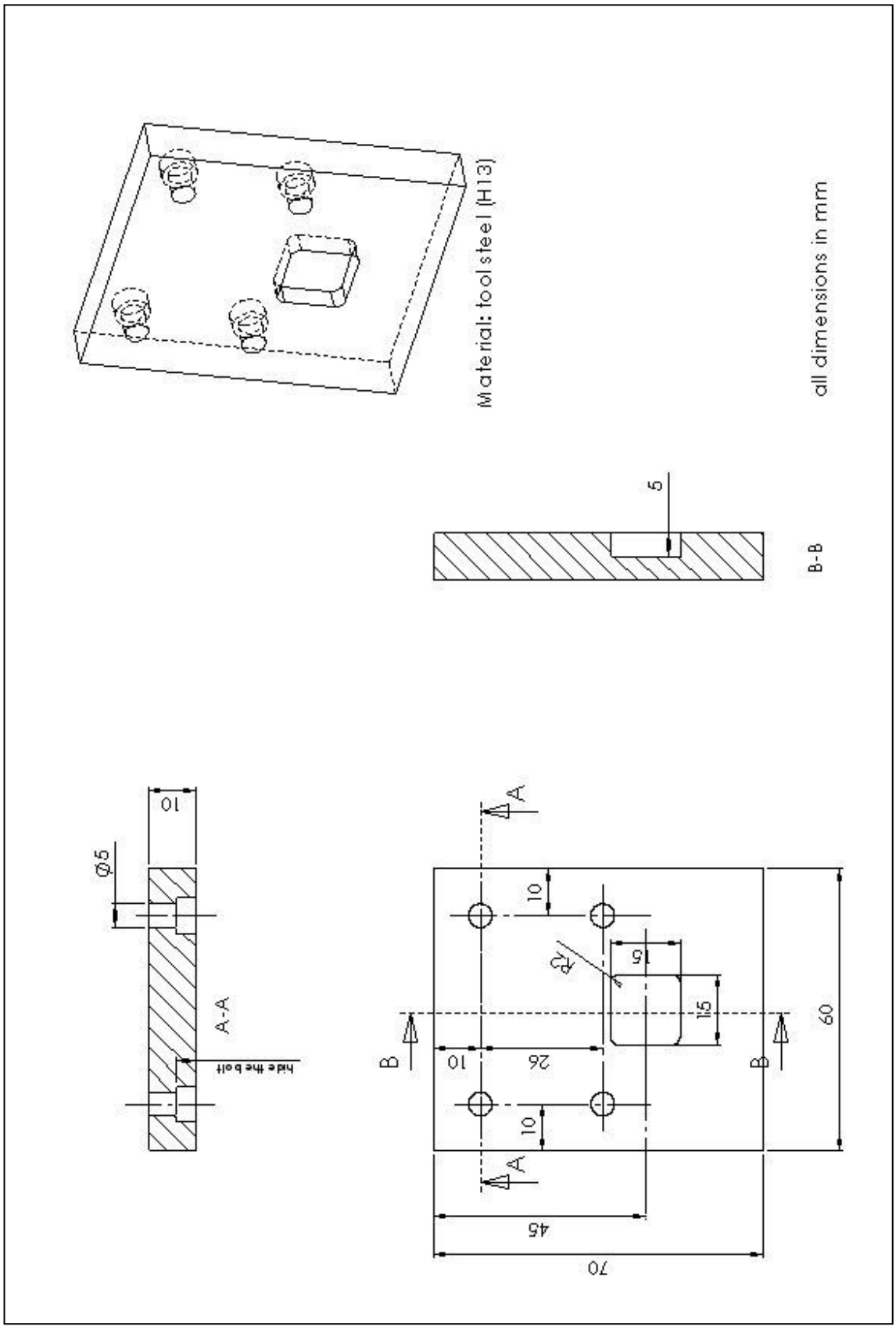

Figure E 4 Base - device 1

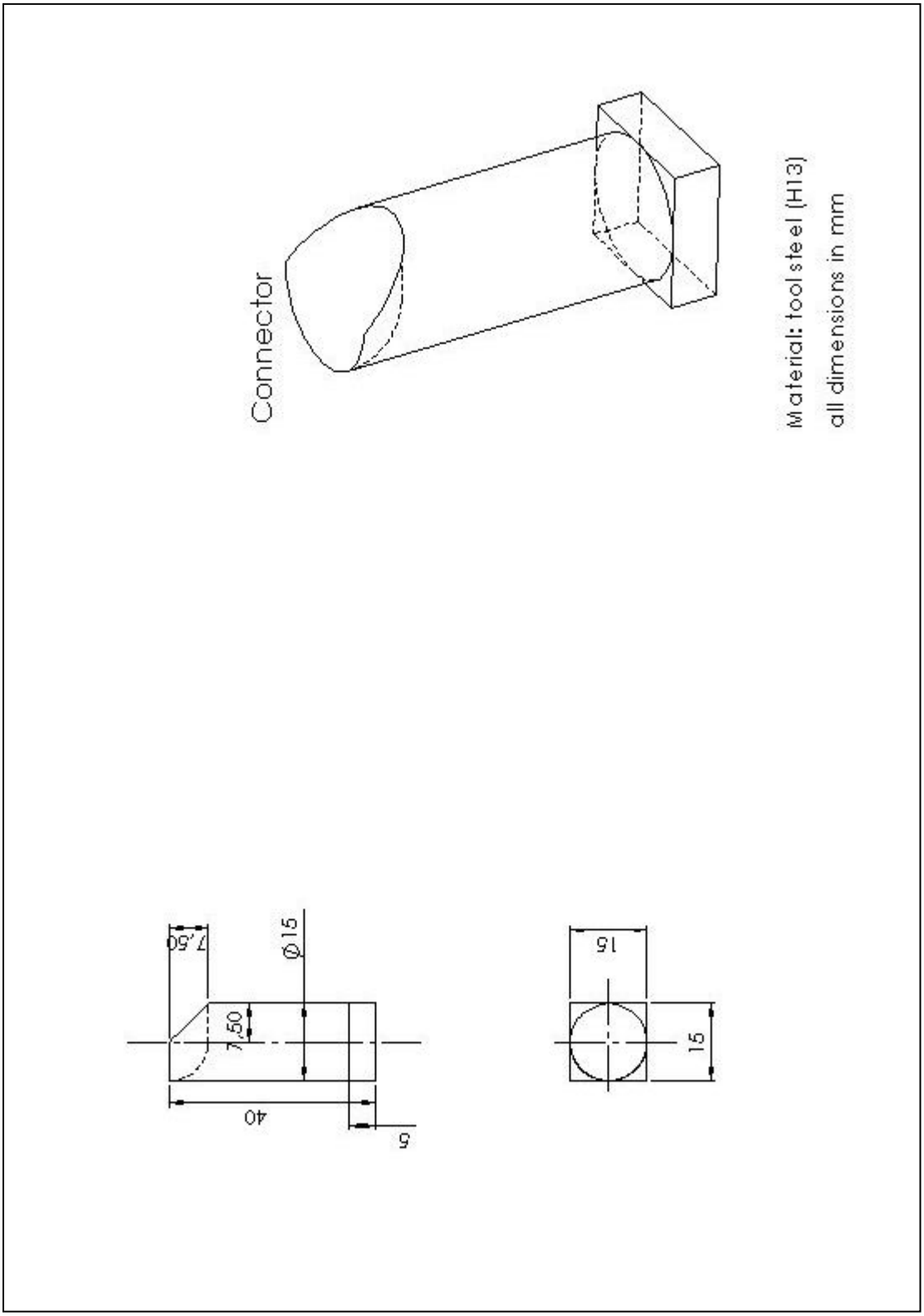

Figure E 5 Connector - device 1

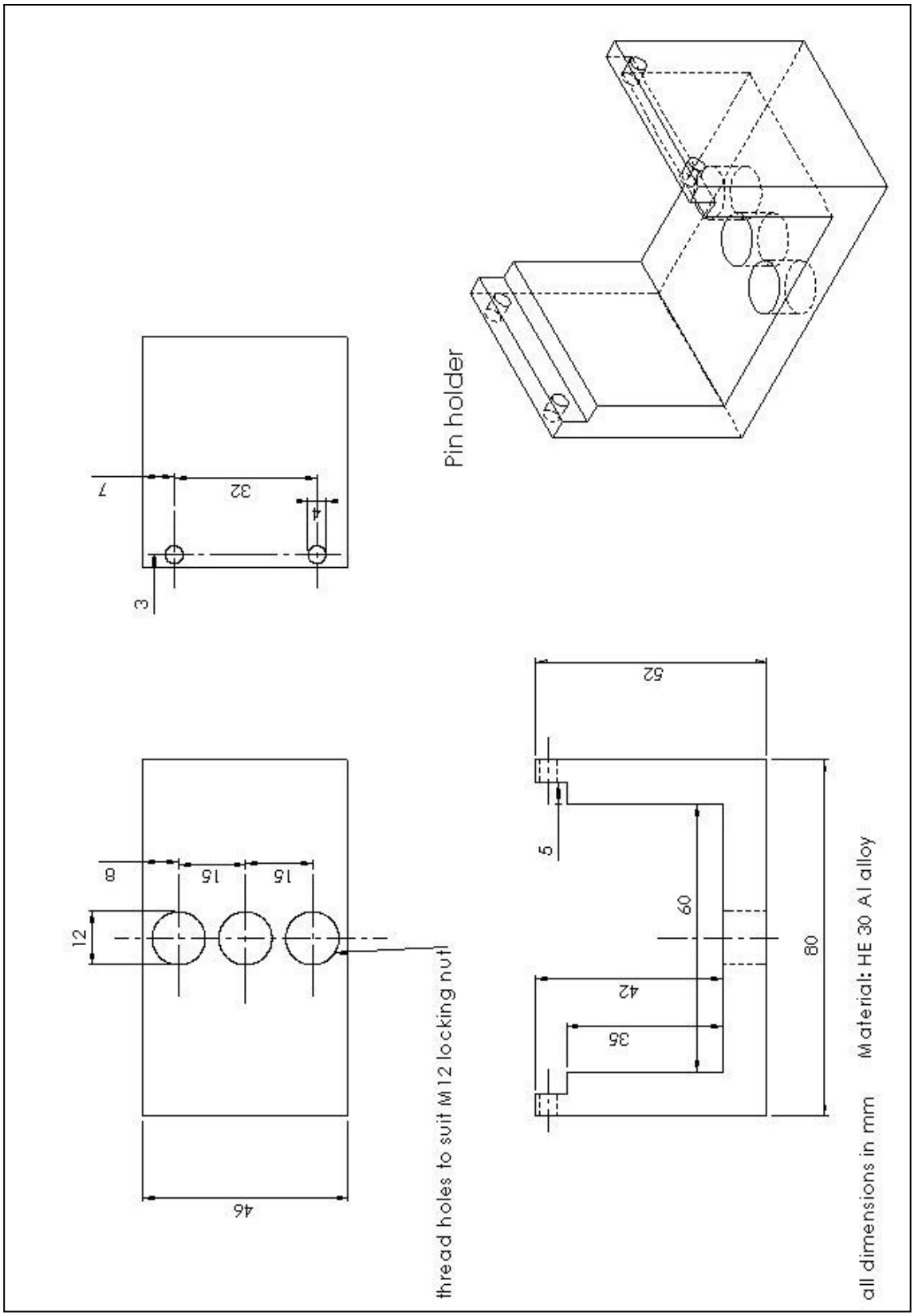

Figure E 6 Pins holder - device 1

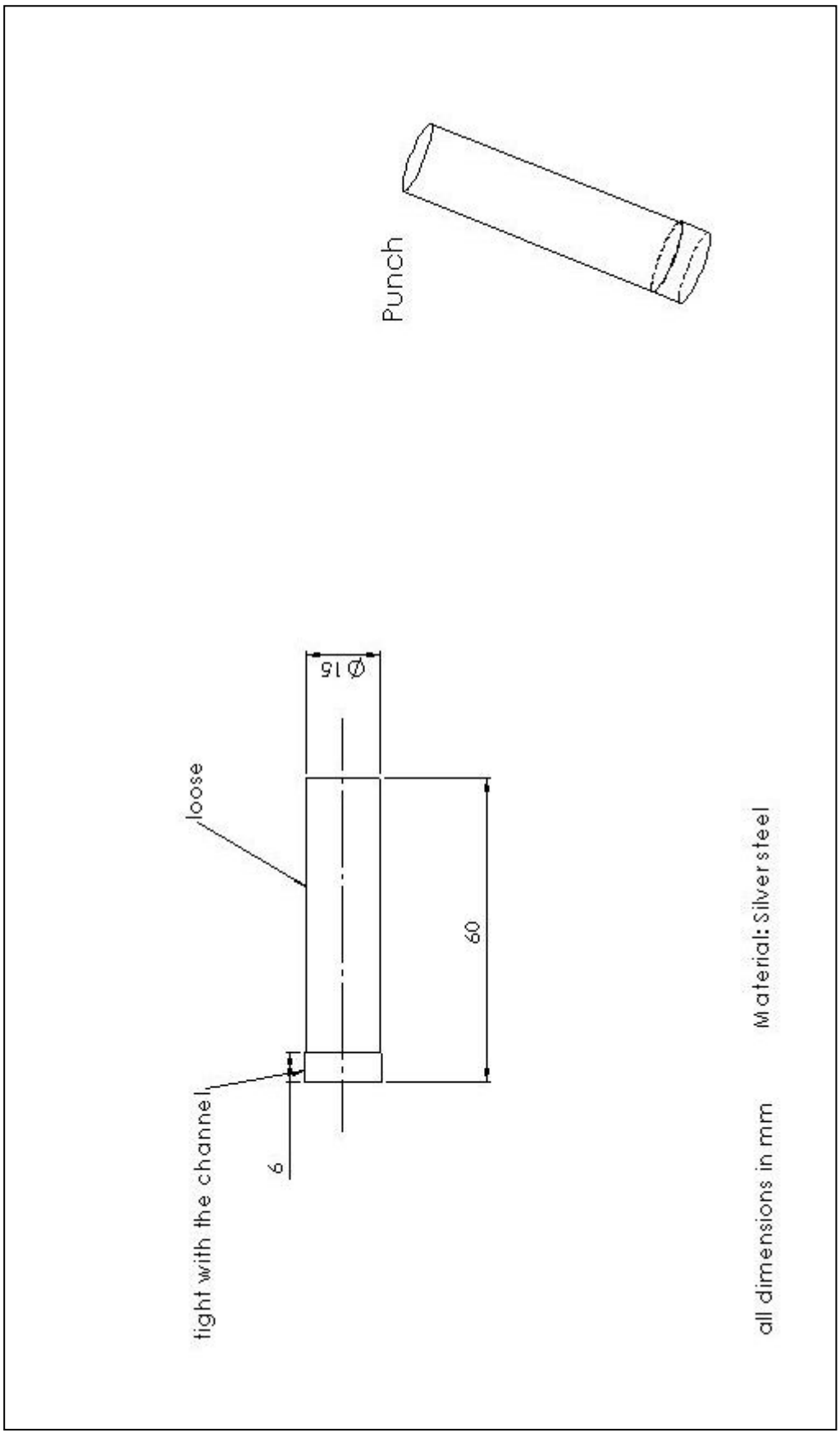

Figure E 7 Punch - device 1

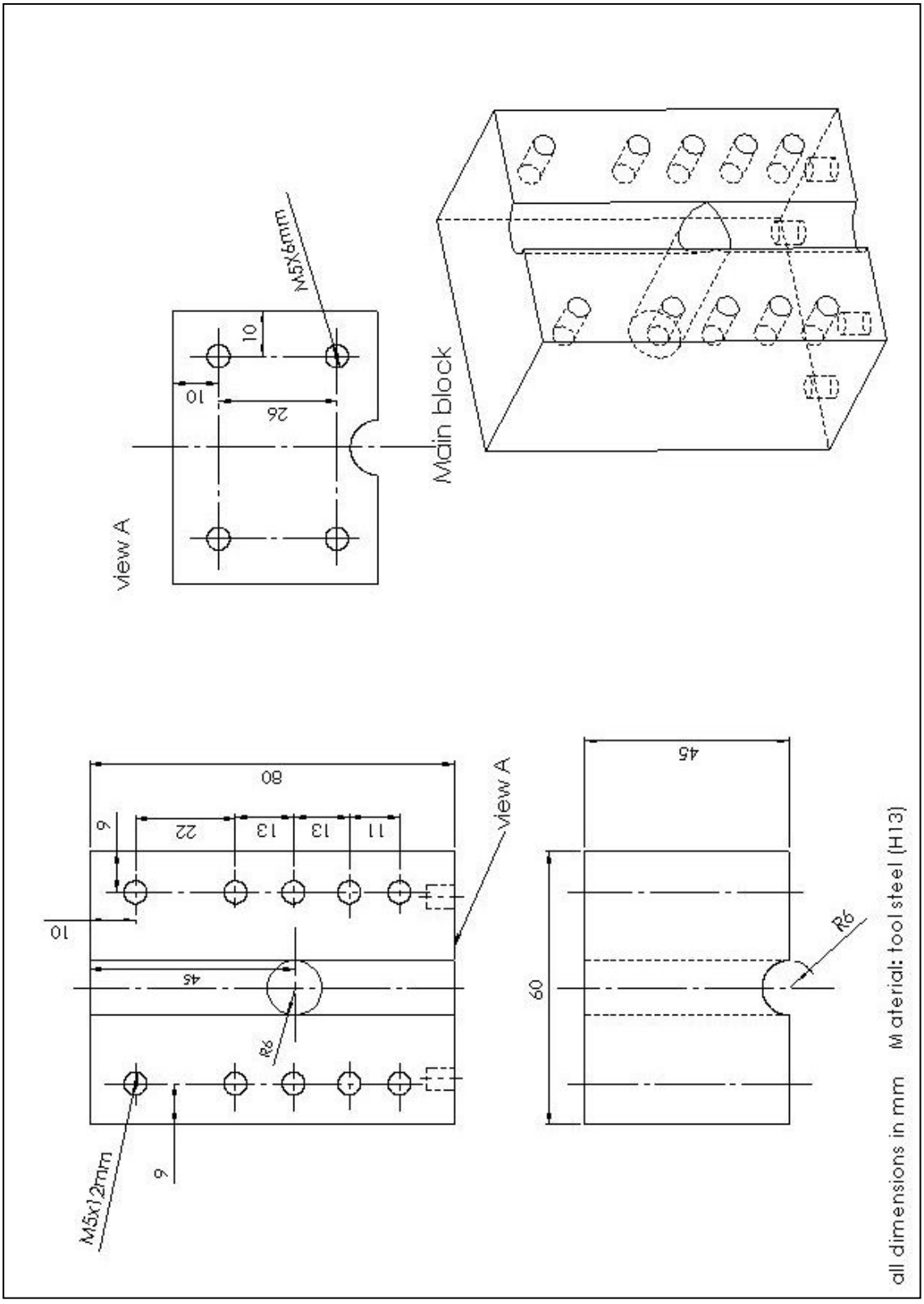

Figure E 8 Main block - device 2

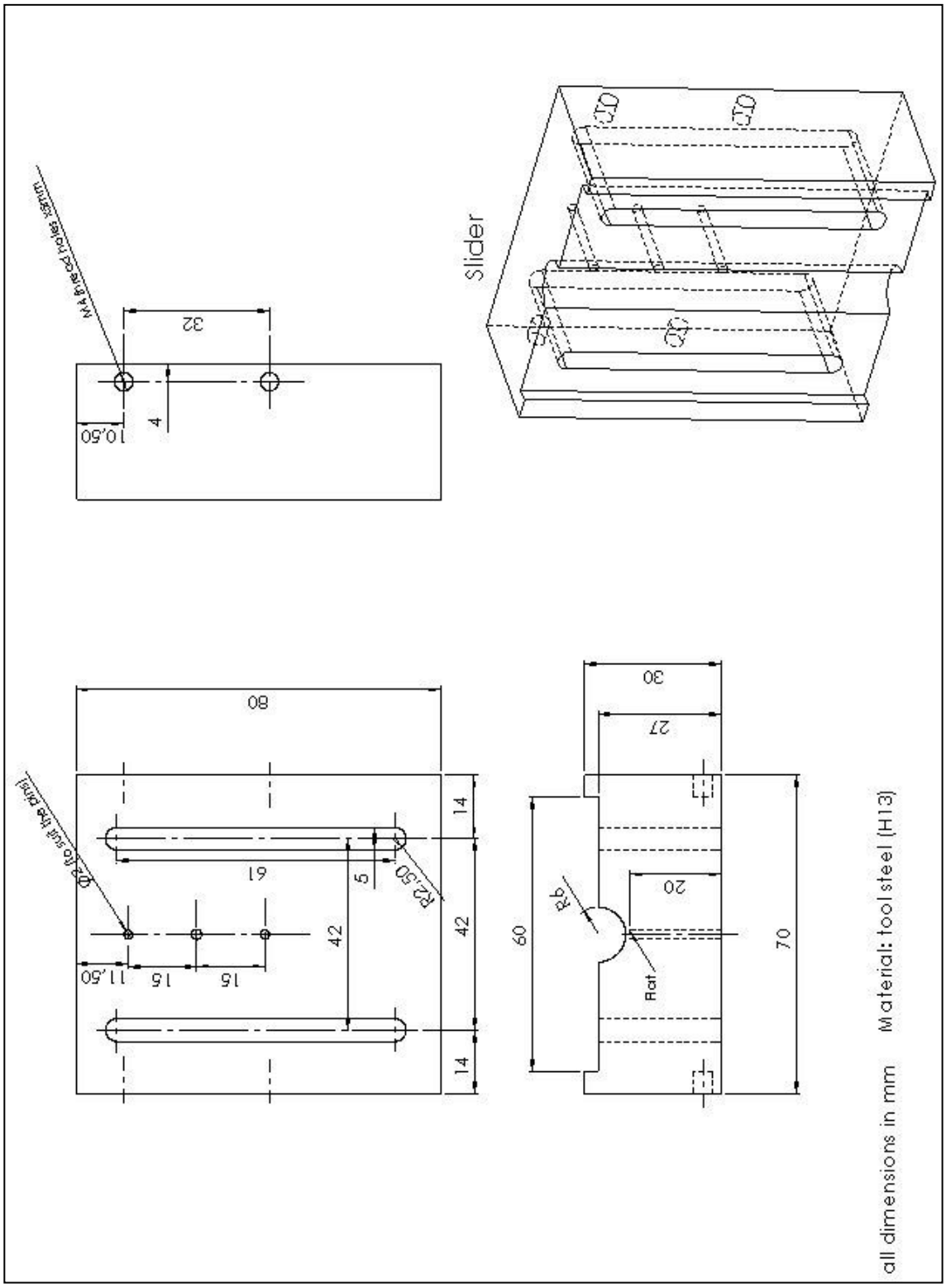

Figure E 9 Slider - device 2

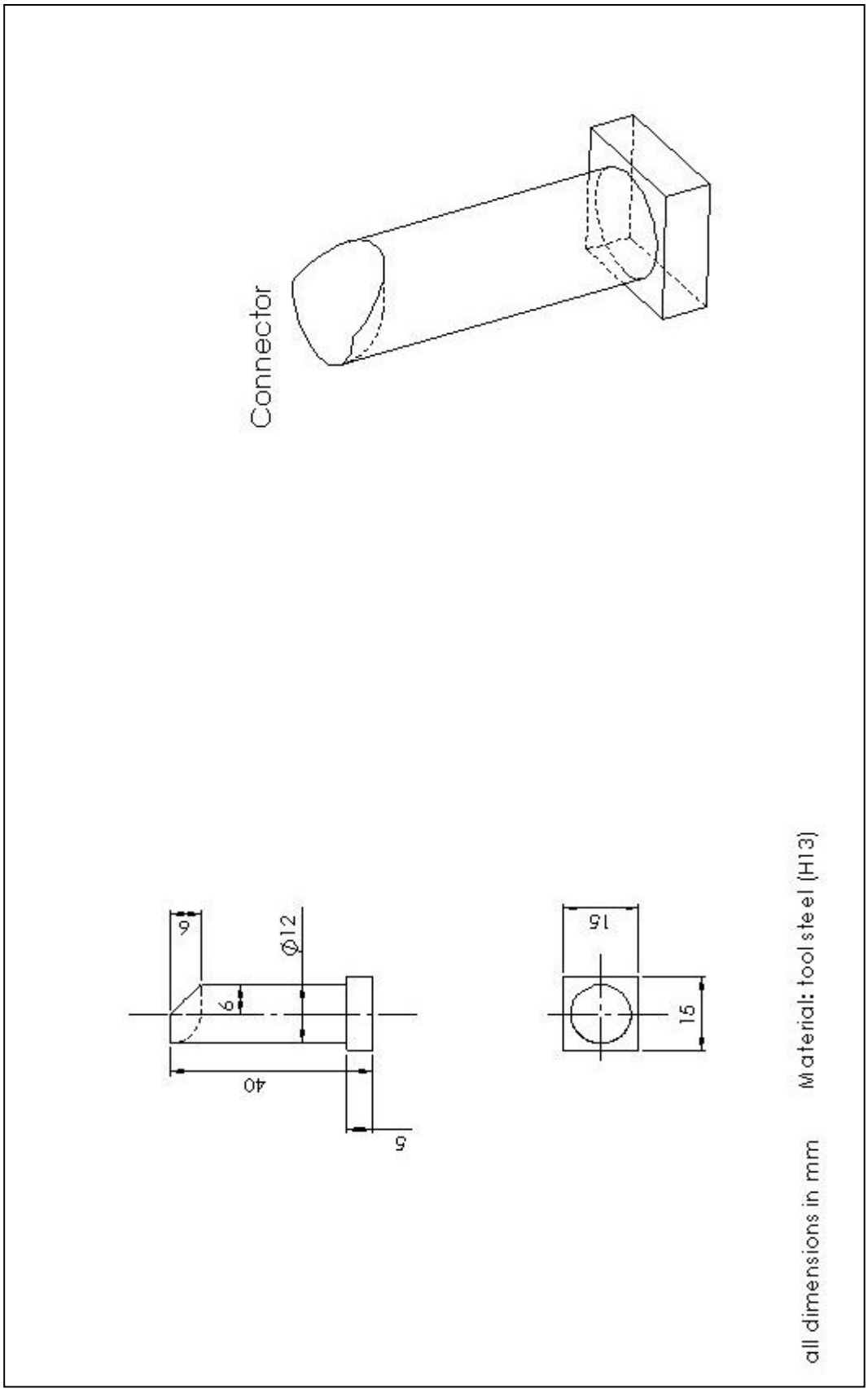

Figure E 10 Connector - device 2

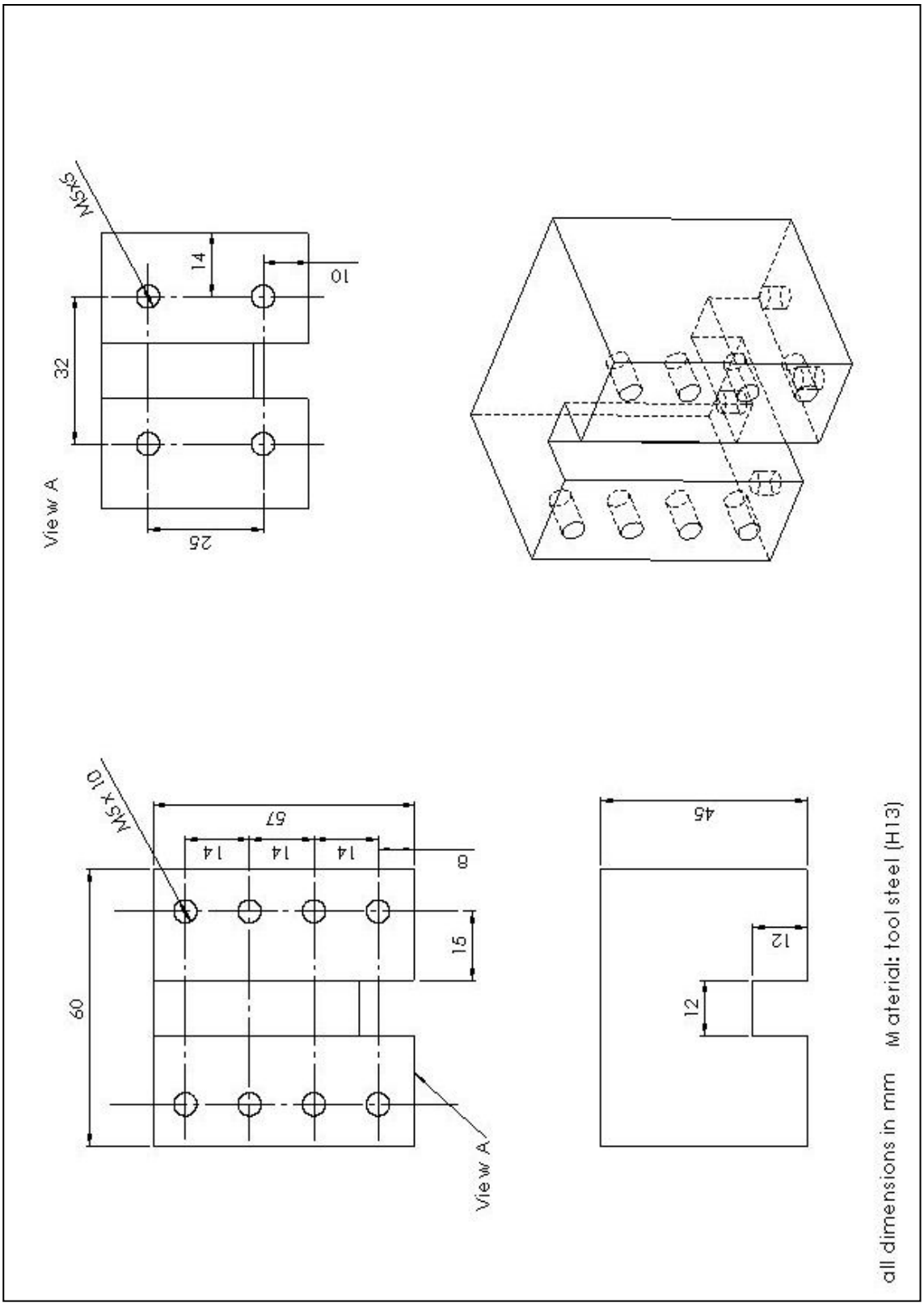

Figure E 11 Main block – device 3

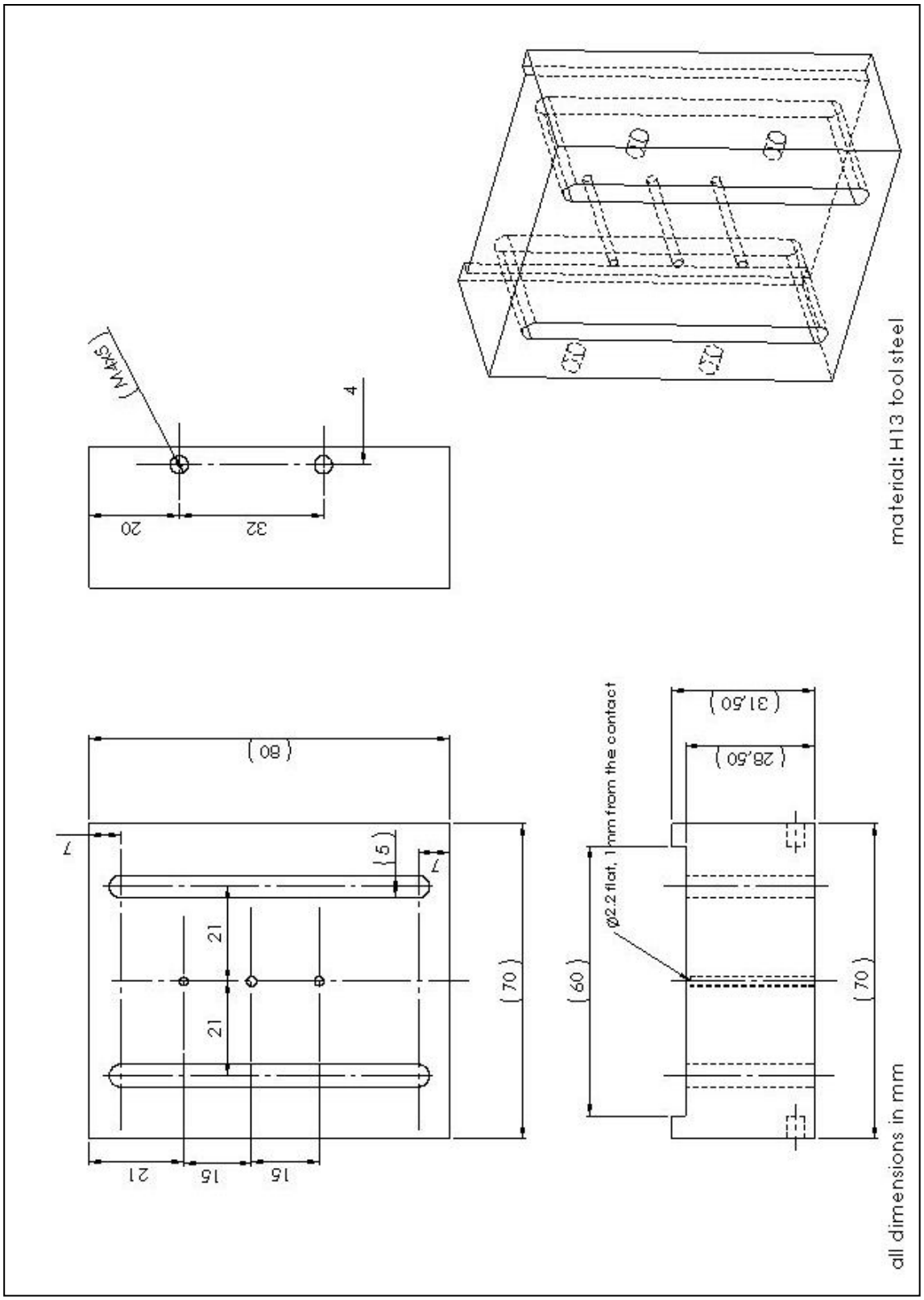

Figure E 12 Slider – device 3

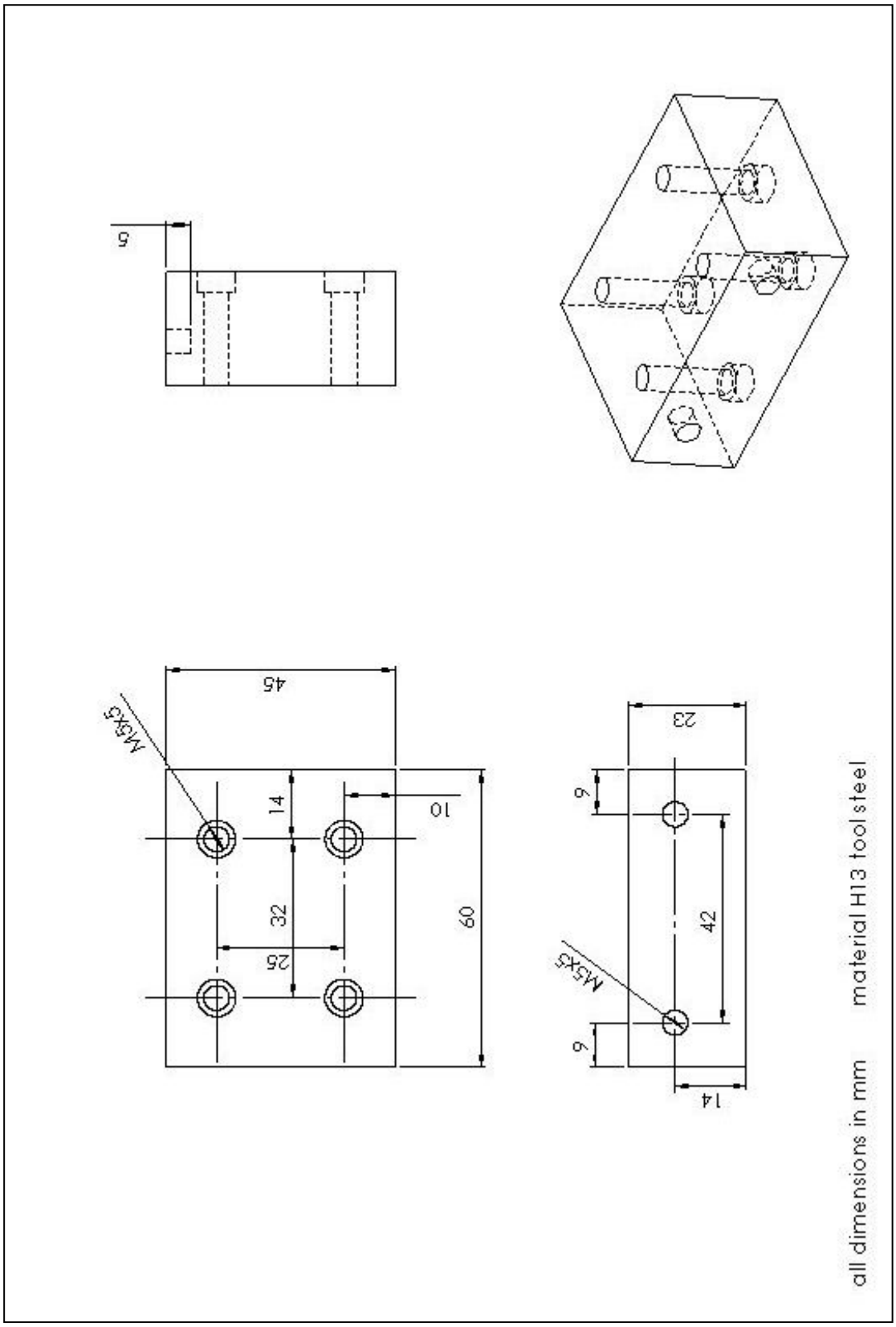

Figure E 13 Base - device 3

APPENDIX F: Landing frame technical drawings of major elements

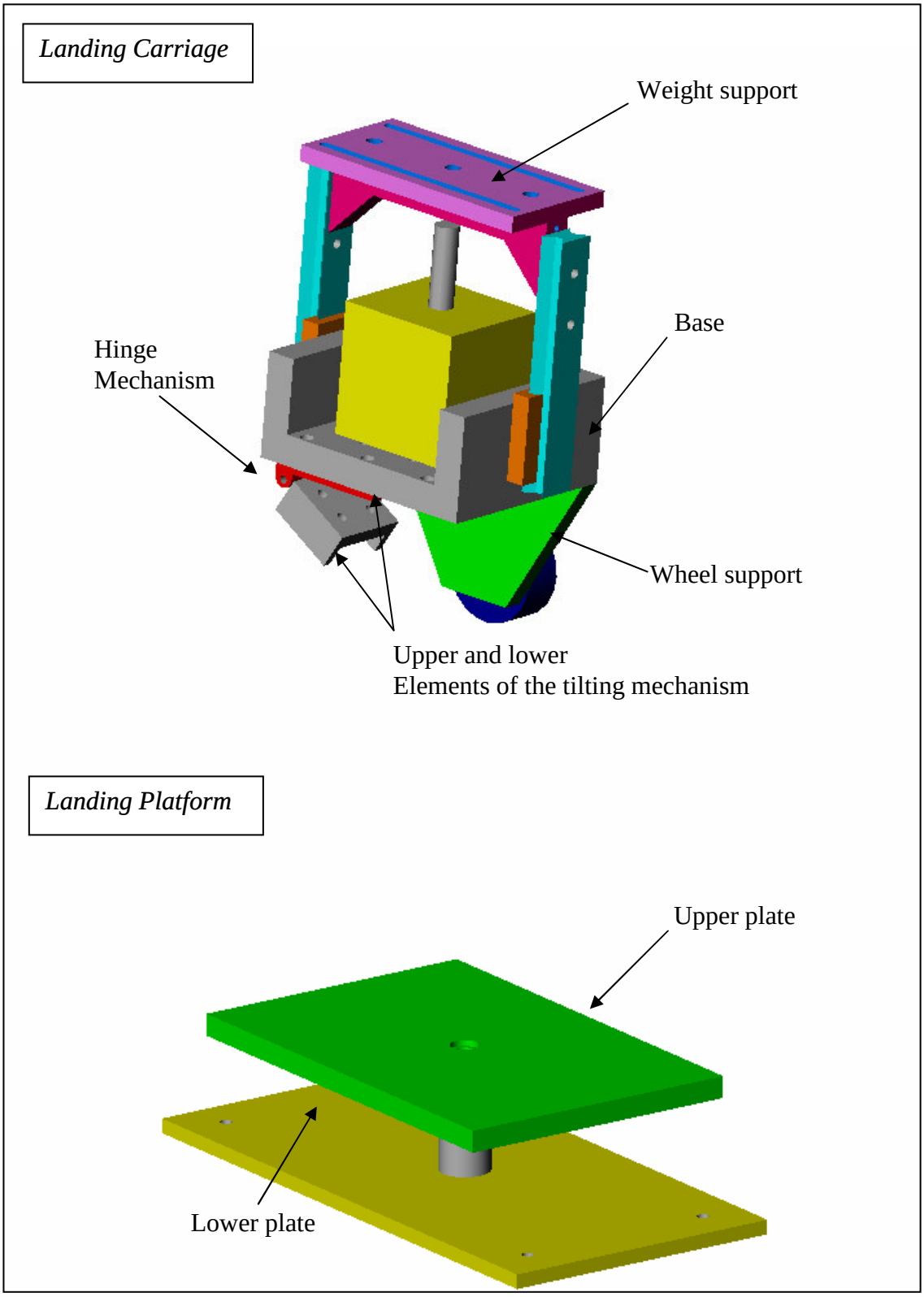

Figure F 1 Landing Carriage and landing Platform

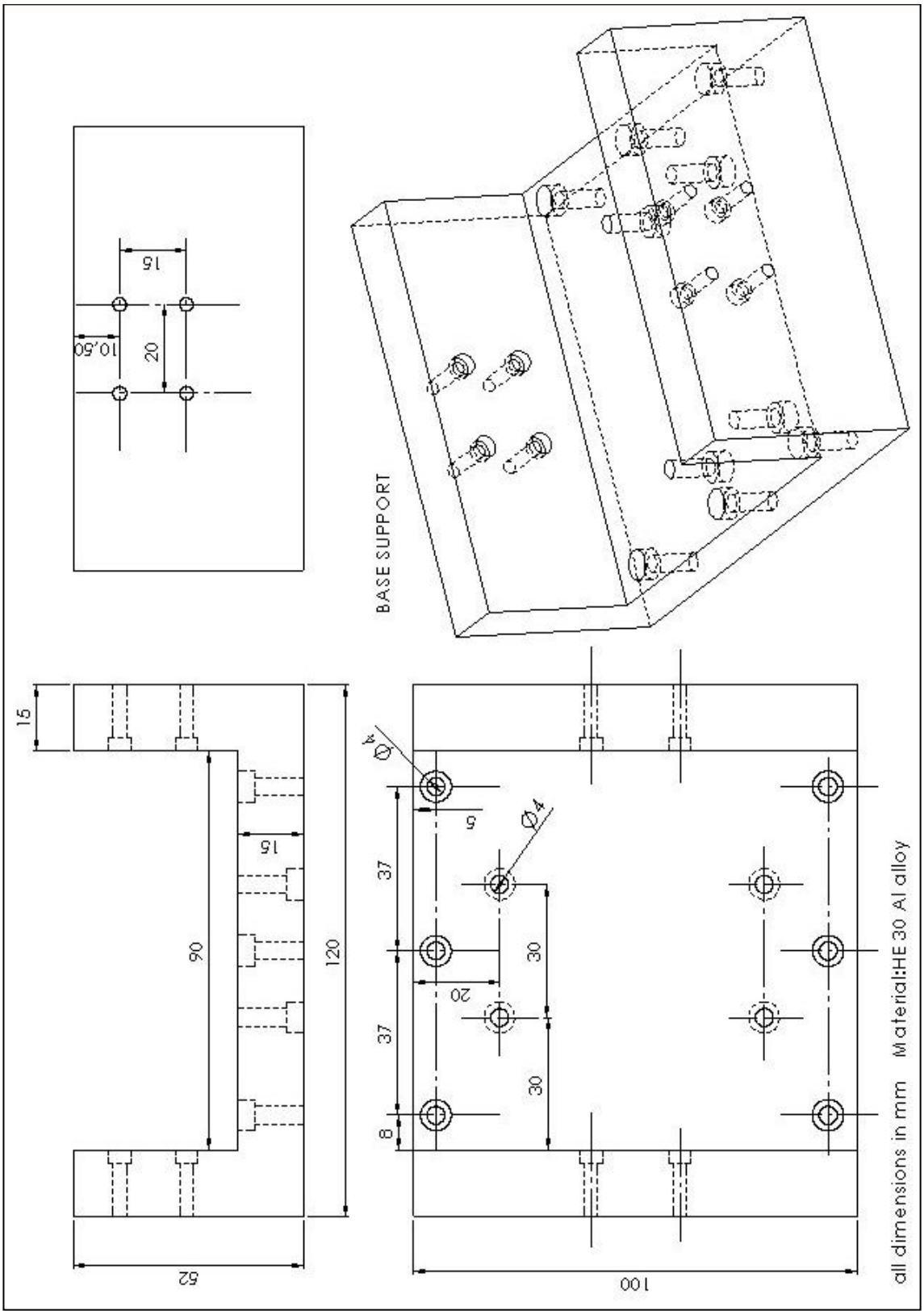

Figure F 2 Landing carriage - base

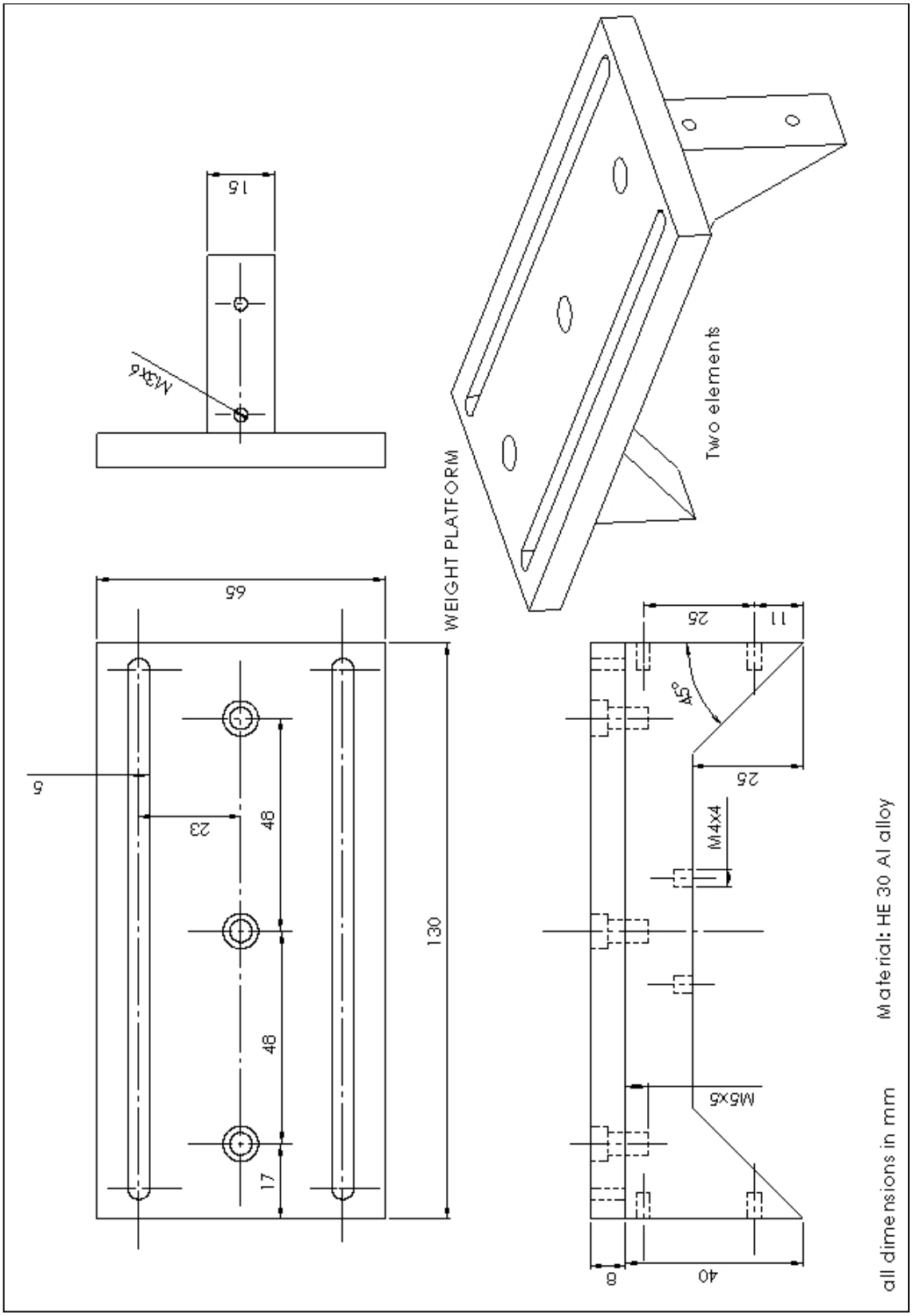

Figure F 3 Landing carriage - weight support

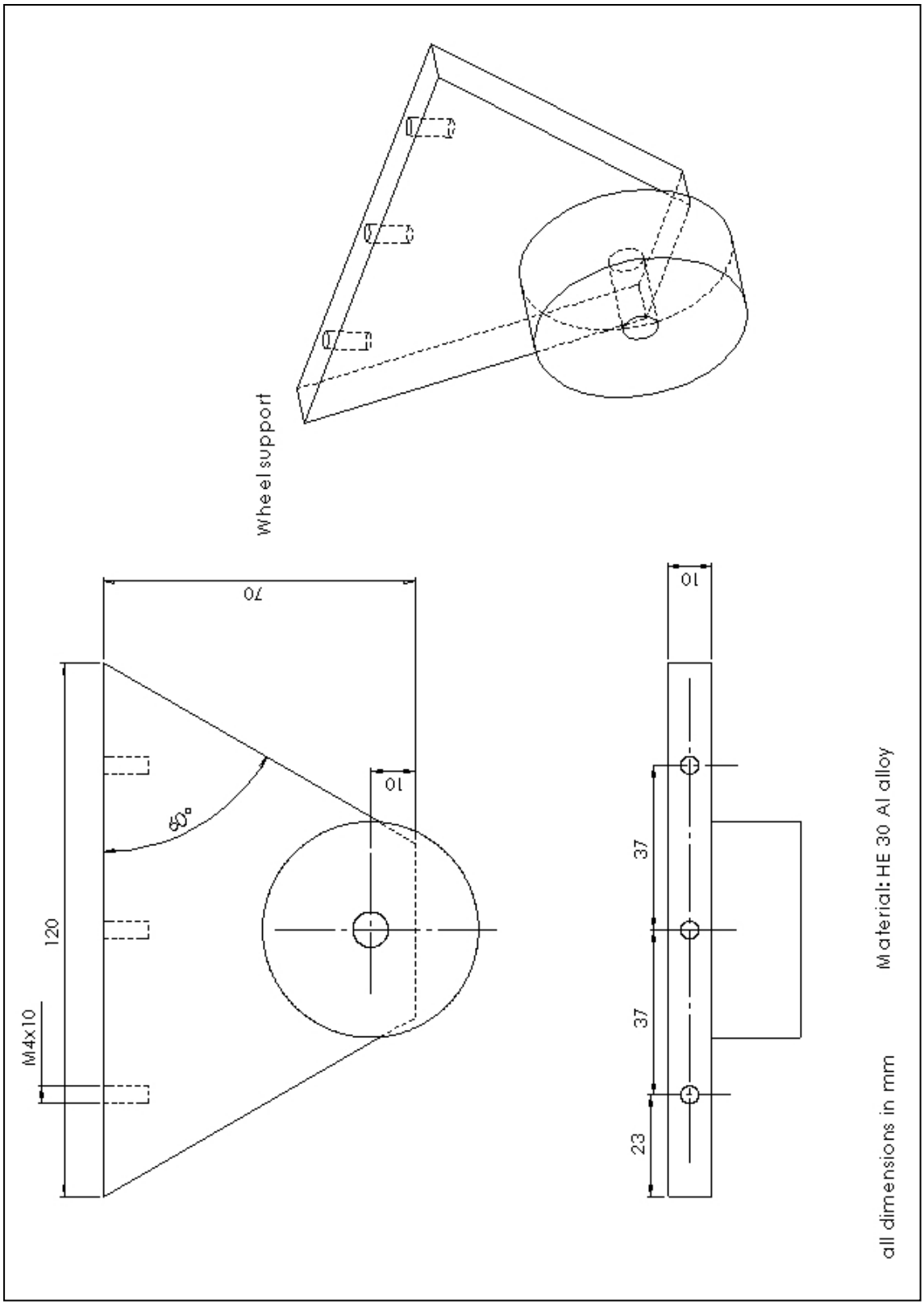

Figure F 4 Landing carriage - wheel support

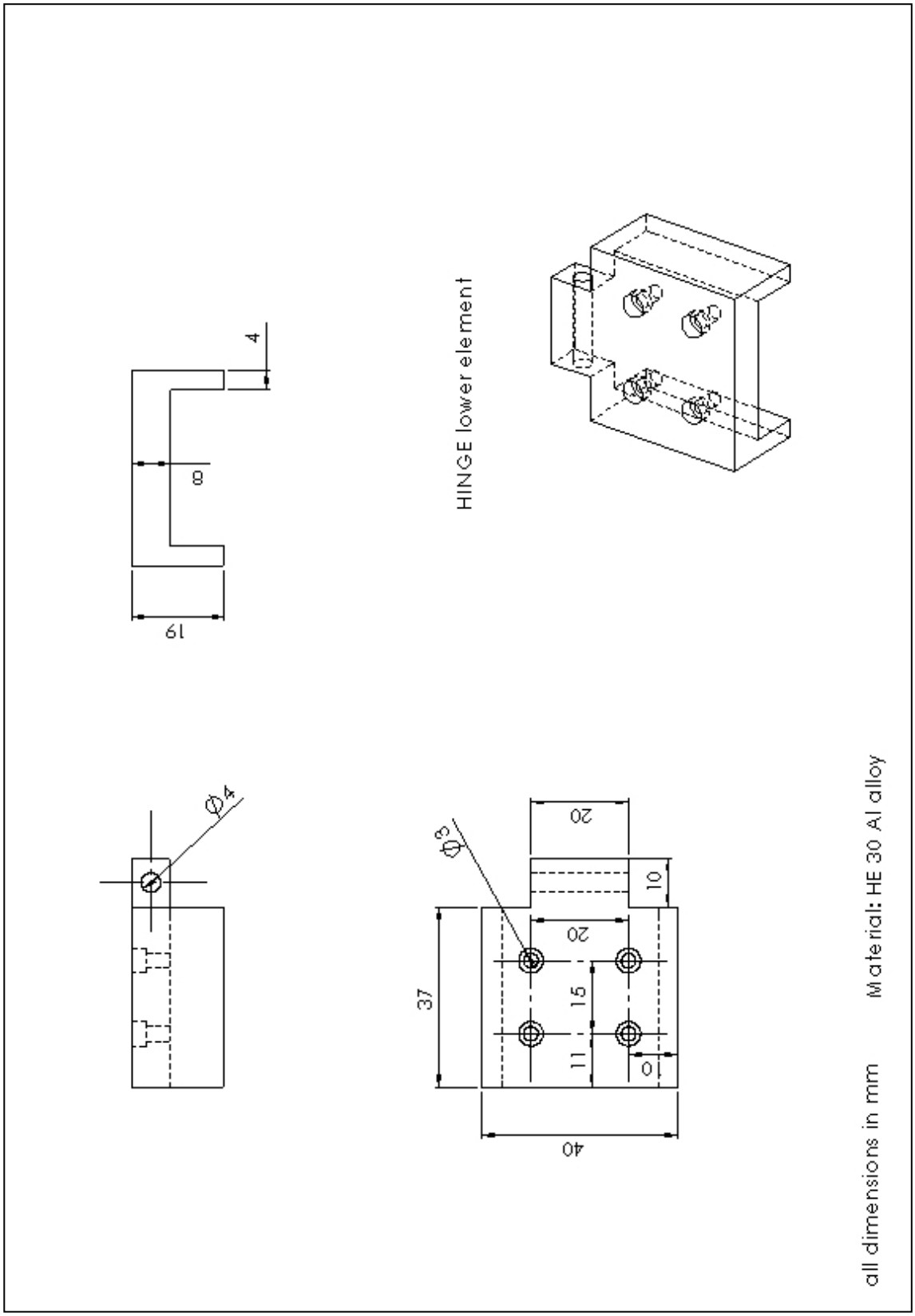

Figure F 5 Tilting mechanism - lower element

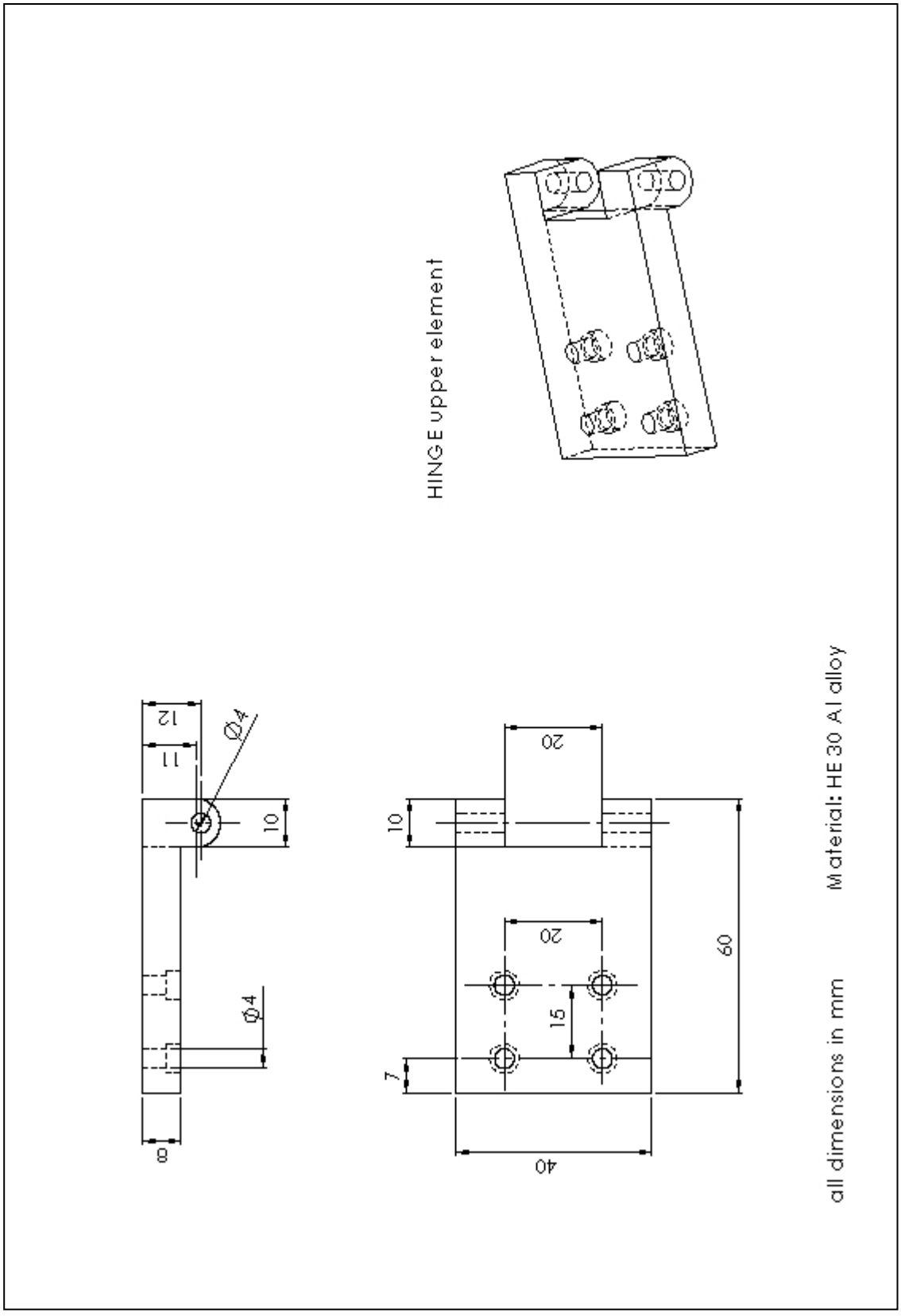

Figure F 6 Tilting mechanism - upper element

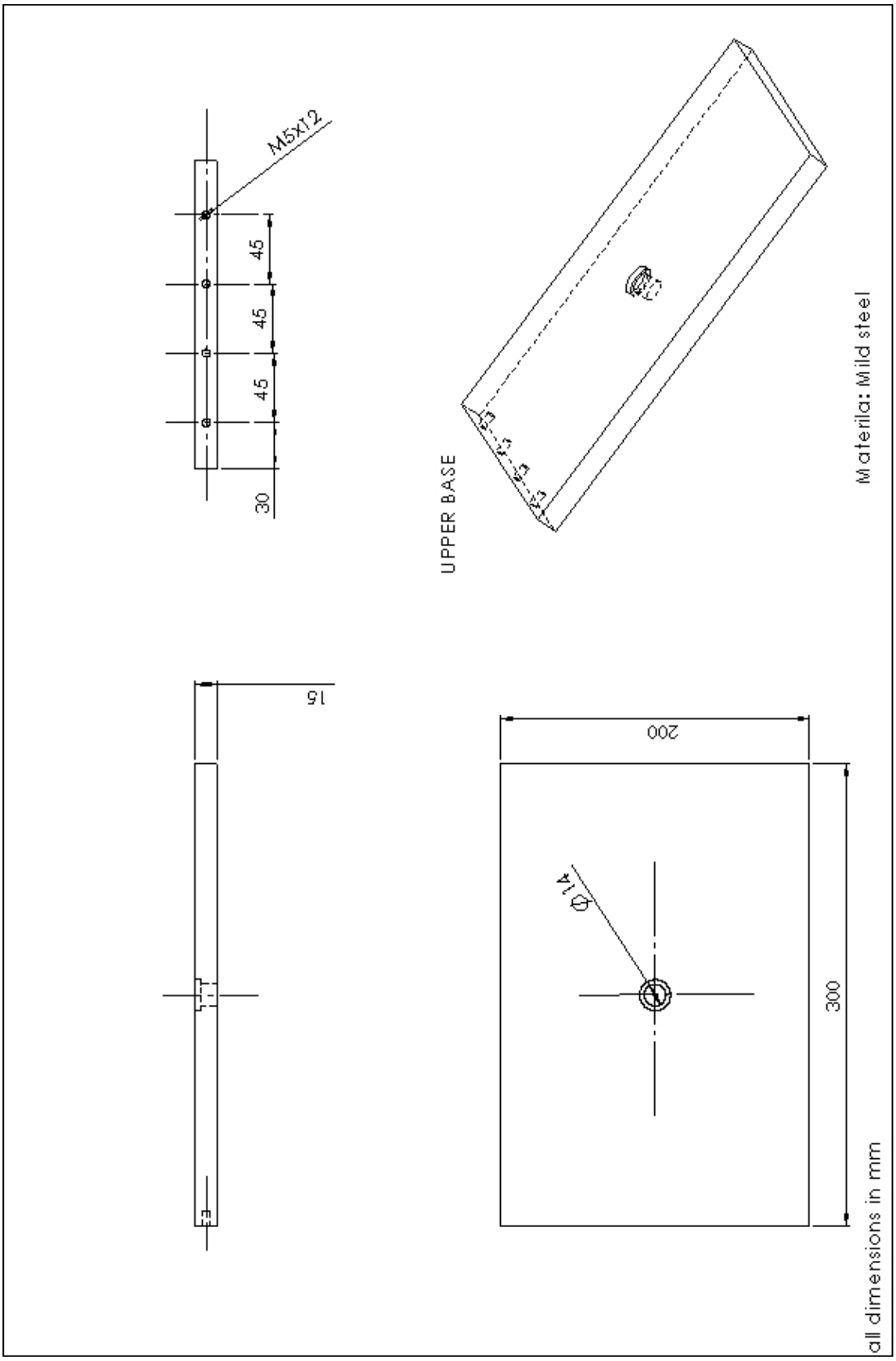

Figure F 7 Landing platform - upper plate

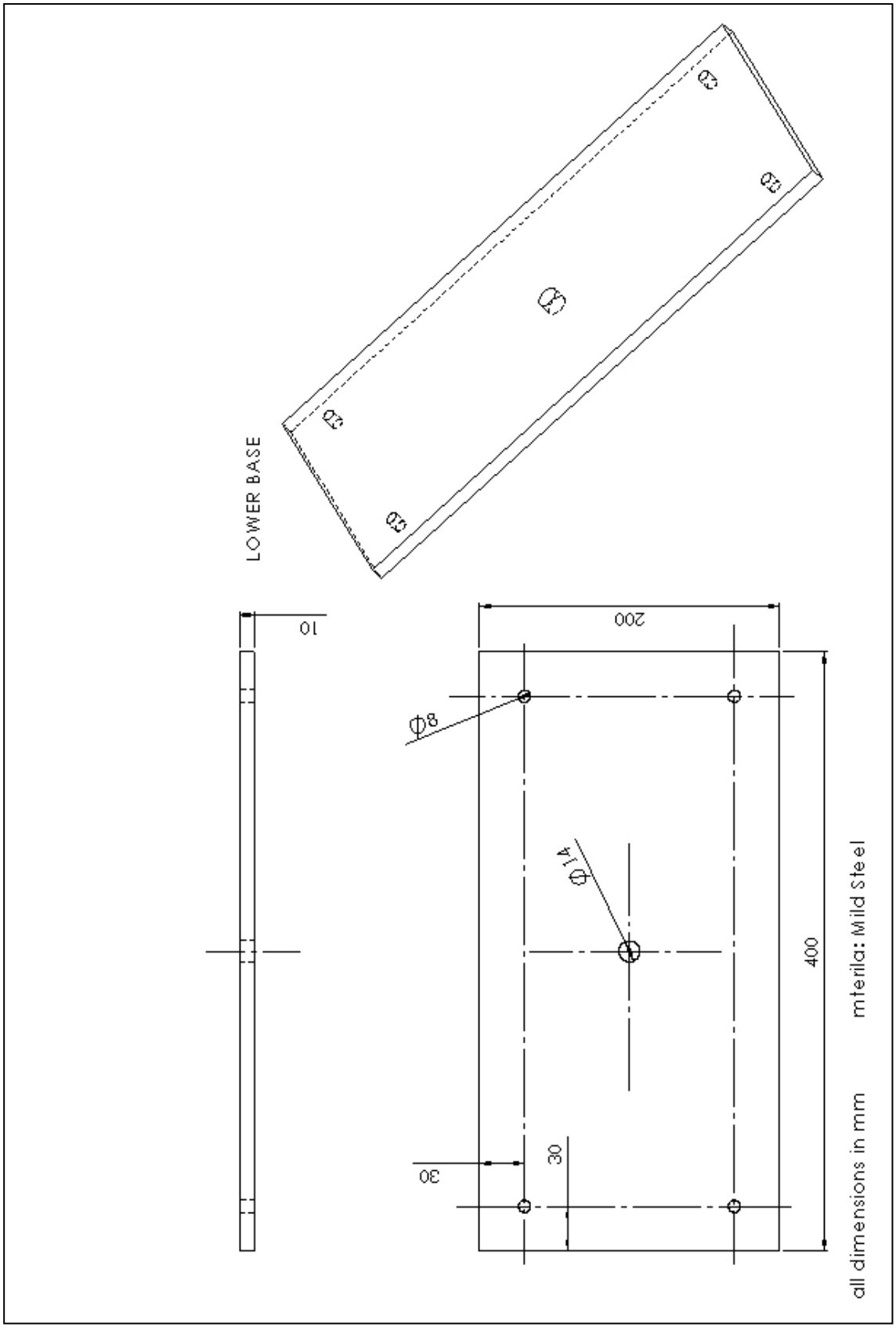

Figure F 8 Landing platform - lower plate

APPENDIX G: Published papers

Journal Publications

1. Rocco Lupoi, F.H. Osman "Loading behaviour of 90^0 'UREAD' energy channels", *International Journal of Crashworthiness*, Vol. 13, No. 2, April 2008, 195-203.

2. Rocco Lupoi, F.H. Osman "Investigation into Channel Angular Extrusion and the UREAD energy absorption technique", *International Journal of Mechanical Sciences*, 50 (2008), 966-973.

3. Rocco Lupoi, F.H.Osman "Analysis of tool cavity stresses in channel angular extrusion", Key-Engineering Materials, Vols. 340-341, (2007),1381-1386.

4. Rocco Lupoi, F.H.Osman "Under surface pressure sensing technique for the evaluation of contact stresses", Journal of Material Processing Technology, 164-165 (2005), 1537-1543.

Conference Publications

1. Rocco Lupoi, F.H.Osman "Analysis of tool cavity stresses in channel angular extrusion", AEPA 2006 conference, September 2006, Nagoya (Japan).

2. Rocco Lupoi, F.H.Osman "Characterization of a single 90-degrees 'UREAD' energy channel ", ICRASH 2006 conference, July 2006, Athens (Greece).

3. Rocco Lupoi, F.H. Osman "Revolutionary devices to dissipate energy in mechanical systems", poster publication in the PGA 2006 conference, June 2006, University of Bath (UK).

4. Rocco Lupoi, F.H.Osman "A new Approach for experimental evaluation of contact stresses", AMPT 2005 conference, May 2005, Wisla (Poland), KEYNOTE paper.

5. Rocco Lupoi, F.H.Osman "Use of concealed pressure pins to determinate contact stresses in ring compression", ESAFORM 2005 conference, April 2005, Cluj-Napoca (Romania).

A New Approach for Experimental Evaluation of Contact Stresses

R. Lupoi and F. H. Osman*

Department of Mechanical Engineering, University of Bath,
Claverton Down, Bath BA2 7AY, UK

Abstract: In metal forming operations, the intensity and distribution of stresses at the tool/material interface have great influence on the pattern and mode of deformation. This is due to the effect of frictional forces in being resistive to material movements and hence affects material flow and the directionality of volume distribution of material inside die cavities. This paper explores the use of the pressure pin technique for the measurement of tool stresses at the interface between the tool and the deforming workpiece material. It also introduces a new experimental methodology for the measurement of stresses where the measuring device is concealed inside the tool and not subjected to the severe conditions at the interface surface. Each tool containing measuring devices is split into two parts, one part has the shape to be formed (industrial die), while the second part includes the pressure pin measuring column. Friction resistance and friction coefficient are evaluated across the billet surface and at different stages of deformation.

Keywords: Pressure pin, Interface Friction, Tool Stresses, Contact Stresses

1. INTRODUCTION

In metal forming operations contact conditions, tool stresses and friction forces in particular, have great influence on the behaviour of material deformation and the mode by which material flow is directed. This applies to almost all contact forming processes, from simple geometry operations like compression, extrusion and rolling to complex forming patterns such as those produced by forging. Under industrial conditions, little is known about the local variation in contact properties and their effects on wear, surface cracks, tool deflection and tool damage. Surface stresses are also important in the tool design process with respect to tool definitions and features. When considering the nature of material deformation and the introduction of full numerical simulation to metal forming analysis, accurate description and characterisation of contact properties become necessary for obtaining a realistic solution.

Measurements of contact stresses using sensitive pins, usually incorporating strain-gauge circuitry and mounted in the pressing tool, have been used to provide estimates of tool stresses at the interface in forming operations, including extrusion and rolling [1,2]. Piezo-electric and optical device sensing techniques have been used in the basic pin construction for signal detection [3,4]. Use of a three-pin system has been introduced so as to evaluate frictional stresses and the coefficient of friction at the tool/material interface [5].

This paper investigates the design of a new experimental set up incorporating the pressure pin technique. Stress components are measured at different angles to the surface of contact and compared with those obtained from the slab analysis technique. The proposed experimental set-up is adaptable to both cold and hot forming operations.

*Corresponding author. *E-mail address*: F.Osman@bath.ac.uk

2. SENSITIVE PRESSURE PIN DESIGN

In order to measure stresses along contact surfaces, sensors must be attached to the tool and have presence at such particular location. Some of the conditions at the interface are complex or severe for the use of sensitive devices, for example the application of lubricants and heat, the presence of scale, and material shearing actions are some of the elements that could seriously affect the measurements.

2.1. Sensitive Pins

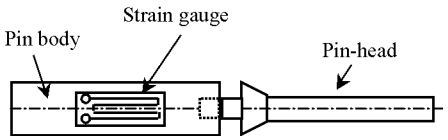

Figure 1. Sensitive pin typical construction

One of the methods that showed some resilience to surface conditions is the use of the sensitive pressure pins. They are made of similar material to that of the tool, therefore they could be considered as part of the tool. Figure 1 shows the shape and construction of a typical sensitive pressure pin. Because of its small size and its deformation characteristics, being similar to the tool, its presence is always assumed not to affect the measurements or the deformation process. The pin-head transmits the load to the main body of the pin, which contains a load cell. Strain gauge bridge or small commercial load cells are commonly used with such pins. The load cell may be insulated from the pin head by introducing a layer of low thermal conductivity material, such as Zirconia, between the two parts.

3. A NEW STRATEGY FOR MEASUREMENTS OF TOOL STRESSES

Figure 2 shows the construction of a two-die system where the pin-head is embedded and concealed inside the forming tool. For this designs, the pin is made from harden tool steel with 2mm diameter pin-head and positioned 1 mm below the contact surface. Therefore, temperature, lubrication and scale will have diminishing effects on the measurements. The stress at the interface may be composed of the vertical component, that is normal to the interface and the horizontal component acting along and parallel to the surface of contact; it may be expressed as 'friction stress'. Using a die with oblique pins, the two components can be evaluated as a function of the oblique angle α, as shown in Figure 3. For this work two inclined pins are used and positioned at 45^0 and 30^0 degrees with the vertical. The forces, *F1 & F2*, acting on a two pins system, may be expressed as shown in Figure 3

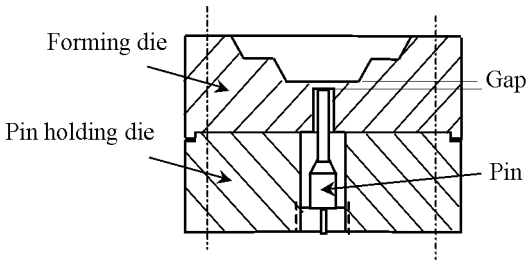

Figure 2. Two-die system

$$\begin{cases} Pin1 \Rightarrow F_1 = A(P\cos\alpha_1 + \tau\sin\alpha_1) \\ Pin2 \Rightarrow F_2 = A(P\cos\alpha_2 + \tau\sin\alpha_2) \end{cases}$$

Where,
A : Contact area of the pin head
P : Vertical pressure component
τ : Shear/Friction component
α : Pin angle with the vertical

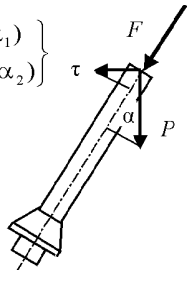

Figure 3. Forces on Pin-head

4. EXPERIMENTAL RESULTS

The new two-die arrangement design, where the pins are split between the industrial and measuring dies, were used to compress, under dry conditions, soft commercial 99.5% purity aluminium. Cylindrical specimens of 25 mm diameter and 30 mm height were used in all experiments. The material yield strength was found to be 100 MPa. The position of the pins is fixed inside the tool and therefore the stress distribution across the interface with the billet is obtained by using several billets. When inclined pins were used flush to the contact surface [5], an anti-rotation mechanism was fitted to the pin column to prevent the pin elliptical cross sectional area from being locked with the die surface. Such complication has been eliminated in the two-die arrangement where the pin-head is not subjected to any rotational force. The calibration of pins was carried out by applying different loads to dies that were perfectly closed on a thin disk of aluminium. Also, a comparison has been performed between the load applied by the press and the total load obtained from the measured local distribution of normal tool stresses to ensure comparability, sensitivity and conformity of the pin calibration.

Using the die with oblique pins, billets were compressed with load of 400kN to reduce them to approximately 8mm in height. Eight billets were used for the measurement of local stress distribution across the deformed billets.

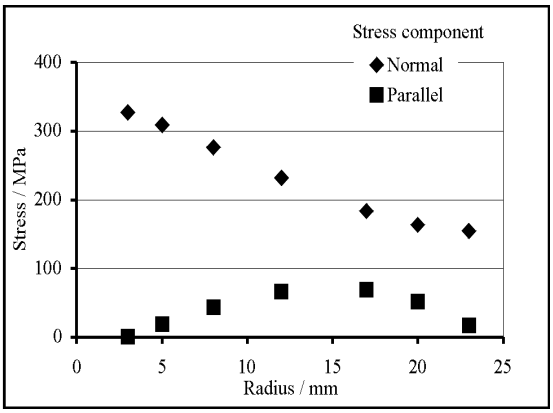

Figure 4. Stress component from angled pins

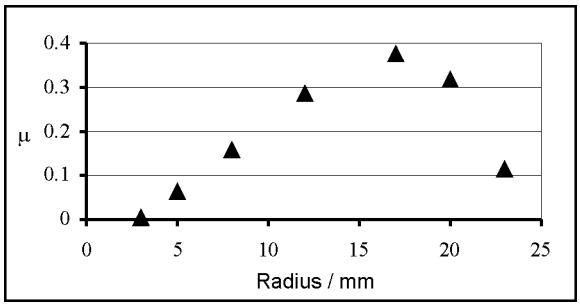

Figure 5. Distribution of friction coefficient

Figure 4 shows the distribution of the two components of stress at the interface. The normal pressure curve exhibits increasing values from the centre of the billet and lower values near the end of the billet. In particular, the pressure value measured near the external radius is close to the material yield stress, this is in agreement with the Tresca criterion [6]. On the other hand, the parallel/friction stress distribution shows a low value, near to zero, in the vicinity of the billet centre. The normal and parallel measured components of stress given in Figure 4 were used to evaluate the coefficient of friction. Figure 5 shows the variation of the coefficient of friction across the surface of the billet. It steadily increases, reaching a peak near $\mu = 0.4$ then decreases towards the end of the billet.

Figure 6 shows a comparison of the measurements of the normal pressure distribution, using the vertical pins, at an early stage of the process (20mm billet height), and at the end of the process (8mm billet height). The figure also includes the results of the oblique pins and the theoretical distribution of the normal component of stress, calculated by the classical slab method [6] using 0.2 as friction coefficient.

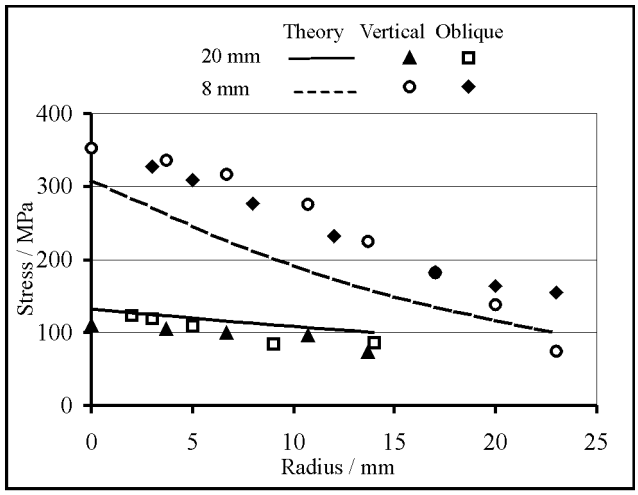

Figure 6. Tool normal stresses oblique/vertical pins and theory comparison

Knowledge of the state of stress and the shape of the friction function at the interface is of significance in many material forming processes. Also, it could be combined with analysis to give better prediction of metal flow, tool stresses and assist in the tool design process.

5. CONCLUSIONS

A new die design methodology, incorporating embedded sensitive pressure pins was introduced. The method provides a set up where industrial dies could be used within laboratory conditions to evaluate contact stresses at the interface between the tool and the deforming material. Experiments showed and demonstrated that friction varies along the tool material interface.

The normal stress component was compared with the results obtained from the classical slab method of analysis, the comparison was favourable but it was noted that the slab method employs a constant friction coefficient and has many limitations. It is therefore concluded that this technique is capable of providing experimental data for the simulation of complex metal forming operations for practical use and under industrial conditions.

REFERENCES

1. Frisch, J., 'An experimental study of metal extrusion at various strain rates, *Trans. ASME*, **76**, (1954), 599-606.
2. Tuncer, C., and Dean, T.A., 'Surface stress measurement techniques in metal forming,, *Int. J. Mach. Tools Manufact*, **28**, 4, (1988), 417-428.
3. Cole, I.M., and Sansome, D.H., 'A review of the application of pin load-cell pressure measurement techniques to metal deformation processes', *Proc. 9th MTDR Conf.* , (1968), 271-286.
4. Christensen, P. 'Computer aided design of forging dies using the Upper Bound Technique", *PhD thesis*, Technical University of Denmark, Denmark, (1986).
5. Osman, F.H., Potel, F., Loveday, M.S., 'Measurement of friction characteristics using three pin system', *Key Engineering Materials*, **177**, (2000), 583-588.
6. Ghosh, A and Malik, A.K., *Manufacturing Science*, Ellis Horwood, 1986.

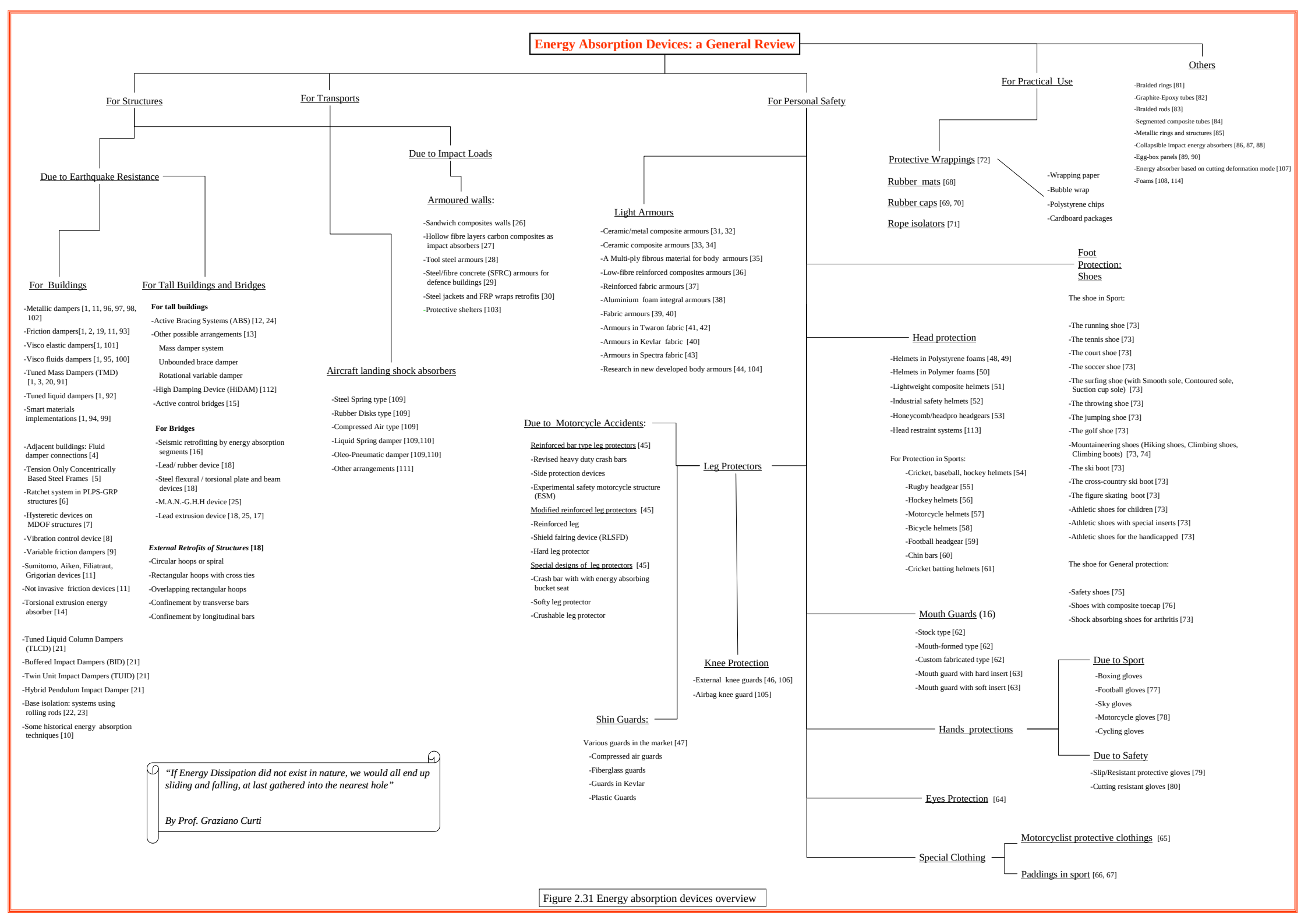

Figure 2.31 Energy absorption devices overview